

ABSOLUTE MOLECULAR ELECTRONIC SPECTROSCOPY AT UV AND SOFT
X-RAY ENERGIES BY HIGH-ENERGY ELECTRON IMPACT

By

Gordon Russell Burton

B.Sc. (Hons.), Queen's University, 1989

A THESIS SUBMITTED IN PARTIAL FULFILLMENT OF
THE REQUIREMENTS FOR THE DEGREE OF
DOCTOR OF PHILOSOPHY

in

THE FACULTY OF GRADUATE STUDIES
CHEMISTRY

We accept this thesis as conforming
to the required standard

C. E. Bruen

A. Mercer

M. C. Gentry

M. B. E.

Andrew Ng

THE UNIVERSITY OF BRITISH COLUMBIA

September 1993

© Gordon Russell Burton, 1993

In presenting this thesis in partial fulfilment of the requirements for an advanced degree at the University of British Columbia, I agree that the Library shall make it freely available for reference and study. I further agree that permission for extensive copying of this thesis for scholarly purposes may be granted by the head of my department or by his or her representatives. It is understood that copying or publication of this thesis for financial gain shall not be allowed without my written permission.

(Signature) Gordon R Burton

Department of Chemistry
The University of British Columbia
Vancouver, Canada

Date October 1, 1993

Abstract

Dipole (e,e) spectroscopy has been used to determine absolute photoabsorption oscillator strengths (cross sections) for electronic excitation of CCl_4 , CH_3OH , NH_3 , CH_3NH_2 , $(\text{CH}_3)_2\text{NH}$, and $(\text{CH}_3)_3\text{N}$ at energy resolutions in the range 0.048–1.0 eV fwhm. These data have been obtained in the valence, and inner shells (Cl 2p,2s; C 1s (CCl_4), and C 1s (CH_3OH)), spanning the visible to soft X-ray equivalent photon energy regions (5.0–400 eV). Absolute scales have been established using the Thomas-Reiche-Kuhn sum rule.

Dipole (e,e+ion) spectroscopy has been employed to study the molecular and dissociative photoionization in the valence shell of CH_3OH , and in the valence and inner shells of CCl_4 . Time-of-flight mass spectroscopy is used to determine photoionization branching ratios and photoionization efficiencies. These data are combined with the corresponding absolute photoabsorption oscillator strength data, to determine the partial oscillator strengths for the molecular and dissociative photoionization channels of these molecules. In addition, the measurements have been used to provide detailed quantitative information on the breakdown pathways of these molecules following the absorption of energetic radiation.

The absolute photoabsorption measurements for ammonia and the methylamines have been used in a collaborative research project with Professor W.J. Meath, involving theoretical work at the University of Western Ontario. The results provide accurate values for many of the dipole properties of these nitrogen-containing molecules, as well as integrated

dipole oscillator strength distributions for the entire photoabsorption spectrum.

In other work, a new high impact energy electron energy-loss spectrometer of high sensitivity has been designed and constructed. This instrument features an open scattering region, high incident electron beam energy, and multichannel detection, in order to measure absolute photoabsorption oscillator strength data for not only stable atoms and molecules, but also for low-density targets including free radicals, ions, and laser-excited species.

Table of Contents

Abstract	ii
List of Tables	viii
List of Figures	xi
List of Abbreviations	xiv
Acknowledgements	xvi
1 Introduction	1
2 Theory	6
2.1 Definition of the Oscillator Strength	6
2.2 Photoabsorption and Electron Energy-Loss Spectroscopy	7
2.3 Photoionization	10
2.4 The Bethe Theory of Electron Impact	12
2.5 Sum Rules	17
2.6 Molecular Orbital Description and Spectral Interpretation	18
2.7 The Variation of Momentum Transfer in Dipole (e,e) Experiments—Effects on Measured Oscillator Strengths	21
2.8 Construction of Dipole Oscillator Strength Distributions	25
3 Experimental Methods	30

3.1	Low-Resolution Dipole (e,e) and (e,e+ion) Spectrometer	31
3.1.1	The Partial TRK Sum Rule and Corrections for Pauli-Excluded Transitions	35
3.1.2	Ion Detector Response Functions	39
3.2	High-Resolution Dipole (e,e) Spectrometer	44
3.3	Sample Handling	47
3.4	High Impact Energy Dipole (e,e) Spectrometer	49
3.4.1	Specialized Sample Introduction Systems	56
4	Photoabsorption and Photoionization Studies of Methanol	59
4.1	Introduction	59
4.2	Results and Discussion	62
4.2.1	Electronic Structure	62
4.2.2	Photoabsorption Oscillator Strengths	63
4.2.2.1	Low-Resolution Measurements	63
4.2.2.2	High-Resolution Measurements	66
4.2.2.3	Carbon K-shell Measurements	68
4.2.3	Molecular and Dissociative Photoionization in the Valence-Shell Region	70
4.2.4	The Dipole-Induced Breakdown of Methanol	74
5	Photoabsorption and Photoionization Studies of Carbon Tetrachloride	100
5.1	Introduction	100
5.2	Results and Discussion	103
5.2.1	Electronic Structure	103

5.2.2	Photoabsorption Oscillator Strengths	103
5.2.2.1	Low-Resolution Measurements	103
5.2.2.2	High-Resolution Measurements	106
5.2.2.3	Inner-Shell (Cl 2p,2s; C 1s) Measurements	108
5.2.3	Dissociative Photoionization in the Valence-Shell Region	111
5.2.4	The Dipole-Induced Breakdown of Carbon Tetrachloride	118
5.2.4.1	The Proposed Dipole-Induced Breakdown Scheme for the Low-Energy Valence Region	118
5.2.4.2	The Dissociative Photoionization of CCl ₄ in the Cl 2p Inner-Shell Region	125
6	Photoabsorption and DOSD Studies of Ammonia	147
6.1	Introduction	147
6.2	Results and Discussion	150
6.2.1	Electronic Structure	150
6.2.2	Absolute Photoabsorption Measurements for Ammonia Obtained at Low Resolution	151
6.2.3	Absolute Photoabsorption Measurements for Ammonia Obtained at High Resolution	157
6.3	Constrained Dipole Oscillator Strength Distributions and Related Properties	164
6.3.1	Dipole Oscillator Strength Distribution for Ammonia	165
6.3.2	Dipole Properties for Ammonia	170
6.3.3	The Reliability of Calculated Dipole Properties	175
7	Photoabsorption and DOSD Studies of the Methylamines	191

7.1	Introduction	191
7.2	Results and Discussion	193
7.2.1	Electronic Structure of the Methylamines	193
7.2.2	Absolute Photoabsorption Measurements for the Methylamines Ob- tained at Low Resolution	194
7.2.3	Absolute Photoabsorption Measurements for the Methylamines Ob- tained at High Resolution	199
7.3	Dipole Oscillator Strength Distributions and Properties for the Methy- lamines	207
7.3.1	General Considerations	207
7.3.2	Monomethylamine	208
7.3.3	Dimethylamine and Trimethylamine	210
7.3.4	The Reliability of the Calculated Dipole Properties	213
8	Concluding Remarks	233
	Bibliography	235

List of Tables

2.1	Photon-matter interaction processes	8
3.1	Sample purity	48
3.2	Inner shell binding energies	54
4.1	Absolute oscillator strengths for the total photoabsorption and the molecular and dissociative photoionization of methanol below 80 eV	83
4.2	Absolute oscillator strengths for the total photoabsorption of methanol from 50 to 280 eV	88
4.3	Absolute oscillator strengths for the total photoabsorption of methanol in the carbon 1s region	90
4.4	Branching ratios for the molecular and dissociative photoionization of methanol	92
4.5	Calculated and measured appearance potentials for the production of positive ions from methanol	96
4.6	Proposed dipole induced breakdown scheme for methanol	99
5.1	Absolute photoabsorption and photoionization oscillator strengths for carbon tetrachloride	130
5.2	Absolute oscillator strengths for the total photoabsorption of carbon tetrachloride from 195 to 400 eV	136

5.3	Branching ratios for the dissociative photoionization of carbon tetrachloride from 11 to 80 eV	141
5.4	Calculated and measured appearance potentials for the production of positive ions from carbon tetrachloride	145
5.5	Branching ratios for the dissociative photoionization of carbon tetrachloride from 195.5 to 220.5 eV	146
5.6	Absolute oscillator strengths for the total photoabsorption and the dissociative photoionization of carbon tetrachloride from 195.5 to 220.5 eV . .	146
6.1	Absolute oscillator strengths for ammonia	178
6.2	Absolute integrated oscillator strengths for ammonia from 5.67 to 7.42 eV	182
6.3	Absolute integrated oscillator strengths for ammonia from 7.42 to 8.62 eV	183
6.4	Absolute integrated oscillator strengths for ammonia from 8.62 to 9.32 eV	184
6.5	Absolute integrated oscillator strengths for ammonia from 9.32 to 10.21 eV	185
6.6	Absolute integrated oscillator strengths for ammonia from 10.21 to 11.53 eV	186
6.7	Integrated dipole oscillator strengths for ammonia	187
6.8	Dipole properties for ammonia	189
6.9	Molar refractivity data for ammonia	190
7.1	Vertical ionization potentials for the electronic states of the methylamines	215
7.2	Oscillator strengths for the total photoabsorption of monomethylamine .	216
7.3	Oscillator strengths for the total photoabsorption of dimethylamine . . .	218
7.4	Oscillator strengths for the total photoabsorption of trimethylamine . . .	220
7.5	Proposed assignments for monomethylamine	222
7.6	Proposed assignments for dimethylamine	223

7.7	Proposed assignments for trimethylamine	224
7.8	Integrated dipole oscillator strengths for monomethylamine	225
7.9	The calculated dipole properties for monomethylamine	226
7.10	Molar refractivity data for monomethylamine	227
7.11	Integrated dipole oscillator strengths for dimethylamine	228
7.12	Integrated dipole oscillator strengths for trimethylamine	229
7.13	The calculated dipole properties for dimethylamine	230
7.14	The calculated dipole properties for trimethylamine	231
7.15	Molar refractivity data for dimethylamine and trimethylamine	232

List of Figures

2.1	Schematic of molecular electronic states	20
3.1	The low-resolution dipole (e,e+ion) spectrometer	32
3.2	Ion detector response functions	41
3.3	The high-resolution dipole (e,e) spectrometer	45
3.4	New high impact energy dipole (e,e) spectrometer	51
3.5	Simulated electron ray traces	52
4.1	Absolute oscillator strengths for the photoabsorption of methanol	64
4.2	Comparison of low- and high-resolution oscillator strengths for methanol	67
4.3	Oscillator strength distribution of methanol in the valence and carbon K-shell regions	69
4.4	Time-of-flight mass spectrum of methanol at 50 eV	72
4.5	Photoionization branching ratios for methanol	73
4.6	Absolute partial photoionization oscillator strengths for methanol	75
5.1	Absolute photoabsorption oscillator strengths for carbon tetrachloride ob- tained at low resolution	105
5.2	Absolute high- and low-resolution oscillator strengths for carbon tetrachlo- ride	107
5.3	Absolute low-resolution oscillator strengths for carbon tetrachloride in the valence- and inner-shell regions	109

5.4	Absolute photoabsorption oscillator strengths for the chlorofluoromethanes	112
5.5	The TOF mass spectrum of carbon tetrachloride at 50 eV	114
5.6	Branching ratios for the dissociative photoionization of carbon tetrachloride in the valence-shell and Cl 2p inner-shell region	115
5.7	Absolute partial photoionization oscillator strengths for carbon tetrachloride in the valence-shell region	117
5.8	The principle dipole-induced breakdown pathways following valence-shell photoionization of carbon tetrachloride below 80 eV	122
5.9	Oscillator strength sums determined from the proposed dipole-induced breakdown scheme for carbon tetrachloride below 80 eV	124
5.10	TOF mass spectra of carbon tetrachloride in the vicinity of the Cl 2p edge	126
5.11	Absolute partial photoionization oscillator strengths for the dissociative photoionization of carbon tetrachloride in the Cl 2p inner-shell region . .	127
6.1	Absolute oscillator strengths for the photoabsorption of ammonia obtained at low resolution	154
6.2	Absolute oscillator strengths for the photoabsorption of ammonia	155
6.3	Absolute high-resolution oscillator strengths for ammonia in the region of the first electronic band	162
6.4	Global view of entire DOSD and measured oscillator strength data	171
6.5	Comparison of DOSD results and presently measured low-resolution oscillator strength data for ammonia	172
7.1	Absolute oscillator strengths for the photoabsorption of monomethylamine	196
7.2	Absolute oscillator strengths for the photoabsorption of dimethylamine .	197

7.3	Absolute oscillator strengths for the photoabsorption of trimethylamine .	198
7.4	High- and low-resolution spectra for monomethylamine	201
7.5	High- and low-resolution spectra for dimethylamine	202
7.6	High- and low-resolution spectra for trimethylamine	203
7.7	High-resolution spectra of the methylamines from 4–10 eV	206

List of Abbreviations

AP	appearance potential
DOS	dipole oscillator strength
DOSD	dipole oscillator strength distribution
E	energy loss or equivalent photon energy
EELS	electron energy-loss spectroscopy
EMS	electron momentum spectroscopy
EXELFS	extended X-ray energy loss fine structure
FWHM	full width at half maximum
GOS	generalized oscillator strength
HOMO	highest occupied molecular orbital
HR	high resolution
IP	ionization potential
ISEELS	inner-shell electron energy-loss spectroscopy
LR	low resolution
PEPICO	photoelectron-photoion coincidence
PES	photoelectron spectroscopy
PIPICO	photoion-photoion coincidence
POS	partial oscillator strength

STD	standard deviation
T	term value
TAC	time-to-amplitude converter
TOF	time of flight
TRK	Thomas-Reiche-Kuhn
VIP	vertical ionization potential
VUV	vacuum ultraviolet
XPS	X-ray photoelectron spectroscopy

Acknowledgements

I would very much like to thank my research supervisor, Dr. C.E. Brion, for his support, encouragement, expertise, and patience throughout the entire course of this thesis. I am also indebted to Dr. Glyn Cooper and Dr. Wing-Fat Chan from whom I have learned the technique and art of dipole (e,e) spectroscopy. I would like to acknowledge the remainder of the research group with whom I have had the very good fortune of working these past four years and from whom I have learned so very much: J. Anderson, J. Au, Dr. S. Clark, P. Duffy, Dr. X. Guo, B. Hollebhone, N. Lermer, J. Neville, T. Olney, J. Rolke, Dr. B. Todd, E. Zarate, Dr. W. Zhang, and Dr. Y. Zheng.

The dipole oscillator strength distribution and dipole property calculations for ammonia and the methylamines were performed by Dr. A. Kumar and Professor W.J. Meath of the University of Western Ontario.

The design and construction of the new high-energy electron spectrometer described in this work was only possible because of the excellent technical expertise of Mr. E. Gomm of Mechanical Engineering Services, and Mr. B. Greene of Electronic Engineering Services, in the Department of Chemistry at the University of British Columbia. Their assistance with the maintenance of the other spectrometers is also acknowledged.

Finally, I gratefully acknowledge the receipt of a Natural Sciences and Engineering Research Council (NSERC) of Canada Postgraduate Scholarship. Funding for this research was provided by NSERC and by the Canadian National Networks of Centres of Excellence (Centres of Excellence in Molecular and Interfacial Dynamics).

Chapter 1

Introduction

The study of the absorption and emission spectra of molecules has provided detailed information about the molecular structure, electron density, and nuclear properties of these systems and has fundamentally influenced the way molecules are described. Essentially the entire electromagnetic spectrum can be used with advantage to probe molecules. For example, microwave radiation can be used to determine molecular geometries, and infrared radiation can provide information about molecular bond energies and fundamental vibrational frequencies. Visible, ultraviolet, and X-ray radiation can be used to probe molecular electronic structure, and proceeding to even higher energies, gamma radiation can be used to probe nuclear energy levels. Thus, a wide-range of complementary “optical” spectroscopic techniques has been developed to study atoms and molecules.

Most of the spectroscopic studies reported in the literature at present are aimed solely at determining the energy positions of the various absorption lines, from which a great deal of spectroscopic information can be gained. However, for many fundamental as well as practical purposes it is also essential to determine the absolute intensity of the absorption lines corresponding to the various excitation processes. The amount of light absorbed by an atomic or molecular target is dependent on the wavelength of the light and is proportional to the absolute photoabsorption oscillator strength (cross section) of the target. Such absolute photoabsorption oscillator strength data are important in many key areas of science and technology including the study of planetary atmospheres

(aeronomy), astrophysics, and radiation chemistry physics and biology [1–4], or indeed in any theoretical or modelling study where atoms and molecules are interacting with energetic particles or radiation.

The bound electrons in atoms and molecules have binding energies from a few electron volts (eV) to a few thousand electron volts. The dominant portion of the electronic photoabsorption spectrum is located in the visible, ultraviolet (UV), vacuum ultraviolet (VUV), and soft X-ray energy regions from about 1 to 1000 eV. At present there is no single optical photoabsorption spectrometer system which can continuously span this energy region. Thus the available absolute photoabsorption data are often limited to certain targets and to restricted energy regions. Prior to the advent of synchrotron radiation, published data were restricted mostly to the region below ~ 25 eV. Many-line sources have been used in conjunction with double ion chambers [4] to provide wide-ranging data in the ionization continuum up to about 150 eV. However, since the use of a double ion chamber for determining absolute photoabsorption oscillator strengths relies on the ionization of the target, no data in the discrete excitation region below the first ionization potential can be determined.

More recently, very intense light sources have been produced at electron and positron synchrotron facilities [5, 6]. It is well known from classical electrodynamics that an accelerated charge will radiate energy [7]. This radiation was first regarded as a nuisance by synchrotron designers because provisions had to be made to give the electrons circulating in the synchrotron back their radiated energy in order to keep them in a circular orbit. Despite the intense brightness of these light sources, and the available photon wavelength range (typically 1–10000 eV, depending on the facility), these facilities are expensive, have limited access, and are remotely located from most user laboratories.

Electron scattering can be used as an alternative to direct optical methods to probe the electronic structure of atoms and molecules. Furthermore, in addition to accessing the full range of dipole-allowed transitions in molecular systems, electron scattering experiments can be used to determine the energies of electronic states which are inaccessible, because of optical selection rules, by direct optical methods. An electron beam is an excellent probe of matter. Electrons are readily produced by thermionic emission from a heated filament, simple to deflect and energy analyze using static electric and magnetic fields, and easy to detect using channel electron multipliers or microchannel plates [8]. For these and other reasons many complementary spectroscopic techniques have been developed using electrons to study atomic and molecular targets.

In the classic experiment of Franck and Hertz [9, 10] the quantization of atomic energy states was demonstrated by scattering electrons off mercury vapour. A general theory for the interaction of charged particle beams with matter was derived using scattering theory and quantum mechanics by H.A. Bethe in 1930 [11], and the Bethe theory has been eloquently reviewed more recently by Inokuti [12, 13]. Bethe determined that under certain scattering conditions the scattered electrons would excite transitions in the target with the same selection rules as in optical spectroscopy. The probability of the electronic excitation using electron beams is, however, different from the optical transition probability, but the two quantities are linked by factors which depend only on the geometry and kinematics of the electron scattering. These factors are only a function of the instrument, and are independent of the electronic structure of the target being studied. The use of electron scattering experiments for studying electronic transitions in atoms and molecules was pioneered by Lassetre [14–16] and Van der Wiel [17, 18] and has been further developed, and extensively applied to a wide range of photoexcitation

and photoionization phenomena, by Brion and co-workers at the University of British Columbia [4, 19–21].

The technique of dipole (e,e) spectroscopy as used in the present work has been shown to provide qualitative and quantitative photoabsorption results which are entirely equivalent to those obtainable using direct optical methods [4, 22]. The electric field associated with a fast electron provides an essentially continuous source of induced electromagnetic radiation often referred to as a “virtual photon field” [7, 23, 24]. In these dipole (e,e) spectroscopic experiments the electrons are inelastically scattered off gaseous target molecules thereby imparting some of their energy to the target. This energy lost by the electron is equal to the electronic excitation energy of the target, and thus equivalent to a photon energy. Thus the continuously tuneable energy loss of the electron is analogous to a continuously tuneable source of energetic radiation. Furthermore, the excitation in this electron-impact-based technique is non-resonant and therefore no errors due to “line-saturation” problems can occur. Serious errors due to such “line-saturation” (or bandwidth) effects can arise for discrete excitations of narrow natural linewidth [25–27] because of the logarithmic transform involved in Beer-Lambert law optical determinations of photoabsorption cross sections [28]. In addition, the dipole (e,e) method normally establishes the absolute intensity scale using the Thomas-Reiche-Kuhn (TRK) sum rule, and this avoids the errors associated with determinations of the sample particle density in conventional absolute measurements.

Accurate absolute differential oscillator strength data are used as input for the construction of the dipole oscillator strength distribution (DOSD) of a molecule [29]. These input data are modified to satisfy certain quantum mechanical constraints, i.e., the TRK sum rule and accurate molar refractivity data. For this reason the DOSD method has

proved useful for evaluating the quality and accuracy of measured photoabsorption data, by determining the best combination of input data that satisfies the imposed constraints. Furthermore, the DOSD spans the entire photoabsorption spectrum from the electronic absorption threshold to infinite energy, and can provide estimates of oscillator strength data where the equivalent experimental data did not previously exist. Once a DOSD is constructed many related dipole properties can be calculated from the DOSD. These results are important because the *ab initio* calculation of the oscillator strengths and dipole properties for molecules the size of those studied during the course of the present thesis, is not at present feasible. Thus with more extensive and improved absolute oscillator strength measurements the DOSD technique can provide the first (reliable) determination of many of the dipole properties.

The remainder of this thesis has been organized as follows. Chapter 2 describes the theory behind the use of fast electron impact for the determination of absolute photoabsorption oscillator strengths. The methods for calculating dipole oscillator strength distributions and dipole properties from accurate input oscillator strength data are also reviewed. The experimental apparatus and procedures used for obtaining the absolute photoabsorption and photoionization oscillator strength data reported in this thesis, as well as the new spectrometer constructed during the course of the present work, are outlined in chapter 3. The presently measured experimental results are given in chapters 4–7. The photoabsorption and photoionization results for CH_3OH , and CCl_4 are given in chapters 4, and 5, respectively. The absolute photoabsorption oscillator strength data, dipole oscillator strength distributions, and calculated dipole properties for ammonia, and the methylamines, are given in chapters 6 and 7, respectively. Chapter 8 contains some closing remarks.

Chapter 2

Theory

2.1 Definition of the Oscillator Strength

The concept of the oscillator strength originated in the classical Thomson model to describe electronic absorption in matter [30]. In this model the electrons were assumed to be fixed to an atomic center by harmonic-oscillator-type forces (force constant k_s , and damping coefficient γ_s) and to oscillate about their equilibrium positions in response to external electric fields, e.g., incident light radiation. The polarizability of a substance, $\alpha(\omega)$, is defined as the net dipole moment produced per unit of applied electric field, and in this model it is determined to be (in c.g.s. units)

$$\alpha(\omega) = \frac{e^2}{m(\omega_s^2 - \omega^2 - i\gamma_s\omega)} \quad (2.1)$$

for a single electron. Here m , and e are the mass and the charge of the electron, respectively, ω is the frequency of the incident radiation, and $\omega_s = \sqrt{k_s/m}$ is the fundamental frequency of the oscillating electron s . For a system of many electrons, if it is assumed that there are f_1 electrons of fundamental frequency ω_1 , and f_2 electrons of fundamental frequency ω_2 , etc., then the polarizability is a sum of the contributions from all these electrons, and can be written as

$$\alpha(\omega) = \frac{e^2}{m} \sum_s \frac{f_s}{(\omega_s^2 - \omega^2 - i\gamma_s\omega)}. \quad (2.2)$$

The quantity f_s defined in this manner is called the “oscillator strength” and gives an indication of the intensity of the absorption at a particular frequency. It is interesting to note that

$$\sum_s f_s = N, \quad (2.3)$$

where N is the total number of electrons in the system.

It is worthwhile mentioning at this point that this is a purely classical model. It has long been known that for any atomic or molecular system there are many more absorption lines than there are electrons. Thus the oscillator strength, f_s , takes on real values, not integral values as assumed in the Thompson model. However, the concept of the oscillator strength has stuck and, furthermore, it can be redefined within the framework of quantum mechanics as we will see in section 2.4.

2.2 Photoabsorption and Electron Energy-Loss Spectroscopy

When a photon of energy $E = h\nu$ is absorbed by a molecular system, AB, many final states of the molecule can be accessed and these are summarized, along with the equivalent atomic processes, in table 2.1. For molecular excitation the process is given by



where AB^* represents the molecule in an excited state. The probability for this process, as a function of energy, E , is given by the absolute total photoabsorption cross section.

The total photoabsorption cross section, σ^T , is often defined with respect to the Beer-Lambert photoabsorption law¹. Consider an optical cell of sample path length, l , filled

¹Note that σ^T is a differential quantity in energy (or wavelength). However, it is written as above, rather than $d\sigma^T/dE$, because it is defined with respect to equation 2.5.

Table 2.1: Atomic and molecular photon-matter interaction processes. Here A, and AB, represent atomic and molecular targets, respectively, with excited states A* and AB*. The term KE refers to extra kinetic energy which is taken away by the ionized electron and the molecular dissociation and ionization products.

	Process	Description
1.	$A + h\nu \longrightarrow A + h\nu$	atomic elastic scattering
2.	$\longrightarrow A^* + h\nu'$	atomic inelastic scattering or atomic excitation
3.	$\longrightarrow A^+ + e^- + KE$	atomic photoionization
4.	$\longrightarrow A^* \longrightarrow A^+ + e^- + KE$	atomic preionization or autoionization
5.	$AB + h\nu \longrightarrow AB + h\nu$	molecular elastic scattering
6.	$\longrightarrow AB^* + h\nu'$	molecular inelastic scattering or molecular excitation
7.	$\longrightarrow A + B + KE$ $\longrightarrow A^* + B + KE$ $\longrightarrow A + B^* + KE$ $\longrightarrow A^* + B^* + KE$	molecular dissociation molecular dissociation molecular dissociation molecular dissociation
8.	$\longrightarrow A^+ + B + e^- + KE$ $\longrightarrow A + B^+ + e^- + KE$	molecular photofragmentation molecular photofragmentation
9.	$\longrightarrow A^+ + B^- + KE$ $\longrightarrow A^- + B^+ + KE$	ion pair formation
10.	$\longrightarrow AB^+ + e^- + KE$	molecular photoionization
11.	$\longrightarrow AB^* \longrightarrow A + B + KE$	molecular predissociation
12.	$\longrightarrow AB^* \longrightarrow AB^+ + e^- + KE$	molecular preionization or autoionization

with the target sample gas to a number density, n . The intensity of the light before and after passing through the cell, I_0 , and I , respectively, are related by

$$I = I_0 \exp(-\sigma^T nl). \quad (2.5)$$

The photoabsorption cross section is a function of the wavelength (energy) of the light source, is dependent on the sample being studied, and gives an indication of the strength of the absorption; if the cross section is large then the incident beam will be strongly attenuated as the radiation is absorbed. The photoabsorption cross section, σ^T , is generally expressed in units of cm^2 or in megabarns ($1 \text{ Mb} = 10^{-18} \text{ cm}^2$) and is related to the differential optical oscillator strength, $(df/dE)^0$, by

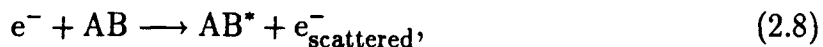
$$\sigma^T = \frac{\pi e^2 h}{mc} \left(\frac{df}{dE} \right)^0, \quad (2.6)$$

or equivalently by

$$\sigma^T [\text{Mb}] = 109.75 \left(\frac{df}{dE} \right)^0 [\text{eV}^{-1}]. \quad (2.7)$$

Thus the terms ‘‘oscillator strength’’ and ‘‘cross section’’ can be used interchangeably since they represent the same quantity (within a constant factor).

It is important to note that the same molecular excitation process shown above in equation 2.4 can occur in an electron scattering experiment using an incident electron beam of energy E_0 . This can be represented by



where now the scattered electron imparts an energy E to the target during the excitation, and is scattered with a final energy $(E_0 - E)$. The kinetic energy imparted to the target molecule is small ($< 1 \text{ meV}$) [31] with the energies and scattering geometries used in the present work, and thus by comparing equation 2.4 and 2.8 it can be seen that the energy

loss, E , of the electron is entirely equivalent to the photon energy $h\nu$. This is the basis for the use of dipole (e,e) spectroscopy to measure photoabsorption oscillator strengths. The technique of dipole (e,e) spectroscopy and other electron energy-loss-based spectroscopies have been reviewed elsewhere [4, 32].

2.3 Photoionization

If the energy supplied to the molecule AB is above the first ionization potential then, excluding any neutral fluorescence processes, a positively charged ion will be formed. The total photoabsorption cross section, σ^T , can be written as

$$\sigma^T = \sigma_n + \sigma_{\text{ion}}^T, \quad (2.9)$$

where σ_n is the cross section for the production of neutral species (e.g., AB*) and σ_{ion}^T is the total photoionization cross section. The photoionization efficiency, η_i , gives a measure, as a function of energy, of how many ions are formed per photon absorbed, and is defined as

$$\eta_i(E) = \frac{\text{total number of ionizing events per second}}{\text{total number of photons absorbed per second}}, \quad (2.10)$$

and relates to the total photoabsorption and photoionization cross sections by

$$\sigma_{\text{ion}}^T = \eta_i \sigma^T. \quad (2.11)$$

A measure of the photoionization efficiency, as a function of photon energy, is therefore important for determining the photoionization cross section and indirectly (using equation 2.9) for determining the cross section for the production of neutral species.

The total photoionization oscillator strength (cross section) distribution, σ_{ion}^T , for an atom or molecule can, in general, be partitioned in two different but complementary

manners. In photoionization mass spectrometry, or in the equivalent electron-impact-based technique of dipole (e,e+ion) spectroscopy used in the present work, mass spectra are measured as a function of the (equivalent) photon energy. Atomic mass spectra can be complicated by the presence of multiply charged ions. Mass spectra of molecular systems can be complicated by not only the presence of multiply charged ions, but also by the products from dissociative fragmentation processes. It is important to determine how the products of molecular and dissociative photoionization vary as a function of the energy absorbed by the target. The branching ratio (BR^{frag}) for a particular fragment ion, frag, determined by integration of the peaks in the baseline-subtracted mass spectra, varies as a function of the photon energy and represents the fraction of the total number of ions formed, as

$$\text{BR}^{\text{frag}} = \frac{N^{\text{frag}}}{N_T}, \quad (2.12)$$

where N^{frag} is the number of ions formed per second of the type, frag, and $N_T = \sum_{\text{frag}} N^{\text{frag}}$ is the total number of ions formed per second. The partial photoionization oscillator strength for the production of an ion, frag, is given by the triple product of the absolute photoabsorption oscillator strength, the photoionization efficiency, and the branching ratio for the fragment, frag, as

$$\sigma_{\text{ion}}^{\text{frag}} = \text{BR}^{\text{frag}} \eta_i \sigma^T = \text{BR}^{\text{frag}} \sigma_{\text{ion}}^T. \quad (2.13)$$

Thus it can be seen from equation 2.13 that the total photoionization oscillator strength distribution is made up from a sum of the partial photoionization oscillator strengths for the production of all the molecular and dissociative ions.

Similarly it is important to determine how the production of the electronic states of the molecular ion varies as a function of the energy absorbed by the target. These data

can be determined from photoelectron spectra measured using tuneable energy PES or equivalently from dipole (e,2e) spectroscopy [4, 33]. These electronic ion state branching ratios, BR^{state} , are determined from the background subtracted photoelectron spectrum in a manner similar to that indicated by equation 2.12 for photoionization branching ratios. The electronic ion state partial oscillator strength for a given electronic state of the molecular ion is defined as

$$\sigma_{\text{ion}}^{\text{state}} = \text{BR}^{\text{state}} \eta_i \sigma^T = \text{BR}^{\text{state}} \sigma_{\text{ion}}^T. \quad (2.14)$$

Thus it can be seen from equation 2.14 that the total photoionization oscillator strength distribution is made up from a sum of the partial photoionization oscillator strengths for the formation of all the electronic ion states of the molecular ion. The ability to partition the total photoionization oscillator strength distribution in these two complementary manners is the basis for determining the dipole-induced breakdown pathways for a molecule, and this is discussed in more detail later in this work for the specific examples of methanol (see section 4.2.4), and carbon tetrachloride (see section 5.2.4).

2.4 The Bethe Theory of Electron Impact

Bethe [11–13] developed a general theory to describe the scattering of fast electrons off matter. Consider an electron of velocity, v , mass, m , and charge, $-e$, colliding with a stationary target of mass, M , in an initial electronic state, $|0\rangle$. The electron scatters into a solid angle, $d\Omega$, and the target is excited to a state $|n\rangle$ which is either part of the discrete or continuum spectrum of the target. The energy difference between the two states of the target $|0\rangle$ and $|n\rangle$, E_n , is gained by the target and hence is lost by the incident electron. When the electron is fast, but still non-relativistic, the scattering cross

section for this interaction, calculated to the lowest order in the interaction potential, V , i.e., in the first Born approximation, is given by [11, 12]²

$$d^2\sigma_n = \frac{\mu^2}{(2\pi)^2\hbar^4} \frac{|\vec{k}'|}{|\vec{k}|} \left| \int e^{i\vec{K}\cdot\vec{r}} \langle n|V|0\rangle d\vec{r}_1 d\vec{r}_2 \dots d\vec{r}_Z d\vec{r} \right|^2 d\Omega. \quad (2.15)$$

Here $\mu = Mm/(M + m)$ is the reduced mass of the system, \vec{r} is the position of the incident electron relative to the centre of the target, $\hbar\vec{k}$ and $\hbar\vec{k}'$ are the incident and final momenta of the electron, respectively, and $\hbar\vec{K} = \hbar(\vec{k} - \vec{k}')$ is the momentum transfer. The eigenfunctions $|0\rangle$ and $|n\rangle$ are represented in the coordinates of the Z target electrons, \vec{r}_j . When the interaction between the incident electron and the target can be described by the Coulomb potential the cross section transforms to

$$d^2\sigma_n = 4 \left(\frac{\mu e^2}{\hbar^2} \right)^2 \frac{|\vec{k}'|}{|\vec{k}|} \frac{1}{|\vec{K}|^4} |\epsilon_n(K)|^2 d\Omega, \quad (2.16)$$

where

$$\epsilon_n(K) = \langle n | \sum_{j=1}^Z e^{i\vec{K}\cdot\vec{r}_j} | 0 \rangle. \quad (2.17)$$

Bethe introduced a quantity called the generalized oscillator strength (GOS) given by

$$f_n(K) = \left(\frac{E_n}{R} \right) \frac{1}{(K a_0)^2} |\epsilon_n(K)|^2. \quad (2.18)$$

where $a_0 = \hbar^2/me^2$ and $R = me^4/2\hbar^2$. This is a generalization of the optical (dipole) oscillator strength associated with photoabsorption which is written as

$$f_n^0 = \left(\frac{E_n}{R} \right) M_n^2, \quad (2.19)$$

²The formulae in this section are expressed in c.g.s. units. It should be noted however that, for the purposes of the present study, the units of these equations are unimportant. This section seeks to derive a proportionality relation between the electron scattering cross section and the optical photoabsorption oscillator strength. The photoabsorption oscillator strength data obtained in the present work are placed on an absolute scale using the TRK sum rule and not *via* these equations. Thus any proportionality constants are unimportant in the present study.

where

$$M_n^2 = \left| \int \langle n | \sum_{j=1}^Z x_j | 0 \rangle d\vec{r} \right|^2 / a_0^2 \quad (2.20)$$

is the dipole transition matrix element, and x_j is the component of \vec{r}_j in the direction of the incident radiation. Equation 2.18 is the proper expression for transitions between two discrete bound states; the generalized oscillator strength for such a transition is just a dimensionless number. If the upper state $|n\rangle$ lies in the continuum, then equation 2.18 is more properly written as

$$\frac{df(K, E)}{dE} = \sum_n \left(\frac{E_n}{R} \right) \frac{|\epsilon_n(K)|^2}{(K a_0)^2} \delta(E_n - E) \quad (2.21)$$

for the differential generalized oscillator strength $df(K, E)/dE$. For the remainder of this thesis we need only consider the differential (generalized) oscillator strength since any real measurement has a finite bandwidth and thus only differential oscillator strengths are measured in the discrete and continuum regions of the absorption spectrum of atoms and molecules. Equation 2.19 represents the quantum mechanical expression of the oscillator strength, f , described earlier in equation 2.2 of section 2.1. Slater [34] has demonstrated that equation 2.19 follows naturally from the quantum theory of electronic polarization when described using perturbation theory. The expression for the generalized oscillator strength can be expanded in terms of even powers of the momentum transfer by expanding the complex exponential, and by including the orthonormality of the initial and final states, and is given by

$$\begin{aligned} f_n(K) &= \frac{E_n}{R a_0^2} \left[\epsilon_1^2 + (\epsilon_2^2 - 2\epsilon_1\epsilon_3)K^2 + (\epsilon_3^2 + 2\epsilon_1\epsilon_5 - 2\epsilon_2\epsilon_4)K^4 + O(K^6) + \dots \right] \quad (2.22) \\ &= f_n^0 + AK^2 + BK^4 + O(K^6) + \dots, \quad (2.23) \end{aligned}$$

where ϵ_t is the t -th order multipole matrix element given by

$$\epsilon_t = \frac{1}{t!} \langle n | \sum_{j=1}^Z x_j^t | 0 \rangle, \quad (2.24)$$

and $O(K^6)$ represents terms of the order K^6 . The coefficients of the terms involving the higher powers of the momentum transfer involve higher multipole moments, e.g., quadrupole and octupole. From equation 2.23 it can be seen that in the limit of zero momentum transfer the generalized oscillator strength approaches the optical oscillator strength. Thus equation 2.16 becomes

$$\frac{d^3\sigma}{dEd\Omega} = \frac{2}{E} \left(\frac{\mu e^2}{\hbar\sqrt{m}} \right)^2 \frac{|\vec{k}'|}{|\vec{k}|} \frac{1}{|\vec{K}|^2} \left(\frac{df}{dE} \right)^0 \quad (2.25)$$

or equivalently,

$$\left(\frac{df}{dE} \right)^0 = \frac{E}{2} \left(\frac{\hbar\sqrt{m}}{\mu e^2} \right)^2 \frac{|\vec{k}|}{|\vec{k}'|} |\vec{K}|^2 \frac{d^3\sigma}{dEd\Omega} \quad (2.26)$$

in the limit of zero momentum transfer. The measured differential electron scattering cross section, $d^3\sigma/dEd\Omega$, is related to the differential optical photoabsorption oscillator strength, $(df/dE)^0$, by a purely kinematical factor which depends only on the scattering geometry and the incident electron beam energy. It is worthwhile mentioning that the electron scattering cross section drops off even more rapidly with energy than does the optical oscillator strength. For scattering in the forward direction, and for energy losses which are small compared with the incident kinetic energy of the electron, T , the relation is given by [12]

$$\left. \frac{d^3\sigma}{d\Omega dE} \right|_{\theta=0} = 16a_0^2 R^2 T E^{-3} \left(\frac{df}{dE} \right)^0. \quad (2.27)$$

The fact that the electron scattering cross section drops off a factor of E^3 faster than the optical oscillator strength requires that a good signal-to-noise ratio be maintained in the electron scattering experiments.

As has already been mentioned, the momentum transfer, \vec{K} , is an important quantity for describing electron collisions. If the momentum transfer is low then predominantly dipole-allowed transitions are excited. As the momentum transferred to the target is increased higher multipole transitions can become excited. The magnitude of the momentum transfer, \vec{K} , is determined from the law of cosines by

$$\begin{aligned} |\vec{K}|^2 &= |\vec{k}|^2 + |\vec{k}'|^2 - 2|\vec{k}||\vec{k}'|\cos\theta \\ &= |\vec{k}|^2 + |\vec{k}'|^2 - 2|\vec{k}||\vec{k}'|(1 - \theta^2/2 + \dots) \\ &\sim (|\vec{k}| - |\vec{k}'|)^2 + |\vec{k}||\vec{k}'|\theta^2 - \dots, \end{aligned} \quad (2.28)$$

where the cosine function has been expanded in a power series in the polar angle, θ . The limit of small momentum transfer, necessary for the determination of optical oscillator strengths from generalized oscillator strength measurements, is achieved by

1. selecting only those electrons which have been scattered in the forward direction (in practice through a small acceptance angle about zero degrees). This ensures that $\theta \sim 0^\circ$.
2. using high incident electron energy, and measuring at small energy losses (relative to the incident energy). This ensures that $|\vec{k}| \sim |\vec{k}'|$.

In practice, equation 2.26 is integrated over the acceptance angles, $d\Omega$, of the spectrometer to yield a simplified equation of the form

$$\left(\frac{df}{dE}\right)^0 = B(E)\frac{d\sigma}{dE}, \quad (2.29)$$

where $B(E)$ is the so-called spectrometer dependent ‘‘Bethe-Born’’ factor. This factor depends on the scattering geometry of the spectrometer and is a function of the energy loss,

E. The Bethe-Born factor for a spectrometer can be determined directly from an analysis of the scattering geometry of the spectrometer (as in the case of the low-resolution dipole (e,e+ion) spectrometer used in the present work—see section 3.1), or from the ratio of the measured energy-loss spectrum ($d\sigma/dE$) and known (theoretical or experimental) accurate photoabsorption oscillator strength data $(df/dE)^0$ in the continuum region [26, 27]. This latter procedure was used to determine the Bethe-Born factor for the high-resolution dipole (e,e) spectrometer used in the present work since no well-defined acceptance angles exist for this instrument—see section 3.2.

Under the conditions of lower incident electron beam energy, and larger scattering angles, information can be determined about other contributions to the generalized oscillator strength [35–37]. Especially, at larger momentum transfers, contributions from dipole-forbidden transitions can become appreciable. Such transitions cannot be observed using direct optical methods and therefore provide information about angular momentum optically forbidden transitions and the production of higher multiplet states in atoms and molecules.

2.5 Sum Rules

There are a number of physical quantities which depend on the various moments (weighted by photon energy) of the oscillator strength distribution [38]. The sum rules can be written as

$$S_k = \sum_n E_n^k f_n^0 + \int_{\text{IP}}^{\infty} E^k \left(\frac{df}{dE} \right)^0 dE \quad (2.30)$$

$$S_k = \int_{E_0}^{\infty} E^k \left(\frac{df}{dE} \right)^0 dE, \quad (2.31)$$

where as shown in equation 2.30 the integral, in theory, represents a sum over the contributions from transitions to the discrete states, and an integral over the contributions from transitions to continuum states. In practice, since only differential oscillator strength data are measured, equation 2.30 is more properly written as the integral over the measured differential oscillator strength spectrum from the electronic absorption threshold (E_0) to infinite energy as indicated by equation 2.31. The TRK sum rule is S_0 and is used in the present work to place the measured relative oscillator strength data on an absolute scale. The TRK sum rule is the quantum mechanical equivalent of equation 2.3 which was derived in section 2.1 with regard to the classical model for electronic absorption. It is worthwhile mentioning at this point that the oscillator strength distribution has an asymptotic limit given by the hydrogenic or Born-dipole function

$$\lim_{E \rightarrow \infty} \left(\frac{df}{dE} \right)^0 = E^{-7/2}. \quad (2.32)$$

Therefore, the sum rules, S_k will diverge for all integer values of k greater than 2. These, and other dipole properties, will be discussed later in conjunction with the construction of dipole oscillator strength distributions and the subsequent evaluation of many important dipole properties.

2.6 Molecular Orbital Description and Spectral Interpretation

The electronic states of a molecule are conveniently described in terms of molecular orbital (MO) theory. In MO theory the electrons are considered to be essentially independent, and the state of an electron in a molecule is described by a one-electron wavefunction which is also referred to as a molecular orbital. Such a description gives rise to two main types of occupied molecular orbitals, namely valence-shell and inner-shell orbitals.

The valence-shell orbitals have binding energies in the range from about 10 to 50 eV. The occupied and unoccupied valence-shell orbitals are delocalized over the molecule and account for most of the chemical bonding and chemical properties of a molecule. In contrast, the inner-shell molecular orbitals are strongly localized at the corresponding atomic centre and have a dominant atomic character. The binding energies of inner-shell orbitals are generally much higher in energy than those of the valence-shell orbitals, and each will be very close to that of the corresponding orbital in the free atom. However, some minor differences result which depend on the chemical environment of the atom and this is the basis of the chemical shifts observed in XPS binding energies [39].

The absorption peaks observed in electron energy loss and photoabsorption spectra of molecules are due to transitions from occupied valence-shell and inner-shell states to unoccupied virtual valence and Rydberg states, and also to the ionization continuum. These transitions are shown schematically by the solid and broken lines on figure 2.1 for transitions from inner-shell (core) states and valence-shell states, respectively. It should be noted that each electronic state will have associated vibrational and rotational levels. In some favorable instances individual vibrational levels can be resolved using the present high-resolution dipole (e,e) spectrometer. However, the rotational levels are too closely spaced to be resolved and tend to broaden the observed vibronic spectral features.

Electronic spectra are most easily assigned if sufficiently accurate *ab initio* calculations are available for both the transition energies and the associated oscillator strengths. However in practice few such calculations exist for molecular systems and semi-empirical methods of assignment must be used. In this situation the concept of Rydberg term values and quantum defects often provides a useful approach. These ideas have been used in chapter 7 for assigning the presently measured photoabsorption spectra of the

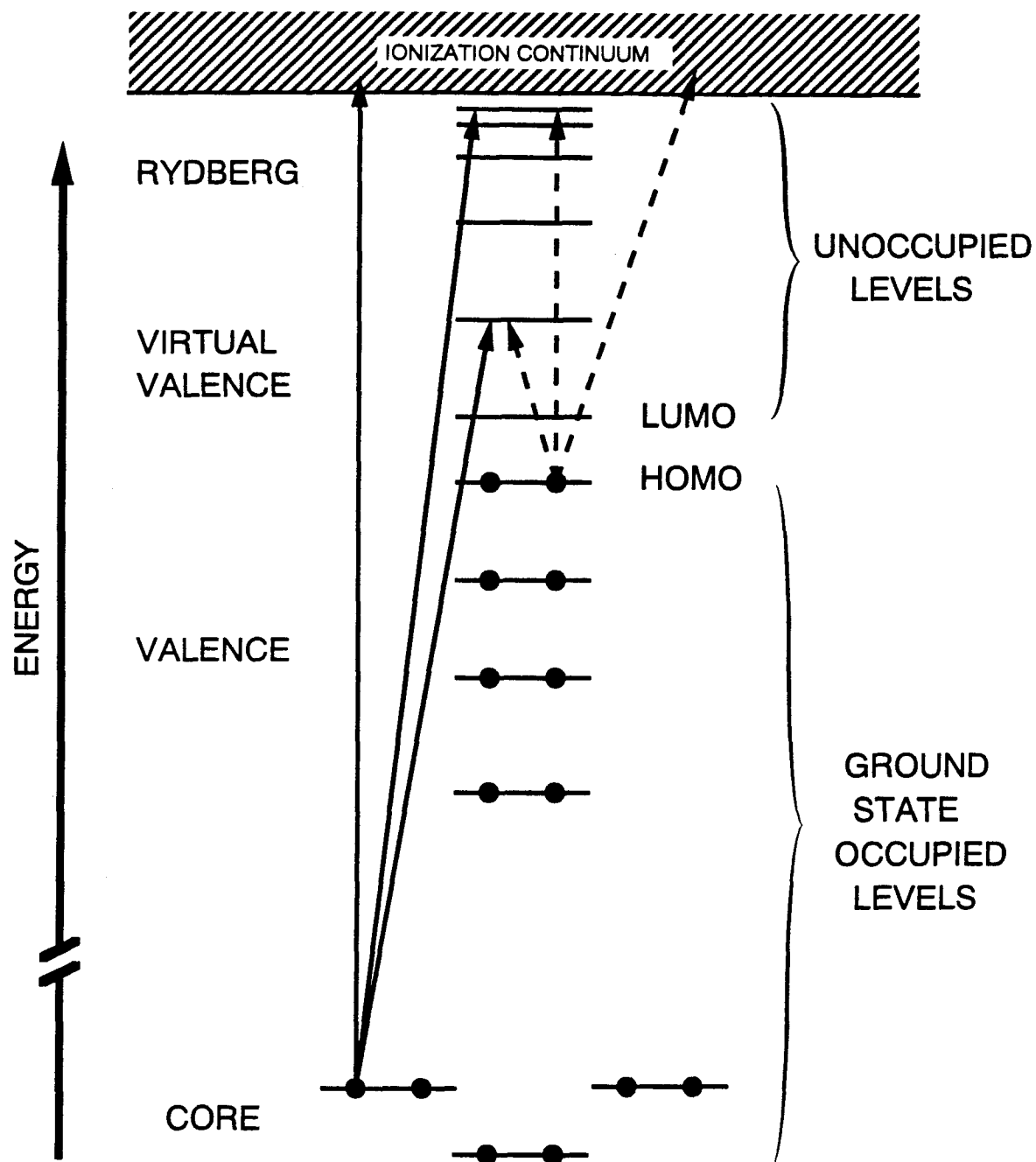


Figure 2.1: Schematic of molecular electronic states. The occupied levels of the ground electronic state are represented by horizontal lines containing filled circles. The solid and dashed lines represent transitions from the inner-shell, and valence-shell states, respectively. Note that the energy scale on the vertical axis is broken; the inner-shell (core) levels lie much lower in energy than the valence-shell levels.

methylamines.

Transitions which have Rydberg upper states can be characterized by the fact that the observed term value for the transition, T , fits into a mathematical progression of the form

$$T = \text{VIP} - E = \frac{R}{(n - \delta_\ell)^2}, \quad (2.33)$$

where E is the measured absorption energy, VIP is the vertical ionization potential of the initial state, R is the Rydberg constant, n is the principal quantum number, and δ_ℓ is the quantum defect for a Rydberg state of orbital angular momentum ℓ [40, 41]. Rydberg molecular orbitals are generally large and diffuse and, as such, an electron in a Rydberg orbital “sees” the molecular ion core as essentially a point charge. There is very little interaction between the electron in a Rydberg orbital and the remainder of the molecule, and hence the term values associated with transitions to Rydberg upper states are generally transferable from one ionization manifold to another. In contrast, the term values for transitions to virtual valence upper states are generally not transferrable, and frequently yield different term values for every ionization manifold.

2.7 The Variation of Momentum Transfer in Dipole (e,e) Experiments— Effects on Measured Oscillator Strengths

In the present work absolute oscillator strengths have been obtained (see above) by TRK sum rule normalization of Bethe-Born converted electron energy-loss spectra obtained under conditions which are assumed to correspond to negligible momentum transfer (see equation 2.23). In practice however, the momentum transfer is finite and increases with increase in energy loss. It is important to assess the effects of these variations on the resulting oscillator strengths. In this regard it should be noted that the TRK sum rule is

only strictly valid for zero momentum transfer. On the other hand, the Bethe sum rule, which is a generalization of the TRK sum rule, states that the integral of the GOS over all energies is equal to the total number of electrons in the system being studied provided that the momentum transfer is constant, i.e.,

$$\int \frac{df}{dE}(K, E)dE = N, \quad K = \text{constant.} \quad (2.34)$$

The varying momentum transfer conditions corresponding to the energy loss spectrum in fact do not correspond exactly to either the TRK or Bethe sum rules. The actual situation corresponds to a diagonal cut across the Bethe surface [12] with a slow variation in the momentum transfer. Thus in light of these considerations there will necessarily be some error associated with the use of dipole (e,e) spectroscopy for determining photoabsorption oscillator strengths. The purpose of this section is to determine the magnitude of this error.

The generalized oscillator strength is a function of energy and momentum transfer, and can be expressed in a Taylor series as

$$\begin{aligned} f(K, E) &= \sum_{n=0}^{\infty} \frac{K^{2n} f^{(n)}}{n!} \\ &= \left(\frac{df}{dE} \right)^0 + K^2 f^{(1)} + \frac{K^4}{2} f^{(2)} + \dots, \end{aligned} \quad (2.35)$$

where $f^{(n)}$ represents the n -th derivative of the generalized oscillator strength with respect to K^2 , evaluated at zero momentum transfer. The first term in this expression, $f^{(1)} = \left. \frac{\partial f}{\partial K^2} \right|_{K^2=0}$, has been calculated [42, 43] and measured experimentally [44, 45] for helium. It was determined [45] that the largest contribution of $f^{(1)}$ to $f(K, E)$ is only 1.5% for a spectrum obtained at zero degrees (as in the present work). Recently, Bonham [46] has studied the validity of using the TRK sum rule to place zero-angle (i.e., low momentum

transfer) electron impact spectra on an absolute scale. The correction [46] to the TRK sum rule is given by

$$S_0 = \int_0^\infty \left(\frac{df}{dE} \right) dE = N + \frac{2m}{\hbar^2 k^2} \{ |E_T| - \frac{4}{5} \bar{V}_{ee} \}, \quad (2.36)$$

where k is the momentum of the incident electron, E_T is the total electronic ground state energy of the target, and \bar{V}_{ee} is the electron-electron repulsion energy of the target. Numerical values for the quantity $(|E_T| - \frac{4}{5} \bar{V}_{ee})$ have been determined [46] to be 1.83 keV for F and 9.91 keV for Ar from data reported by Clementi [47]. For 8 keV electron impact energy this corresponds to corrections to the TRK sum rule of 0.85% and 2.3% for F, and Ar, respectively. In this connection it is of interest to consider the generalized oscillator strength for atomic hydrogen which can be calculated exactly. This should provide a further test of the magnitude of the errors associated with the methods used in the present work for determining absolute oscillator strength scales from dipole (e,e) spectra. The GOS for a transition from the ground electronic state of the hydrogen atom, to a state of principal quantum number, n , is given by [12]

$$\begin{aligned} f_n(K) &= 2^8 n^5 (n^2 - 1) \left\{ \frac{1}{3} (n^2 - 1) + (nKa_0)^2 \right\} \\ &\times [(n-1)^2 + (nKa_0)^2]^{n-3} \\ &\times [(n+1)^2 + (nKa_0)^2]^{-n-3} \end{aligned} \quad (2.37)$$

in the discrete region, and by

$$\begin{aligned} \frac{df}{dE}(K, E) &= \frac{2^7 \{ (Ka_0)^2 + (E/3R) \} ER^{-2}}{\{ (K+k)^2 a_0^2 + 1 \}^3 \{ (K-k)^2 a_0^2 + 1 \}^3} \\ &\times (1 - \exp(-2\pi/ka_0))^{-1} \\ &\times \exp \left(-\frac{2}{ka_0} \arctan \left(\frac{2ka_0}{(Ka_0)^2 - (ka_0)^2 + 1} \right) \right) \end{aligned} \quad (2.38)$$

in the continuum region. Here the momentum of the ejected (ionized) electron, $\hbar k$, is related to the photon energy, E , by

$$ka_0 = (E/R - 1)^{1/2}. \quad (2.39)$$

In the present work, these expressions for the GOS of hydrogen were evaluated for an incident electron beam energy (E_e) of 8 keV. For zero degree scattering the momentum transfer is given by,

$$Ka_0 = \sqrt{\frac{E_e}{R}} - \sqrt{\frac{E_e - E}{R}}. \quad (2.40)$$

To simulate our present experimental Bethe-Born converted EELS method a data file of generalized oscillator strength data for the ionization continuum of the hydrogen atom versus photon energy was prepared using equations 2.38–2.40 at energies from 14 to 100 eV, in steps of 1 eV, and from 100 to 300 eV, in steps of 2 eV. Then a curve of the form, AE^{-B} , was fitted to this data from 100 to 300 eV and used to extrapolate the data to infinite energy. The contribution from the discrete region was determined by evaluating the sum of the slowly converging terms given by equation 2.37. Using this procedure, the sum S_0 was evaluated and found to be 1.002618 compared with the true integrated oscillator strength value of exactly one. Thus there is only 0.26% error in S_0 when the TRK sum rule is applied to the prepared data using the present normalization procedure. The agreement is extremely good, and well within the present estimated experimental uncertainty of $\pm 5\%$.

In summary, it can be concluded that the effects of the finite but varying momentum transfer in the present experiment are negligible (i.e., $< 3\%$ error) in the determination of absolute oscillator strengths for atoms as large as argon. Since all the molecular systems in the present study have fewer (valence-shell) electrons than argon it is reasonable to assume the effects of momentum transfer variation are comparably small.

2.8 Construction of Dipole Oscillator Strength Distributions

The reliable direct experimental determination or *ab initio* calculation of most of the dipole properties for molecules the size of those studied in the present work is not at present feasible. However, Professor W.J. Meath and co-workers at the University of Western Ontario have ably demonstrated that these properties can be evaluated if globally reliable molecular dipole oscillator strength distributions (DOSDs) are available for all values of the excitation energy from the electronic photoabsorption threshold to very high energy. Such DOSDs can be constructed, by using quantum mechanical constraint techniques [29, 48–52], if sufficient photoabsorption oscillator strength (cross section) and accurate molar refractivity data are available for the molecules of interest. Molecular dipole properties [29, 30, 53] of particular interest include the dipole oscillator strength sums S_k , the analogous logarithmic dipole sums L_k , and the related mean excitation energies I_k , defined by

$$S_k = \int_{E_0}^{\infty} \left(\frac{E}{E_H} \right)^k \left(\frac{df}{dE} \right) dE \quad (2.41)$$

$$L_k = \int_{E_0}^{\infty} \left(\frac{E}{E_H} \right)^k \left(\frac{df}{dE} \right) \ln(E/E_H) dE \quad (2.42)$$

$$I_k = E_H \exp[L_k/S_k], \quad (2.43)$$

where E_0 is the electronic absorption threshold for the molecule, and E_H is 27.212 eV (the Hartree unit of energy). The index, k , can take on many different values and each corresponds to a different molecular property with respect to equations 2.41–2.43. These properties are important in a variety of areas [29, 30, 53–63]. For example, I_1 and S_1 , I_0 , and I_{-1} and S_{-1} , respectively, are part of the expressions for the straggling, stopping and the total inelastic scattering cross sections of fast charged particles in matter. The dipole sum S_2 is related to charge densities at nuclei, I_2 to the Lamb shifts, S_{-2} to the

static dipole polarizability ($\alpha_d = a_0^3 S_{-2}$), and the moments of the DOSD ($S_{-2}, S_{-4}, S_{-6}, \dots$) occur in the Cauchy expansion of the molar refractivity of molecules, and in the power series expansion of the Verdet constant. The quantities $S_{-1}, S_{-3}, S_{-3/2}, S_{-2}$, and L_{-2} can be used to obtain estimates for the dipole-dipole dispersion energies between molecules, and accurate values for the dipole properties are of importance in testing *ab initio*, non-empirical, or other methods for evaluating the properties [57, 64–70].

Another important property related to molecular DOSDs, is the molar refractivity, R_λ , of a dilute molecular gas. R_λ is related to the refractive index, $n(\lambda)$, and the dynamic dipole polarizability, $\alpha(\lambda)$, of the gas at wavelength λ by

$$\begin{aligned} R_\lambda &= \frac{1}{\rho} \left[\frac{n^2(\lambda) - 1}{n^2(\lambda) + 2} \right] \\ &= \frac{4\pi}{3} \mathcal{N} (E_H)^2 a_0^3 \int_{E_0}^{\infty} \frac{(df/dE)}{E^2 - (hc/\lambda)^2} dE \\ &= \frac{4\pi}{3} \mathcal{N} \alpha(\lambda), \end{aligned} \quad (2.44)$$

where ρ is the molar density of the gas, h is Planck's constant, \mathcal{N} is Avogadro's number, and c is the speed of light [52, 53, 71].

The procedure for calculating the constrained dipole oscillator strength distribution, $(df/dE)^c$, has been outlined in other work [54, 72]. The available absolute photoabsorption oscillator strength data for a given molecule are used to prepare an initial data base of $(df/dE)^0$ versus E values. The excitation energies for the molecule are divided into N_0 energy regions from the electronic absorption threshold to very large photon energies. These energy regions are determined from the input data and from the structure of the molecular photoabsorption spectrum. The initial differential dipole oscillator strength data for the i -th spectral region are modified according to

$$(df/dE)_i^c = (1 + a_i)(df/dE)_i^0, \quad i = 1, 2, \dots, N_0. \quad (2.45)$$

These initial $(df/dE)^0$ data are modified to satisfy two constraints, the TRK sum rule, $S_0 = N$, and molar refractivity data for two well-separated wavelengths [73–75]. The choice of the constraints is important since the initial data, in general, come from many different sources and these constraints are therefore not satisfied by the initial data.

In order to determine the best $\{a_i\}$ the function

$$G = \sum_{i=1}^{N_0} \omega_i a_i^2 \quad (2.46)$$

is minimized with respect to the $\{a_i\}$ subject to the chosen constraints. This process requires that the value of the dipole property (or molar refractivity at a wavelength λ_j) obtained with the constrained distribution, S_k^c (or $R^c(\lambda_j)$), be equal to the experimental value, S_k^e (or $R^e(\lambda_j)$), namely

$$\begin{aligned} C_k &= S_k^c - S_k^e = 0, & k = 1, 2, \dots, M_S \\ C_j &= R^c(\lambda_j) - R^e(\lambda_j) = 0, & j = 1, 2, \dots, M_R. \end{aligned} \quad (2.47)$$

In these generalized formulae there are M_S chosen dipole property constraints and M_R chosen molar refractivity constraints. In practice, for the studies undertaken in the present work, $M_S = 1$ and $M_R = 2$. Note that any of the other dipole properties, L_k and I_k , can be used in the constraint procedure provided that accurate values are known for these properties for particular values of k . This minimization procedure ensures that the final constrained oscillator strength distribution agrees as closely as possible with the initial distribution, while still satisfying the imposed constraints. In equation 2.46, ω_i is a weighting factor which reflects the uncertainty in the initial $(df/dE)^0$ in the i -th region. The problem of determining the modified DOSD, $(df/dE)^c$, is solved by using the method of Lagrange multipliers. The M Lagrange multipliers are $\{\gamma_k\}$ and $\{\gamma_j\}$, where

$M = M_S + M_R$. The problem is then to minimize the function

$$F = G - \sum_{k=1}^{M_S} \gamma_k C_k - \sum_{j=1}^{M_R} \gamma_j C_j \quad (2.48)$$

with respect to the $\{a_i\}$. A minimum is found by solving the N_0 equations

$$\frac{\partial F}{\partial a_i} = 2a_i\omega_i - \sum_{k=1}^{M_S} \gamma_k S_{ki}^0 - \sum_{j=1}^{M_R} \gamma_j R_i^0(\lambda_j) = 0, \quad i = 1, 2, \dots, N_0, \quad (2.49)$$

from which the $\{a_i\}$ can be determined once the Lagrange multipliers are known. These quantities can be found by solving the M linear differential equations given by equation 2.50 and 2.51:

$$\begin{aligned} \sum_{i=1}^{N_0} \frac{S_{mi}^0}{\omega_i} \frac{\partial F}{\partial a_i} &= 2(S_m^e - S_m^0) - \sum_{k=1}^{M_S} \gamma_k \sum_{i=1}^{N_0} S_{ki}^0 S_{mi}^0 / \omega_i \\ &\quad - \sum_{j=1}^{M_R} \gamma_j \sum_{i=1}^{N_0} R_i^0(\lambda_j) S_{mi}^0 / \omega_i = 0, \quad m = 1, 2, \dots, M_S \end{aligned} \quad (2.50)$$

$$\begin{aligned} \sum_{i=1}^{N_0} \frac{R_i^0(\lambda_p)}{\omega_i} \frac{\partial F}{\partial a_i} &= 2(R^e(\lambda_p) - R^0(\lambda_p)) - \sum_{j=1}^{M_R} \gamma_j \sum_{i=1}^{N_0} R_i^0(\lambda_j) R_i^0(\lambda_p) / \omega_i \\ &\quad - \sum_{k=1}^{M_S} \gamma_k \sum_{i=1}^{N_0} S_{ki}^0 R_i^0(\lambda_p) / \omega_i = 0, \quad p = 1, 2, \dots, M_R. \end{aligned} \quad (2.51)$$

A DOSD can be constructed for each initial data base for a given molecule. The amount of modification of the initial $(df/dE)^0$ versus E data that is required to satisfy the constraints can be represented by the standard deviation (STD) defined by

$$(\text{STD}) = \left[\sum_{i=1}^{N_0} (a_i - \bar{a})^2 / N_0 \right]^{\frac{1}{2}}, \quad (2.52)$$

where \bar{a} is the mean of the a_i values.

Once the modified DOSD $(df/dE)^c$ is determined the values of S_k^c and $R^c(\lambda_j)$ are easily computed using equations 2.41, 2.44, and 2.45 as

$$S_k^c = \sum_{i=1}^{N_0} (1 + a_i) S_{ki}^0 \quad (2.53)$$

$$R^c(\lambda_j) = \sum_{i=1}^{N_0} (1 + a_i) R_i^0(\lambda_j), \quad (2.54)$$

where

$$S_{ki}^0 = \int_{E_i}^{E_{i+1}} \left(\frac{E}{E_H} \right)^k \left(\frac{df}{dE} \right)^0 dE \quad (2.55)$$

$$R_i^0(\lambda_j) = \frac{4\pi\mathcal{N}}{3} (E_H)^2 a_0^3 \int_{E_i}^{E_{i+1}} \frac{(df/dE)^0}{E^2 - (hc/\lambda_j)^2} dE. \quad (2.56)$$

Chapter 3

Experimental Methods

The photoabsorption and photoionization oscillator strength data presented in this work have been measured on two high impact energy electron energy-loss spectrometers. The dipole (e,e+ion) spectrometer, described in section 3.1, was used to obtain photoabsorption and photoionization data over a wide energy range at low resolution (1 eV fwhm). The second dipole (e,e)¹ spectrometer used in the present work is described in section 3.2, and was used to measure photoabsorption data at a much higher resolution (0.048 eV fwhm) with special emphasis in the discrete excitation region below the first ionization potential. This high electron resolution capability has allowed individual vibronic transitions associated with electronic states of the molecule to be identified.

During the course of the present work a third, more specialized, dipole (e,e) spectrometer has been designed and constructed. This new apparatus is described in section 3.4. Whereas the two existing dipole (e,e) spectrometers were designed to study stable gaseous (and volatile solid and liquid) samples, this spectrometer will be used to make more extensive and detailed studies of these targets as well as of unstable species like free radicals, ions, and excited species.

¹The notation "dipole (e,e)" uses nuclear physics nomenclature and describes that the scattering event involves the scattering of one incident electron followed by detection of one energy analyzed scattered electron. Dipole (e,e+ion) spectroscopy on the other hand involves the scattering of one incident electron followed by coincident detection of an energy analyzed scattered electron and an ion formed during the ionization process. The term "dipole" means that the scattering conditions used favour the excitation of dipole-allowed transitions.

3.1 Low-Resolution Dipole (e,e) and (e,e+ion) Spectrometer

The apparatus and experimental procedures used to obtain the absolute photoabsorption oscillator strengths and partial photoionization oscillator strengths using time-of-flight mass spectrometry (TOFMS) and electron energy loss spectroscopy (EELS) on the dipole (e,e+ion) spectrometer, shown in figure 3.1, have been fully described elsewhere [21, 45, 76, 77]. Electrons are produced from an indirectly heated barium oxide cathode in a black-and-white TV gun (Phillips 6AW59) which is floated at a potential of -4 kV. The electrons are accelerated to 8 keV and the resulting electron beam is focussed on the collision chamber (floated at a potential of $+4$ kV) using three sets of electrostatic (X,Y) deflectors. The electron beam scatters off the gaseous sample admitted into the collision chamber, and an angular selection aperture (P3) serves to select only those electrons which have been scattered in the forward direction (solid angle of acceptance of 1.4×10^{-4} sr). The scattered electrons can impart some of their incident energy to the target to excite electronic transitions and thereby lose energy. Electrons of a particular energy loss are selected by adding the energy loss potential to the last lens element in the deceleration lens, and to the whole analyzer. The analyzer operates with a constant pass energy to ensure that the resolution and focussing properties of the analyzer remain constant as the energy loss is varied. On leaving the collision region the scattered electron beam is focussed by a series of Einzel lenses, and is decelerated to the pass energy of the hemispherical analyser, plus any selected energy loss. The majority of the electron beam, including the dominant primary incident beam, is not of the selected energy loss and is collected in the primary beam dump. The deceleration lens is used to focus a beam of the selected energy loss at the entrance of the electron analyzer and these electrons are bent around by the analyzer and detected by a channel electron multiplier

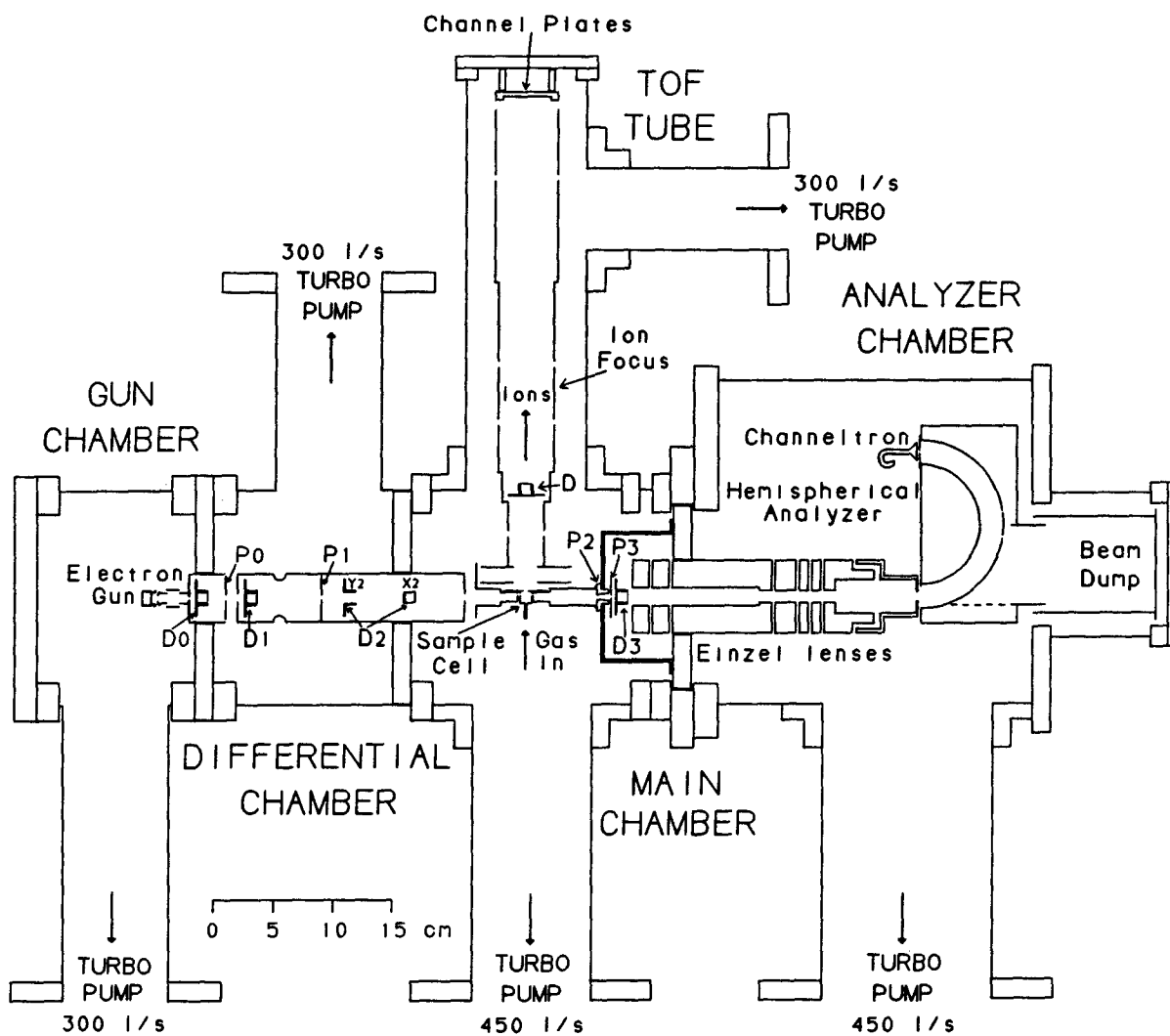


Figure 3.1: The low-resolution dipole (e,e+ion) spectrometer. The time-of-flight (TOF) mass spectrometer is actually perpendicular to the focal plane of the electron analyzer, and was used to obtain the TOF mass spectra.

(Mullard B419AL) operating in a saturated pulse counting mode. During the course of this work a further stage of differential pumping was added between the collision region and the electron gun chamber. The barium oxide cathodes used in the low-resolution dipole (e,e) spectrometer are easily "poisoned" when reactive gases are admitted into the spectrometer. The extra stage of pumping has been found to prolong the lifetime of these cathodes and has permitted the study of more reactive species like SiF₄ [78, 79]. However, no such differential pumping can be perfect and recent work on H₂ had to be abandoned because the pumping was not sufficient to keep this light, fast moving molecule, which is not easily pumped by turbo molecular pumps, from affecting the gun. The low background pressure in the spectrometer (typically 2×10^{-7} Torr) is maintained by five turbo molecular pumps.

There is an electrostatic field of $400 \text{ V} \cdot \text{cm}^{-1}$ across the collision region which extracts any positively charged ions formed during the electron scattering (ionization) events. The ions travel down a time-of-flight tube, are focussed by ion lenses, and detected with either a Johnston Multiplier or a microchannel plate (40 mm diameter, model VUW-8920ES, Electro-Optical Sensors (Intevac)) ion detector. The mass resolution ($m/\Delta m$) of this TOF mass spectrometer is about 50. Great care has been taken in the present work to characterize the response of both of these detectors to ions of different mass to charge (m/e) ratios. The procedures, and results of this study, are detailed in section 3.1.2. The spectrometer is controlled by an IBM-286-type computer and the acquisition and data analysis programs were written in PASCAL by Dr. G. Cooper.

The dipole (e,e+ion) spectrometer has two "modes" of operation. In the dipole (e,e) mode the forward scattered electron beam is analyzed as a function of energy loss. This EELS spectrum (i.e., relative differential electron scattering cross section) is converted to

a relative optical photoabsorption oscillator strength spectrum by multiplying the signal by the known Bethe-Born conversion factor [4, 12, 13, 80] for the spectrometer (see equation 2.29). The relative photoabsorption spectrum is obtained by means of overlapping data sets and is broken up in this fashion because the electron scattering signal decreases very rapidly with energy loss (approximately as the third power of the energy loss, see equation 2.27) and therefore, in order to maintain a good signal to noise ratio, a higher incident electron current must be used as the energy loss is increased. The incident current is therefore different for each data set but is monitored to ensure that it is constant during each data acquisition and background subtraction. Background subtraction is performed to eliminate any effects due to non-spectral electrons and residual gases. The ambient sample gas pressure in the scattering chamber was typically 6×10^{-6} Torr during measurements and this was reduced by $\sim 75\%$ to about 2×10^{-6} Torr for background subtraction.

The photoionization mass spectra were obtained in the dipole (e,e+ion) mode by detection of the forward scattered electrons at a particular energy loss in coincidence with the TOF mass analyzed ions. The flight time is proportional to the square root of the m/e for each ion and is determined from a single-stop time-to-amplitude converter using the ion signal as the “start” and the delayed electron signal as the “stop”. The baseline of random coincidences for such an experimental arrangement decays exponentially with increasing time [81]. The TOF mass spectrometer was designed to extract and collect all ions with equal efficiency and has strong draw-out fields to ensure uniform collection of energetic ions with excess kinetic energies of fragmentation up to 20 eV [76]. This is especially important to prevent discrimination against the low mass ions since they can carry significant kinetic energies of fragmentation. TOF mass spectra were obtained at

an energy resolution of 1 eV fwhm over overlapping energy ranges. The branching ratios for the individual ions formed were obtained by integrating the baseline-subtracted TOF mass spectra which had been corrected for the response function of the ion multiplier as a function of m/e (see section 3.1.2 and reference [82] for more details).

3.1.1 The Partial TRK Sum Rule and Corrections for Pauli-Excluded Transitions

In the technique of dipole (e,e) spectroscopy a relative oscillator strength spectrum is obtained by Bethe-Born conversion of the measured, background-subtracted electron energy-loss spectrum. There are two main ways to place the relative oscillator strength spectrum on an absolute scale. If accurate cross sections have been reported in the smooth continuum region of the photoabsorption spectrum of the system being studied, then the relative oscillator strength spectrum can be placed on an absolute scale by (one-point) normalization to the previously published data. However, such accurate data are not always available. A second method, often used in this laboratory for placing relative oscillator strength spectra on an absolute scale, involves the use of a modified Thomas-Reiche-Kuhn (TRK) sum rule. Such a procedure requires that measurements extend to high photon energy (typically ~ 200 eV) and while this is usually not feasible in optical measurements, it is readily accomplished with the dipole (e,e) method due to the extensive flat “virtual photon field” [21]. Use of the TRK sum rule provides a simpler and more accurate alternative to the tedious measurements of absolute target gas pressures which are required in traditional approaches to absolute photoabsorption measurements. The only requirement for using the TRK procedures is that the pressure and incident electron flux remain constant during the measurements.

The TRK sum rule [12, 83] may be expressed as

$$\int_{E_0}^{\infty} \left(\frac{df}{dE} \right)^0 dE = N. \quad (3.1)$$

This states that the integral of the absolute differential oscillator strength distribution $(df/dE)^0$ for photoabsorption, from the electronic threshold (E_0) to infinite energy (i.e., over all excitation and ionization processes), equals the *total* number of electrons (N) in all shells of the given target atom or molecule. Therefore, in order to utilize the TRK sum rule a complete knowledge of the shape of the differential oscillator strength distribution from the electronic absorption threshold to infinite energy would be required (i.e., the data would have to cover not only the complete valence shell but also all inner-shell regions of the spectrum). In practice, however, for molecules containing first- and second-row elements it is usually only feasible to obtain the relative valence-shell photoabsorption oscillator strength distribution out to a moderately high energy-loss, below the inner-shell thresholds which typically lie above 200 eV. In these circumstances a valence-shell modification of the full TRK sum rule has been used to place the measured relative oscillator strength spectrum on an absolute scale. We refer to this as the partial (valence-shell) TRK sum rule and it is used as follows. A curve is fitted through the higher energy data points in the relative valence-shell oscillator strength spectrum (i.e., the Bethe-Born converted electron energy-loss spectrum) and the area under the curve is integrated to infinite energy. The upper limit of the energy-loss measurements must be high enough to ensure that molecular effects, such as shape resonances, have died out, and so that there are a reasonable number of data points to fit over a sufficient range at higher energies to ensure a good fit and an accurate extrapolation. The total area under the measured relative oscillator strength distribution, plus that under the integrated fitted curve to higher energy (typically < 10% of the total), is then set equal to the total number of

valence-shell electrons (N_{val}) plus a small correction (N_{PE}) to account for Pauli-excluded transitions from the inner shells to the already-occupied valence-shell molecular orbitals. This correction for already-occupied levels is typically only $\sim 5\%$ of the number of valence electrons. These procedures are the basis of the normalization used in the present work according to the partial TRK sum rule given by

$$\int_{E_0}^{\infty} \left(\frac{df}{dE} \right)_{\text{val}} dE = N_{\text{val}} + N_{\text{PE}}. \quad (3.2)$$

This normalization procedure is best explained with the aid of an example. The ammonia molecule has the ground state electronic configuration $(1a_1)^2(2a_1)^2(1e)^4(3a_1)^2$. In the particular case of NH_3 , the correction N_{PE} to the number of valence-shell electrons N_{val} arises because transitions from the $1a_1$ nitrogen K-shell to the already occupied $2a_1$, $1e$, and $3a_1$ valence orbitals are obviously forbidden (impossible) according to the Pauli Exclusion Principle. The contribution from the nitrogen K-shell would be 2, the number of electrons in the $1a_1$ orbital, if these transitions were allowed. However, in reality the integrated K-shell oscillator strength contribution must be equal to $(2 - N_{\text{PE}})$ and correspondingly the valence-shell oscillator strength must be $(8 + N_{\text{PE}})$ according to equation 3.2 in order to satisfy the TRK sum rule (equation 3.1).

The determination of N_{PE} is not straightforward in the case of molecular targets. For atoms, the corrections (N_{PE}) can be obtained from numerical values of the oscillator strength contribution for excitations from the K-shells which have been calculated by Wheeler and Bearden [84] for several atoms ranging in atomic number from $Z=2$ to 82. More recently, Inokuti [85] has calculated the contributions from all the individual shells of all the atoms up to an atomic number of 38 using Hartree-Slater methods. In the absence of such calculations for molecules the atomic values for the contributions from inner-shell transitions can be used to provide approximate values of the Pauli excluded

corrections for molecular systems.

For one-center hydrides (as discussed in section 6.2.2 for ammonia) the best method for estimating the partial TRK sum rule normalization is to sum up the valence-shell contributions for the atom which is isoelectronic with the molecule being studied. For complex molecular systems (e.g., molecules with more than one central heavy atom) the normalization factor can be determined by first breaking the molecule down into components that are, or are isoelectronic with, an atom in the periodic table. For example, silicon tetrafluoride [78]: $\text{SiF}_4 \equiv \text{Si}+4\text{F}$; methanol [86]: $\text{CH}_3\text{OH} \equiv \text{F}+\text{F}$; butane [87]: $\text{CH}_3\text{CH}_2\text{CH}_2\text{CH}_3 \equiv \text{F}+\text{O}+\text{O}+\text{F}$; and toluene: $\text{C}_6\text{H}_6\text{CH}_3 \equiv 6\text{N}+\text{F}$. The normalization factor is then obtained by summing up the calculated [85] total contributions from the valence shells of the equivalent isoelectronic atoms. It should be pointed out that this procedure for normalizing the valence-shell of complex molecular systems has recently been used to obtain very accurate photoabsorption oscillator strengths for the linear alkanes from methane to octane [87].

The above discussion was based on the fact that the inner (K) shell excitation thresholds of the second-row atoms are high in energy and thus beyond the upper limit to which the valence shell measurements are usually obtained. However, for larger atoms and correspondingly larger molecules, the measured oscillator strength spectra will not only involve the valence shell but also include contributions from any inner shells which are excited over the measured energy region. In this event, a similar procedure as was outlined above for using the partial TRK sum rule is followed, and the area under the relative oscillator strength spectrum (to infinity) is set equal to the sum of the calculated contributions [85] from the valence shell plus the contributions from all inner shells excited over the measured energy region. One must still ensure that there is a large

enough region of measurement at higher energies to permit the necessary curve-fit for the extrapolation (see above). If this is not the case (e.g., when the system has many closely spaced shells, or when the oscillator strength spectrum is complicated by Cooper minima or shape resonances, as for example in the oscillator strength spectra of argon, krypton, and xenon [88]) then the partial TRK sum rule becomes difficult to use and some alternative method for normalization or absolute scale determination is needed. In the studies of the photoabsorption oscillator strength spectra of argon, krypton, and xenon [88] the normalization was achieved using the highly accurate continuum cross-section measurements obtained by Samson and Yin [89] using resonance line radiation sources.

3.1.2 Ion Detector Response Functions

During the course of the present work a new MCP detector was built and installed on the TOF tube of the dipole (e,e+ion) spectrometer. It was noted however that the results obtained using this new detector were slightly different, for the same molecule, than those obtained earlier using the Johnston multiplier ion detector. These observed differences prompted us to determine the detector response function for each detector to ions of different mass to charge ratio (m/e). In any branch of quantitative mass spectrometry, e.g., photoionization mass spectroscopy or dipole (e,e+ion) spectroscopy, it is important to fully characterize the detection system of the spectrometer if accurate results are to be obtained.

For the present purposes the noble gas atoms He, Ne, Ar, Kr, and Xe were found to be ideal targets. The energy loss (equivalent to a photon energy) was selected such that only singly charged cations were formed. That is, the energy deposited to the target

noble gas atom was above the first IP, but below the IP for double ionization, of the target. Furthermore, since the ionization efficiency of the noble gas atoms is unity above the first IP [90] any forward scattered electron detected with an energy loss above the first IP will have produced an ion. Molecular targets were not used in this study because of the greater possibility of fluorescent decay of super excited neutral states, and because of the formation of several types of ions due to fragmentation.

The ion detector response was determined for each detector as follows. For each noble gas studied the energy loss was set to be above the first IP, but below the second IP. A TOF mass spectrum was collected in the dipole (e,e+ion) mode in coincidence with forward scattered electrons of the selected energy loss. The ratio of the number of ions formed, determined by integrating the baseline-subtracted TOF mass peak, to the number of true energy-loss events gives the relative detection efficiency. The number of true energy loss events was determined by collecting an energy loss spectrum at the full pressure used for the TOF measurements, and subtracting a similar energy loss spectrum at the base pressure of the spectrometer. Thus the fraction of “true” energy-loss events at a particular energy loss was determined.

The ion detector response functions for the Johnston multiplier and microchannel plate detectors are shown in figure 3.2. It is worth mentioning at this point that the ion extraction and transportation systems of the dipole (e,e+ion) spectrometer are independent of the mass to charge ratio of the ions studied and were therefore the same for each detector. For this reason, the relative detection efficiency of each detector could be determined.

A smooth curve consisting of two quadratic functions was fitted to the experimental

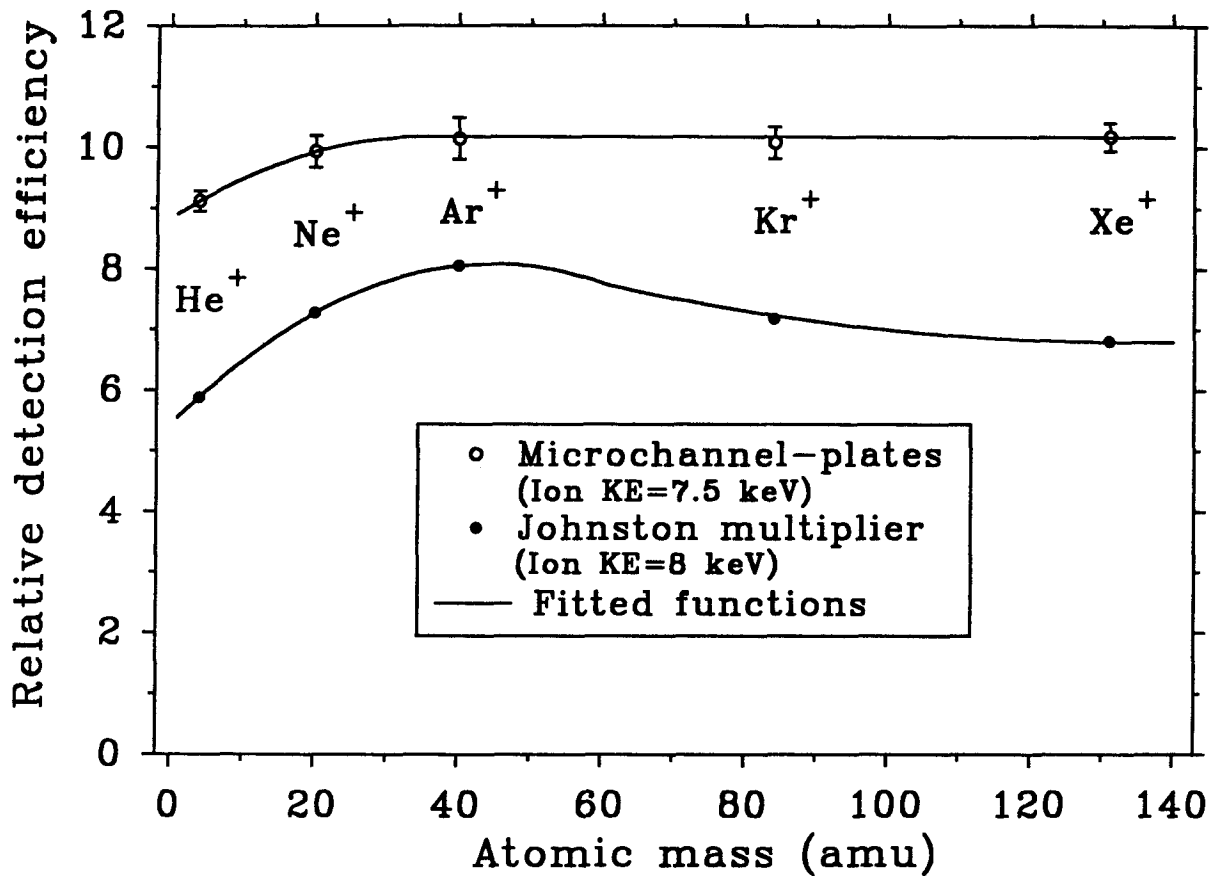


Figure 3.2: Relative ion detector sensitivities determined for a Johnston multiplier and for a microchannel plate ion detection as a function of singly charged ionic mass. The error bars represent the standard deviation of a number of experimental determinations.

data points for each multiplier, and these functions were found to be,

$$d_{\text{MCP}} = \begin{cases} a_1 + a_2m + a_3m^2 & 1 \leq m \leq 34 \\ 10.175 & m \geq 35 \end{cases} \quad (3.3)$$

$$d_{\text{JM}} = \begin{cases} b_1 + b_2m + b_3m^2 & 1 \leq m \leq 60 \\ c_1 + c_2m + c_3m^2 & 61 \leq m \leq 140 \end{cases} ,$$

where $a_1 = 8.8289$, $a_2 = 0.077208$, $a_3 = -0.0011076$, $b_1 = 5.4311$, $b_2 = 0.11879$, $b_3 = -0.0013299$, $c_1 = 9.9672$, $c_2 = -0.047567$, and $c_3 = 0.0001787$, and m is the mass to charge ratio of the ion. It is apparent that both detectors show a decreased sensitivity to lower mass ions, specifically below ~ 40 amu for the Johnston multiplier and below ~ 30 amu for the microchannel plate detector. The relative detection efficiency of a Johnston multiplier was determined by Backx and Van der Wiel [76] for 8 keV ion impact energy using essentially the same apparatus as used in the present work. However, their study [76] was performed over the very limited energy range from 1 to 16 amu. Of the ions produced from the electron impact ionization of methane, it was concluded [76] that all the ions were detected with equal efficiency except H^+ , for which there was a 10% reduction in sensitivity. The relative detection efficiency of the microchannel plate detector remains constant at higher masses, but that of the Johnston multiplier decreases relative to its value at 40 amu. The relative detection efficiency of the microchannel plate detector is greater than, and less variable than that of the Johnston multiplier, and the TOF mass spectra measured with the microchannel plate detector have a better signal-to-noise ratio.

It is possible that the decrease in sensitivity observed for the Johnston multiplier at masses greater than 40 amu is similar to the “velocity effect” observed by Peart and

Harrison [91]. Peart and Harrison [91] studied the detection efficiency of a Johnston multiplier for atomic ions ranging in mass from helium to cesium and reported that the detection efficiency is dependent on the velocity with which the ions strike the first dynode of the detector. They measured absolute detection efficiencies of $\sim 70\%$ for incident ion velocities of $10^5 \text{ m}\cdot\text{s}^{-1}$, which increased to 90% for $3 \times 10^5 \text{ m}\cdot\text{s}^{-1}$. Above this velocity the detection efficiency was found to be essentially constant and independent of the mass of the incident ions. In the present study where 8 keV ion impact energy is used, a velocity of $2 \times 10^5 \text{ m}\cdot\text{s}^{-1}$ corresponds to $\sim 38 \text{ amu}$.

The decrease in detector efficiency at low masses must be due to some other phenomenon. In the situation of constant ion impact energy at the multiplier input, as in the present spectrometer, the momentum of the incident ions increases as the square root of the ion mass. Lower mass ions have the least momentum when striking the ion multiplier. Thus the decrease in sensitivity to low mass ions for both detectors could be due to some ion impact momentum-dependent phenomenon. One way to check this hypothesis would be to repeat the measurements for both detectors using a much higher ion impact energy, say 20 keV . This should substantially reduce the variation of multiplier sensitivity to mass to charge ratio. The ion impact energy could be increased by post-accelerating the ion beam at the multiplier input. However, the present experimental arrangement of the dipole ($e, e+\text{ion}$) spectrometer does not readily allow for such an experiment to be performed.

The relative detection efficiency response curves (figure 3.2) have been used in the present work to correct the measured TOF mass spectra to account for the variation of the detector to ions of different mass to charge ratio. It has been shown [82] that such correction procedures are very effective for small polyatomic molecules (C_2H_2 , C_2H_4 ,

SiF₄, CCl₄). However, such results should be put into perspective. First, the detector efficiencies were determined using singly charged atomic ions. The detection efficiency of a doubly charged ion is not necessarily the same as that of the corresponding singly charged ion of the same mass to charge ratio. Furthermore, these molecular studies [82] involve polyatomic molecular and fragment ions. It has been reported by Dietz [92], in a study of many singly charged atomic ions and the polyatomic ion, Na₂BO₂⁺, that the polyatomic species was more efficient at producing secondary electrons, when hitting the emitting surface of a discrete dynode electron multiplier, than were the atomic cation species like Na⁺ or Pb⁺, which are of lower and higher mass, respectively. Thus care should be taken when applying these correction factors to multiply charged and polyatomic ions. Finally, the present study has shown that, except for low mass ions (< 20 amu) the ion detection sensitivity correction factors for both detectors are relatively small for 8 keV ion impact energy.

3.2 High-Resolution Dipole (e,e) Spectrometer

The high resolution (0.048 eV fwhm) photoabsorption oscillator strength data were measured using the dipole (e,e) spectrometer shown in figure 3.3. Details of the design and construction of this spectrometer have been reported previously [93]. The spectrometer consists of four chambers, each pumped by a turbo molecular pump (Seiko-Seiki STP-300 or STP-400), which house the electron gun, the electron beam monochromator, the electron beam analyzer, and the scattering (collision) chamber. The electron beam in this instrument is produced from a heated thoriated tungsten filament located within an oscilloscope electron gun body (Clifftronics CE5AH). The cathode or filament (C), grid (G), anode (A), and focus (F) are all floated at a potential of -3 keV with respect

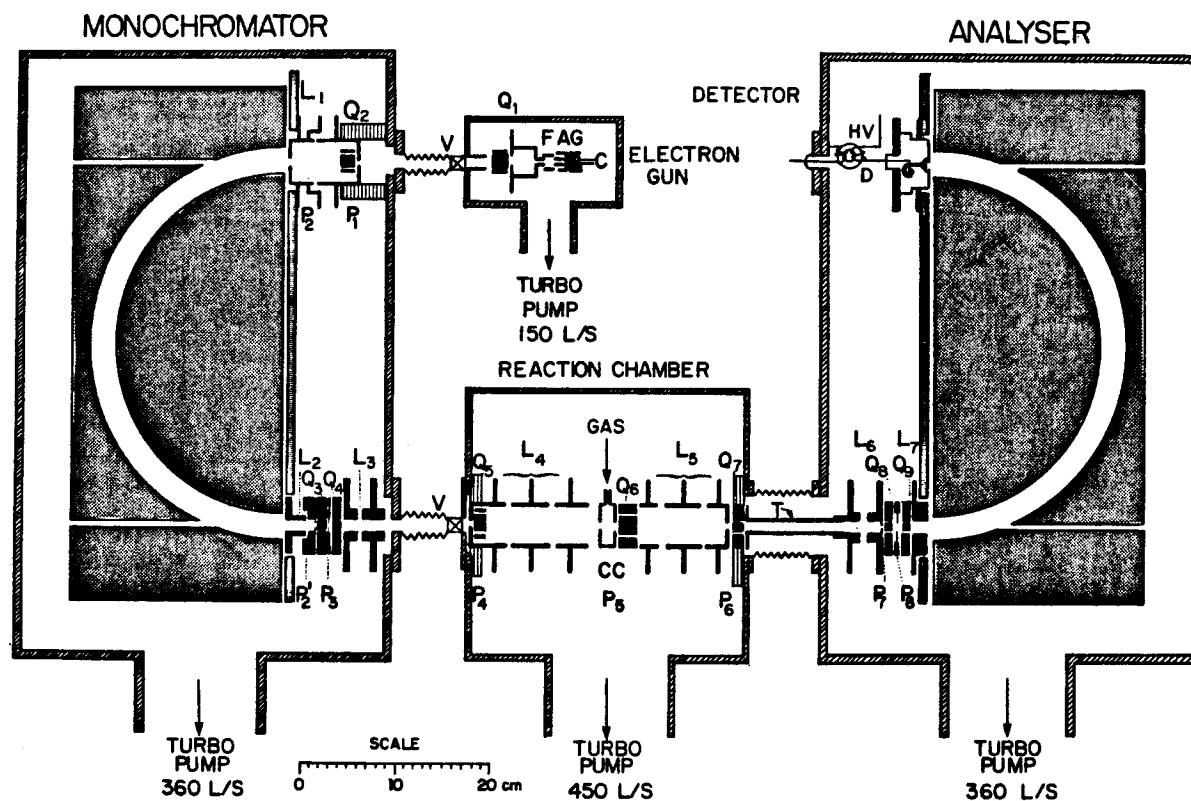


Figure 3.3: The high-resolution dipole (e,e) spectrometer.

to the collision region which is held at ground potential. The electron beam produced by the electron gun is decelerated and passed through the large radius (19 cm) electrostatic hemispherical analyzer (labelled monochromator) [94]. The monochromator is not a full hemispherical analyzer in that the hemispheres are truncated. Side plates hold the truncated hemispherical sections in place and can be appropriately biased with voltages to compensate for any field non-uniformity. A similar type of analyzer design has been suggested by Jost [95]. The primary electron beam from the heated filament has an energy spread of ~ 0.8 eV fwhm and the monochromator serves to reduce this energy spread. The electron beam that passes through the monochromator is reaccelerated to 3 keV and then is scattered off the sample gas admitted to the collision chamber (CC). Electrons scattered in the forward direction are energy-analyzed by the large radius (19 cm) hemispherical electron analyzer. Finally, the electrons are detected by a channel electron multiplier (Mullard B419AL) and the signal is decoupled using a ferrite core transformer. The spectrometer is controlled by an IBM 386 computer and the data acquisition and spectral analysis programs were written by Dr. G. Cooper.

Nine sets of deflectors (Q_1 - Q_9) and eight apertures (P_1 - P_8) are used to steer and to define the electron beam. Carefully designed electron lenses (L_1 - L_7) are used to transport and to characterize the beam. Using these advanced electron optics, defining apertures, and large hemispherical analyzer and monochromator, a resolution of 36 meV fwhm can be achieved for the main (unscattered) electron beam. The inelastically scattered electron beam has been determined to have a resolution of 48 meV fwhm from recent measurements of the electronic excitation spectrum of helium in the discrete region [96].

The operation and data analysis procedures of this instrument [27, 93] have recently been adapted to provide highly accurate dipole (e,e) measurements of absolute oscillator

strengths for discrete transitions at high resolution [26, 27, 96]. The Bethe-Born factor for this spectrometer was used to transform the high resolution EELS spectra to a relative oscillator strength spectrum. The high-resolution relative oscillator strength spectrum was then placed on an absolute scale by normalization to the absolute low-resolution data obtained in the present work in the smooth continuum region. The photoabsorption oscillator strengths thus obtained are considered to be accurate within $\pm 5\%$. Furthermore, the measurements are free of the “line-saturation” (or bandwidth) effects which can cause serious errors in photoabsorption cross sections obtained for discrete transitions using the Beer-Lambert Law [26] in situations where the natural linewidth of transitions is comparable to or less than the incident photon bandwidth.

3.3 Sample Handling

The base pressure of each turbo molecular pumped spectrometer is $\sim 2 \times 10^{-7}$ Torr. Samples are admitted into the spectrometer to a pressure of $\sim 2 \times 10^{-5}$ Torr. This pressure is high enough to ensure that most of the scattering events are from the sample, rather than from the residual background gas in the spectrometer, and low enough to avoid double scattering. More importantly, since the aim of the present work is to determine absolute oscillator strength data for the sample being studied, the small but significant contributions from the background gases, and non-spectral electrons, must be eliminated. To achieve this, a second spectrum is collected at about one-quarter the pressure and this spectrum is subtracted from the first, full pressure spectrum. The sample is not entirely removed from the spectrometer to avoid any shift in the energy scale because of changing contact potentials (resulting from adhesion of the admitted sample gas to the components of the spectrometer).

Table 3.1: Purity of samples used in the present work.

Compound	Molecular Formula	Supply Company	Minimum Stated Purity
Methanol	CH ₃ OH	BDH (Omnisolv)	99.9%
Carbon Tetrachloride	CCl ₄	BDH	99%
Ammonia	NH ₃	Matheson Chemicals Inc.	99.99%
Monomethylamine	CH ₃ NH ₂	Matheson Chemicals Inc.	98.0%
Dimethylamine	(CH ₃) ₂ NH	Matheson Chemicals Inc.	99.0%
Trimethylamine	(CH ₃) ₃ N	Matheson Chemicals Inc.	99.0%

The gaseous and liquid samples used in the present work are listed in table 3.1 along with their stated purity and the company which supplied the chemicals. Gaseous samples were used as supplied from lecture bottles. The residual air in all liquid samples studied was removed by repeated freeze-thaw-pump cycles using liquid nitrogen. No residual air peaks, or significant impurities, were observed in any of the TOF mass spectra, or high-resolution electron energy-loss spectra.

3.4 High Impact Energy Dipole (e,e) Spectrometer

During the course of this thesis a new spectrometer has been designed and constructed. The spectrometer uses a number of the features found on the other two spectrometers described in the present work (see sections 3.1 and 3.2). However, the two earlier spectrometers were designed primarily to study gas phase targets at room temperature, and to provide high-resolution oscillator strength data, respectively. The present high-impact energy dipole (e,e) spectrometer has been designed and constructed to permit absolute photoabsorption oscillator strength (cross-section) measurements of

1. the K-shell spectra of molecules containing third-row atoms (e.g., Si, P, S, Cl), which require the energy-loss range to be extended up to at least 3 keV,
2. the L-shell spectra of molecules containing fourth-row atoms (e.g., Ge, As, Se, Br, and transition metal compounds such as $\text{Cr}(\text{CO})_6$, $\text{Ni}(\text{CO})_4$, $\text{Fe}(\eta^5\text{-C}_5\text{H}_5)_2$, $\text{Mo}(\eta^6\text{-C}_6\text{H}_6)_2$),
3. unstable species and reaction intermediates including
 - (a) ions (e.g., He^+ , Ne^+ , Ar^+ , Kr^+ , Xe^+ , O^+ , N^+ , H_2^+ , O_2^+ , N_2^+)
 - (b) metastables (e.g., He^* , Ne^* , Ar^* , N_2^*)
 - (c) free-radicals (e.g., CH_3 , C_2H_5 , H, F)
 - (d) laser-excited species (e.g., Na 3p),
4. compounds of biological, biomedical and pharmaceutical interest (e.g., amino acids, amides, glyoxal, urea),

5. low melting point (mp < 200 °C) solids (e.g., polycyclic hydrocarbons and other organic molecules),
6. metal vapours (e.g., Li, Na, K, Rb, Cs).

Furthermore, the potential of using electron energy-loss spectroscopy as a microanalysis tool for low Z elements [97] will be explored.

The high-impact energy electron energy-loss spectrometer is shown in figure 3.4. The electron beam is produced at a potential equal to the negative of the electron impact energy, that is, 0 to -10 kV (with respect to the collision region which is at ground potential), by a black and white TV gun with an indirectly heated barium oxide cathode (Phillips 6AW59, or equivalent). Adjustment of the grid (G), anode (A) and focus (F) potentials result in a well-focussed, high current density electron beam. The electron beam passes through two apertures (P1 and P2, which are 3 mm and 2 mm, respectively) before being scattered off the sample gas in the collision chamber (CC). As the 10 keV energy electron beam passes through each aperture its direction is maintained by two pairs of deflector plates (D). The angular selection aperture (P3) at the exit of the main chamber selects only those electrons which are scattered through small angles in the forward direction. These electrons are focussed by an Einzel lens system and decelerated to the pass energy of the analyzer (typically 100–500 eV) by the last two lens elements. The lens element voltages, electrostatic contours, and simulated electron ray traces are shown in figure 3.5. The electrons are energy-analyzed by a large (16 inch mean diameter) hemispherical electrostatic analyzer. The electrons are counted by a channeltron electron multiplier (CEM, Mullard B419AL) or a microchannel plate detector (MCP), and the amplified output signal is sent to an IBM-PC compatible personal computer for data storage and analysis. The MCP detector was built at UBC and features two MCPs

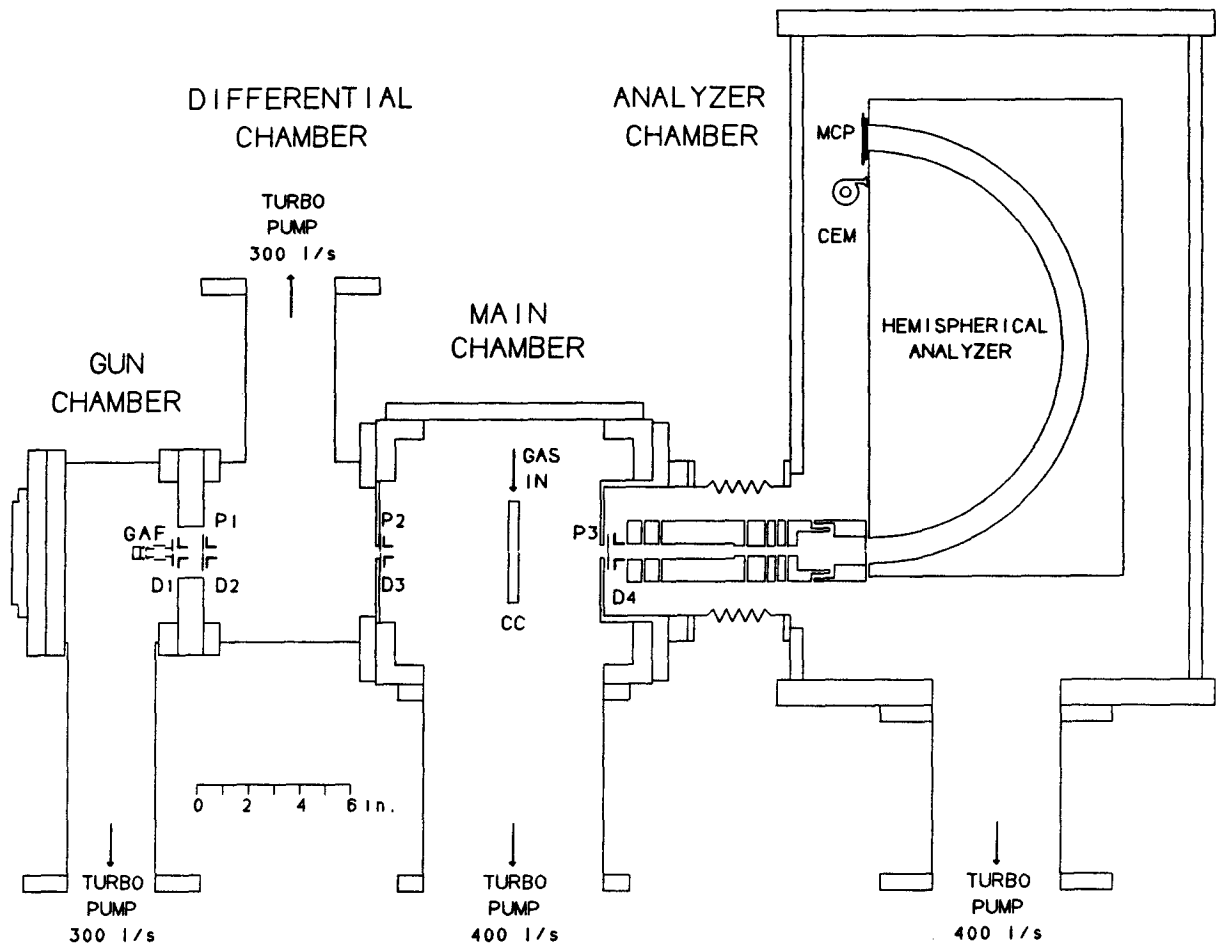


Figure 3.4: A schematic of the new high impact energy dipole (e,e) spectrometer designed and constructed in the present work. See text for details.

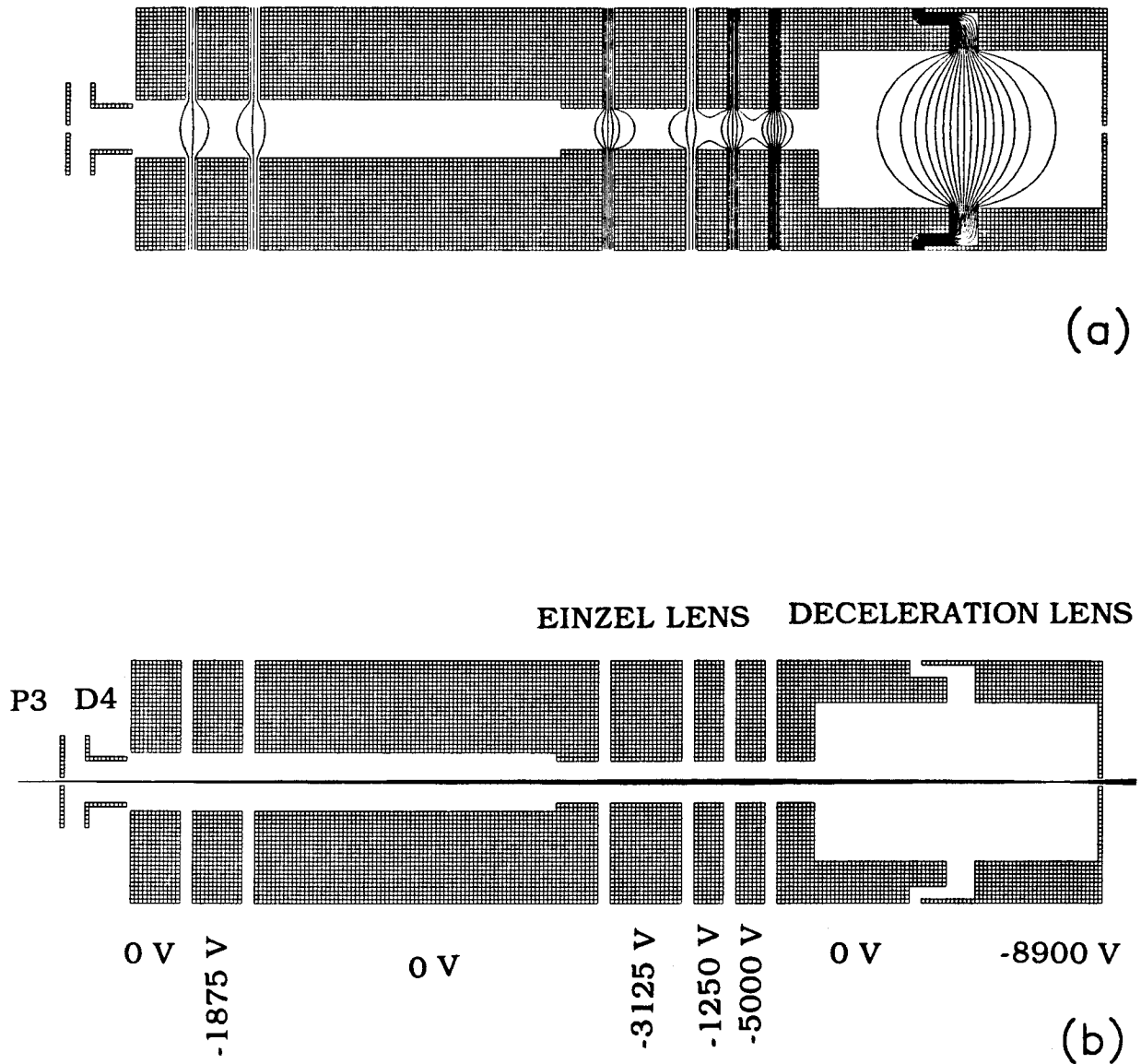


Figure 3.5: Simulation of the Einzel and deceleration lens systems for an incident electron beam energy of 10 keV, an energy loss of 1000 eV, and a pass energy of 100 eV. The electrode potentials are reported with respect to ground. (a) A potential contour plot of the system. The contours are from 0 to -10 keV at intervals of 500 eV. (b) Simulated electron ray traces at 0 , ± 0.1 , and ± 0.2 degrees.

(Electro-Optical Sensors (Intevac) VUW-8920ES) in a chevron configuration. The entire scanning and data collection processes are controlled by computer programs written in PASCAL.

The present high-energy dipole (e,e) spectrometer will incorporate the following design features:

1) High Electron Impact Energy

The incident electron beam energy will be tuneable to as high as 10 keV. This should permit the measurement of photoabsorption oscillator strength data at energy losses (equivalent photon energies) up to ~ 3000 eV. As can be seen from table 3.2, this will permit the study of electronic excitations from third-row K-shells and fourth-row L-shells and all higher (lower binding energy) shells.

2) Open Scattering Region at Ground Potential

Experiments involving laser-excited species can best be accomplished if the spectrometer has an open and easily accessible scattering region. The open architecture will also be optimal for the study of unstable species produced using insertion devices such as an oven, a pyrolysis unit, a microwave cavity, or an inductively coupled plasma (ICP) ion source. Furthermore, since the collision region is at ground potential these insertion devices, and the associated electronics, will also be conveniently operated at ground potential.

3) Multichannel Detection

The electron detection system of the spectrometer will be switchable between a single-channel detector (channeltron electron multiplier) and a multichannel detector (two microchannel plates stacked in a chevron configuration, plus a resistive anode). There are two reasons why multichannel detection will be important in this spectrometer:

Table 3.2: Atomic inner-shell binding energies adapted from Egerton [97]. All energies are in electron volts (eV).

Element		Atomic Shell						Row Number
		1s K	2s L ₁	2p _{1/2} L ₂	2p _{3/2} L ₃	3p M ₂₃	3d M ₄₅	
3	Li	55						ROW 2
4	Be	111						
5	B	188						
6	C	284						
7	N	400						
8	O	532						
9	F	685						
10	Ne	867			18			
11	Na	1072			32			ROW 3
12	Mg	1305			52			
13	Al	1560	118		73			
14	Si	1839	149		100			
15	P	2149	189		135			
16	S	2472	229		165			
17	Cl	2823	270		200			
18	Ar	3203	320		246			
19	K	3608	377		294			ROW 4
20	Ca	4038	438	350	347			
21	Sc	4493	500	402	406			
22	Ti	4965	564	461	455	47		
23	V	5465	628	520	513	47		
24	Cr	5989	695	584	575	48		
25	Mn	6539	770	652	640	51		
26	Fe	7113	846	721	708	57		
27	Co	7709	926	794	779	62		
28	Ni	8333	1008	872	855	68		
29	Cu	8979	1096	951	931	74		
30	Zn	9659	1194	1043	1020	87		
31	Ga		1298	1142	1115	105		
32	Ge		1414	1248	1217	125	30	
33	As		1527	1359	1323	144	41	
34	Se		1654	1476	1436	162	57	
35	Br		1782	1596	1550	182	70	
36	Kr		1921	1727	1675	214	89	

- The electron scattering cross section drops off very rapidly as a function of energy loss relative to the photoabsorption cross section (approximately as the third power of the energy loss—see equation 2.27). Therefore, at high energy losses the cross section will be very low and thus high detection sensitivity will be required.
- Unstable species (laser-excited species, free radicals, ions, etc.) are difficult to produce in large quantities, therefore there will be a very low sample target density in these experiments.

The improved signal-to-noise ratio provided by multichannel detection devices will be essential to the success of these types of studies.

4) Known Scattering Geometry

When the scattering geometry of an electron energy-loss spectrometer is known completely, the Bethe-Born factor, $B(E)$, which converts the measured electron scattering cross section to a relative oscillator strength scale, can be calculated (see section 2.4). Using $B(E)$, the relative oscillator strength data can be placed on an absolute oscillator strength scale using the TRK sum rule or by one-point normalization to a known photoabsorption value.

5) Differential Pumping

The four separate vacuum chambers in the spectrometer are each pumped by a Seiko-Seiki turbomolecular pump (two model STP-450 and two model STP-300). The differential pumping is achieved by placing small apertures between the chambers which are just large enough to allow a well-focussed electron beam to pass through. The apertures are the only openings between the chambers, which means that the four chambers are pumped essentially independently. Typically, the scattering chamber can be filled to a pressure that is two orders of magnitude greater than base pressure with little or no change in the

pressure in the electron gun chamber. Differential pumping has the advantages that it prolongs the life of the oxide cathode electron guns which are used in the spectrometer, and provides a more stable electron beam since the electron emitting surface of the gun will not be affected by the sample gas. These considerations are especially important for quantitative work when very reactive gases are being studied.

3.4.1 Specialized Sample Introduction Systems

The new dipole (e,e) spectrometer has an open scattering region at ground potential. Several different sample introduction systems have been designed to produce a range of chemically interesting target species.

1) Microwave Source

A microwave cavity with a flow tube and needle valve has been constructed in-house and mounted on one of the side flanges of the main chamber of the spectrometer. Such a source has been used by other groups [98–101] to produce free radicals (H, F, PH₂, PH, O, N) and metastable species (He^{*}). The sample gas is flowed through the cavity, and the microwave discharge is initiated by a spark from a hand-held tesla coil. The quarter-wavelength microwave cavity operates at 2450 MHz and the power is supplied by a conventional control unit (Microtron 200). The electrons accelerated inside the microwave cavity collide with the sample gas, and the resulting products flow into the collision chamber through a narrow (1.4 mm) quartz tube. Prior to this transportation tube, the bulk of the gas is pumped away by a large roughing pump (160 L·min⁻¹) to keep the background pressure in the spectrometer as low as possible. In order to assess what fraction of the species formed are radicals, the spectra obtained when the microwave source is on, and off, will be compared. Such a procedure has been used to obtain accurate

absolute oscillator strength data for atomic nitrogen and atomic oxygen [100, 101].

2) Heated Inlet System

A cylindrical copper block (0.675 inch i.d., 1.25 inch o.d.) has been attached to the collision chamber. Slots were cut lengthwise in the block to hold two heaters (HOT-WATT), or alternatively an externally wound heater can be used. Current is supplied to the heaters through non-inductively wound wires using a Variac and the resulting temperature rise in the copper block is monitored with a chromel/alumel thermocouple, or a conventional thermocouple device (Dyna-Sense). The large slot in the copper block holds a glass ampule which is attached to the end of a sample probe. The glass ampule has a 1 mm hole in one end. The ampule is filled with the solid sample to be studied, and positioned in the copper block with the sample probe rod through a Goddard valve interlock attached to the side of the spectrometer in line with the collision chamber. As the ampule is heated the vapour emerges from the hole and into the heated collision region. Such a system permits the repeated insertion of solid samples directly into the high vacuum chamber without having to take the spectrometer up to atmosphere. This interlock system is therefore convenient and efficient.

3) Oven

Designs are being drawn for the construction of an oven to be used to produce vapours from much higher melting point ($mp < 800\text{ }^{\circ}\text{C}$) solids (e.g., Na, Cs). This device will be mounted beside the collision chamber and in all likelihood will be used along with a cold trap. The cold trap will be positioned on the opposite side of the collision chamber from the oven and will serve to keep the background pressure low in the spectrometer. This will allow for the use of higher fluxes from the oven.

4) Inductively Coupled Plasma (ICP) Source

We are considering the use of an ICP source for producing large fluxes of ions, especially Ar^+ [102]. The ions formed from the ICP torch flame, or from samples admitted into the flame, will be mass selected using an in-line quadrupole mass analyser, before being steered and focussed on the collision region. Since the ICP torch operates at atmospheric pressure several stages of differential pumping and skimmer cones will be necessary in order to maintain a low background pressure in the spectrometer when this type of device is in operation.

Chapter 4

Photoabsorption and Photoionization Studies of Methanol

4.1 Introduction

The photoabsorption and photoionization of methanol in the vacuum UV and soft X-ray regions are of interest in many fields of science and technology. For example, methanol has been observed in the interstellar medium and its interaction with energetic radiation is therefore of importance to astrophysicists [103, 104]. Methanol has also been studied as a chromophore contributing to the total photoabsorption of glucose at low photon energies and this is of interest in biochemistry and radiation biology [105]. The present work is of importance since it is the only data set providing photoabsorption oscillator strengths (cross sections) over the continuous energy region from 6 to 360 eV, covering both the valence and carbon K-shell regions. Since previously published photoabsorption cross-section data [105–119] cover only limited energy regions the presently reported measurements also provide the first experimental test of the wide-ranging dipole oscillator strength distributions (DOSD) predicted semi-empirically by Jhanwar and Meath [120] on the basis of various constraints, including sum rule considerations, mixture rules, and the limited experimental data available. The present work also represents the first reported absolute partial oscillator strengths for the molecular and dissociative photoionization of CH_3OH .

Absolute photoabsorption cross sections for the valence shell of methanol have been

measured by many groups, in various energy regions, using direct optical techniques. Several studies have been reported in the photon energy range below 30 eV [105–116, 121–123] while de Reilhac and Damany [117] have reported measurements in the range 31 to 124 eV. Some additional data have been obtained by Gluskin *et al.* [118] from 90 to 220 eV using synchrotron radiation.

The carbon K-shell excitation and ionization of methanol extends above 285 eV but there have been comparatively few spectroscopic studies of this region. In 1974 Wight and Brion [124] reported a high impact energy, small angle (2°), low resolution (0.5 eV fwhm) carbon K-shell electron energy loss (EELS) spectrum of CH₃OH on a relative electron impact excitation cross-section scale. Later, Ishii and Hitchcock [119] reported the carbon K-shell dipole oscillator strength spectrum (0.6 eV fwhm) on an approximate absolute scale over the energy range 282 to 324 eV. These absolute oscillator strength data [119] were obtained by semi-empirical Bethe-Born conversion of an electron energy loss spectrum (mean scattering angle 2°) followed by normalization to the calculated [125] atomic carbon oscillator strengths in the continuum region at 25 eV above the carbon K-shell ionization edge of CH₃OH. In this procedure [119] the valence shell photoabsorption oscillator strength underlying the carbon K-shell region was estimated and subtracted from the measured spectra. It is important to test the validity of using such absolute normalization procedures based on summed atomic photoionization oscillator strengths at 20–30 eV above the appropriate inner shell edge. This type of normalization is typically applied at least 20–30 eV above the particular inner shell ionization edge, since at such photoelectron energies it has usually been assumed that molecular effects (e.g., shape resonances) have subsided. In earlier studies from this laboratory by making absolute dipole oscillator strength determinations in the Si 2p,2s regions of SiH₄ [126, 127], the

P 2p,2s regions of PH₃ [128, 129] and the S 2p,2s regions of SO₂ [130, 131] we have demonstrated that such atomic normalization procedures can be considered reasonably accurate for third row L-shells provided that the normalization is carried out at least 30 eV above the inner shell ionization threshold. This proviso was especially important in the case of SO₂ [130, 131], where molecular effects are strongly manifested in the S 2p region. While preliminary investigations made of the C 1s (K-shell) region of CF₄ [132], using approximate procedures, have also indicated similar conclusions, it is important to make more direct tests for the case of second row K-shells. In the present work, the effectiveness of atomic normalization procedures is assessed by comparing the TRK sum-rule normalized, Bethe-Born converted, electron energy loss spectrum of CH₃OH with published atomic cross-section sums in the carbon K-shell region.

The ionization energies of methanol have been studied extensively by photoelectron spectroscopy (PES) in both the valence [133–143] and inner shell [39, 144] regions. The complete outer and inner valence shell binding energy spectra have also been studied by electron momentum spectroscopy [145]. To the best of our knowledge, no partial photoionization oscillator strengths (cross sections) have been reported for the production of the electronic states of CH₃OH⁺ by PES or dipole (e,2e) spectroscopic techniques. Similarly, no absolute intensity data have been previously reported for the molecular and dissociative photoionization of methanol. However, relative photoionization yield curves [146–151] and appearance potentials [147, 149–156] for the major photofragments of methanol at m/e 32, 31, 30, 29, 28, and 15 have been reported.

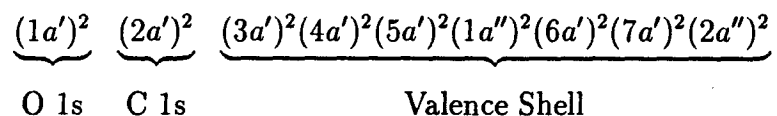
In this chapter results are reported for the photoabsorption of methanol measured at low resolution (~ 1 eV fwhm) from 6 to 360 eV, and at high resolution (0.048 eV fwhm) from 5 to 30 eV, using dipole (e,e) spectroscopy. The latter results were obtained

using the recently developed high-resolution dipole (e,e) method [26] which has been demonstrated to give very accurate optical oscillator strengths for discrete transitions in helium [96] as well as for a wide range of other atoms and molecules [25, 27, 88, 157–160]. In addition, dipole (e,e+ion) spectroscopy has been used to measure the photoionization efficiency and the photoion branching ratios for the molecular and all major dissociative photoionization channels for methanol from 10.5 to 80 eV. Absolute partial photoionization oscillator strengths for the molecular and dissociative channels of methanol have been obtained as a function of the photon energy from the triple product of the presently measured photoionization efficiency, the branching ratio for each ion and the absolute photoabsorption oscillator strength (see section 2.3).

4.2 Results and Discussion

4.2.1 Electronic Structure

Methanol has a highest symmetry of C_s , and the molecular orbital electronic configuration of the ground state in the independent particle model is:



The vertical ionization potentials (VIPs) of the six outermost orbitals have been reported to be 10.96, 12.62, 15.21, 15.64, 17.62 and 22.65 eV respectively as determined by high resolution He(I) and He(II) PES [140]. Using high resolution X-ray photoelectron spectroscopy (XPS), Nordfors *et al.* have determined the VIP of the most deeply bound valence shell orbital ($3a'$) to be 32.02 eV [144]. The carbon ($2a'$) and oxygen ($1a'$) K-shell IPs were measured by XPS [39] to be 292.3 and 538.9 eV respectively.

4.2.2 Photoabsorption Oscillator Strengths

4.2.2.1 Low-Resolution Measurements

The absolute photoabsorption oscillator strengths obtained at a resolution of 1 eV fwhm for the valence shell region of methanol in the energy range 5 to 280 eV are presented in figures 4.1a and 4.1b and given numerically in tables 4.1 and 4.2. The results are compared with previously reported absolute photoabsorption data for methanol in those energy regions where such data exist. In figure 4.1b the higher energy region of the valence shell continuum is also compared with experimental [161] and theoretical [162] summed (4H+C+O) atomic oscillator strengths (cross sections).

The absolute photoabsorption spectrum in the valence shell was obtained by normalizing the total area under the Bethe-Born converted EELS spectrum (i.e., the relative photoabsorption spectrum) to the number of valence electrons in methanol plus a small correction for Pauli excluded transitions, using the valence-shell TRK sum rule (see equation 3.1). The contribution to the valence shell region above the carbon K-shell excitation region was estimated by fitting a polynomial of the form $AE^{-1.5} + BE^{-2.5} + CE^{-3.5}$ to the relative oscillator strength data from 90 eV to 280 eV and integrating to infinite energy (E is the energy loss and A , B , and C are the best-fit parameters which were determined to be $A=9.0364 \text{ eV}^{0.5}$, $B=710.68 \text{ eV}^{1.5}$, and $C=4.0917 \times 10^4 \text{ eV}^{2.5}$). This particular functional form was chosen because of the goodness of the fit and because of the previous success of this type of formula in fitting the shape of the high energy valence-shell photoabsorption region of several small polyatomic molecules containing second row atoms [130, 132]. The fitted curve is shown as a solid line in figure 4.1b. Dillon and Inokuti [163–166] have described several functional forms for interpolating and

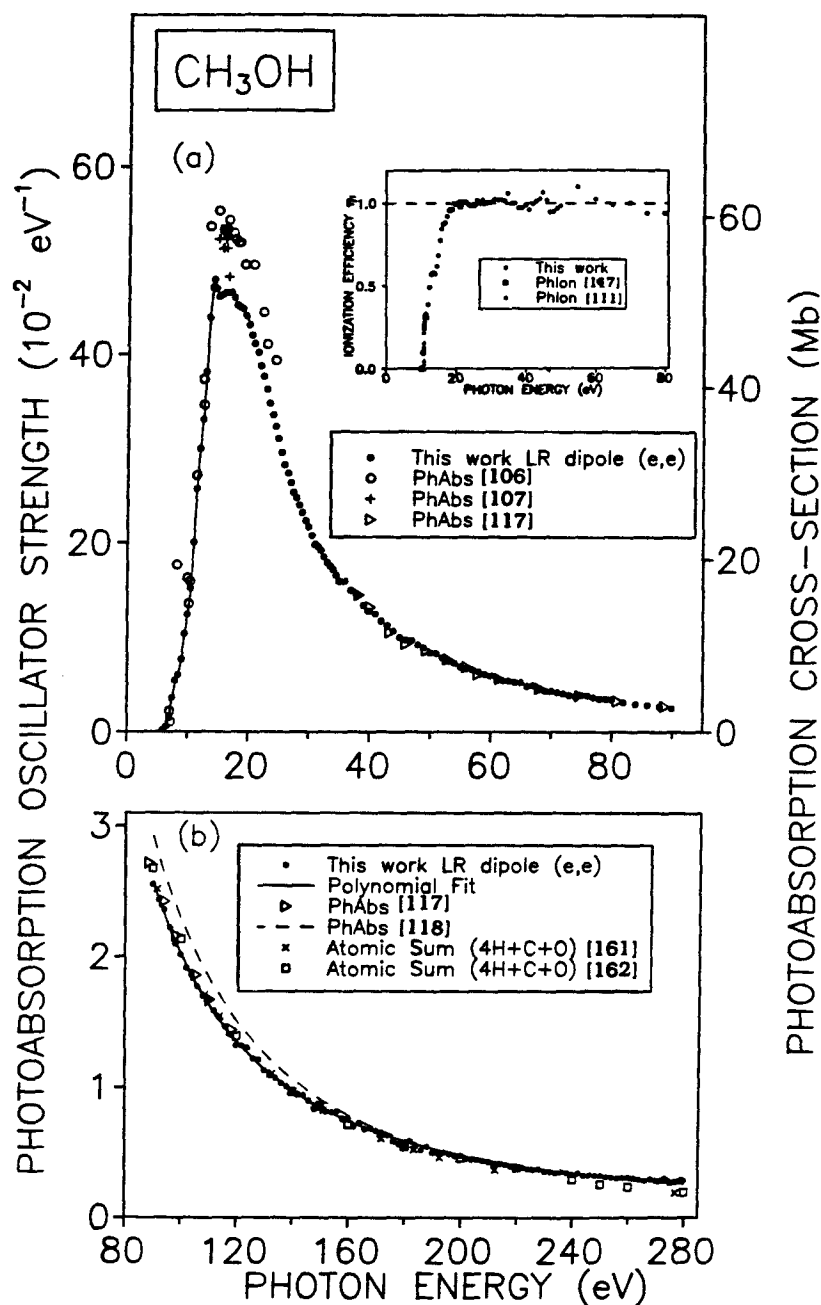


Figure 4.1: Absolute oscillator strengths for the photoabsorption of CH_3OH . (a) The low-resolution (~ 1 eV fwhm) dipole (e,e) measurements below 90 eV. (b) The valence shell region at higher energies. Also shown are previously published direct photoabsorption measurements for CH_3OH [106, 107, 117, 118] and summed atomic oscillator strengths [161, 162]. The insert to (a) shows the photoionization efficiency measured in the present work and from photoionization studies [111, 147].

extrapolating GOS data as a function of photon energy, and as a function of momentum transfer. For the purposes of the present work the extrapolation function is used solely to estimate the total area above the last measured data point and should not be used to provide differential oscillator strength data at high photon energies. The area under the curve from 6 eV to infinity was set to a total integrated oscillator strength of 14.54 which corresponds to the 14 valence electrons of methanol plus an estimated contribution of 0.54 for the Pauli excluded transitions from the inner shells to already occupied valence orbitals (see section 3.1.1). With the implementation of these procedures, the percentage of the total valence shell oscillator strength in the extrapolated region from 280 eV to infinity was found to be 8.2%. The use of the above formula also provides a means of partitioning the total measured photoabsorption oscillator strength above 285 eV into separate valence shell and carbon K-shell contributions (see section 4.2.2.3 below).

The dipole (e,e) spectrum presented in figure 4.1 shows very little pre-edge structure since it was obtained at a resolution of 1 eV fwhm. The small shoulder at 8.5 eV is comprised of a superposition of unresolved Rydberg transitions while the maximum at 14.3 eV corresponds to the strong ($5a' \rightarrow 3s$) Rydberg transition [167]. A much higher resolution dipole (e,e) spectrum (0.048 eV fwhm) of the valence region of methanol has been obtained in the present work and will be detailed in section 4.2.2.2. It can be seen from figure 4.1a that the data reported by Ogawa and Cook [106, 107] are about 10% higher than the present work at the valence peak maximum. Ogawa and Cook [106, 107] state that the reproducibility of their results was within 3% but that their total error may be higher since they did not correct their pressure readings for possible condensation in their pressure gauge. Such corrections would make their real number density higher and thus their cross sections lower. Excellent agreement is obtained between the present work

and the data reported by de Reilhac and Damany [117] in the 40 to 124 eV region as well as with the summed atomic oscillator strengths in the 80–240 eV region [161, 162]. The parameterized data reported by Gluskin *et al.* [118] at 100 eV (dashed line in figure 4.1b) lie somewhat above the presently reported measurements.

4.2.2.2 High-Resolution Measurements

Recently, the Bethe-Born conversion factor has been obtained experimentally for the high-resolution dipole (e,e) spectrometer [26, 96]. Using this instrument, the valence shell oscillator strength spectrum (5–30 eV) of CH₃OH shown in figure 4.2 was obtained at a resolution of 0.048 eV fwhm. The spectrum was made absolute by normalizing the Bethe-Born converted electron energy-loss spectrum to the low resolution absolute photoabsorption oscillator strength (see figure 4.1a and table 4.1) at 25.0 eV in the smooth continuum region where there are no sharp structures. From figure 4.2a it can be seen that the shapes of the dipole (e,e) oscillator strength spectra obtained in the present work at low resolution and at high resolution are the same within experimental error over the 20 to 30 eV smooth continuum region. This is a good consistency check since the low- and high-resolution dipole (e,e) spectrometers have significantly different Bethe-Born conversion factors, reflecting their different impact energies, dimensions and acceptance angles about zero degree mean scattering angle. The average integrated oscillator strengths of methanol recommended by Jhanwar and Meath [120] are also shown for comparison in figure 4.2a. In order to predict results between 21 and 40 eV where no previously measured data existed, Jhanwar and Meath [120] fitted and extrapolated the data (figure 4.1) of de Reilhac and Damany [117] to lower energies and the data of Ogawa and Cook [106, 107] to higher energies. Since the data of Ogawa and Cook are

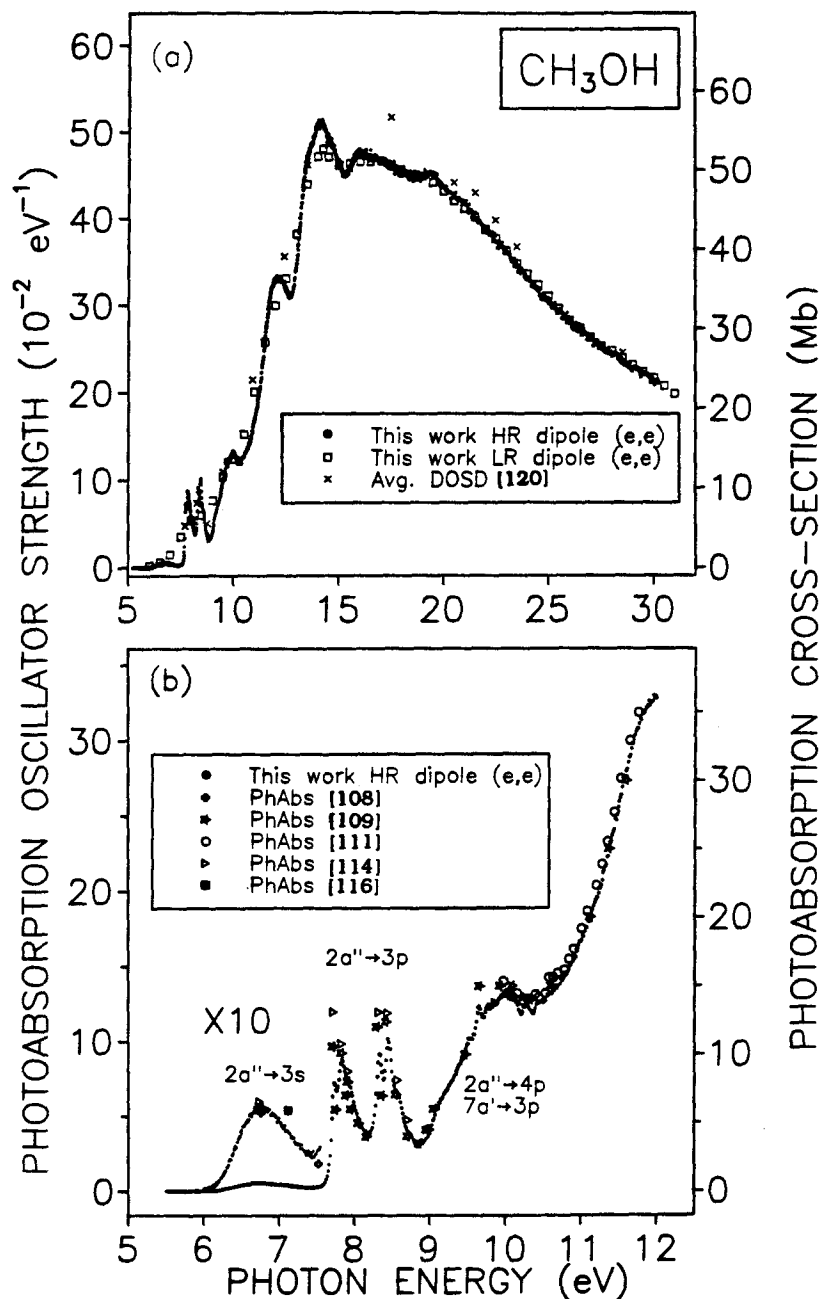


Figure 4.2: (a) Comparison of the experimental photoabsorption oscillator strengths (cross sections) for CH₃OH (5–30 eV) determined by high-resolution (0.048 eV fwhm) and low-resolution (~ 1 eV fwhm) dipole (e,e) spectroscopy (dots and open squares, respectively). Photoabsorption data recommended in reference [120] are also shown (crosses). (b) The high-resolution (0.048 eV fwhm) dipole (e,e) photoabsorption oscillator strength spectrum of CH₃OH (dots) in the valence-shell region from 5 to 12 eV. Direct photoabsorption data for CH₃OH are shown for comparison [108, 110, 111, 114, 116].

higher than the present data below 20 eV, as seen in figure 4.1a, it is not surprising that the average integrated oscillator strength data [120] do not agree with the present work between 20 and 30 eV. The low energy portion of the high-resolution valence-shell spectrum from 5 to 12 eV is shown on an expanded energy scale in figure 4.2b. There is excellent agreement between the present data and the data reported by Nee *et al.* [110] while the data of Person and Nicole [111] are about 4% higher in the 10 to 12 eV region. The positions of the peaks in the $2a'' \rightarrow 3p$ region correspond well with the data of Nee *et al.* [110] and of Salahub and Sandorfy [114] which were measured using optical methods. The differences in peak heights and widths reflect the different energy resolutions used in the various measurements of these discrete excitation processes.

4.2.2.3 Carbon K-shell Measurements

Measurements of the photoabsorption oscillator strength have been extended into the carbon K-shell region of methanol using the low-resolution dipole (e,e) spectrometer and the results are shown in figure 4.3 and table 4.3. The full photoabsorption spectrum of methanol from 6 to 360 eV is shown in figure 4.3a, while figure 4.3b shows the carbon K-shell region in greater detail. The absolute scale in the K-shell region was obtained by referencing the intensity in the below edge region to the TRK sum rule normalized valence shell spectrum below 285 eV as reported in section 4.2.2.1 above. The results obtained are in good quantitative agreement with previously reported data recorded at a somewhat higher resolution (0.5 eV fwhm) [119] than the present work. The spectrum reported earlier [119] was obtained for the carbon K-shell alone by subtracting the estimated valence shell contribution from the total energy loss spectrum, applying an approximate,

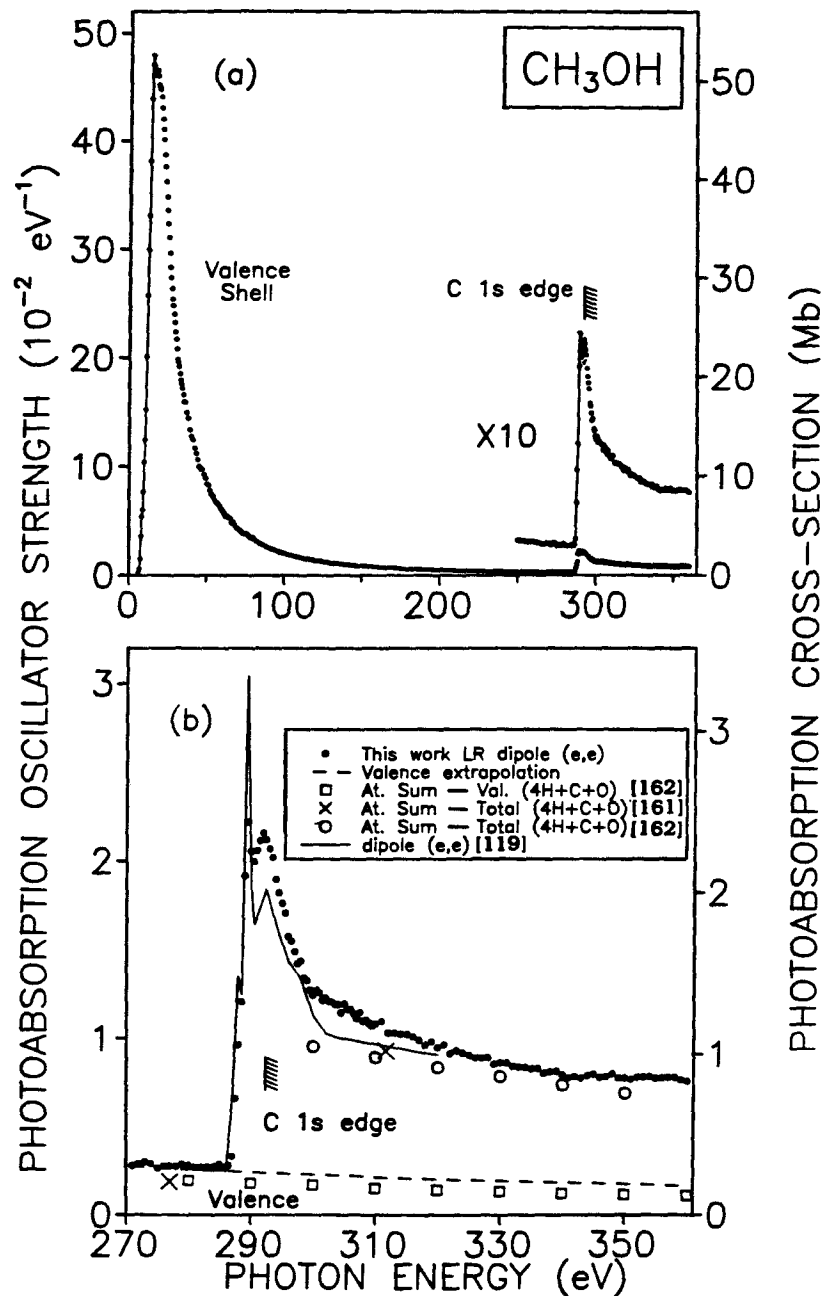


Figure 4.3: (a) The low-resolution (~ 1 eV fwhm) dipole (e,e) photoabsorption oscillator strength spectrum (dots) for CH₃OH from 5 to 360 eV. (b) Detailed view of the low-resolution (~ 1 eV fwhm) dipole (e,e) photoabsorption oscillator strength spectrum in the carbon K-shell region (dots). Also shown are the dipole (e,e) data of reference [119] and summed atomic oscillator strengths [161, 162].

empirically determined Bethe-Born conversion factor and normalizing on the carbon K-shell atomic cross-section reported by Doolan and Liberman [125] at 25 eV above the carbon K edge. The carbon K-shell oscillator strength data of reference [119] have been added to the extrapolated valence shell tail as obtained in the present work (the dashed line in figure 4.3b, section 4.2.2.1) to permit comparison with the other data shown in the figure. The summed atomic total (i.e., valence-shell plus carbon K-shell) photoabsorption data (4H+C+O) also shown on figure 4.3b (open circles [162] and crosses [161]) are seen to be in reasonable agreement with the present absolute measurements (based on TRK sum rule normalization of the valence shell) at energies in excess of about 30 eV above the K-shell ionization edge. This experimental assessment of such normalization procedures in the carbon K-shell region of CH₃OH is paralleled by similar recent observations for L-shell spectra of molecules containing third row atoms [127, 129, 131].

The sharp pre-edge structure observed in the carbon K-shell electron energy-loss spectrum of methanol at 289.4 eV in references [119, 124] is also seen in the present work (see figure 4.3b) and was used to set the energy scale in the carbon K-shell region. The oxygen K-shell spectrum was not studied in the present work because of the very low electron scattering signal at higher energy loss.

4.2.3 Molecular and Dissociative Photoionization in the Valence-Shell Region

Time-of-flight mass spectra for methanol were measured as a function of (photon) energy in the energy loss range up to 80 eV. Analysis of this data provides information concerning the molecular and dissociative photoionization channels resulting from valence shell photoabsorption by CH₃OH. The positive ions detected in the TOF mass

spectra of CH_3OH were: CH_3OH^+ , $\text{CH}_3\text{O}^+/\text{CH}_2\text{OH}^+$ at $m/e=31$, $\text{CH}_2\text{O}^+/\text{CHOH}^+$ at $m/e=30$, $\text{CHO}^+/\text{COH}^+$ at $m/e=29$, CO^+ , OH^+ , CH_3^+ , CH_2^+ , CH^+ , C^+ , H_2^+ , H^+ . No doubly charged species were observed although the products of dissociative double photoionization cannot be ruled out in the singly charged ion yields. Such processes can be investigated by PIPICO techniques [168]. The TOF mass spectrum obtained at an equivalent photon energy of 50 eV is shown in figure 4.4. The ions of m/e ratios 29, 30, and 31 have double labels since the explicit structure of the detected TOF ion cannot be determined. The insert to figure 4.4 shows the mass 28 to mass 32 region on an expanded scale. Isotopic studies have shown [146] that at low photon energy, near threshold, mainly CHO^+ , CHOH^+ , and CH_2OH^+ are formed, whereas at higher energies there are also contributions from the structural isomers COH^+ , CH_2O^+ , and CH_3O^+ . Photoion branching ratios for the molecular and dissociative ions, determined as percentages of the total photoionization from integration of the background subtracted TOF peaks, are presented in figure 4.5 and are given numerically in table 4.4. These data were recorded using the Johnston multiplier ion detector prior to the determination of the detector response functions (see section 3.1.2). For this reason only the branching ratio for the H^+ cation was corrected in this study, and this was increased by 10% as determined by Backx and Van der Wiel [76].

The relative photoionization efficiency in dipole ($e, e+\text{ion}$) experiments is given by the ratio of the total coincident ion signal to the number of forward scattered electrons as a function of energy-loss. The presently measured ratio for methanol is found to be constant within experimental error above 19.5 eV. Making the reasonable assumption that the absolute photoionization efficiency (η_i) is unity at higher energies we therefore conclude that η_i reaches 1.0 at 19.5 eV. The photoionization efficiency from threshold

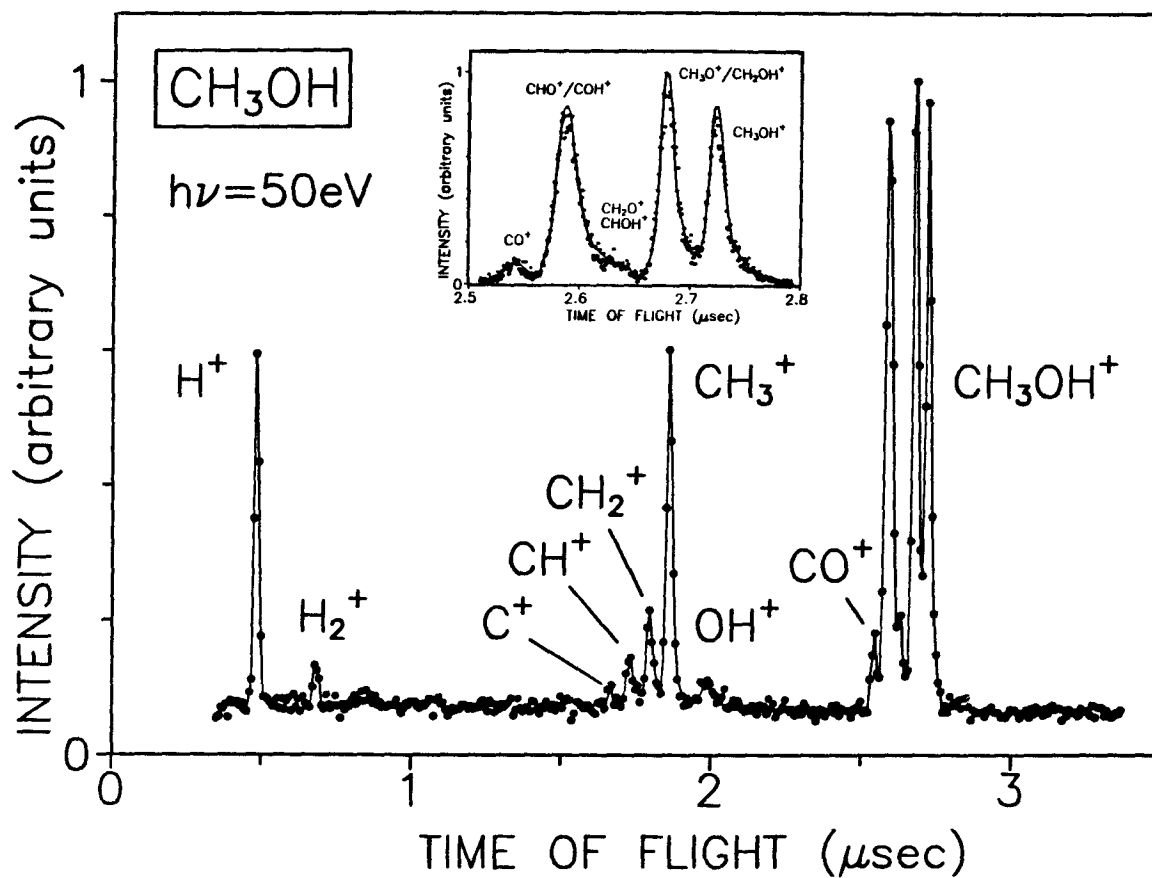


Figure 4.4: The time-of-flight mass spectrum of CH_3OH taken at an equivalent photon energy of 50 eV. The insert to the figure shows the ions in the mass range m/e 28–32 in more detail.

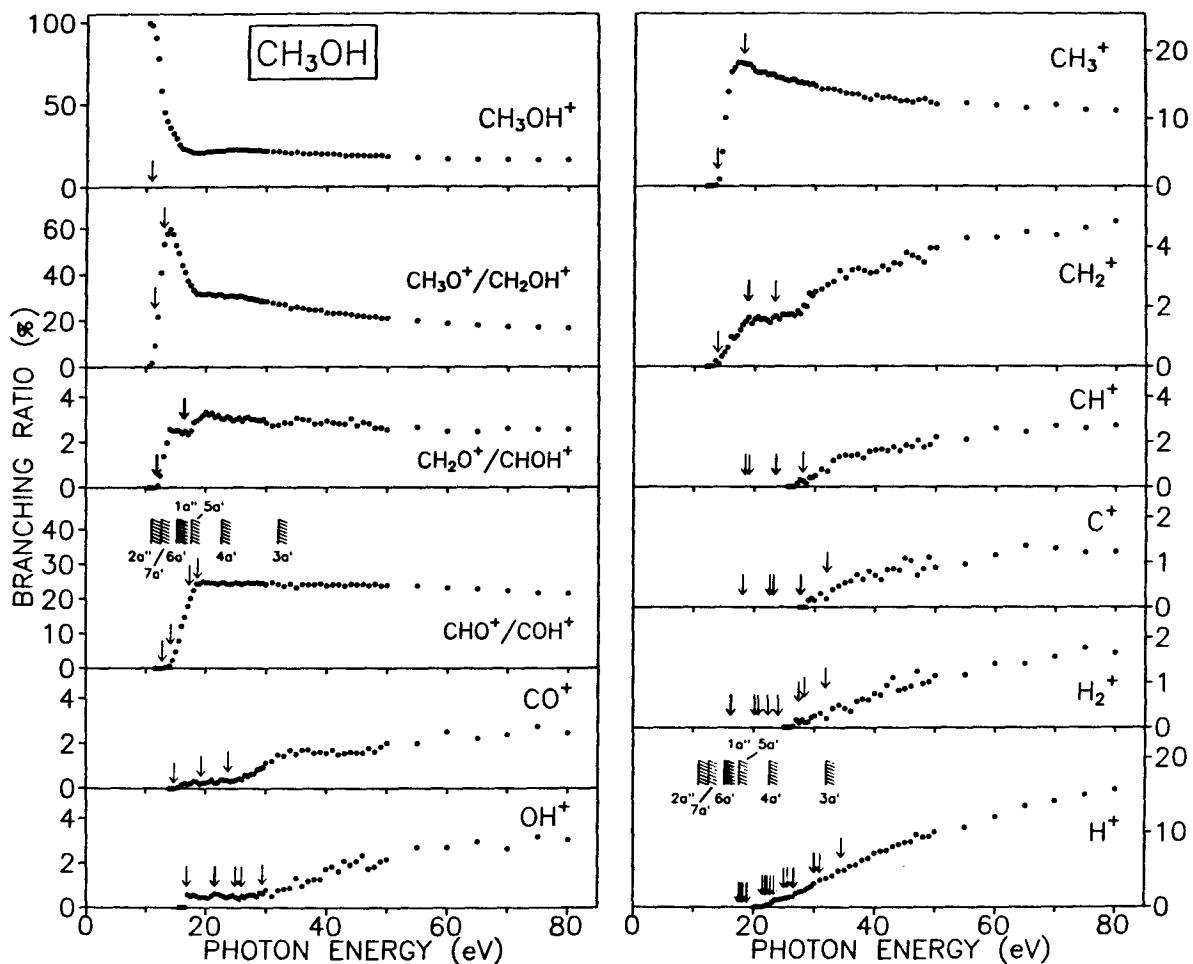


Figure 4.5: Photoionization branching ratios for molecular and dissociative photoionization of CH_3OH . The vertical arrows indicate calculated appearance potentials (see table 4.5).

to 80 eV is shown as an insert to figure 4.1 and is given numerically in the last column of table 4.1. It can be seen (figure 4.1) that there is good agreement with previously published measurements in the near threshold region [111] and at 21.22 eV [147].

Absolute partial photoionization oscillator strengths for the production of the molecular and fragment ions of CH₃OH, obtained by taking the triple product of the photoionization efficiency, the branching ratio and the total photoabsorption oscillator strength at each photon energy, are shown in figure 4.6 and given numerically in table 4.1. The *relative* photoion yields in the energy range up to 20 eV given diagrammatically in reference [146] are consistent with the presently obtained absolute partial oscillator strengths.

The fragment ion appearance potentials (± 1 eV) from CH₃OH measured in the present work are given in table 4.5 where they are compared with previously reported values [149–151, 153–156]. Table 4.5 also includes the calculated appearance potentials for all possible fragmentation processes leading to the production of a particular ion calculated from thermodynamic data [169], assuming zero kinetic energy of fragmentation. These thermochemical thresholds for ion production are indicated by the vertical arrows on figures 4.5 and 4.6.

4.2.4 The Dipole-Induced Breakdown of Methanol

The total absolute photoionization (i.e., absolute photoabsorption \times photoionization efficiency) oscillator strength distribution for an atom or molecule can, in general, be partitioned in two different but complementary manners. By measuring the photoionization branching ratios, as in the present chapter for CH₃OH using dipole (e,e⁺ion) spectroscopy, absolute partial oscillator strengths for molecular and dissociative photoionization

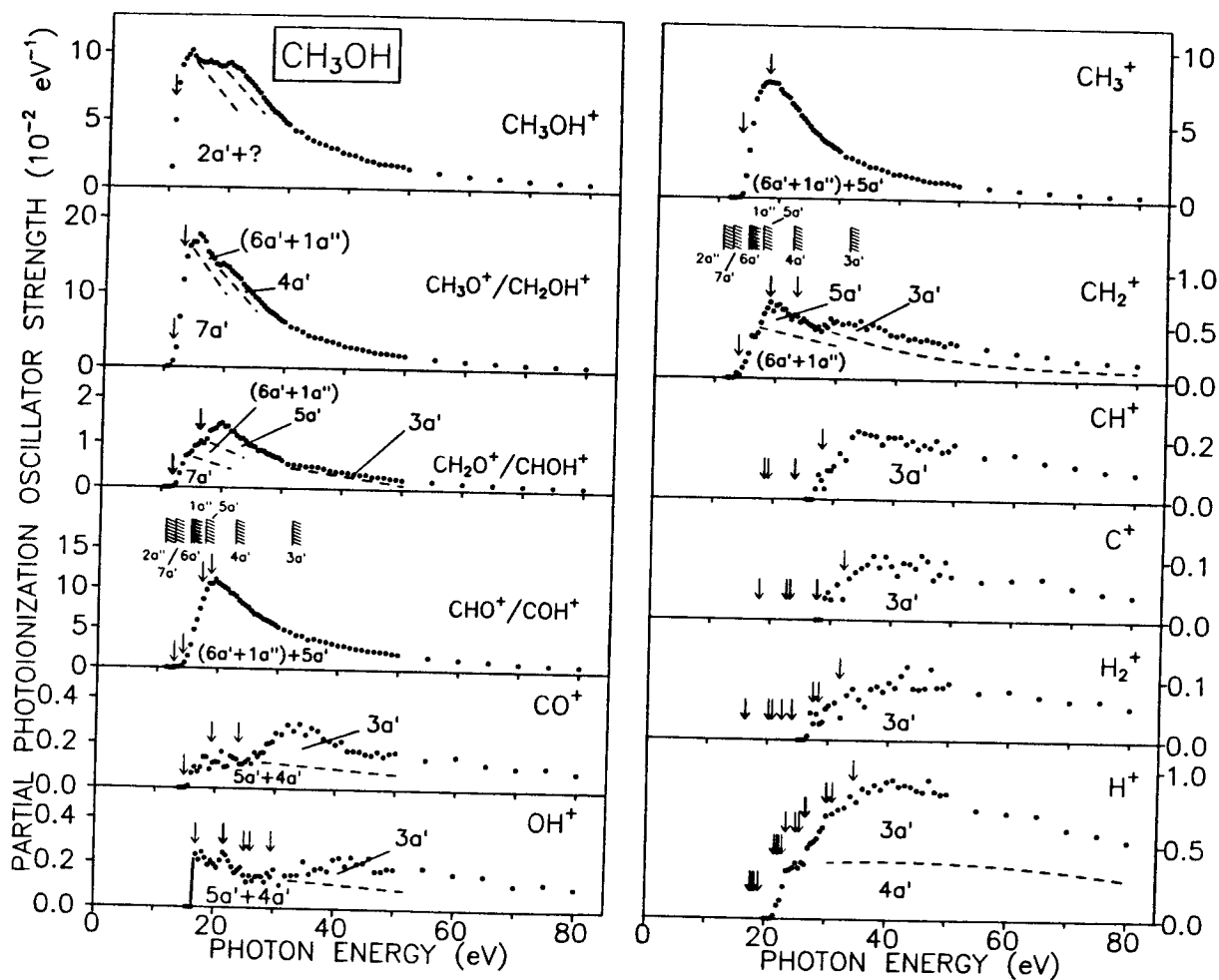


Figure 4.6: Absolute partial photoionization oscillator strengths (cross sections) for molecular and dissociative photoionization of CH_3OH . The vertical arrows indicate calculated appearance potentials (see table 4.5). Estimated contributions from the breakdown of the electronic states of the methanol ion are indicated (see table 4.6 and text for details).

can be determined. However, it is also possible to partition the total absolute photoionization oscillator strength distribution into the partial electronic ion state oscillator strengths by measuring the branching ratios for the production of the different electronic states of the molecular ion. The latter data can be obtained using tuneable energy PES or the equivalent electron impact technique of dipole (e,2e) spectroscopy [4] (see also section 2.3). Details of the dipole-induced breakdown scheme for a molecule can be deduced from these two sets of data since the partial oscillator strength for a specific molecular or dissociative ion will involve contributions from the breakdown of the various electronic states of the molecular ion [4, 170, 171]. Once the photon energy exceeds the upper limit of the Franck-Condon region for the production of a given electronic state of the molecular ion, its internal energy distribution is independent of the photon energy and the remainder of the energy is carried away by the ejected photoelectron. Thus the branching ratios for ionic photofragmentation into stable molecular and/or fragment ions are also determined for each electronic state of the molecular ion. Thereafter only the overall probability of direct ionization to that state will vary with increase in photon energy for each electronic state. Thus the partial oscillator strengths for the production of a given molecular or fragment ion are expected to be given by a fixed linear combination of partial electronic ion state oscillator strengths (or vice-versa). It should be noted however that local departures from the above simple breakdown model, based on linear combinations of oscillator strengths, are to be expected at lower photon energies where autoionization occurs, and also at higher photon energies if significant multiple photoionization processes occur [170].

On the basis of the simple breakdown model presented above, a series of studies of molecular photoabsorption and photoionization (for recent examples see references [78,

132, 172–174]) has shown that significant quantitative information on the dipole induced breakdown pathways of a molecule can be deduced from an overall consideration of as much of the following types of information as is available.

1. measured ion appearance potentials as determined by mass spectrometry,
2. predicted minimum thresholds for various ionic photofragmentation processes and associated neutral products, calculated using thermodynamic data and assuming zero kinetic energy of fragmentation,
3. the molecular ionization potentials and associated Franck-Condon widths determined from UV and X-ray photoelectron spectroscopy, or from electron momentum spectroscopy,
4. the shapes of branching ratio curves for molecular and dissociative photoionization determined from dipole (e,e+ion) spectroscopy, or photoionization mass spectrometry,
5. the shapes and magnitudes of the partial oscillator strength distributions for molecular and dissociative photoionization determined from dipole (e,e+ion) spectroscopy, or photoionization mass spectrometry,
6. the shapes and magnitudes of the partial oscillator strength distributions for the production of the electronic states of the ions determined from tuneable light source PES, or dipole (e,2e) spectroscopy [4],
7. photoelectron-photoion coincidence (PEPICO) measurements.

In the case of methanol, the information in items (1), (2), (4), and (5) is available from the present work (see tables 4.1 and 4.4, and figures 4.5 and 4.6) while that of (3) is known

from PES [140] and EMS [145] studies of the binding energy spectra. No information on partial oscillator strengths for the production of electronic states (item (6)) of CH_3OH^+ is available since no tuneable energy PES, or dipole (e,2e), measurements have been reported for methanol to date. Nevertheless, using the available data it has been possible to deduce some aspects of the probable dipole-induced breakdown pathways of methanol and these are discussed below. Previously reported studies of methanol and methanol-d₄ using photoionization by tuneable light sources [146, 148–151] and photoelectron-photoion coincidence spectroscopy (PEPICO) [148, 155, 175–177] have proven helpful in determining various aspects of the possible dipole breakdown scheme for methanol. However, it should be pointed out that these studies were performed in the limited energy region below ~ 20 eV with the exception of the photoionization work reported by Warneck [151] which extended to 28 eV. Thus most previous studies [146, 148–151, 155, 175–177] are restricted to the production and breakdown of the outer valence ionization states and only *relative* cross sections are reported in the photoionization work [146, 148–151]. The present work contains the first reported absolute partial oscillator strength data for the molecular and all dissociative photoionization channels of methanol from threshold up to photon energies of 80 eV. It also represents the first information on the breakdown of the $4a'$ and $3a'$ inner-valence ion states. However, the present procedures for determining the dipole-induced breakdown scheme are limited in the case of methanol by the relatively close spacing of the outer valence IPs and the modest energy resolution (~ 1 eV fwhm) of the dipole (e,e+ion) method. The analysis has been aided by the use of the electronic ion state Franck-Condon widths, as indicated by the respective widths in the complete valence shell binding energy spectrum of methanol measured by electron momentum spectroscopy (EMS) at a comparable energy resolution [145]. The

EMS spectrum [145] clearly reveals the existence of extensive many-body (correlated) ion states belonging to the $4a'$ and $3a'$ inner-valence ionization manifolds throughout the 20–40 eV binding energy range.

It is to be expected that molecular ions, stable with respect to dissociation (i.e., CH_3OH^+), will be formed from the $2a''$ ground state of the methanol cation and possibly also from various excited ionic states. The ground state ($2a''$) contribution to CH_3OH^+ is confirmed by PEPICO experiments [148, 155, 175–177]. Above the initial threshold the partial oscillator strength (POS) curve for CH_3OH^+ clearly shows further onsets (indicated by dashed lines on figure 4.6) at ~ 15 – 16 eV and ~ 20 eV which suggest additional contributions from the ($6a' + 1a''$) and $4a'$ states of CH_3OH^+ , respectively. All previous work has suggested that the parent molecular ion, CH_3OH^+ , comes solely from the $2a''$ state. However, the higher photon energy PEPICO spectra reported by Niwa *et al.* [175–177] show considerable tailing on the high m/e side of CD_2OD^+ , suggesting a small amount of CD_3OD^+ production from the $6a'$, $1a''$ and possibly higher states. No PEPICO experiments extend beyond 21.22 eV and therefore the $4a'$ contribution to CH_3OH^+ indicated in the present work cannot, as yet, be independently confirmed.

The lowest appearance potential of $\text{CH}_3\text{O}^+/\text{CH}_2\text{OH}^+$ and the shape of the POS suggest a dominant contribution from the $7a'$ state, but the curve also shows evidence of smaller additional contributions corresponding to new thresholds at ~ 15 eV ($(6a' + 1a'')$ or possibly $5a'$) and at ~ 20 eV ($4a'$). Contributions to $\text{CH}_3\text{O}^+/\text{CH}_2\text{OH}^+$ from the $7a'$ state have been observed previously in PEPICO experiments by von Puttkamer [155], Brehm *et al.* [148], and by Niwa *et al.* [175–177]. Further contributions from the $6a'$ and $1a''$ states have also been measured in PEPICO experiments [175–177]. It should be noted in this regard that the PEPICO studies by von Puttkamer [155] did not extend

beyond 14 eV. The POS for $\text{CH}_2\text{O}^+/\text{CHOH}^+$ exhibits thresholds indicative of contributions from the $7a'$, $(6a' + 1a'')$, $5a'$ and $3a'$ states. Photoionization studies [146, 151] have also suggested contributions to the POS of $\text{CH}_2\text{O}^+/\text{CHOH}^+$ from the $7a'$, $(6a'$ and/or $1a'')$ and $5a'$ states [146, 151] but the contribution of these ions cannot be confirmed from the PEPICO measurements [175–177] because of insufficient m/e resolution. The POS for $\text{CHO}^+/\text{COH}^+$ (figure 4.6) shows no obvious additional onsets above the initial threshold (13.0 eV) and it is thus likely that this fragment ion POS reflects the shape of a dominant contribution from the $(6a' + 1a'')$ POS. The ‘clean’ step function nature of the $\text{CHO}^+/\text{COH}^+$ branching ratio (figure 4.5) supports the above assignment corresponding to a contribution from only one ion electronic state. PEPICO experiments [175–177] confirm this assignment but also suggest that a small additional contribution may come from the $5a'$ state.

The CO^+ and OH^+ ions show thresholds strongly suggesting that each has contributions from each of the $5a'$, $4a'$ and $3a'$ states (see figure 4.6). The inner-valence $4a'$ and $3a'$ states both show extensive many-body structures in the binding energy spectrum [145] over the range 20–46 eV in addition to the main poles at 22.7 and 32.2 eV, respectively. Similarly, from an examination of the POS threshold for CH_3^+ and the similarity of its shape with the POS for $\text{CHO}^+/\text{COH}^+$, it is likely that CH_3^+ arises mainly from the $(6a' + 1a'')$ states with an additional onset at ~ 20 eV indicating a further small contribution from the $5a'$ state. Results from PEPICO experiments [175–177] confirm contributions to the POS of CH_3^+ from $(6a'$ and/or $1a'')$ and a further contribution from the $5a'$ state. The CH_2^+ POS (see also the branching ratio data in figure 4.5) shows a break in the leading edge at ~ 16 eV indicative of significant contributions from the $(6a' + 1a'')$ and $5a'$ ion states. A further major onset in the CH_2^+ POS at ~ 28 eV corresponds well with the

$3a'$ inner-valence ionization threshold. The similar threshold energies and POS shapes for the CH^+ , C^+ , and H_2^+ cations and also for the process corresponding to the higher onset for H^+ suggest a common origin for these four processes, namely ionization from the $3a'$ orbital. The sum of the POS data for the CH^+ , C^+ , and H_2^+ cations has been calculated to obtain the shape of the electronic ion state POS for the $3a'$ ion state and this has been used to determine the approximate contributions of the $3a'$ state to the POSs of $\text{CH}_2\text{O}^+/\text{CHOH}^+$, CO^+ , OH^+ , CH_2^+ , and H^+ . These contributions are indicated by dashed lines in figure 4.6. In the case of H^+ the initial onset at ~ 21 eV corresponds to a major contribution from the $4a'$ state. The approximate shape of the $4a'$ ion state POS has been determined (see figure 4.6) after the contribution of the $3a'$ ion state was subtracted from the POS of the H^+ cation. The different electronic ion state contributions to the molecular and various fragment ions suggested by the above analysis are summarized in table 4.6.

It is clear from the data shown in figure 4.6 that the $3a'$ and $4a'$ inner-valence states each have “step function” type POS distributions which decrease relatively slowly with increasing photon energy. This is to be expected considering the dominant C 2s and O 2s characters of these orbitals. In contrast, the outer valence orbitals ($2a''$, $7a'$, $(6a' + 1a'')$, and $5a'$) exhibit a rather different POS shape in keeping with their more dominant 2p orbital characters.

To date no direct measurements or calculations of the electronic ion state partial oscillator strengths of methanol are available for comparison with the present shape (i.e., relative partial oscillator strength) estimates as indicated on figure 4.6. However, the procedures used in the present work have been shown to be quite effective in other less complicated molecules such as PH_3 [128], H_2O [171], and CH_4 [178], where photoelectron

or dipole (e,2e) data were available for verification. Given the approximations involved in the present work, the results obtained (figure 4.6 and table 4.6) for the dipole induced breakdown of methanol and for the *relative* shapes of the $4a'$ and the $3a'$ electronic ion state POSs of methanol should only be regarded as preliminary estimates of these quantities. Further evaluation of these results and of the suggested dipole breakdown pathways must await direct PES studies of the electronic state partial oscillator strengths and also more extensive PEPICO studies as a function of photon energy.

Table 4.1: Absolute oscillator strengths for the total photoabsorption and the molecular and dissociative photoionization of CH₃OH from 6.0 to 80.0 eV.

Photon Energy eV	Photo-Absorption	Oscillator Strength ($10^{-2}eV^{-1}$) ^a												Photoionization Efficiency η_i
		H ⁺	H ₂ ⁺	C ⁺	CH ⁺	CH ₂ ⁺	CH ₃ ⁺	OH ⁺	CO ⁺	CHO ⁺ COH ⁺	CH ₂ O ⁺ CHOH ⁺	CH ₃ O ⁺ CH ₂ OH ⁺	CH ₃ OH ⁺	
6.0	0.21													
6.5	0.59													
7.0	1.50													
7.5	3.58													
8.0	5.39													
8.5	6.00													
9.0	7.65													
9.5	10.37													
10.0	12.42													0.00
10.5	15.19											0.01	1.48	0.10
11.0	20.06											0.09	4.90	0.25
11.5	25.70											0.79	7.65	0.33
12.0	29.92										0.01	2.52	9.01	0.39
12.5	33.04										0.09	6.64	9.47	0.49
13.0	38.11									0.01	0.30	11.57	9.77	0.57
13.5	43.88					0.05	0.03			0.10	0.50	14.65	10.12	0.58

Table 4.1: (continued) Absolute oscillator strengths for the total photoabsorption and the molecular and dissociative photoionization of CH₃OH.

Photon Energy eV	Photo-Absorption	Oscillator Strength ($10^{-2}eV^{-1}$) ^a											Photoionization Efficiency η_i	
		H ⁺	H ₂ ⁺	C ⁺	CH ⁺	CH ₂ ⁺	CH ₃ ⁺	OH ⁺	CO ⁺	CHO ⁺ COH ⁺	CH ₂ O ⁺ CHOH ⁺	CH ₃ O ⁺ CH ₂ OH ⁺		CH ₃ OH ⁺
14.0	47.05					0.03	0.27			0.21	0.69	16.12	9.67	0.57
14.5	46.99					0.10	1.46			0.67	0.73	16.67	9.42	0.62
15.0	46.09					0.15	3.18			1.50	0.79	16.63	9.29	0.68
15.5	46.24					0.23	4.99	0.01	2.85	0.91	17.70	9.20	0.78	
16.0	46.47					0.39	6.63	0.07	4.77	0.94	17.33	9.19	0.85	
16.5	46.47					0.38	7.10	0.09	5.99	1.02	16.73	9.36	0.87	
17.0	46.54					0.42	7.47	0.24	0.07	7.40	0.97	15.40	9.17	0.88
17.5	45.99					0.51	7.72	0.21	0.09	8.60	1.07	15.04	9.18	0.92
18.0	45.19					0.60	7.82	0.25	0.14	9.75	1.25	14.44	9.01	0.96
18.5	44.96					0.65	7.77	0.22	0.14	10.56	1.28	13.72	8.91	0.96
19.0	44.78					0.71	7.73	0.19	0.08	10.53	1.31	13.56	8.94	0.96
19.5	44.07					0.62	7.70	0.21	0.11	11.07	1.40	13.83	9.14	1.00 ^b
20.0	43.05					0.67	7.29	0.19	0.12	10.59	1.44	13.53	9.22	
20.5	42.00					0.69	7.03	0.18	0.12	10.35	1.35	13.32	8.98	
21.0	41.06					0.64	6.91	0.21	0.16	10.10	1.36	12.83	8.85	
21.5	40.11	0.02				0.64	6.76	0.25	0.09	9.86	1.25	12.45	8.79	

Table 4.1: (continued) Absolute oscillator strengths for the total photoabsorption and the molecular and dissociative photoionization of CH₃OH.

Photon Energy eV	Photo-Absorption	Oscillator Strength ($10^{-2}eV^{-1}$) ^a												Photoionization Efficiency η_i
		H ⁺	H ₂ ⁺	C ⁺	CH ⁺	CH ₂ ⁺	CH ₃ ⁺	OH ⁺	CO ⁺	CHO ⁺ COH ⁺	CH ₂ O ⁺ CHOH ⁺	CH ₃ O ⁺ CH ₂ OH ⁺	CH ₃ OH ⁺	
22.0	38.69	0.09				0.59	6.37	0.23	0.10	9.37	1.24	12.13	8.57	
22.5	37.59	0.12				0.55	6.15	0.21	0.14	9.27	1.15	11.79	8.20	
23.0	36.23	0.22				0.59	5.94	0.18	0.14	8.98	1.10	11.08	8.00	
23.5	34.75	0.32				0.58	5.56	0.16	0.13	8.48	1.10	10.65	7.77	
24.0	33.53	0.33				0.52	5.37	0.17	0.11	8.17	1.03	10.31	7.53	
24.5	32.30	0.34				0.55	5.12	0.18	0.11	7.89	0.95	9.90	7.25	
25.0	31.02	0.38				0.53	4.86	0.14	0.12	7.65	0.93	9.40	7.01	
25.5	29.56	0.34				0.50	4.59	0.11	0.13	7.23	0.91	9.10	6.63	
26.0	28.25	0.38				0.49	4.44	0.14	0.11	6.84	0.83	8.66	6.36	
26.5	27.32	0.37	0.01			0.46	4.30	0.12	0.16	6.70	0.84	8.21	6.14	
27.0	26.30	0.48	0.05		0.03	0.48	4.03	0.14	0.14	6.50	0.82	7.78	5.84	
27.5	25.33	0.51	0.03		0.08	0.44	3.87	0.14	0.16	6.20	0.77	7.51	5.61	
28.0	24.75	0.52	0.04		0.06	0.50	3.74	0.14	0.16	6.07	0.75	7.26	5.50	
28.5	23.97	0.54	0.03		0.04	0.48	3.64	0.12	0.20	5.93	0.72	7.00	5.30	
29.0	23.19	0.59	0.03	0.04	0.10	0.56	3.46	0.16	0.20	5.69	0.69	6.61	5.06	
29.5	22.33	0.61	0.05	0.05	0.10	0.52	3.38	0.14	0.21	5.49	0.68	6.30	4.80	

Table 4.1: (continued) Absolute oscillator strengths for the total photoabsorption and the molecular and dissociative photoionization of CH₃OH.

Photon Energy eV	Photo-Absorption	Oscillator Strength ($10^{-2}eV^{-1}$) ^a												Photoionization Efficiency η_i
		H ⁺	H ₂ ⁺	C ⁺	CH ⁺	CH ₂ ⁺	CH ₃ ⁺	OH ⁺	CO ⁺	CHO ⁺ COH ⁺	CH ₂ O ⁺ CHOH ⁺	CH ₃ O ⁺ CH ₂ OH ⁺	CH ₃ OH ⁺	
30.0	21.67	0.69	0.06	0.03	0.11	0.54	3.20	0.17	0.25	5.21	0.62	6.12	4.67	
30.5	20.76													
31.0	19.81	0.71	0.06	0.06	0.15	0.51	2.83	0.10	0.24	4.89	0.54	5.48	4.24	
31.5	19.56													
32.0	19.16	0.73	0.04	0.03	0.13	0.52	2.76	0.15	0.29	4.63	0.53	5.22	4.13	
32.5	18.49													
33.0	17.90	0.75	0.08	0.07	0.21	0.50	2.56	0.15	0.26	4.23	0.51	4.85	3.74	
33.5	17.51													
34.0	17.15	0.82	0.09	0.08	0.23	0.54	2.41	0.15	0.29	4.18	0.49	4.36	3.51	
34.5	16.56													
35.0	15.91	0.79	0.07	0.09	0.22	0.47	2.18	0.21	0.24	3.71	0.49	4.12	3.33	
36.0	15.88	0.87	0.06	0.09	0.22	0.51	2.16	0.15	0.27	3.83	0.48	4.03	3.20	
37.0	14.93	0.85	0.09	0.11	0.21	0.49	2.03	0.18	0.26	3.59	0.45	3.71	2.98	
38.0	14.41	0.90	0.09	0.09	0.18	0.46	1.89	0.18	0.23	3.48	0.41	3.57	2.95	
39.0	13.35	0.87	0.08	0.11	0.21	0.41	1.70	0.17	0.22	3.26	0.38	3.30	2.64	
40.0	12.76	0.92	0.10	0.09	0.21	0.40	1.71	0.22	0.20	3.04	0.38	2.97	2.52	

Table 4.1: (continued) Absolute oscillator strengths for the total photoabsorption and the molecular and dissociative photoionization of CH₃OH.

Photon Energy eV	Photo-Absorption	Oscillator Strength ($10^{-2}eV^{-1}$) ^a												Photoionization Efficiency η_i
		H ⁺	H ₂ ⁺	C ⁺	CH ⁺	CH ₂ ⁺	CH ₃ ⁺	OH ⁺	CO ⁺	CHO ⁺ COH ⁺	CH ₂ O ⁺ CHOH ⁺	CH ₃ O ⁺ CH ₂ OH ⁺	CH ₃ OH ⁺	
41.0	12.46	0.93	0.09	0.07	0.21	0.41	1.62	0.23	0.21	2.99	0.36	2.87	2.46	
42.0	11.69	0.89	0.11	0.10	0.19	0.37	1.54	0.19	0.17	2.81	0.33	2.72	2.26	
43.0	11.21	0.90	0.12	0.09	0.20	0.39	1.45	0.23	0.17	2.65	0.32	2.58	2.09	
44.0	10.64	0.89	0.09	0.09	0.17	0.36	1.33	0.21	0.17	2.58	0.32	2.41	2.03	
45.0	9.99	0.87	0.09	0.11	0.19	0.38	1.26	0.21	0.16	2.41	0.27	2.21	1.86	
46.0	9.75	0.86	0.09	0.10	0.17	0.36	1.20	0.23	0.15	2.35	0.28	2.13	1.83	
47.0	9.71	0.94	0.12	0.07	0.20	0.35	1.23	0.17	0.17	2.30	0.27	2.09	1.79	
48.0	9.22	0.86	0.09	0.08	0.16	0.32	1.19	0.17	0.15	2.23	0.24	2.00	1.73	
49.0	8.88	0.84	0.09	0.10	0.17	0.35	1.10	0.18	0.16	2.11	0.23	1.87	1.68	
50.0	8.37	0.85	0.10	0.07	0.19	0.33	1.01	0.18	0.17	2.00	0.21	1.77	1.50	
55.0	6.90	0.74	0.08	0.07	0.14	0.29	0.84	0.19	0.14	1.64	0.18	1.38	1.21	
60.0	5.94	0.72	0.08	0.07	0.15	0.26	0.70	0.16	0.15	1.38	0.15	1.12	1.00	
65.0	5.23	0.70	0.07	0.07	0.13	0.23	0.61	0.15	0.12	1.20	0.13	0.95	0.86	
70.0	4.30	0.61	0.07	0.06	0.12	0.19	0.52	0.11	0.10	0.96	0.101	0.75	0.71	
75.0	3.86	0.58	0.07	0.05	0.10	0.18	0.44	0.12	0.11	0.84	0.10	0.66	0.63	
80.0	3.40	0.53	0.06	0.04	0.09	0.16	0.38	0.10	0.08	0.73	0.09	0.57	0.55	

^a $\sigma(\text{Mb})=109.75df/dE(\text{eV}^{-1})$.

^bThe photoionization efficiency is normalized to unity above 19.5 eV (see text for details).

Table 4.2: Absolute oscillator strengths for the total photoabsorption of CH₃OH from 50 to 280 eV.

Photon Energy eV	Oscillator Strength (10 ⁻² eV ⁻¹) ^a	Photon Energy eV	Oscillator Strength (10 ⁻² eV ⁻¹) ^a
50	8.37	68	4.64
51	8.27	69	4.36
52	7.80	70	4.30
53	7.45	71	4.17
54	7.27	72	4.04
55	6.90	73	3.87
56	6.68	74	3.82
57	6.58	75	3.86
58	6.39	76	3.80
59	6.11	77	3.64
60	5.94	78	3.48
61	5.71	79	3.51
62	5.43	80	3.40
63	5.40	85	2.89
64	5.28	90	2.55
65	5.23	95	2.29
66	4.79	100	2.01
67	4.90	105	1.82

Table 4.2: (continued) Absolute oscillator strengths for the total photoabsorption of CH₃OH from 50 to 280 eV.

Photon Energy eV	Oscillator Strength (10 ⁻² eV ⁻¹) ^a	Photon Energy eV	Oscillator Strength (10 ⁻² eV ⁻¹) ^a
110	1.66	200	0.48
115	1.50	205	0.45
120	1.33	210	0.43
125	1.26	215	0.41
130	1.13	220	0.39
135	1.05	225	0.37
140	0.97	230	0.36
145	0.92	235	0.35
150	0.86	240	0.33
155	0.81	245	0.33
160	0.76	250	0.32
165	0.70	255	0.31
170	0.67	260	0.31
175	0.61	265	0.29
180	0.55	270	0.28
185	0.53	275	0.27
190	0.50	280	0.28
195	0.50		

^a $\sigma(\text{Mb})=109.75df/dE(\text{eV}^{-1})$.

Table 4.3: Absolute oscillator strengths for the total photoabsorption of CH₃OH in the carbon 1s region.

Photon Energy eV	Oscillator Strength (10 ⁻² eV ⁻¹) ^a			Photon Energy eV	Oscillator Strength (10 ⁻² eV ⁻¹) ^a		
	total	valence	C 1s		total	valence	C 1s
280.0	0.28	0.28		292.5	2.12	0.24	1.88
281.0	0.27	0.27		293.0	2.07	0.24	1.83
282.0	0.27	0.27		293.5	2.02	0.24	1.78
283.0	0.27	0.27		294.0	1.90	0.24	1.66
284.0	0.27	0.27		294.5	1.82	0.24	1.58
285.0	0.28	0.28		295.0	1.76	0.24	1.53
286.0	0.27	0.27		295.5	1.71	0.23	1.47
286.5	0.28	0.25 ^b	0.03 ^b	296.0	1.58	0.23	1.34
287.0	0.33	0.25	0.09	296.5	1.55	0.23	1.32
287.5	0.66	0.25	0.41	297.0	1.49	0.23	1.25
288.0	0.96	0.25	0.72	297.5	1.42	0.23	1.19
288.5	1.21	0.24	0.96	298.0	1.43	0.23	1.20
289.0	1.92	0.24	1.67	298.5	1.34	0.23	1.11
289.5	2.22	0.24	1.98	299.0	1.33	0.23	1.10
290.0	2.05	0.24	1.81	299.5	1.27	0.23	1.05
290.5	2.00	0.24	1.76	300.0	1.25	0.23	1.02
291.0	2.06	0.24	1.82	300.5	1.27	0.23	1.05
291.5	2.12	0.24	1.88	301.0	1.26	0.23	1.03
292.0	2.16	0.24	1.92	301.5	1.21	0.23	0.99

Table 4.3: (continued) Absolute oscillator strengths for the total photoabsorption of CH₃OH in the carbon 1s region.

Photon Energy eV	Oscillator Strength (10 ⁻² eV ⁻¹) ^a			Photon Energy eV	Oscillator Strength (10 ⁻² eV ⁻¹) ^a		
	total	valence	C 1s		total	valence	C 1s
302.0	1.23	0.23	1.00	312.0	1.03	0.21	0.82
302.5	1.21	0.22	0.98	314.0	1.02	0.21	0.81
303.0	1.21	0.22	0.98	316.0	1.01	0.21	0.80
303.5	1.19	0.22	0.97	318.0	0.96	0.21	0.75
304.0	1.19	0.22	0.97	320.0	0.95	0.20	0.74
304.5	1.14	0.22	0.92	322.0	0.91	0.20	0.71
305.0	1.20	0.22	0.97	324.0	0.92	0.20	0.72
305.5	1.16	0.22	0.94	326.0	0.89	0.20	0.70
306.0	1.16	0.22	0.94	328.0	0.89	0.19	0.70
306.5	1.14	0.22	0.92	330.0	0.86	0.19	0.67
307.0	1.11	0.22	0.89	335.0	0.83	0.19	0.64
307.5	1.15	0.22	0.93	340.0	0.79	0.18	0.61
308.0	1.10	0.22	0.88	345.0	0.80	0.18	0.62
308.5	1.11	0.22	0.89	350.0	0.78	0.17	0.60
309.0	1.08	0.22	0.87	355.0	0.77	0.17	0.60
309.5	1.07	0.22	0.85	360.0	0.76	0.17	0.59
310.0	1.08	0.22	0.86				

$$^a \sigma(\text{Mb}) = 109.75 df/dE (\text{eV}^{-1}).$$

^bThe separate valence and C 1s shell contributions above 286.5 eV are obtained by extrapolation of the fit to the valence shell spectrum (90 to 280 eV) to higher photon energies (see figure 4.1 and text for details).

Table 4.4: Branching ratios for the molecular and dissociative photoionization of CH₃OH.

Photon Energy eV	Photoionization Branching Ratio (%)											
	H ⁺	H ₂ ⁺	C ⁺	CH ⁺	CH ₂ ⁺	CH ₃ ⁺	OH ⁺	CO ⁺	CHO ⁺ COH ⁺	CH ₂ O ⁺ CHOH ⁺	CH ₃ O ⁺ CH ₂ OH ⁺	CH ₃ OH ⁺
10.5											0.37	99.63
11.0											1.88	98.12
11.5											9.36	90.64
12.0										0.11	21.82	78.06
12.5										0.53	41.00	58.47
13.0									0.06	1.39	53.44	45.11
13.5					0.18	0.12			0.39	1.99	57.56	39.75
14.0					0.10	1.01			0.78	2.56	59.72	35.83
14.5					0.33	5.02			2.32	2.50	57.39	32.44
15.0					0.47	10.07			4.77	2.51	52.74	29.45
15.5					0.63	13.91		0.03	7.94	2.53	49.33	25.63
16.0					0.99	16.87		0.17	12.14	2.39	44.07	23.38
16.5					0.93	17.46		0.23	14.73	2.51	41.13	23.01
17.0					1.02	18.17	0.58	0.17	17.99	2.36	37.43	22.29
17.5					1.21	18.19	0.50	0.22	20.26	2.52	35.44	21.65
18.0					1.38	18.07	0.57	0.32	22.54	2.90	33.40	20.83

Table 4.4: (continued) Branching ratios for the molecular and dissociative photoionization of CH₃OH.

Photon Energy eV	Photoionization Branching Ratio (%)											
	H ⁺	H ₂ ⁺	C ⁺	CH ⁺	CH ₂ ⁺	CH ₃ ⁺	OH ⁺	CO ⁺	CHO ⁺ COH ⁺	CH ₂ O ⁺ CHOH ⁺	CH ₃ O ⁺ CH ₂ OH ⁺	CH ₃ OH ⁺
18.5					1.50	17.96	0.51	0.32	24.41	2.96	31.73	20.61
19.0					1.64	17.95	0.44	0.19	24.45	3.05	31.50	20.77
19.5					1.41	17.47	0.47	0.26	25.11	3.18	31.38	20.73
20.0					1.57	16.93	0.45	0.27	24.59	3.33	31.43	21.42
20.5					1.63	16.73	0.42	0.27	24.65	3.20	31.71	21.38
21.0					1.55	16.82	0.51	0.40	24.60	3.31	31.25	21.56
21.5	0.05				1.59	16.87	0.62	0.23	24.59	3.11	31.04	21.91
22.0	0.23				1.53	16.46	0.61	0.25	24.21	3.21	31.35	22.15
22.5	0.33				1.45	16.36	0.55	0.38	24.66	3.07	31.37	21.82
23.0	0.60				1.62	16.42	0.50	0.37	24.80	3.03	30.59	22.07
23.5	0.93				1.66	16.01	0.45	0.37	24.40	3.16	30.65	22.37
24.0	0.97				1.56	16.01	0.50	0.32	24.37	3.09	30.74	22.45
24.5	1.06				1.71	15.86	0.56	0.33	24.43	2.94	30.65	22.45
25.0	1.21				1.71	15.65	0.47	0.38	24.66	3.01	30.32	22.60
25.5	1.16				1.71	15.54	0.39	0.44	24.47	3.09	30.78	22.44
26.0	1.35				1.73	15.71	0.51	0.39	24.20	2.94	30.66	22.52
26.5	1.34	0.02			1.67	15.72	0.44	0.59	24.53	3.07	30.14	22.48

Table 4.4: (continued) Branching ratios for the molecular and dissociative photoionization of CH₃OH.

Photon Energy eV	Photoionization Branching Ratio (%)											
	H ⁺	H ₂ ⁺	C ⁺	CH ⁺	CH ₂ ⁺	CH ₃ ⁺	OH ⁺	CO ⁺	CHO ⁺ COH ⁺	CH ₂ O ⁺ CHOH ⁺	CH ₃ O ⁺ CH ₂ OH ⁺	CH ₃ OH ⁺
27.0	1.81	0.17		0.13	1.84	15.33	0.53	0.54	24.70	3.12	29.59	22.23
27.5	1.99	0.11		0.32	1.74	15.29	0.56	0.63	24.50	3.02	29.66	22.17
28.0	2.09	0.18		0.26	2.03	15.11	0.57	0.65	24.53	3.02	29.34	22.22
28.5	2.25	0.11		0.15	1.99	15.17	0.48	0.83	24.74	2.99	29.16	22.13
29.0	2.54	0.13	0.16	0.42	2.42	14.93	0.68	0.88	24.54	2.98	28.52	21.82
29.5	2.75	0.23	0.21	0.43	2.33	15.11	0.63	0.94	24.60	3.03	28.23	21.54
30.0	3.20	0.27	0.16	0.51	2.47	14.75	0.80	1.15	24.07	2.85	28.23	21.56
31.0	3.57	0.31	0.30	0.77	2.56	14.29	0.52	1.23	24.70	2.72	27.64	21.40
32.0	3.82	0.20	0.18	0.69	2.71	14.38	0.76	1.49	24.19	2.76	27.25	21.57
33.0	4.17	0.42	0.39	1.16	2.81	14.32	0.83	1.45	23.64	2.88	27.07	20.87
34.0	4.81	0.50	0.46	1.33	3.15	14.06	0.87	1.70	24.38	2.85	25.42	20.46
35.0	4.94	0.43	0.55	1.38	2.93	13.68	1.32	1.53	23.30	3.09	25.90	20.95
36.0	5.51	0.36	0.58	1.36	3.19	13.60	0.98	1.72	24.14	3.04	25.37	20.15
37.0	5.72	0.57	0.72	1.42	3.25	13.57	1.18	1.75	24.06	2.99	24.81	19.97
38.0	6.25	0.63	0.61	1.28	3.19	13.10	1.26	1.57	24.11	2.81	24.73	20.47
39.0	6.53	0.61	0.80	1.56	3.10	12.73	1.26	1.63	24.41	2.84	24.72	19.81
40.0	7.22	0.76	0.71	1.63	3.14	13.38	1.73	1.58	23.85	2.96	23.28	19.76

Table 4.4: (continued) Branching ratios for the molecular and dissociative photoionization of CH₃OH.

Photon Energy eV	Photoionization Branching Ratio (%)											
	H ⁺	H ₂ ⁺	C ⁺	CH ⁺	CH ₂ ⁺	CH ₃ ⁺	OH ⁺	CO ⁺	CHO ⁺ COH ⁺	CH ₂ O ⁺ CHOH ⁺	CH ₃ O ⁺ CH ₂ OH ⁺	CH ₃ OH ⁺
41.0	7.50	0.71	0.60	1.68	3.32	13.01	1.84	1.72	24.00	2.89	23.00	19.73
42.0	7.62	0.93	0.82	1.59	3.20	13.16	1.64	1.49	24.06	2.85	23.29	19.34
43.0	8.06	1.10	0.84	1.76	3.43	12.95	2.08	1.55	23.69	2.83	23.02	18.69
44.0	8.38	0.82	0.82	1.59	3.41	12.47	1.91	1.62	24.22	3.05	22.65	19.06
45.0	8.68	0.86	1.09	1.85	3.77	12.57	2.08	1.60	24.12	2.74	22.07	18.58
46.0	8.78	0.90	1.02	1.79	3.68	12.31	2.36	1.59	24.14	2.87	21.83	18.72
47.0	9.66	1.24	0.70	2.05	3.60	12.70	1.75	1.77	23.73	2.82	21.55	18.42
48.0	9.34	0.97	0.85	1.74	3.46	12.88	1.85	1.62	24.20	2.62	21.72	18.76
49.0	9.46	1.01	1.11	1.86	3.93	12.38	2.06	1.85	23.69	2.64	21.09	18.94
50.0	10.10	1.15	0.88	2.21	3.95	12.04	2.15	2.01	23.92	2.56	21.12	17.90
55.0	10.68	1.17	0.95	2.10	4.26	12.18	2.70	2.00	23.74	2.67	20.01	17.54
60.0	12.10	1.41	1.16	2.60	4.30	11.85	2.70	2.52	23.22	2.49	18.88	16.76
65.0	13.55	1.41	1.36	2.44	4.48	11.57	2.96	2.23	22.88	2.48	18.11	16.53
70.0	14.19	1.57	1.30	2.70	4.37	12.01	2.63	2.39	22.34	2.62	17.39	16.48
75.0	15.03	1.77	1.22	2.60	4.62	11.26	3.16	2.75	21.70	2.57	17.12	16.21
80.0	15.70	1.65	1.23	2.71	4.84	11.15	3.02	2.45	21.51	2.58	16.86	16.30

Table 4.5: (continued) Calculated and measured appearance potentials for the production of positive ions from CH₃OH.

Process	Appearance Potential (eV)									
	Calculated ^a	This Work ^b	[151]	[155]	[149]	[150]	[156]	[154]	[179]	[153]
(51) H ⁺ + CH ₂ OH	17.57	21.5								
(52) H ⁺ + CH ₃ O	17.97									
(53) H ⁺ + CHO + H ₂	18.27									
(54) H ⁺ + CO + H ₂ + H	18.87									
(55) H ⁺ + CH ₂ O + H	18.97									
(56) H ⁺ + H ₂ O + CH	21.48									
(57) H ⁺ + CH ₃ + O	21.92									
(58) H ⁺ + CH ₂ + OH	22.25									
(59) H ⁺ + CHO + 2H	22.76									
(60) H ⁺ + CO + 3H	23.35									
(61) H ⁺ + H ₂ O + C + H	24.95									
(62) H ⁺ + OH + H ₂ + C	25.58									
(63) H ⁺ + CH + H ₂ + O	26.51									
(64) H ⁺ + OH + CH + H	26.59									
(65) H ⁺ + CH ₂ + O + H	26.65									
(66) H ⁺ + H ₂ + O + C + H	29.98									
(67) H ⁺ + OH + C + 2H	30.06									
(68) H ⁺ + CH + O + 2H	30.99									
(69) H ⁺ + O + C + 3H	34.46									
(70) H ⁺ + CHOH + H	???									
(71) H ⁺ + COH + H ₂	???									
(72) H ⁺ + COH + 2H	???									

^aValues calculated using thermodynamic data for the enthalpy of formation of ions and neutrals (taken from [169]) and assuming zero kinetic energy of fragmentation.

^b±1 eV.

Table 4.6: Proposed dipole induced breakdown scheme for CH₃OH.

Electronic Ion State	VIP (eV)	Possible Ionic Photofragmentation products
$(2a'')^{-1}$	10.96	CH ₃ OH ⁺
$(7a')^{-1}$	12.62	CH ₃ O ⁺ /CH ₂ OH ⁺ , CH ₂ O ⁺ /CHOH ⁺
$(6a')^{-1}$	15.2	CH ₃ OH ⁺ , CH ₃ O ⁺ /CH ₂ OH ⁺ , CH ₂ O ⁺ /CHOH ⁺ , CHO ⁺ /COH ⁺ , CH ₃ ⁺ , CH ₂ ⁺
$(1a'')^{-1}$	15.6	CH ₃ OH ⁺ , CH ₃ O ⁺ /CH ₂ OH ⁺ , CH ₂ O ⁺ /CHOH ⁺ , CHO ⁺ /COH ⁺ , CH ₃ ⁺ , CH ₂ ⁺
$(5a')^{-1}$	17.6	CH ₂ O ⁺ /CHOH ⁺ , CHO ⁺ /COH ⁺ , CO ⁺ , OH ⁺ , CH ₃ ⁺ , CH ₂ ⁺
$(4a')^{-1}$	22.6	CH ₃ OH ⁺ , CH ₃ O ⁺ /CH ₂ OH ⁺ , CO ⁺ , OH ⁺ , H ⁺
$(3a')^{-1}$	32.2	CH ₂ O ⁺ /CHOH ⁺ , CO ⁺ , OH ⁺ , CH ₂ ⁺ , CH ⁺ , C ⁺ , H ₂ ⁺ , H ⁺

Chapter 5

Photoabsorption and Photoionization Studies of Carbon Tetrachloride

5.1 Introduction

Following the initial photographic work of Leifson [180], a range of measurements of the absolute photoabsorption oscillator strength (cross section) distribution of carbon tetrachloride have been reported in the valence shell below 25 eV [113, 116, 181–190] and in the vicinity of the Cl 2p absorption edge [191]. The discrete region below the Cl 2p edge has been studied by O’Sullivan [192] from 199 to 208 eV. In other work, small momentum transfer electron energy-loss spectroscopy (EELS) has been used throughout the 100–400 eV region to study the electronic transitions associated with the Cl 2p, 2s and C 1s inner shell excitations [193], but no absolute data were reported. More recently using empirical procedures, approximate values of absolute differential oscillator strengths have been estimated [194] for the inner-shell regions (Cl 2p, 2s; C 1s) of CCl₄ from the EELS spectra reported earlier by Hitchcock and Brion [193]. However, these absolute measurements [113, 116, 181–191, 194] have been made over only limited energy regions, and there is no comprehensive absolute photoabsorption data set which spans the valence- and inner-shell regions.

The valence-shell ionization energies of CCl₄ have been extensively studied by photoelectron spectroscopy (PES) [195–201], and by angle-resolved PES [202–205] in the

gas phase, and also by tuneable photon energy PES of a solid film of carbon tetrachloride [206]. These latter measurements [202–206] were made using either line sources [205] or synchrotron radiation [202–204, 206] to determine the variation of the asymmetry parameter [202–205], and absolute [202] or relative [206] electronic state partial cross sections, as a function of photon energy. In other work, the technique of X-ray photoelectron spectroscopy (XPS) has been used to determine the ionization energies for the inner-shells of CCl_4 [207–214]. Photoionization and electron-impact methods [215–229] have provided information about the relative photoionization yield curves [215, 217, 222, 223, 226] and the appearance potentials [215, 216, 218–222, 224, 227–229] for the major ionic photofragments of carbon tetrachloride.

Absolute oscillator strength data for electronic excitation and ionization in the VUV and soft X-ray regions are useful in a number of areas of science and technology including aeronomy, astrophysics, and radiation chemistry and physics [4]. Wide-ranging absolute oscillator strength data for atoms and molecules are also required for the construction of dipole oscillator strength distributions, which cover the entire photoabsorption spectrum, and for calculating a wide range of dipole properties [72]. More specifically, carbon tetrachloride has been found to contribute to the “greenhouse effect”, and is a trace gas component and harmful pollutant of the atmosphere whose amount is increasing significantly [230]. Carbon tetrachloride is a useful electron scavenger [231], is a source of CCl_3 and CCl_2 radicals by photodecomposition [189, 232] and is also used in the production of chlorofluorocarbons by catalyzed fluorination with HF [233]. The absolute inner-shell [194] and valence-shell [132, 172–174] photoabsorption oscillator strengths for the chlorofluoromethanes (i.e., the freons $\text{CF}_x\text{Cl}_{4-x}$, $x=1-4$) have been reported previously by Zhang *et al.* and the present work extends these results to the related molecule, CCl_4 .

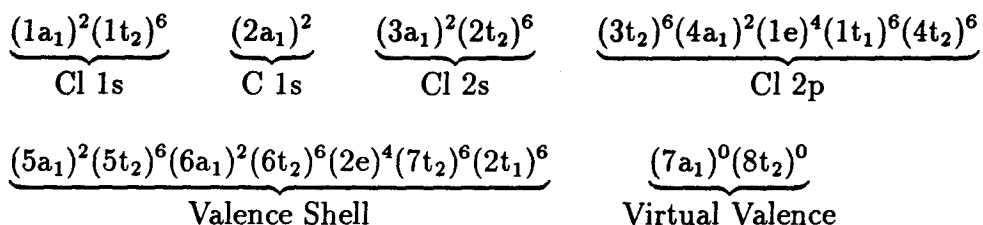
Studies of such a series of molecules as the chlorofluorocarbons allow for the investigation and evaluation of systematic trends and additivity concepts [234] in the photoabsorption spectra of these molecules, and larger systems containing similar functional groups.

In this chapter measurements of the absolute photoabsorption oscillator strength distribution of CCl_4 are reported from 5.5 to 400 eV, obtained using low-resolution (1 eV fwhm) dipole (e,e) spectroscopy. These low-resolution photoabsorption data span the visible through to the soft X-ray photon energy region of the electromagnetic spectrum. High-resolution dipole (e,e) spectroscopy has also been used in the present work to measure oscillator strength data in the low-energy valence-shell region from 5.0 to 30 eV where sharp discrete excitation features exist. In addition to the photoabsorption studies, the technique of dipole (e,e+ion) spectroscopy has been used in the present work at a resolution of 1 eV fwhm to measure the photoionization efficiency and the photoionization branching ratios for CCl_4 in the valence shell from 11.0 to 80 eV and also in the Cl 2p ionization region from 195.5 to 220.5 eV. Absolute partial photoionization oscillator strengths for the dissociative photoionization channels of CCl_4 have been obtained as a function of photon energy from the triple product of the presently measured photoionization efficiencies, photoionization branching ratios, and absolute photoabsorption oscillator strength data. The presently obtained results have been used along with other spectroscopic information to determine quantitative and qualitative information concerning the dipole-induced breakdown of CCl_4 caused by VUV and soft X-ray radiation in both the valence- and Cl 2p inner-shell regions.

5.2 Results and Discussion

5.2.1 Electronic Structure

Carbon tetrachloride has tetrahedral symmetry (T_d) and the molecular orbital configuration of the ground electronic state in an independent particle model is:



The vertical ionization potentials (VIPs) for the five outermost occupied valence orbitals have been measured to be 11.69 ($2t_1^{-1}$); 12.44, 12.65, 12.78 ($7t_2^{-1}$); 13.37, 13.50 ($2e^{-1}$); 16.58 ($6t_2^{-1}$); and 20.0 eV ($6a_1^{-1}$) using He(I) and He(II) PES [197]. The inner-valence and the inner-shell VIPs, as determined using XPS [213, 214], are as follows: 24.8 ($5t_2^{-1}$), 28.0 ($5a_1^{-1}$), 207.04 $2p_{3/2}$, 208.73 $2p_{1/2}$ (Cl 2p), 278.0 (Cl 2s), and 296.3 eV (C 1s).

5.2.2 Photoabsorption Oscillator Strengths

5.2.2.1 Low-Resolution Measurements

The low-resolution (~ 1 eV fwhm) relative oscillator strength spectrum, obtained from the Bethe-Born converted EELS spectrum (see section 3.1), was placed on an absolute scale by valence-shell TRK sum rule normalization. A curve of the form

$$\frac{df}{dE} = AE^{-1.5} + BE^{-2.5} + CE^{-3.5}$$

was used to fit the high-energy portion of the valence-shell oscillator strength spectrum from 98–198 eV. Here df/dE is the differential oscillator strength, E is the energy loss (or equivalent photon energy) and A , B , and C are best fit parameters which were determined to be $21.099 \text{ eV}^{0.5}$, $4829.4 \text{ eV}^{1.5}$, and $-3.4397 \times 10^5 \text{ eV}^{2.5}$, respectively. This particular functional form was also used in the methanol study (see section 4.2.2.1) and was chosen because of the good quality of the fit to the present data and because of its previous effectiveness in fitting the high-energy portion of the valence shell of the chlorofluoromethanes [132, 172–174]. Using this fitted curve the portion of the valence-shell oscillator strength above 198 eV is estimated to be 11.8%. The total area under the presently measured data from 5.5–198 eV plus the contribution above 198 eV (to infinity), estimated from the extrapolation of the fitted polynomial, was set to an integrated oscillator strength value of 33.14. This corresponds to the 32 valence-shell electrons of CCl_4 plus an estimated contribution of 1.14 to account for Pauli-excluded transitions from the inner-shell orbitals to the already-occupied valence-shell orbitals (see section 3.1.1).

The absolute photoabsorption oscillator strengths for the valence shell of CCl_4 obtained in the present work at a resolution of 1 eV fwhm are shown in figure 5.1a from 5.5 to 198 eV, and are given numerically in table 5.1 from 5.5 to 195 eV. The peak observed at 9.5 eV in this spectrum corresponds to contributions from the two strongest transitions in the discrete region of CCl_4 below the first IP. However, because of the limited resolution only one peak is observed. A high-resolution spectrum has been measured in the present work in the discrete region below the first IP and will be discussed in section 5.2.2.2 below. In the vicinity of ~ 40 eV the photoabsorption spectrum of CCl_4 progresses through a local minimum. This so-called “Cooper minimum” has been observed previously [202] in several of the electronic state partial photoionization cross sections of CCl_4 and is due

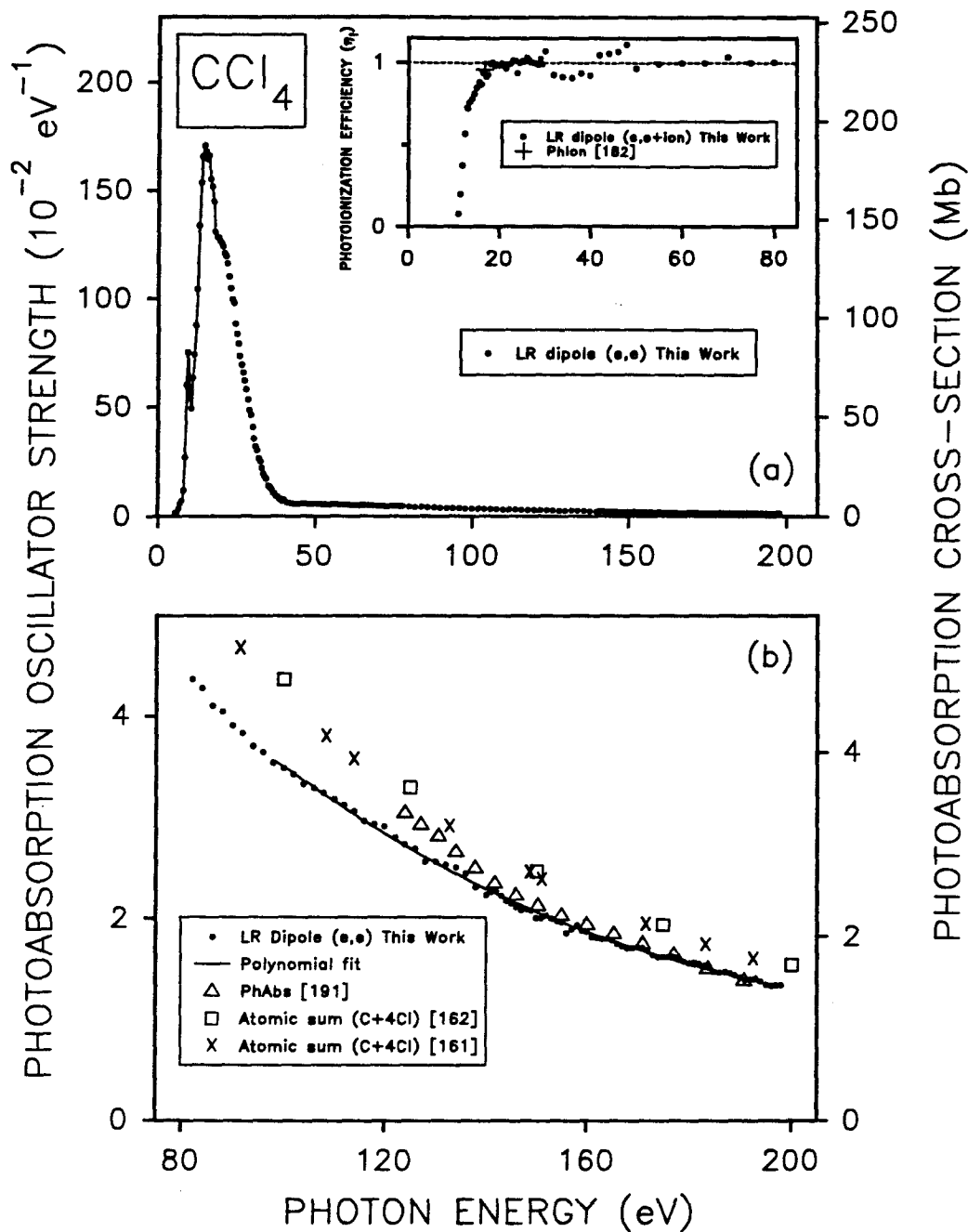


Figure 5.1: Absolute photoabsorption oscillator strengths for CCl_4 obtained using low-resolution (1 eV fwhm) dipole (e,e) spectroscopy: (a) The valence-shell region from 5.5 to 198 eV; (b) The high-energy portion of the valence shell region from 82 to 198 eV. Also shown are previously published photoabsorption data [191], and summed experimental [161] and theoretical [162] atomic oscillator strengths for the constituent atoms of CCl_4 . The insert to (a) shows the photoionization efficiency measured in the present work from 11–80 eV (see section 5.2.3).

to the fact that the 3p wavefunction of atomic Cl has a radial node. Figure 5.1b shows the low-resolution absolute oscillator strength data for CCl_4 from 82–198 eV along with previously measured absolute photoabsorption data [191] and both experimental [161] and theoretical [162] atomic oscillator strength sums for the constituent atoms (C+4Cl). From figure 5.1b it can be seen that there is quite good agreement from 142–191 eV between the presently measured dipole (e,e) data and the previously reported photoabsorption measurements of Cole and Dexter [191]. However, the latter data [191] are higher than the present results between 124 and 142 eV. In addition, it can be seen that although the summed atomic oscillator strength data sets [161, 162] are consistent with each other, they are $\sim 25\%$ higher than the present experimental results from 90 to 200 eV.

5.2.2.2 High-Resolution Measurements

The high-resolution (0.048 eV fwhm) photoabsorption spectrum of CCl_4 measured in the present work is shown in figure 5.2. This spectrum was placed on an absolute scale by one-point normalization to the present absolute low-resolution photoabsorption spectrum (see section 5.2.2.1) at 25 eV in the smooth continuum region. The assignments of the spectral features in the discrete region below the first IP have been reported previously [116, 167, 181, 183, 184, 186, 189, 190]. These high-resolution data are shown in figure 5.2a along with the presently measured low-resolution (~ 1 eV fwhm) data and previously reported photoabsorption data [113, 182, 183]. The lower resolution data reported by Sowers *et al.* [183] below ~ 11 eV are reasonably consistent with the present work. The data reported by Person and Nicole [113] in the 13–22 eV region and the single data point reported by Rebbert and Ausloos [182] at ~ 17 eV are about 16% higher than the present

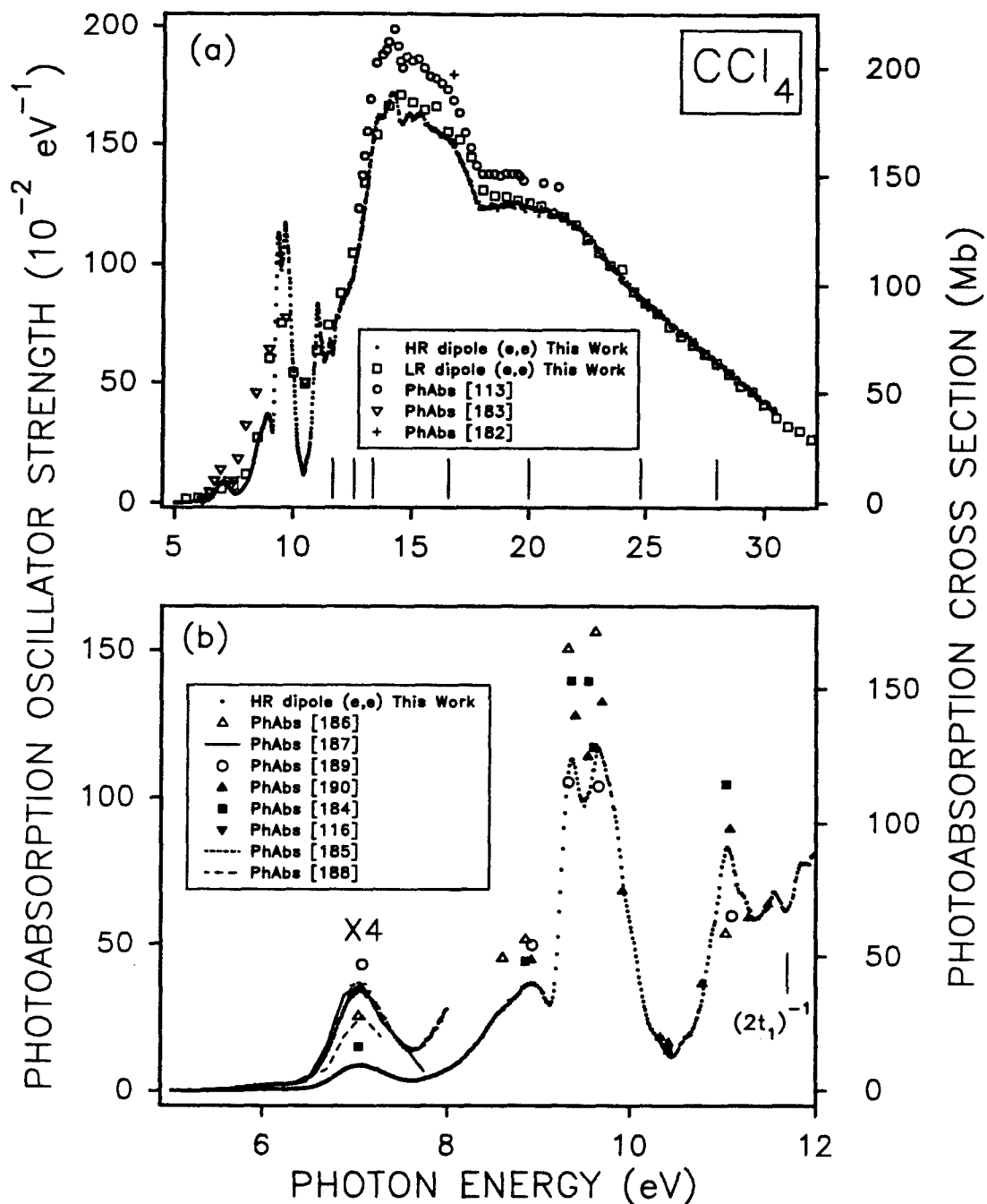


Figure 5.2: Absolute photoabsorption oscillator strengths measured in the present work at high resolution (0.048 eV fwhm) and at low resolution (1 eV fwhm) using dipole (e,e) spectroscopy (solid dots and open squares, respectively): (a) The low-energy valence-shell region from 5 to 32 eV; (b) The valence-shell discrete region from 5 to 12 eV, below the first IP. Previously reported absolute photoabsorption measurements are also shown for comparison [113, 116, 182–190]. The vertical lines in (a) and (b) indicate the positions of the valence-shell VIPs [197, 213].

work. The low-energy portion of the presently measured high-resolution spectrum is shown in figure 5.2b from 5–12 eV, along with previously reported photoabsorption data for comparison [116, 184–190]. The present high-resolution absolute data are in good agreement with the measurements reported by Tsubomura *et al.* [116], Robbins [185], and Hubrich and Stuhl [187] in the vicinity of the broad absorption peak at ~ 7 eV. In the same region the data of Russell *et al.* [184], Causley and Russell [186], Roxlo and Mandl [188], and Ibuki *et al.* [189] are $\sim 90\%$, $\sim 40\%$, and $\sim 40\%$ lower and 17% higher, respectively, than the present work. From 8–12 eV the present results agree best with the recently reported optical work of Lee and Suto [190]. Most of the photoabsorption oscillator strength data obtained using optical methods are higher than the present work at absorption peak maxima in the region of sharp structure (8.5–11 eV) because of the much higher resolution in the optical work [184, 186, 189, 190].

5.2.2.3 Inner-Shell (Cl 2p,2s; C 1s) Measurements

Absolute photoabsorption oscillator strengths have been measured at a resolution of 1 eV fwhm for the inner-shells (Cl 2p,2s; C 1s) of CCl_4 from 195–400 eV. These data are given numerically in table 5.2. The absolute scale was obtained by normalization to the high-energy tail of the absolute valence-shell oscillator strength distribution determined as in section 5.2.2.1. The assignments of the spectral features in these inner-shell regions (Cl 2p, 2s; C 1s) have been reported previously [192, 193]. The complete photoabsorption spectrum (valence plus inner shells) measured in the present work is shown in figure 5.3a from 5.5–400 eV while the inner-shell regions are shown in greater detail in figure 5.3b. The direct optical photoabsorption measurements reported by Cole and Dexter [191] shown on figure 5.3b are in very good agreement with the present work below the Cl 2p

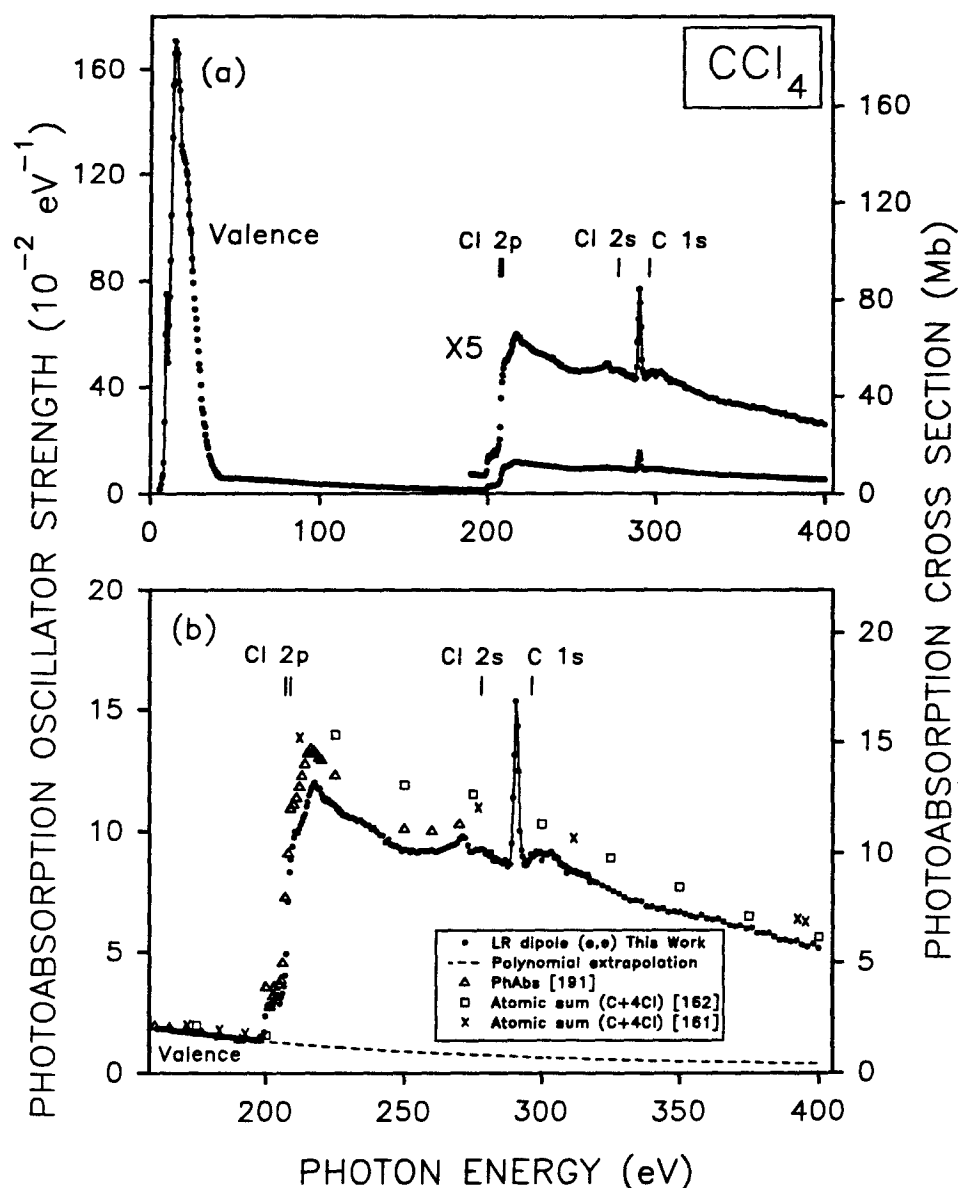


Figure 5.3: Absolute photoabsorption oscillator strengths obtained at a resolution of 1 eV fwhm: (a) The measured low-resolution photoabsorption spectrum from 5.5–400 eV; (b) The inner-shell (Cl 2p,2s; C 1s) region from 150 to 400 eV on an expanded scale. The Cl 2p absolute inner-shell photoabsorption measurements of Cole and Dexter [191] are shown along with experimental [161] and theoretical [162] atomic oscillator strength sums for the constituent atoms of CCl_4 . The vertical lines represent the positions of the indicated inner-shell VIPs [213, 214]. The solid line in (b) is the extrapolation of the polynomial which was fitted to the high-energy valence-shell region from 98–198 eV. This curve was used to estimate the contribution of the valence-shell oscillator strength above 198 eV.

absorption threshold at ~ 198 eV but are $\sim 12\%$ higher above 198 eV to the limit of their data at 270 eV. The experimental [161] and theoretical [162] atomic oscillator strength sums for the total (valence plus inner shells) photoabsorption of CCl_4 from ~ 190 – 400 eV are ~ 10 – 20% higher than the present measurements. However, the agreement improves above 300 eV. Although summed atomic oscillator strength data for the constituent atoms of a molecule have been used at 20–30 eV above an absorption edge to place inner-shell electron energy-loss spectra on an absolute scale (for examples see [119, 194]) such a normalization assumes that there are no further molecular effects (e.g., shape resonances) beyond this energy range. However, it can be seen from a comparison of the oscillator strength scales of the present work (figure 5.3b) and figure 6 of reference [194] that such a procedure is not particularly satisfactory for CCl_4 . The discrepancies are due to the relatively close proximity of the Cl 2s and C 1s excitation features to the Cl 2p edge, and to the presence of oscillating extended fine structure (EXELFS) in the molecular case [194]. Similar findings and conclusions have resulted from other recent inner-shell oscillator strength studies of SiF_4 [79], SiH_4 [127], PH_3 [129], and SO_2 [131]. Consideration of these studies and the results for methanol (see section 4.2.2.3), and the present results for carbon tetrachloride suggest that absolute scales determined for molecular inner-shell spectra using atomic oscillator strength data are likely to be subject to appreciable errors and that such calibrations are at best only approximate.

From figure 5.3a it can be seen that the valence-shell region oscillator strength distribution is strongly peaked in the low energy region due to the large contribution from the 3p and 3s orbitals of the third-row chlorine atoms [235]. The inner-shell oscillator strength distribution, on the other hand, involves second row orbitals and therefore is

much less peaked and does not fall off as quickly with increasing photon energy. As a general rule, the more diffuse the electron density (i.e., the greater the average electron orbit radius) in a molecule, the more the oscillator strength distribution will become peaked at lower energies and therefore will fall off more quickly with increasing energy. The effects are well illustrated by a consideration of the photoabsorption spectra shown in figure 5.4 where the presently reported low-resolution absolute oscillator strength data for CCl_4 are compared with corresponding valence-shell data measured earlier in this laboratory for the chlorofluoromethanes [132, 172–174]. Since these molecules are all valence-shell isoelectronic, the absolute oscillator strength scale has been obtained in all cases by normalization to 33.1 electrons. It can be seen from figure 5.4 that with a systematic successive replacement of fluorine by chlorine the oscillator strength distribution of the chlorofluoromethanes becomes increasingly peaked at lower photon energies and drops off much more rapidly with increasing photon energy as the number of chlorine atoms is increased. The outermost electrons in a chlorine atom are in the 3p orbital, whereas they are in a 2p orbital in a fluorine atom. The 3p orbital is more diffuse and therefore the 3p electron is on average farther away from the nucleus than the electron in a 2p orbital. As the number of electrons farther from the nucleus is increased the valence-shell oscillator strength distribution is seen to peak at lower photon energies with correspondingly lower oscillator strength values at higher energies.

5.2.3 Dissociative Photoionization in the Valence-Shell Region

The technique of dipole ($e, e^+ \text{ion}$) spectroscopy has been used to provide information on the dissociative photoionization of CCl_4 in the valence-shell region. Time-of-flight (TOF) mass spectra have been measured as a function of energy-loss (equivalent photon energy)

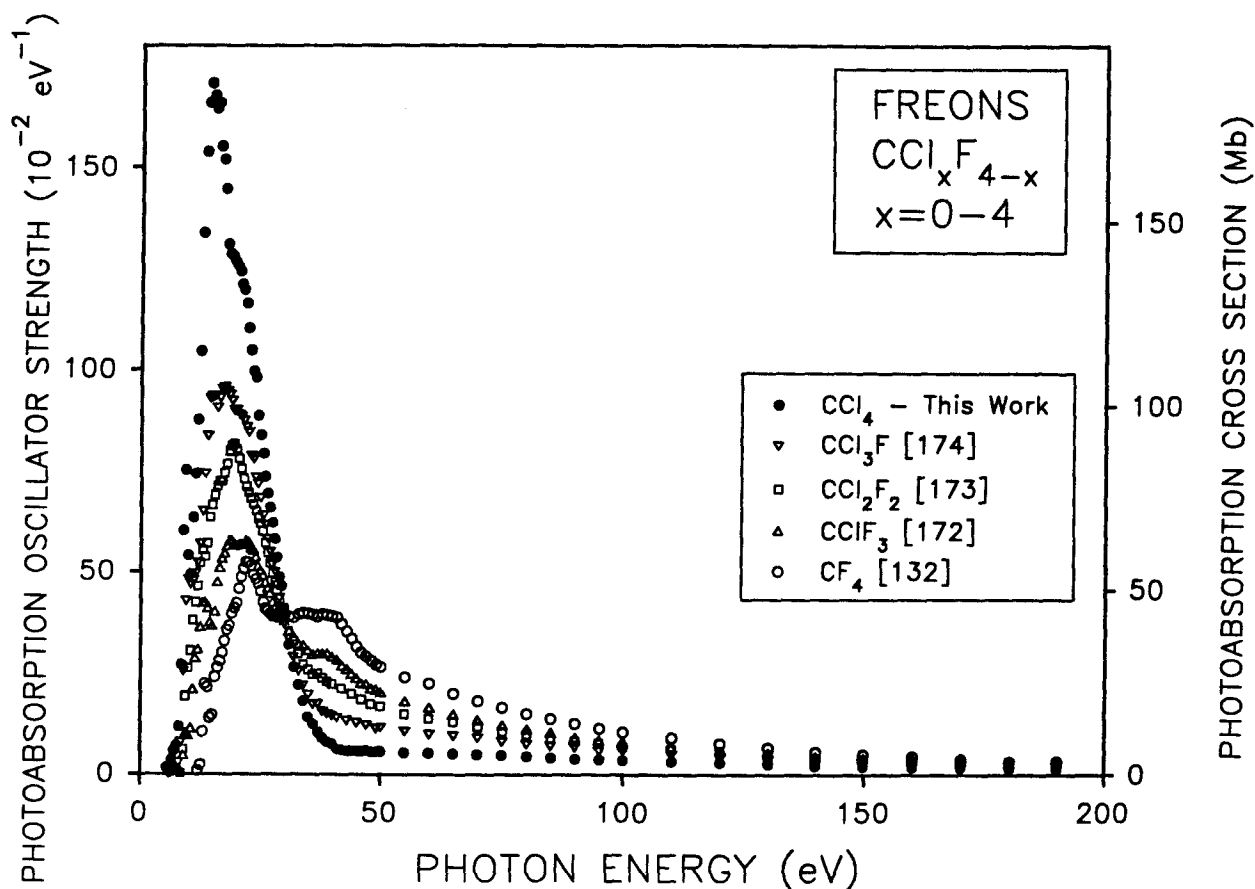


Figure 5.4: Absolute photoabsorption oscillator strengths for the chlorofluoromethanes in the valence-shell region from 5–190 eV. The presently measured low-resolution photoabsorption spectrum of CCl_4 is shown in comparison with those of the freons, $\text{CCl}_{4-x}\text{F}_x$ ($x=1-4$) which have been measured previously at the same resolution (1 eV fwhm) using dipole (e,e) spectroscopy [132, 172–174].

from 11.0–80.0 eV. Figure 5.5 shows the TOF mass spectrum obtained in the present work at 50 eV. The cations produced from the dissociative photoionization of CCl_4 observed in the present work are: CCl_3^+ , CCl_2^+ , Cl_2^+ , CCl_3^{2+} , CCl^+ , Cl^+ , and C^+ . The chlorine-containing peaks show structure reflecting the ^{35}Cl and ^{37}Cl isotopic composition. The N_2^+ and O_2^+ peaks shown on figure 5.5 (and the N^+ , and O^+ peaks at m/e 14 and 16, respectively) are due to photoionization events involving the background gases in the spectrometer. The base pressure of the dipole (e,e+ion) spectrometer used in the present work is $\sim 2 \times 10^{-7}$ Torr, and the TOF mass spectral measurements were made at a total pressure of 6×10^{-6} Torr. The background gas peaks become appreciable in TOF mass spectra where the photoabsorption cross section of the target being studied is very low, as in the present case of CCl_4 above about 40 eV (see figure 5.1). It should be noted that the background contributions to photoabsorption have been eliminated by background subtraction (see section 3.1). No CCl_4^+ molecular ion was observed in the present work which is consistent with previous studies [227] which have indicated that the carbon tetrahalide ions, CX_4^+ ($X=\text{F}, \text{Cl}, \text{Br}$), are thermodynamically unstable and dissociate exothermically to $\text{CX}_3^+ + \text{X}$. The only stable multiply charged cation observed in the present work was CCl_3^{2+} .

Branching ratios for the various dissociative photoionization channels were obtained by first integrating the peaks of the baseline subtracted TOF mass spectra. The TOF mass spectra for carbon tetrachloride were measured using the microchannel plate-based ion detector. These branching ratio data were then corrected using the recently determined (see section 3.1.2) ion detector response function for ions of different m/e . The valence-shell branching ratios are shown in figure 5.6 and given numerically in table 5.3. The mass resolution of the TOF mass spectrometer used in the present study was suffi-

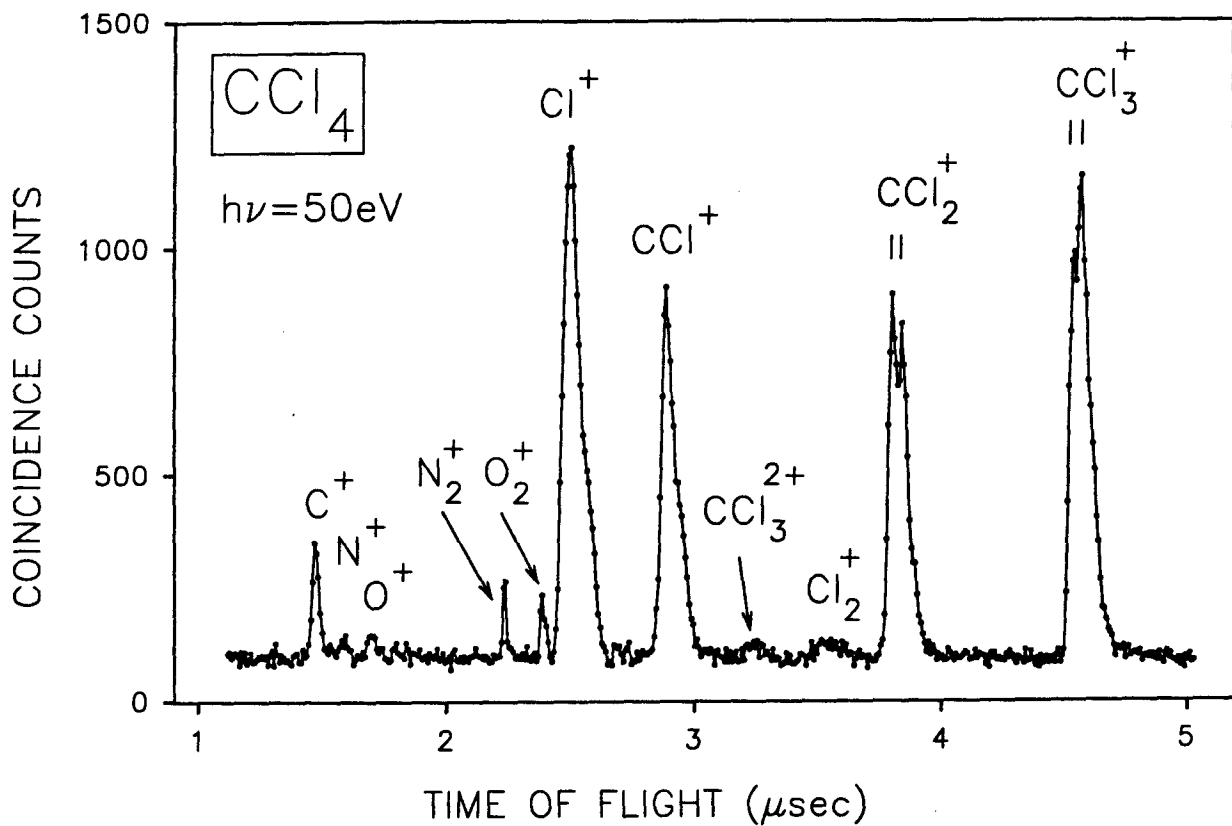


Figure 5.5: The time-of-flight mass spectrum of CCl_4 measured at an equivalent photon energy of 50 eV. The peaks associated with fragment ions containing chlorine atoms are broadened or multiply peaked because of isotopic contributions from ^{35}Cl and ^{37}Cl .

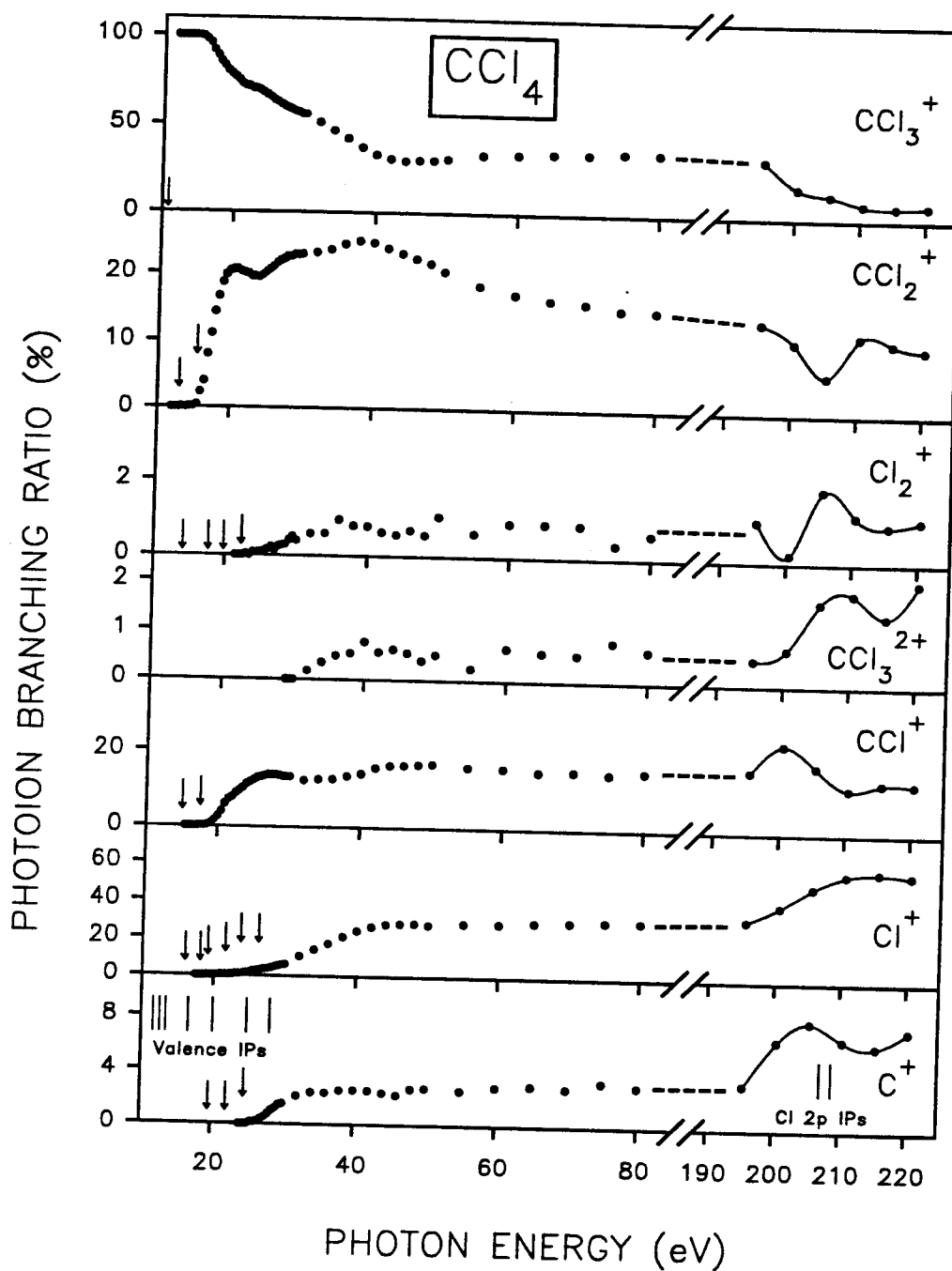


Figure 5.6: The branching ratios for the dissociative photoionization of CCl_4 in the valence-shell region from 11 to 80 eV and in the vicinity of the Cl 2p edge from 195.5 to 220.5 eV. The vertical arrows indicate the position of calculated appearance potentials for the various fragment ions (see table 5.4). The vertical line represent the valence-shell and Cl 2p VIPs [197, 213, 214].

cient to resolve all the fragment ions of a particular stoichiometry and charge, but was insufficient to resolve the individual peaks for all the chlorine-containing isotopomers for each ion. Therefore, the reported branching ratios for the fragment ions from CCl_4 include the contributions from both the ^{35}Cl and ^{37}Cl isotopes.

The relative photoionization efficiency in dipole (e,e+ion) spectroscopy is given by the ratio of the total coincident ion signal to the number of forward scattered electrons as a function of energy loss. The presently measured ratio for carbon tetrachloride is found to be essentially constant above 18.0 eV, within experimental error. Making the reasonable assumption that the absolute photoionization efficiency (η_i) is unity at higher energies, we therefore conclude that η_i reaches 1 at 18.0 eV. The absolute photoionization efficiency data from 11.0–80 eV are shown as an insert on figure 5.1 and are given numerically in the last column of table 5.1.

Absolute partial photoionization oscillator strengths for the production of fragment ions from CCl_4 were obtained from the triple product of the absolute photoabsorption oscillator strength, the absolute photoionization efficiency, and the branching ratio for each ion, as a function of photon energy. The absolute partial photoionization oscillator strength data thus obtained for the valence shell of CCl_4 from 11.0 to 80 eV are shown in figure 5.7 and given numerically in table 5.1.

The molecular and fragment ion appearance potentials from CCl_4 measured in the present work are compared in table 5.4 along with literature values [215, 216, 218–222, 227]. It can be seen that there is excellent agreement (within the present experimental uncertainty of ± 1 eV) between the present ion appearance potentials and those reported previously [215, 216, 218–222, 227] using electron-impact and photoionization methods. Table 5.4 also includes the calculated appearance potentials for all possible fragmentation

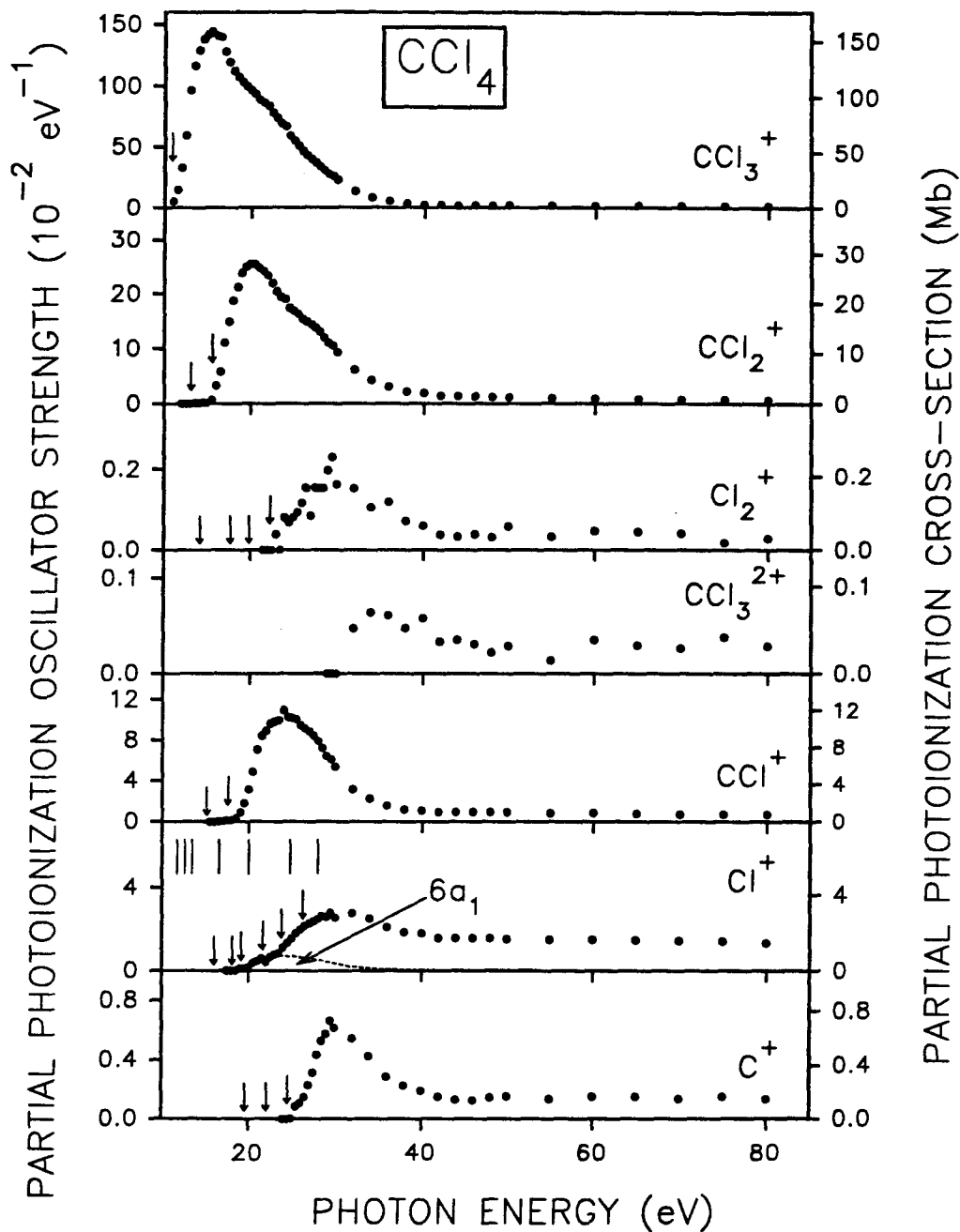


Figure 5.7: Absolute partial photoionization oscillator strengths (cross sections) for the dissociative photoionization of CCl_4 in the valence-shell region from 11–80 eV. The vertical arrows indicate the positions of calculated appearance potentials for the various fragment ions (see table 5.4). The vertical lines represent the valence-shell VIPs [197, 213]. The contribution from the $(6a_1)^{-1}$ ion state to the production of Cl^+ , estimated in the present work, is indicated by the dashed line in the POS for the Cl^+ cation.

processes leading to the production of a particular singly charged cation of CCl_4 . These values have been calculated from thermodynamic data [169], assuming zero kinetic energy of fragmentation, and are indicated by vertical arrows on figures 5.6 and 5.7.

5.2.4 The Dipole-Induced Breakdown of Carbon Tetrachloride

The procedures and theoretical background for the determination of the dipole-induced breakdown scheme for a molecule have been summarized in sections 2.3 and 4.2.4. The determination of the dipole-induced breakdown scheme for CCl_4 has been aided by two tuneable energy PES measurements of electronic ion state partial photoionization oscillator strength data [202, 206].

5.2.4.1 The Proposed Dipole-Induced Breakdown Scheme for the Low-Energy Valence Region

The various types of theoretical and experimental data which can assist in the elucidation of the dipole-induced breakdown pathways of a molecule have been summarized previously in section 4.2.4. Of these, the present work only provides branching ratios (figure 5.6 and table 5.3) and partial oscillator strength curves for dissociative photoionization (figure 5.7 and table 5.1), as well as the appearance potentials (table 5.4) for the many fragment ions formed from CCl_4 . Additional insights can be gained from the photoelectron-photoion coincidence (PEPICO) work of Kischlat and Morgner [226] which lists the electronic states that contribute to the production of the CCl_n^+ ($n=1-3$) cations for photon energies below 21 eV. Although PES studies of the photoionization cross sections for production of the electronic states of CCl_4^+ have been reported on an absolute scale by Carlson *et al.* [202] in the gas phase, and on a relative scale for solid

films by Fock and Koch [206] neither of these data sets included the contributions from the inner-valence region. As such, the reported [202, 206] electronic ion state branching ratios are in error above ~ 30 eV. Furthermore, the sum of the absolute partial cross sections reported by Carlson *et al.* [202] in the region below 30 eV is not consistent with the TRK sum rule since it is only $\sim 60\%$ of the total photoabsorption cross section determined in the present work (figure 5.1, table 5.1). Therefore, we have recalculated the electronic state partial oscillator strengths from both [202, 206] photoelectron studies as follows. Firstly, the contribution from the inner-valence ($5t_2$ and $5a_1$) orbitals was estimated from the sum of the presently measured partial oscillator strengths for Cl_2^+ , C^+ , and part of Cl^+ (see discussion below) and was subtracted from the total photoionization oscillator strength distribution determined in the present work. In addition the CCl_3^{2+} yield was subtracted since doubly charged ions are not expected to arise from the decomposition of singly charged ions. The total photoionization sum, corrected in this fashion, was then multiplied by the respective electronic ion state branching ratios for the outer valence orbitals, according to the data reported by Carlson [202] and by Fock and Koch [206]. In this way, new partial oscillator strengths for the production of each of the five outer valence states of CCl_4^+ were derived which are consistent with the present total photoionization results.

From an examination of the shape of the branching ratio curves (figure 5.6, table 5.3), and the shapes and magnitudes of the partial oscillator strength curves (figure 5.7, table 5.1), for the dissociative photoionization of CCl_4 , as well as the VIPs [197, 213] and the Franck-Condon widths [213] of the electronic ion states, certain aspects of the dipole-induced breakdown scheme for CCl_4 may be deduced as follows. Firstly, the molecular

ion CCl_4^+ is unstable [227] since it is not observed on the time scale of the TOF mass spectrometer used in the present work. The branching ratio (figure 5.6 and table 5.3) of the CCl_3^+ cation is 100% from 11.0–13.0 eV indicating that ionization from the $2t_1^{-1}$ and $7t_2^{-1}$ states yields only this ion. The branching ratio remains greater than 97% up to 16.0 eV suggesting a further major contribution from the $2e^{-1}$ state. The change in slope of the partial oscillator strength (POS) curve for CCl_3^+ (figure 5.7) at ~ 20 eV corresponds closely to the energy positions of additional peaks observed in the relative partial electronic ion state oscillator strength spectra for the $2t_1^{-1}$ and $7t_2^{-1}$ states in solid CCl_4 [206]. These maxima have been assigned [203] to shape resonance channels. The present observations concerning the production of CCl_3^+ are in good agreement with PEPICO studies [226], where it was found that the CCl_3^+ cation was produced by ionization from the $2t_1^{-1}$, $7t_2^{-1}$, and $2e^{-1}$ states. Contributions to the CCl_3^+ cation from the $2t_1^{-1}$, $7t_2^{-1}$, and $2e^{-1}$ states have also been suggested by charge-exchange mass spectroscopy experiments [236].

The appearance potential (AP) of the CCl_3^{2+} dication is ~ 32 eV, which is above the highest valence-shell VIP of CCl_4 . It is reasonable to assume that doubly charged ions are formed directly by single photon absorption and not *via* singly ionized electronic states. Therefore the production of the CCl_3^{2+} dication has not been attributed to ionization from any of the valence-shell states.

The CCl_2^+ cation has an AP of 13.5 eV, which, along with the shape of the partial oscillator strength curve for this ion (figure 5.7), indicates a very small contribution from the $2e^{-1}$ state. The major increase in the POS curve of CCl_2^+ at ~ 16 eV suggests a dominant contribution to the CCl_2^+ POS from the $6t_2^{-1}$ state. From an examination of the branching ratio curve for the CCl_2^+ cation, and the small shoulder in the POS curve for CCl_2^+ at ~ 25 eV, these features are perhaps attributable to a contribution from the

$5t_2^{-1}$ state and possibly also from the $5a_1^{-1}$ state. The PEPICO experiments [226] confirm a contribution to the production of CCl_2^+ from the $6t_2^{-1}$ state.

The AP of the CCl^+ cation at ~ 17 eV, and the shape of the POS curve for this ion, suggest that a small portion of CCl^+ comes from the $6t_2^{-1}$ state. However, the steep rise in the POS at ~ 20 eV clearly indicates that the dominant contribution to the CCl^+ POS comes from the $6a_1^{-1}$ state. The PEPICO experiments [226] confirm that the CCl^+ cation is formed dominantly from the $6a_1^{-1}$ state, and the relative intensity of this contribution is quoted [226] as about one-half of the $6t_2^{-1}$ state contribution to the POS for CCl_2^+ , which is in good agreement with the present work (see figure 5.7).

The Cl^+ cation has an AP of 19 eV which suggests a contribution to the production of this ion from the $6a_1^{-1}$ state. The POS curve (figure 5.7) for this ion shows a change in slope at ~ 25 eV which suggests a further major contribution from the $5t_2^{-1}$ state. The Cl_2^+ and C^+ cations have very similar APs (~ 24 eV) which suggest contributions to the production of these ions from the $5t_2^{-1}$ state although contributions from the $5a_1^{-1}$ state (which is close in energy) cannot be discounted. It should be noted that the shapes of the POSs for these two ions are somewhat different on their leading edges. The shape of the POS curve for the Cl_2^+ cation suggests a contribution from each of the $5t_2^{-1}$ and $5a_1^{-1}$ states, whereas the dominant contribution to the POS for C^+ apparently comes from the $5a_1^{-1}$. This is logical since the AP of the C^+ cation is at the high-energy side of the Franck-Condon region of the $5t_2^{-1}$ state, and thus any contribution from this electronic ion state will likely be small.

The principle contributions from the different electronic ion states to the various ionic photofragmentation products of CCl_4 suggested by the above analysis are summarized in the proposed dipole breakdown scheme shown in figure 5.8.

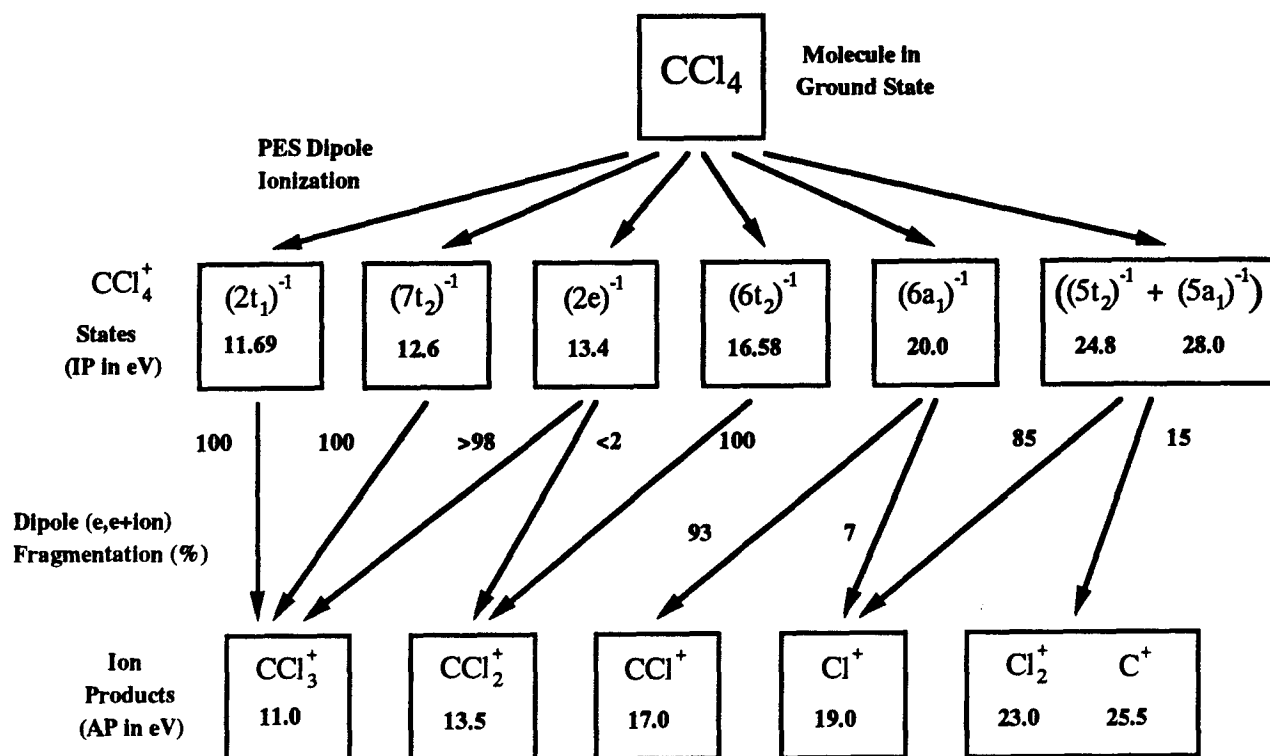


Figure 5.8: The principle dipole-induced breakdown pathways following valence-shell photoionization of CCl_4 below 80 eV.

In summary, the above considerations suggest that

1. The $(2t_1)^{-1}$, $(7t_2)^{-1}$, and essentially all of the $(2e)^{-1}$ electronic ion states of CCl_4^+ dissociate to give CCl_3^+ as the only charged product.
2. Almost all of the CCl_2^+ is formed from the $(6t_2)^{-1}$ state.
3. The $(6a_1)^{-1}$ state dissociates to give essentially all the CCl^+ and part (8%) of the Cl^+ .
4. The Cl_2^+ and C^+ cations and the remaining portion (92%) of the Cl^+ cation are formed from processes involving the breakdown of the $(5t_2)^{-1}$ and $(5a_1)^{-1}$ states. Therefore this oscillator strength sum $(\text{Cl}_2^+ + \text{C}^+ + 0.92\text{Cl}^+)$ provides an estimate of the summed inner-valence $(5t_2 + 5a_1)$ electronic ion state partial oscillator strengths. This estimate has been used (see above) in the calculation of the electronic ion state partial oscillator strengths from the previously published PES data [202, 206].

These findings are illustrated by the oscillator strength sum comparisons shown in figure 5.9. It can be seen that quite good agreement exists for CCl_3^+ and CCl_2^+ with the respective electronic ion state oscillator strength sums. The situation is less satisfactory in the case of $(6a_1)^{-1}$ (see figure 5.9). In the case of the present estimate for the electronic ion state partial oscillator strength sum $(5t_2 + 5a_1)$ it should be noted that the resulting shape is consistent with expectations for inner-valence orbitals having large Cl 3s and C 2s contributions. In making these comparisons it should be noted that the electronic ion state partial oscillator strengths from Fock and Koch [206] are for solid and not gaseous CCl_4 and thus some shape differences might be expected. In addition, the proposed dipole breakdown scheme should only be regarded as a first approximation reflecting the

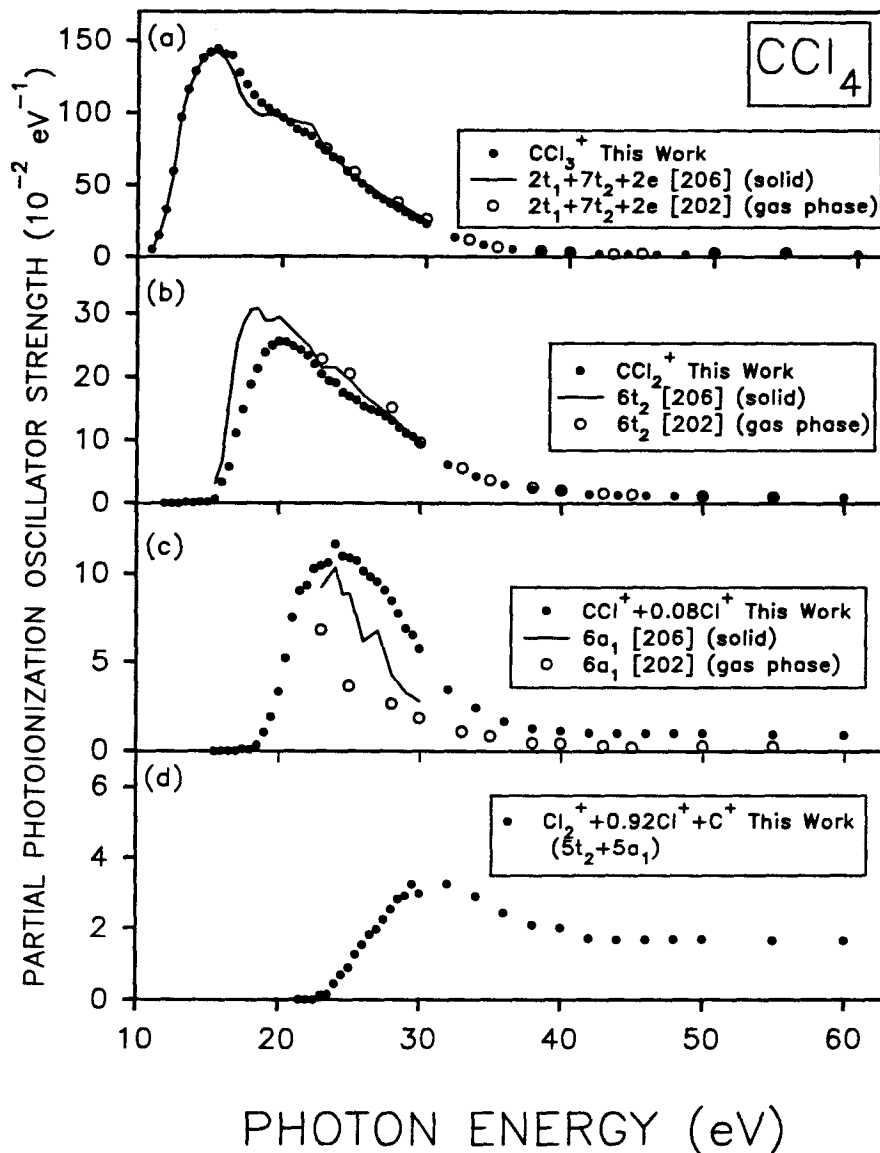


Figure 5.9: Oscillator strengths sums determined from the proposed dipole-induced breakdown scheme for CCl_4 below 80 eV (see figure 5.8 and section 5.2.4 for details). The presently measured absolute partial photoionization oscillator strength sums are compared with electronic ion state oscillator strength sums determined from the PES measurements reported by Fock and Koch [206] (solid line) for a solid film of CCl_4 and by Carlson *et al.* [202] (open circles) for gas phase CCl_4 . It should be noted that the electronic ion state data of references [202, 206] have been reanalyzed as branching ratios including the inner-valence contributions as derived from the present measurements. These revised electronic ion state branching ratio data have then been placed on an absolute photoionization oscillator strength scale by using the presently measured absolute photoabsorption data (see text for details).

major breakdown processes. Undoubtedly there are other smaller contributions to the various breakdown channels and a more detailed understanding can be provided only by high-resolution photoelectron-photoion and photoion-photoion coincidence experiments.

5.2.4.2 The Dissociative Photoionization of CCl_4 in the Cl 2p Inner-Shell Region

Time-of-flight mass spectra (figure 5.10) have been recorded at 195.5 eV (valence-shell continuum, below the Cl 2p edge), 200.5 eV (Cl 2p $\rightarrow \sigma^*$ excitation), 205.5 eV (2p \rightarrow Rydberg excitation), and at 210.5, 215.5, and 220.5 eV in the (Cl 2p) $^{-1}$ ionization continuum, in order to investigate the changes in the dipole-induced breakdown in going from valence-shell ionization to Cl 2p excitation and ionization. It can be seen (figure 5.11) that significant changes in the fragmentation pattern occur particularly with regard to the increased relative yields (see also the branching ratios in figure 5.6) of Cl^+ and C^+ and also in the significant increase in the yield of CCl_3^+ in the inner-shell region. The branching ratio (figure 5.6, table 5.5) and partial oscillator strength (figure 5.11, table 5.6) data for the ionic photofragmentation products of CCl_4 measured in the vicinity of the Cl 2p edge provide information on the dipole-induced breakdown of CCl_4 in the Cl 2p inner-shell energy region. It has been assumed that the absolute photoionization efficiency is 1.0 throughout the 195–220 eV energy region. From figure 5.6 it can be noted that the branching ratio curves from 195–220 eV for the dissociative fragment ions can be grouped into three classes, depending on their trend as the photon energy increases: (1) ions whose branching ratio curves markedly decrease relative to the valence-shell contribution (CCl_3^+), (2) ions whose branching ratio curves remain approximately constant (CCl_2^+ , Cl_2^+ , and CCl^+), and (3) ions whose branching ratio curves increase (CCl_3^{2+} , Cl^+ ,

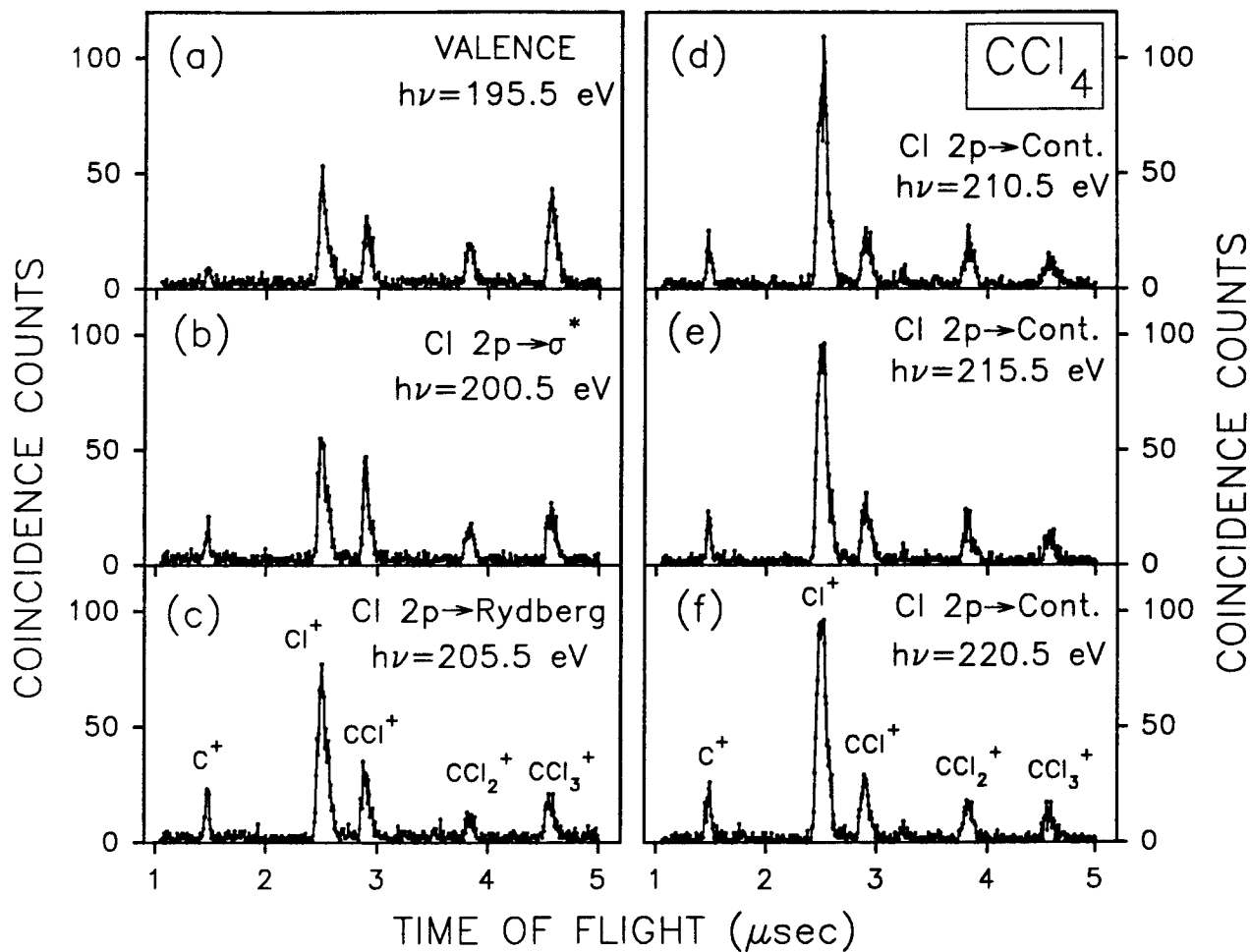


Figure 5.10: Time-of-flight mass spectra measured in the vicinity of the Cl 2p edge of CCl_4 : (a) in the valence-shell region at 195.5 eV; (b) in the region of discrete excitation at 200.5 eV; (c) in the region of discrete (Rydberg) excitation at 205.5 eV; (d), (e), and (f) at 210.5, 215.5 and 220.5 eV, respectively, in the ionization continuum region above the Cl 2p edge at ~ 208 eV.

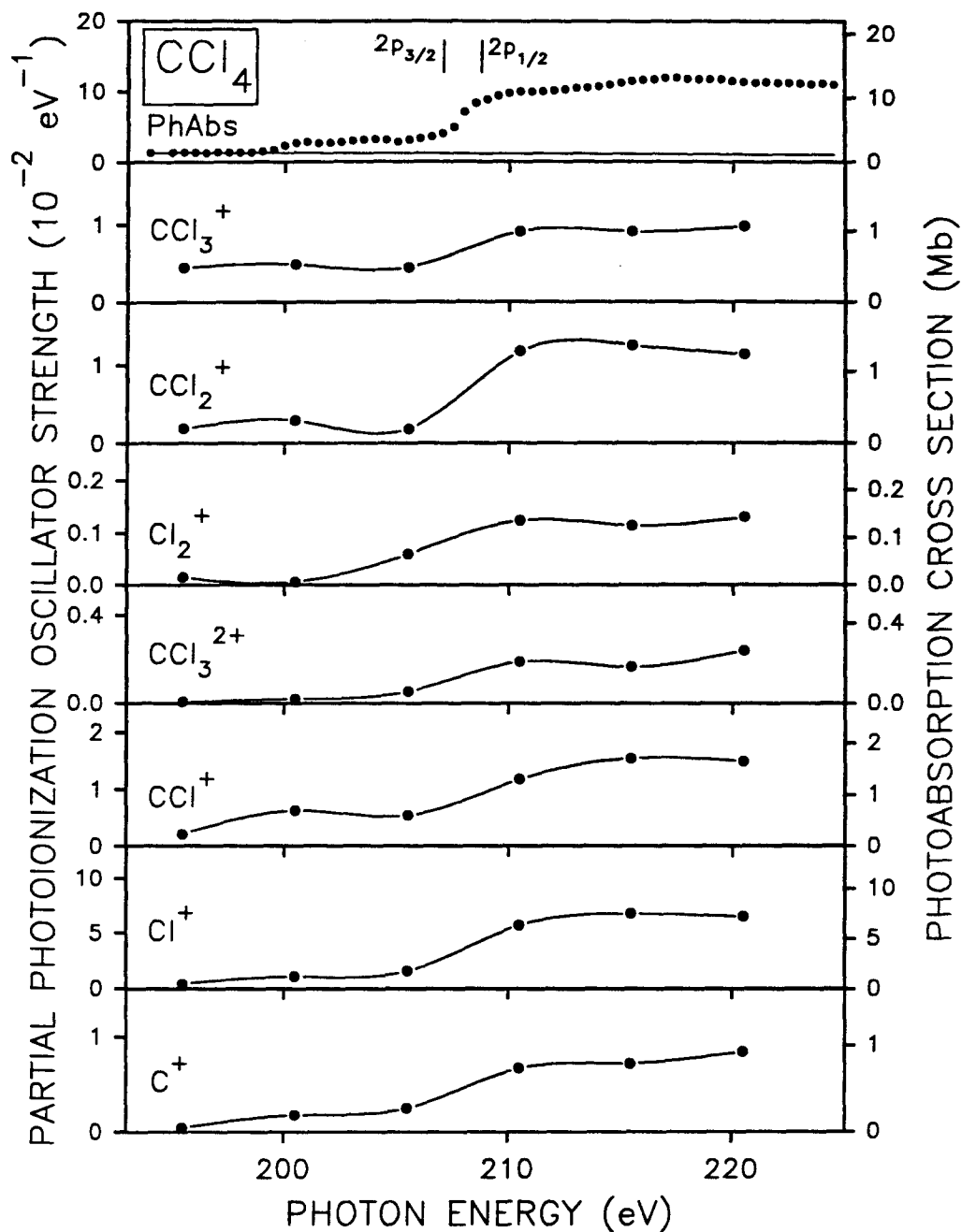


Figure 5.11: Absolute partial photoionization oscillator strengths (cross sections) for the dissociative photoionization of CCl_4 in the Cl 2p region from 195.5–220.5 eV (see table 5.6). The top panel shows the total (valence plus Cl 2p) absolute oscillator strength spectrum from 194–224 eV. The solid line in the top panel represents the fit to the valence-shell region from 98–198 and gives an indication of the valence-shell contribution in the 195–220 eV region. The vertical lines in the top panel indicate the positions of the Cl 2p VIPs [214].

and C^+). These trends indicate that in general, as the photon energy is increased to access the Cl 2p inner-shell excitation and ionization regions, the production of low m/e , and multiply charged cationic fragments is favoured over the production of larger, higher m/e cations. For example, in the 11–40 eV region (see figure 5.6) the dominant ion is CCl_3^+ , however in the 195–220 eV region the dominant ion is Cl^+ .

When analyzing the partial oscillator strength data from 200–220 eV it should be remembered that the ions detected in the TOF mass spectrum can be produced by excitations in both the Cl 2p region and the underlying valence-shell continuum region. However, the contribution from the underlying valence-shell continuum is quite small and, as shown in the top panel of figure 5.11 (and figure 5.3b), comprises only $\sim 10\%$ of the total photoabsorption at 220 eV. The partial oscillator strength curves for all the fragment ions show an increase over the 195.5–220.5 eV region. However, the CCl_3^+ cation shows the smallest relative increase with approximately 50% of the ion intensity at higher energies still coming from the underlying valence-shell continuum. The POS distributions for the other ions (CCl_2^+ , Cl_2^+ , CCl_3^{2+} , CCl^+ , Cl^+ , and C^+) each show much more pronounced increases as the photon energy increases through the Cl 2p region.

At 200.5 eV, in the region of the Cl 2p $\rightarrow \sigma^*$ virtual valence orbital excitation [192, 193] local increases in ion yield are observed for all ions except Cl_2^+ and possibly CCl_3^+ with local enhancements due to fragmentation from the σ^* excited state being particularly noticeable for CCl_2^+ and CCl^+ . Whereas only minor further differences in fragmentation are observed in the region of Cl 2p \rightarrow Rydberg excitation at 205.5 eV, very significant changes occur above the (Cl 2p) $^{-1}$ ionization edges as can be seen from the data points (figure 5.11) at 210.5, 215.5, and 220.5 eV. In considering both the POS (figure 5.11) and branching ratio (figure 5.6) curves above the (Cl 2p) $^{-1}$ edge it can be seen that

the dominant product consists of Cl^+ atomic cations which are (table 5.6) more than 15 times as intense as in the valence-shell region at 195.5 eV. While the absolute intensities are lower, similar large relative increases in intensity are also observed above 210 eV for CCl_2^+ , Cl_2^+ , CCl_3^{2+} , CCl^+ , and C^+ . The large yield of Cl^+ reflects the strong tendency for the decomposition of the Cl 2p hole to involve further carbon-chlorine bond breaking since CCl_3^+ is the most abundant species (in the absence of the molecular ion CCl_4^+) throughout the valence-shell region. The large relative increase in the yield of CCl_3^{2+} above the $(\text{Cl } 2p)^{-1}$ edge (figure 5.11) can be attributed to Auger decay processes. The much lower yield of doubly charged ions (see also figure 5.11) from the $\text{Cl } 2p \rightarrow \sigma^*$ excited state at 205.5 eV is consistent with earlier findings for core excited molecules which have been found to preferentially decay to singly charged products [237] *via* participator or spectator resonance Auger processes [238–240].

Table 5.1: Absolute oscillator strengths for the total photoabsorption (5.5–195 eV) and the dissociative photoionization (11–80 eV) of CCl₄.

Photon Energy eV	Oscillator Strength ($10^{-2}eV^{-1}$) ^a								Photoionization Efficiency η_i
	Photo-absorption	C ⁺	Cl ⁺	CCl ⁺	CCl ₃ ²⁺	Cl ₂ ⁺	CCl ₂ ⁺	CCl ₃ ⁺	
5.5	1.65								
6.0	1.76								
6.5	3.53								
7.0	5.74								
7.5	7.02								
8.0	11.64								
8.5	26.87								
9.0	60.08								
9.5	75.10								
10.0	53.94								
10.5	49.35								
11.0	63.39							5.06	0.08
11.5	74.17							14.76	0.20
12.0	87.67							33.02	0.38
12.5	104.5							59.52	0.57
13.0	133.8							96.77	0.72
13.5	153.8						0.13	116.4	0.76

Table 5.1: (continued) Absolute oscillator strengths for the total photoabsorption (5.5–195 eV) and the dissociative photoionization (11–80 eV) of CCl₄.

Photon Energy eV	Oscillator Strength (10^{-2}eV^{-1}) ^a								Photo- ionization Efficiency η_i
	Photo- absorption	C ⁺	Cl ⁺	CCl ⁺	CCl ₃ ²⁺	Cl ₂ ⁺	CCl ₂ ⁺	CCl ₃ ⁺	
14.0	165.9						0.03	129.1	0.78
14.5	170.7						0.20	137.9	0.81
15.0	167.8						0.21	141.7	0.85
15.5	164.5						0.68	144.3	0.88
16.0	166.0						3.30	140.8	0.87
16.5	155.2						5.76	140.0	0.94
17.0	151.9			0.02			11.10	127.9	0.92
17.5	144.7			0.12			14.87	119.4	0.93
18.0	131.0			0.10			18.73	112.2	1.00 ^b
18.5	128.6			0.32			21.25	107.1	
19.0	128.1		0.12	0.91			23.80	103.3	
19.5	126.7		0.13	1.80			24.97	99.82	
20.0	125.6		0.18	3.16			25.51	96.74	
20.5	124.3		0.37	4.87			25.50	93.53	
21.0	121.1		0.46	7.06			24.89	88.72	
21.5	119.7		0.61	8.44			24.28	86.40	
22.0	116.5		0.43	8.93			23.39	83.73	

Table 5.1: (continued) Absolute oscillator strengths for the total photoabsorption (5.5–195 eV) and the dissociative photoionization (11–80 eV) of CCl_4 .

Photon Energy eV	Oscillator Strength (10^{-2}eV^{-1}) ^a								Photo- ionization Efficiency η_i
	Photo- absorption	C^+	Cl^+	CCl^+	CCl_3^{2+}	Cl_2^+	CCl_2^+	CCl_3^+	
22.5	110.3		0.66	9.63			21.95	78.04	
23.0	104.8		0.78	9.80		0.04	20.44	73.78	
23.5	99.56		0.85	9.96		0.00	19.40	69.35	
24.0	98.07		1.13	10.92		0.08	19.04	66.90	
24.5	88.48		1.34	10.29		0.07	17.42	59.36	
25.0	83.73		1.54	10.20		0.08	16.86	55.05	
25.5	79.32	0.08	1.81	10.07		0.09	16.34	50.92	
26.0	73.53	0.10	1.97	9.48		0.12	15.39	46.46	
26.5	69.29	0.15	2.16	9.20		0.15	14.87	42.76	
27.0	65.78	0.23	2.27	8.93		0.08	14.40	39.87	
27.5	62.06	0.31	2.38	8.46		0.15	13.73	37.01	
28.0	58.10	0.44	2.49	7.92		0.15	13.06	34.05	
28.5	53.52	0.53	2.63	7.24		0.15	12.03	30.94	
29.0	48.63	0.58	2.58	6.45		0.20	11.07	27.75	
29.5	46.45	0.67	2.78	6.12		0.23	10.56	26.09	
30.0	40.79	0.62	2.56	5.36		0.16	9.31	22.78	
32.0	26.37	0.55	2.78	3.21	0.05	0.15	6.09	13.54	

Table 5.1: (continued) Absolute oscillator strengths for the total photoabsorption (5.5–195 eV) and the dissociative photoionization (11–80 eV) of CCl₄.

Photon Energy eV	Oscillator Strength ($10^{-2}eV^{-1}$) ^a								Photoionization Efficiency η_i	
	Photo-absorption	C ⁺	Cl ⁺	CCl ⁺	CCl ₂ ⁺	CCl ₃ ⁺	Cl ₂ ⁺	CCl ₂ ⁺		CCl ₃ ⁺
180.0	1.55									
185.0	1.47									
190.0	1.41									
195.0	1.34									

^a $\sigma(\text{Mb})=109.75df/dE(eV^{-1})$.

^bThe photoionization efficiency is normalized to unity above 18.0 eV. See text for details.

Table 5.2: Absolute oscillator strengths for the total photoabsorption in the inner-shell region (Cl 2p, 2s; C 1s) of CCl₄ from 195 to 400 eV.

Photon Energy eV	Oscillator Strength (10 ⁻² eV ⁻¹) ^a			Photon Energy eV	Oscillator Strength (10 ⁻² eV ⁻¹) ^a		
	Total	Valence	Cl 2p + Cl 2s + C 1s		Total	Valence	Cl 2p + Cl 2s + C 1s
195.0	1.34	1.34		205.5	3.11	1.24	1.87
196.0	1.33	1.33		206.0	3.27	1.23	2.04
197.0	1.33	1.33		206.5	3.57	1.23	2.34
198.0	1.34	1.32	0.02 ^b	207.0	4.02	1.22	2.80
198.5	1.35	1.31	0.03	207.5	4.92	1.22	3.71
199.0	1.47	1.31	0.17	208.0	7.11	1.21	5.90
199.5	1.68	1.30	0.37	208.5	8.33	1.21	7.12
200.0	2.34	1.30	1.05	209.0	8.86	1.20	7.66
200.5	2.72	1.29	1.43	209.5	9.38	1.20	8.18
201.0	2.82	1.28	1.53	210.0	9.76	1.19	8.57
201.5	2.67	1.28	1.39	210.5	9.98	1.19	8.79
202.0	2.71	1.27	1.43	211.0	9.98	1.18	8.80
202.5	2.77	1.27	1.50	211.5	9.96	1.18	8.78
203.0	2.98	1.26	1.72	212.0	10.08	1.17	8.91
203.5	3.13	1.26	1.88	212.5	10.27	1.17	9.11
204.0	3.21	1.25	1.95	213.0	10.41	1.16	9.24
204.5	3.10	1.25	1.86	213.5	10.56	1.16	9.40
205.0	2.82	1.24	1.58	214.0	10.68	1.15	9.53

Table 5.2: (continued) Absolute oscillator strengths for the total photoabsorption in the inner-shell region (Cl 2p, 2s; C 1s) of CCl₄ from 195 to 400 eV.

Photon Energy eV	Oscillator Strength (10 ⁻² eV ⁻¹) ^a			Photon Energy eV	Oscillator Strength (10 ⁻² eV ⁻¹) ^a		
	Total	Valence	Cl 2p + Cl 2s + C 1s		Total	Valence	Cl 2p + Cl 2s + C 1s
214.5	11.01	1.15	9.86	223.5	11.12	1.07	10.04
215.0	11.21	1.15	10.07	224.0	11.16	1.07	10.09
215.5	11.48	1.14	10.34	224.5	11.08	1.06	10.02
216.0	11.65	1.14	10.52	225.0	11.02	1.06	9.96
216.5	11.81	1.13	10.68	225.5	10.91	1.06	9.86
217.0	11.97	1.13	10.84	226.0	10.92	1.05	9.87
217.5	12.00	1.12	10.88	228.0	10.68	1.04	9.64
218.0	11.87	1.12	10.76	230.0	10.58	1.02	9.56
218.5	11.75	1.11	10.63	232.0	10.52	1.01	9.52
219.0	11.80	1.11	10.69	234.0	10.46	0.99	9.47
219.5	11.77	1.11	10.66	236.0	10.26	0.98	9.29
220.0	11.55	1.10	10.45	238.0	10.10	0.96	9.14
220.5	11.38	1.10	10.28	240.0	10.00	0.95	9.05
221.0	11.28	1.09	10.18	242.0	9.84	0.93	8.90
221.5	11.38	1.09	10.29	244.0	9.67	0.92	8.75
222.0	11.24	1.08	10.15	246.0	9.42	0.91	8.51
222.5	11.31	1.08	10.23	248.0	9.34	0.90	8.45
223.0	11.22	1.08	10.15	250.0	9.27	0.88	8.39

Table 5.2: (continued) Absolute oscillator strengths for the total photoabsorption in the inner-shell region (Cl 2p, 2s; C 1s) of CCl₄ from 195 to 400 eV.

Photon Energy eV	Oscillator Strength (10 ⁻² eV ⁻¹) ^a			Photon Energy eV	Oscillator Strength (10 ⁻² eV ⁻¹) ^a		
	Total	Valence	Cl 2p + Cl 2s + C 1s		Total	Valence	Cl 2p + Cl 2s + C 1s
252.0	9.16	0.87	8.28	288.0	8.74	0.69	8.05
254.0	9.17	0.86	8.31	288.5	8.67	0.69	7.98
256.0	9.20	0.85	8.35	289.0	9.50	0.69	8.82
258.0	9.17	0.84	8.34	289.5	11.38	0.68	10.70
260.0	9.26	0.82	8.43	290.0	13.15	0.68	12.47
262.0	9.17	0.81	8.36	290.5	15.36	0.68	14.68
264.0	9.28	0.80	8.48	291.0	14.33	0.68	13.65
266.0	9.35	0.79	8.55	291.5	12.49	0.68	11.81
268.0	9.43	0.78	8.65	292.0	10.02	0.67	9.35
270.0	9.68	0.77	8.91	292.5	9.24	0.67	8.57
272.0	9.75	0.76	8.98	293.0	8.98	0.67	8.31
274.0	9.17	0.75	8.42	293.5	8.63	0.67	7.96
276.0	9.26	0.74	8.52	294.0	8.60	0.67	7.93
278.0	9.28	0.73	8.54	294.5	8.63	0.66	7.97
280.0	9.15	0.72	8.43	295.0	8.82	0.66	8.16
282.0	8.96	0.72	8.24	295.5	8.81	0.66	8.15
284.0	8.87	0.71	8.17	296.0	9.07	0.66	8.41
286.0	8.78	0.70	8.08	296.5	9.02	0.66	8.36

Table 5.2: (continued) Absolute oscillator strengths for the total photoabsorption in the inner-shell region (Cl 2p, 2s; C 1s) of CCl₄ from 195 to 400 eV.

Photon Energy eV	Oscillator Strength (10 ⁻² eV ⁻¹) ^a			Photon Energy eV	Oscillator Strength (10 ⁻² eV ⁻¹) ^a		
	Total	Valence	Cl 2p + Cl 2s + C 1s		Total	Valence	Cl 2p + Cl 2s + C 1s
297.0	8.95	0.65	8.30	319.0	7.91	0.58	7.33
297.5	9.03	0.65	8.38	320.0	7.89	0.57	7.32
298.0	9.19	0.65	8.54	325.0	7.61	0.56	7.05
298.5	9.10	0.65	8.45	330.0	7.28	0.54	6.73
299.0	9.12	0.65	8.47	335.0	7.15	0.53	6.62
299.5	9.16	0.64	8.52	340.0	6.91	0.52	6.39
300.0	8.80	0.64	8.16	345.0	6.76	0.50	6.26
301.0	9.10	0.64	8.46	350.0	6.68	0.49	6.19
302.0	9.05	0.63	8.42	355.0	6.48	0.48	6.00
303.0	9.17	0.63	8.54	360.0	6.40	0.47	5.94
304.0	9.09	0.63	8.46	365.0	6.33	0.46	5.88
305.0	8.99	0.62	8.37	370.0	6.08	0.44	5.64
306.0	8.92	0.62	8.30	375.0	6.00	0.43	5.56
307.0	8.70	0.62	8.09	380.0	5.80	0.42	5.38
308.0	8.56	0.61	7.94	385.0	5.57	0.41	5.15
309.0	8.29	0.61	7.68	390.0	5.45	0.41	5.04
310.0	8.38	0.61	7.77	395.0	5.25	0.40	4.85
311.0	8.36	0.60	7.76	400.0	5.15	0.39	4.76
312.0	8.38	0.60	7.78				

Table 5.2: (continued) Absolute oscillator strengths for the total photoabsorption in the inner-shell region (Cl 2p, 2s; C 1s) of CCl₄ from 195 to 400 eV.

Photon Energy eV	Oscillator Strength (10 ⁻² eV ⁻¹) ^a		
	Total	Valence	Cl 2p + Cl 2s + C 1s
313.0	8.26	0.60	7.66
314.0	8.29	0.59	7.70
315.0	8.24	0.59	7.65
316.0	8.16	0.59	7.58
317.0	8.13	0.58	7.55
318.0	7.96	0.58	7.38

^a $\sigma(\text{Mb})=109.75df/dE(\text{eV}^{-1})$.^bThe valence-shell contribution above 198 eV was obtained by extrapolating the fit to the valence shell spectrum (98–198 eV) to higher photon energies. The inner-shell (Cl 2p + Cl 2s + C 1s) contribution was obtained by subtracting the valence-shell contribution from the total (valence- plus inner-shell) photoabsorption oscillator strength.

Table 5.3: Branching ratios for the dissociative photoionization of CCl_4 from 11.0 to 80.0 eV.

Photon Energy eV	Photoionization Branching Ratio (%)						
	C^+	Cl^+	CCl^+	CCl_3^+	Cl_2^+	CCl_2^+	CCl_3^+
11.0							100.00
11.5							100.00
12.0							100.00
12.5							100.00
13.0							100.00
13.5						0.11	99.89
14.0						0.02	99.98
14.5						0.14	99.86
15.0						0.15	99.85
15.5						0.47	99.53
16.0						2.29	97.71
16.5						3.95	96.05
17.0			0.02			7.98	92.00
17.5			0.09			11.07	88.84
18.0			0.08			14.30	85.63
18.5			0.25			16.52	83.23
19.0	0.10	0.71				18.58	80.61

Table 5.3: (continued) Branching ratios for the dissociative photoionization of CCl_4 .

Photon Energy eV	Photoionization Branching Ratio (%)						
	C^+	Cl^+	CCl^+	CCl_3^+	Cl_2^+	CCl_2^+	CCl_3^+
19.5		0.10	1.42			19.71	78.77
20.0		0.14	2.52			20.31	77.03
20.5		0.30	3.92			20.52	75.26
21.0		0.38	5.83			20.55	73.24
21.5		0.51	7.05			20.28	72.16
22.0		0.37	7.66			20.08	71.88
22.5		0.60	8.73			19.91	70.76
23.0		0.75	9.35		0.04	19.50	70.37
23.5		0.85	10.01		0.00	19.49	69.65
24.0		1.15	11.13		0.08	19.41	68.22
24.5		1.52	11.63		0.08	19.69	67.09
25.0		1.84	12.19		0.09	20.14	65.74
25.5	0.10	2.29	12.70		0.12	20.60	64.19
26.0	0.14	2.68	12.89		0.16	20.94	63.19
26.5	0.21	3.11	13.28		0.22	21.47	61.70
27.0	0.35	3.46	13.57		0.13	21.88	60.60
27.5	0.51	3.84	13.64		0.25	22.12	59.65

Table 5.3: (continued) Branching ratios for the dissociative photoionization of CCl_4 .

Photon Energy eV	Photoionization Branching Ratio (%)						
	C^+	Cl^+	CCl^+	CCl_3^{2+}	Cl_2^+	CCl_2^+	CCl_3^+
28.0	0.75	4.28	13.63		0.26	22.48	58.60
28.5	0.99	4.92	13.52		0.29	22.47	57.80
29.0	1.19	5.31	13.27		0.41	22.77	57.06
29.5	1.43	5.98	13.18		0.50	22.73	56.17
30.0	1.51	6.28	13.15		0.40	22.82	55.84
32.0	2.07	10.55	12.18	0.18	0.58	23.11	51.34
34.0	2.36	13.98	12.55	0.35	0.58	23.52	46.65
36.0	2.32	17.12	12.62	0.49	0.95	24.32	42.18
38.0	2.53	20.90	13.41	0.54	0.80	24.78	37.05
40.0	2.55	24.15	14.09	0.77	0.79	24.60	33.07
42.0	2.50	26.27	15.57	0.56	0.63	23.77	30.69
44.0	2.35	27.60	16.21	0.62	0.57	23.03	29.61
46.0	2.22	28.07	16.32	0.56	0.69	22.28	29.87
48.0	2.66	28.35	16.53	0.40	0.56	21.60	29.90
50.0	2.74	27.67	16.78	0.52	1.05	20.44	30.81
55.0	2.58	28.69	15.99	0.26	0.62	18.41	33.45
60.0	2.87	28.54	15.86	0.67	0.89	17.15	34.02

Table 5.3: (continued) Branching ratios for the dissociative photoionization of CCl_4 .

Photon Energy eV	Photoionization Branching Ratio (%)						
	C^+	Cl^+	CCl^+	CCl_2^+	CCl_3^+	CCl_2^{2+}	CCl_3^{2+}
65.0	2.97	29.40	15.04	0.59	0.90	16.38	34.73
70.0	2.84	29.89	15.26	0.56	0.87	15.90	34.69
75.0	3.28	30.30	14.67	0.82	0.38	15.07	35.48
80.0	3.01	30.30	15.23	0.65	0.65	14.87	35.31

Table 5.4: Calculated and measured appearance potentials for the production of positive ions from CCl₄.

Products	Appearance Potential (eV)									
	Calculated ^a	This Work ±1 eV	EI [215]	EI [216]	EI [218]	Experimental [ref.] ^b EI [219]	EI [220]	PhIon [221, 241] ^c	PhIon [222]	EI [227]
(1) CCl ₄ ⁺	11.47	—	11.0±1.0				—			11.5±0.1
(2) CCl ₃ ⁺ + Cl	10.84	11.0	12.2±0.2	11.83±0.05	11.67±0.1	11.90±0.07	11.65±0.10	11.47±0.01	11.28±0.03	11.6±0.3
(3) CCl ₂ ⁺ + Cl ₂	13.04	13.5								
(4) CCl ₂ ⁺ + 2Cl	15.52	16.0	16.0±0.2	16.10±0.01		16.10±0.02				
(5) Cl ₂ ⁺ + CCl ₂	14.16		16.4±0.5							
(6) Cl ₂ ⁺ + CCl + Cl	17.69									
(7) Cl ₂ ⁺ + C + Cl ₂	19.84									
(8) Cl ₂ ⁺ + C + 2Cl	22.32	23.0	23.0±1.0							
(9) CCl ₃ ²⁺	—	32.0	31.8±1.0							
(10) CCl ₂ ⁺ + Cl ₂ + Cl	15.11									
(11) CCl ₂ ⁺ + 3Cl	17.59	17.0 19.0	17.1±0.2 19.5±0.2	19.3±0.02		19.35±0.05				
(12) CCl ₂ ²⁺	—	—	34.0±1.0							
(13) Cl ⁺ + CCl ₃	16.01						16.10±0.2			
(14) Cl ⁺ + CCl ₂ + Cl	18.12									
(15) Cl ⁺ + CCl + Cl ₂	19.17	19.0	19.1±0.2							
(16) Cl ⁺ + CCl + 2Cl	21.65									
(17) Cl ⁺ + C + Cl + Cl ₂	23.80	23.5								
(18) Cl ⁺ + C + 3Cl	26.28									
(19) C ⁺ + 2Cl ₂	19.62									
(20) C ⁺ + Cl ₂ + 2Cl	22.09		23.5±0.2			23.05±0.07				
(21) C ⁺ + 4Cl	24.57	25.5								

^aValues calculated using thermodynamic data for the enthalpy of formation of ions and neutrals (taken from Lias *et al.* [169]), and assuming zero kinetic energy of fragmentation.

^bMeasured using electron impact (EI) or photoionization (PhIon) methods.

^cReported as IP of CCl₄⁺.

Table 5.5: Branching ratios for the dissociative photoionization of CCl_4 from 195.5 to 220.5 eV.

Photon Energy eV	Photoionization Branching Ratio (%)						
	C^+	Cl^+	CCl^+	CCl_3^{2+}	Cl_2^+	CCl_2^+	CCl_3^+
195.5	3.32	32.38	16.18	0.53	1.09	13.57	32.94
200.5	6.62	40.32	23.34	0.75	0.23	10.79	17.95
205.5	8.08	50.51	17.64	1.70	1.93	5.87	14.28
210.5	6.74	57.37	11.91	1.89	1.25	11.73	9.11
215.5	6.29	59.02	13.53	1.43	1.00	10.84	7.90
220.5	7.44	57.55	13.25	2.11	1.14	9.94	8.57

Table 5.6: Absolute oscillator strengths for the total photoabsorption and the dissociative photoionization of CCl_4 from 195.5 to 220.5 eV^a.

Photon Energy eV	Photo-absorption	Oscillator Strength (10^{-2}eV^{-1}) ^b						
		C^+	Cl^+	CCl^+	CCl_3^{2+}	Cl_2^+	CCl_2^+	CCl_3^+
195.5	1.36	0.05	0.44	0.22	0.01	0.01	0.18	0.45
200.5	2.72	0.18	1.10	0.64	0.02	0.01	0.29	0.49
205.5	3.11	0.25	1.57	0.55	0.05	0.06	0.18	0.44
210.5	9.98	0.67	5.72	1.19	0.19	0.12	1.17	0.91
215.5	11.48	0.72	6.78	1.55	0.16	0.11	1.24	0.91
220.5	11.38	0.85	6.55	1.51	0.24	0.13	1.13	0.98

^a Assuming a photoionization efficiency of unity.^b $\sigma(\text{Mb}) = 109.75 df/dE (\text{eV}^{-1})$.

Chapter 6

Photoabsorption and DOSD Studies of Ammonia

6.1 Introduction

Ammonia has been observed in the interstellar medium, molecular clouds [103, 104], and in the atmospheres of Saturn and Jupiter [242] and is of importance in photochemistry, being a low energy source of NH_2 and NH radicals [243]. Therefore the absolute photoabsorption oscillator strengths (cross sections) for NH_3 over the entire electromagnetic spectrum, and the related dipole properties, are of interest to astrophysicists and others wishing to model the interaction of energetic radiation and particles with this molecule. There is also considerable interest in the possibility of using additivity concepts and mixture rules to estimate the quantitative aspects of the interaction of energetic electromagnetic radiation with large and complex molecules and to evaluate the properties of these molecules from those of smaller, related species [54, 55, 244–246]. Therefore the present analysis for NH_3 will be used to provide a foundation which will be extended in chapter 7 to include the absolute photoabsorption oscillator strength distributions and dipole properties for monomethylamine (methanamine), dimethylamine (N-methylmethanamine), trimethylamine (N,N-dimethylmethanamine) and subsequent work involving the higher n-alkylamines. By comparing the oscillator strength distributions and dipole properties of ammonia and the methylamines an indication of the effect on the oscillator strength distribution, and the dipole properties, of adding methyl or

amino groups to larger molecules can be assessed.

There is a wealth of spectroscopic information available in the literature regarding the electronic excitation of ammonia [16, 180, 247–284]. However most of these studies have been concerned with energy levels and only a few have reported measurements of the absolute transition probabilities (oscillator strengths) for photoabsorption. Seven excited states (labelled \tilde{A} to \tilde{G}) have been observed in the discrete valence-shell electronic spectrum of NH_3 as studied by single photon absorption [285]. The energies of the various vibronic transitions within these bands have been determined using very high resolution optical absorption spectroscopy [180, 247–258]. In more recent work, multiphoton ionization has been used to show the existence of other less intense lines (labelled with primes) which lie beneath the stronger absorption lines in the same energy regions [262–265]. In other work, electron energy loss spectroscopy (EELS) has been used to study the valence-shell discrete excitation region of ammonia [16, 259, 260] as a function of scattering angle, and also to determine the absolute integrated oscillator strength of the first excited band [261] by extrapolation of generalized oscillator strength measurements. It should be noted however that the lower impact energies and finite scattering angles used in some of these studies [16, 259, 260] are such that non-dipole contributions are expected to make appreciable contributions to the spectra. In other work, using much higher electron impact energies, oscillator strength measurements for the photoabsorption and photoionization of NH_3 have been obtained directly using dipole (e,e), (e,2e), and (e,e+ion) spectroscopies at low resolution [282–284].

The constrained least squares method used by Meath and co-workers at the University of Western Ontario to construct the DOSD, and to evaluate the dipole properties, for ammonia has been used with considerable success previously for a variety of molecules.

The previous DOSD studies of NH_3 [29] were, of course, based on the then available absolute photoabsorption oscillator strength data. While they were reasonably successful, the results were limited by inconsistencies between, and the limited energy ranges of, the various available oscillator strength data sets; for details see reference [29]. Recent DOSD analyses [286], which served as a preliminary basis for the study reported here, have confirmed the inconsistencies and limitations of the currently available absolute photoabsorption oscillator strength data for ammonia and indicated the need for new comprehensive measurements over as wide an energy range as possible. New measurements should also include the valence-shell discrete excitation spectrum at high-resolution since no reliable continuous absolute data set is available throughout this low-energy region. Recently the dipole (e,e) method has been further developed and extended to permit absolute oscillator strengths to be obtained at significantly higher resolution (0.048 eV fwhm) than that (~ 1 eV fwhm) which was possible in earlier work [4]. The high-resolution technique has been used to obtain absolute photoabsorption oscillator strengths of high accuracy in the discrete excitation region of the noble gas atoms [26, 27, 88] and several diatomic molecules [25, 158].

Although there have been several absolute oscillator strength data measurements for ammonia obtained using optical [266–281] techniques, these absolute data have mostly been measured only below 25 eV with the exception of the work of de Reilhac and Damany [274] and Samson *et al.* [279]. In this chapter newly obtained absolute photoabsorption oscillator strength data for ammonia are reported over an extended range from the UV to the soft X-ray region of the electromagnetic spectrum from 5.0–31 eV and 5.5–200 eV measured using high- (0.048 eV fwhm) and low-resolution (1 eV fwhm) dipole (e,e) spectroscopy, respectively. The present work includes a detailed quantitative

study of the electronic spectrum in the pre-edge excitation region at high resolution. The technique has been considerably refined since the earlier work [282–284] and careful attention has been given to background subtraction on both instruments. In addition, in order to improve the accuracy of the background subtraction procedures efficient differential pumping has recently been installed [78] in the region containing the oxide cathode of the electron gun in the low-resolution instrument.

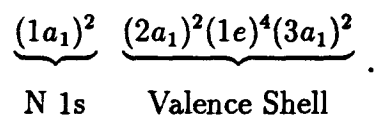
In this chapter the results of a constrained DOSD analysis of new high- and low-resolution measurements of the absolute oscillator strengths for NH_3 over the entire energy range from the first excitation threshold to 200 eV are presented. The present low- and high-resolution oscillator strength data measurements were used by Kumar and Meath [72] together with molar refractivity data [287–289], to obtain constrained DOSDs which in turn were used to calculate results of improved reliability for a wide variety of the dipole properties of NH_3 . The relatively recent oscillator strength data of Samson *et al.* [279], for 11.07–150 eV, are also included explicitly in the DOSD analysis for NH_3 . However it should be noted that the latter data [279] do not include the discrete excitation region below the first ionization potential. The results obtained in the present work provide updated values of the dipole properties of ammonia, relative to those reported earlier by Zeiss *et al.* [29], and provide the most reliable values yet available for many of the dipole properties of NH_3 .

6.2 Results and Discussion

6.2.1 Electronic Structure

Ammonia is a molecule with pyramidal geometry in its ground electronic state and belongs to the C_{3v} symmetry point group. The absorption spectrum will be discussed with

reference to the electronic configuration of the ground state of the ammonia molecule, which in the independent particle model, is:



The vertical ionization potentials (VIPs) of the outer valence orbitals of ammonia have been determined to be 10.85 eV for the $3a_1$ orbital, and 15.8 eV and 16.5 eV for the $1e$ orbitals by He(I) photoelectron spectroscopy (PES) [290]. The VIP of the $2a_1$ orbital has been found to be ~ 27 eV using He(II) PES [139], while the VIP of the $1a_1$ orbital has been measured as 405.52 eV using X-ray photoelectron spectroscopy [291].

6.2.2 Absolute Photoabsorption Measurements for Ammonia Obtained at Low Resolution

The low-resolution relative photoabsorption spectrum (1 eV fwhm) was obtained by Bethe-Born conversion of the background subtracted, relative energy-loss spectrum measured from 5.5 to 200 eV. This spectrum was placed on an absolute scale by first fitting a curve of the form

$$\frac{df}{dE} = AE^{-B}$$

to the high-energy valence-shell tail of the spectrum from 90 to 200 eV (df/dE is the oscillator strength (in units of eV^{-1}), E is the energy loss (or equivalent photon energy in units of eV), and A and B are best-fit parameters which were determined to be 158.88 and 2.1210, respectively, from a least squares fit to the presently measured experimental data). This functional form was chosen because of the goodness of the fit to the low-resolution data and because of the previous success in fitting this type of function to the high-energy valence-shell photoabsorption tail of other small polyatomic molecules [78, 126, 128]. The

fitted curve was then extrapolated to infinity and the total area under the entire relative photoabsorption spectrum was set to 8.34. The portion of the total valence-shell oscillator strength above 200 eV was found to be 4.5%. The value 8.34 corresponds to the 8 valence-shell electrons in ammonia, plus a small estimated contribution (0.34) to account for the Pauli-excluded transitions from the inner shell $1a_1$ orbital to the already-occupied valence orbitals (see section 3.1.1). The value of 8.34 is 2.8% higher than the value of 8.13 used previously to normalize relative oscillator strength spectra for NH_3 (see reference [284] and the DOSD results presented in section 6.3), and the difference between these values, and the reasons for the choice of the higher value in this section, is discussed below. The slightly lower value used in the earlier normalization is expected to have an almost negligible effect on the dipole properties derived in section 6.3.2.

It should be noted that the value (8.13) of $N_{\text{val}} + N_{\text{PE}}$ used previously to normalize relative, Bethe-Born converted valence-shell electron energy-loss spectra of ammonia (see reference [284] and section 6.3.1), is slightly too low because it was determined assuming a value of 1.87 (interpolated by Wight *et al.* [284] from the data of reference [84]) to account for the transitions from the nitrogen K-shell. This choice is not optimal because the correction was based on the calculated value for the K-shell of *atomic* nitrogen. Since atomic nitrogen has the valence-shell configuration $2s^2 2p^3$, transitions will be allowed from the nitrogen K-shell to the three half empty 2p valence levels and thus the contribution to the oscillator strength from excitations from the K-shell of nitrogen in atomic nitrogen will be greater than that from nitrogen in ammonia where the corresponding valence molecular orbitals ($2a_1$, $1e$, and $3a_1$) are all filled. Thus the partial TRK sum rule normalization factor for ammonia should in fact be greater than 8.13. The best method for estimating the partial TRK sum rule normalization for one-center hydrides

is to sum up the calculated [85] valence-shell contributions for the atom which is isoelectronic with the molecule being studied. In the case of ammonia the isoelectronic atom is neon (i.e., all 2p orbitals filled). The calculated [85] contribution to the total oscillator strength distribution from the valence-shell of neon is 8.34 which corresponds to a K-shell contribution of 1.66.

The absolute photoabsorption oscillator strength (cross section) data, obtained from 5.5–200 eV using low-resolution (~ 1 eV fwhm) dipole (e,e) spectroscopy, are shown in figure 6.1a and given numerically in table 6.1. The sharp structure observed at 6.5 eV and the shoulder at 9.5 eV correspond to valence-shell discrete excitation processes. These structures are much better resolved using the high-resolution spectrometer and the detailed vibronic structures are discussed in section 6.2.3 below. Figure 6.1b shows the presently measured photoabsorption oscillator strength data for ammonia from 30 to 100 eV along with two other wide-ranging data sets [279, 284] for comparison. The data below 35 eV are shown in more detail in figure 6.2. The absolute photoabsorption measurements reported by Samson *et al.* [279] are generally in very good agreement with the present data over the energy range from 12–120 eV. However, these data [279] are slightly lower from 17–30 eV, and higher in the 11–12 eV region, than the present work. The earlier dipole (e,e) data of Wight *et al.* [284] are higher than those of the present work above ~ 35 eV and diverge away from the present results as the limit of their data [284] at 60 eV is approached. The differences in the two dipole (e,e) measurements are likely due to a lack of background subtraction in the earlier work [284]. Similar inconsistencies between earlier reported [292, 293] absolute photoabsorption data obtained using dipole (e,e) spectroscopy and more recent measurements have also been observed for N₂ [25], CH₄ [87], and CO [157]. These differences, as well as inconsistencies observed between

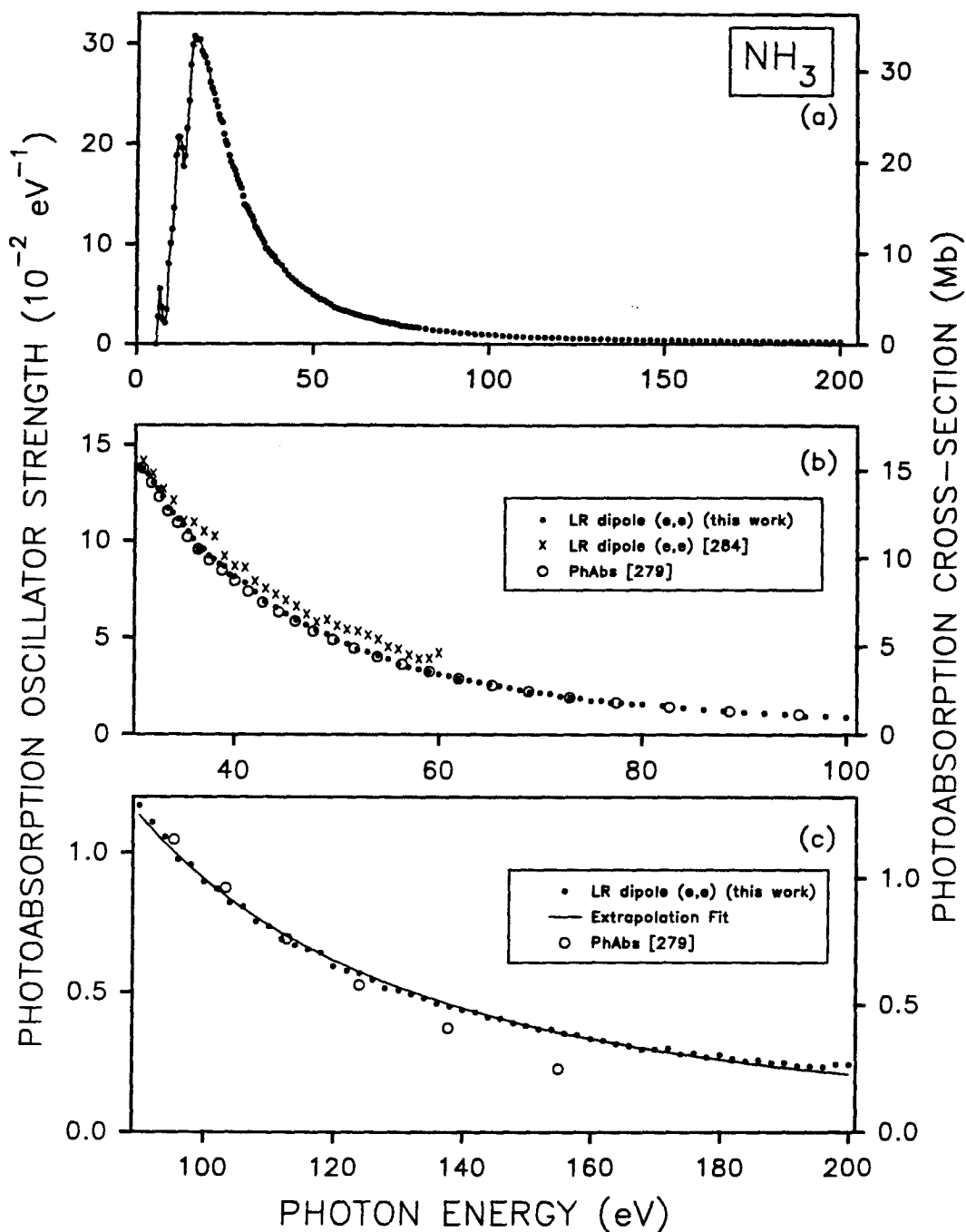


Figure 6.1: Absolute oscillator strengths for the photoabsorption of NH_3 obtained at low-resolution (~ 1 eV fwhm): (a) 6–200 eV, (b) 30–100 eV and (c) 90–200 eV. Also shown are the photoabsorption data reported by Samson *et al.* [279] (open circles) and Wight *et al.* [284] (crosses). The solid line in (c) represents a best-fit to the present data over the energy region from 90–200 eV and has been used in the extrapolation of the data to infinity (see text for details.)

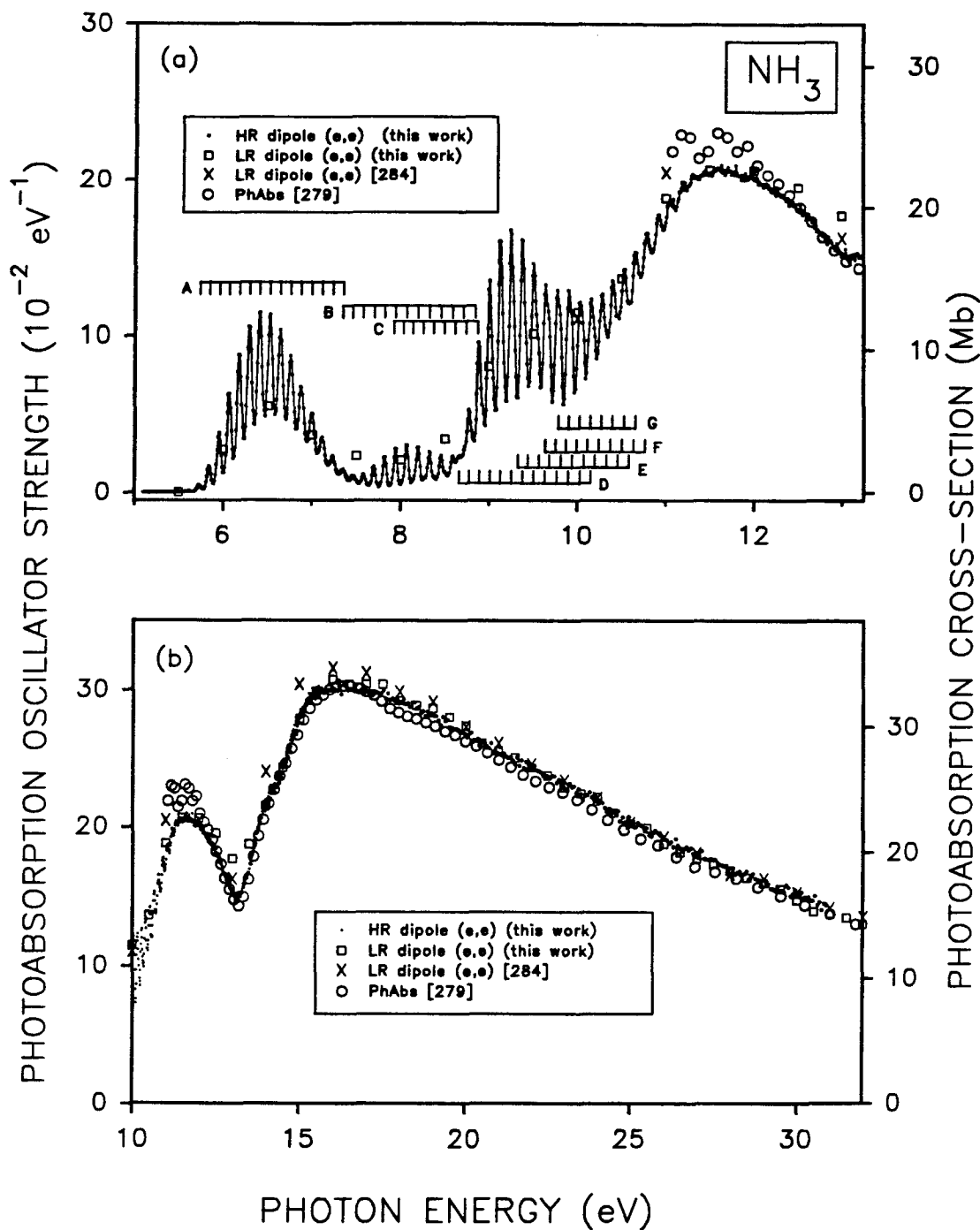


Figure 6.2: Absolute oscillator strengths for the photoabsorption of NH_3 obtained at a resolution of 0.048 eV fwhm (a) 5–13 eV, (b) 10–34 eV. The vertical bars in (a) represent the individual vibronic transitions which have been resolved using optical spectroscopy at higher resolution. The left-most vertical bar shows the position of the $v_2=0$ level in each band.

the other wide-ranging data sets for ammonia [279, 284] and the present work, assessed using constrained dipole oscillator strength distribution techniques [72], have provided an additional motivation for obtaining the new low-resolution measurements. The earlier dipole (e,e) photoabsorption measurements [284] were made without any correction for background gases or non-spectral electrons and were restricted to a much more limited energy range than the present work. In turn, the rather limited energy range resulted in the extrapolation estimates to infinite energy having greater uncertainties. In the more recent dipole (e,e) measurements very careful attention has been given to the background subtraction procedures to correct both for background gases and non-spectral electrons. For background subtraction a quarter of the sample pressure has been used instead of entirely removing the sample gas. Such a procedure has been found to minimize changes in the electron gun and electron beam conditions when sample gas pressures are changed. Optimization of these conditions has been further assisted by the installation of an additional stage of differential pumping between the gun and collision regions (see section 3.1).

In the higher energy region (figure 6.1c) it can be seen that the data reported by Samson *et al.* [279] are again in excellent agreement with the present work up to about 120 eV, but show lower oscillator strength values than the present work from 120 eV to the extent of their data at 155 eV. Extrapolation of this rapidly decreasing high-energy tail [279] to infinite energy results in a total valence-shell oscillator strength for the direct photoabsorption that is less than the expected value of 8.34 (see above). When a curve (equation 6.2.2) is fitted to the data of Samson *et al.* [279] from 90 to 155 eV and extrapolated to infinity the integrated oscillator strength above 155 eV is found to be 0.23 which is significantly lower than the value of 0.51 obtained from the present work.

Also shown on figure 6.1c is the fit to the presently measured experimental data from 90 to 200 eV which was used to estimate the amount of the total valence-shell oscillator strength distribution above 200 eV.

There have been several photoabsorption measurements made in the smooth continuum region of NH_3 above the first ionization potential [269–271, 273, 274] which are reported only in rather limited energy ranges and have not been included on figure 6.1. The cross-section data points reported by Sun and Weissler [269] from 9.0–25 eV and at 33 eV show a very large scatter and appear to have a greater statistical error than their quoted average error of 10%. Nevertheless, these data [269] are consistent with the present data within their highest calculated error of 25%. The data of Walker and Weissler [270] agree well with the present data above 10.5 eV, but are lower than the present work below 10.5 eV. Metzger and Cook [271] have reported measurements from 12 to 22 eV which differ significantly from the present data in both shape and magnitude. The measurements reported by Watanabe and Sood [273] in the continuum region from 12.5 to 21 eV are in very good agreement for both shape and magnitude with the present work. In contrast, the absorption data reported by de Reilhac and Damany [274] from 28 to 99 eV are as much as 30% lower than the presently reported oscillator strengths, and these differences exceed their estimated uncertainty of between 5 and 15%.

6.2.3 Absolute Photoabsorption Measurements for Ammonia Obtained at High Resolution

The high-resolution (0.048 eV fwhm) photoabsorption oscillator strength spectrum of ammonia was obtained in the present work by Bethe-Born conversion of a background subtracted electron energy-loss spectrum, followed by normalization at 25 eV in the

smooth continuum region to the new low-resolution data presented above in section 6.2.2 and table 6.1. The presently reported high-resolution oscillator strength measurements for NH_3 shown in figure 6.2 and tables 6.2–6.6 are considered to be extremely accurate since the high-resolution dipole (e,e) technique has produced results [26, 158] for helium and molecular hydrogen which are in excellent agreement with the highest level *ab initio* calculations reported in the literature [294–296]. It should also be noted that the high-resolution dipole (e,e) method is not subject to the large cross-section errors which can occur in Beer-Lambert Law photoabsorption measurements because of “line-saturation” effects (i.e., linewidth/bandwidth interactions) as discussed elsewhere [26, 158]. The high-resolution absolute oscillator strength data for NH_3 are shown in figures 6.2a and 6.2b. The absolute photoabsorption oscillator strength (cross-section) data obtained from the three different independent spectroscopic measurements shown in figure 6.2, namely low- ([284] and present results) and high-resolution dipole (e,e) spectroscopy and direct photoabsorption [279], show excellent agreement in the smooth continuum region above about 13 eV. However, differences occur in the 10–12.5 eV region between the present high-resolution work and the data of reference [279]. It should be noted however that there is very good agreement between the presently measured low- and high-resolution data, and the data reported by Wight *et al.* [284] in this energy region, which suggests that the data reported by Samson *et al.* [279] are ~10–15% too high around the peak maximum at about 12 eV. In the 6–13 eV region (figure 6.2a) the present high- and low-resolution measurements show good consistency, given the differences in the energy resolution of the two spectrometers.

The presently reported high-resolution spectrum of ammonia shows several vibrational progressions that have been studied in more detail in previously published photoabsorption spectra obtained at higher resolution [247, 248, 251, 252, 254]. However these measurements did not report absolute cross sections. All the excited electronic states of ammonia have been shown to involve transitions to Rydberg orbitals and are planar with D_{3h} symmetry [285]. The $\tilde{A} \leftarrow \tilde{X}$, $\tilde{D} \leftarrow \tilde{X}$, $\tilde{E} \leftarrow \tilde{X}$, $\tilde{F} \leftarrow \tilde{X}$, and $\tilde{G} \leftarrow \tilde{X}$ bands correspond to electronic transitions from the $3a_1$ orbital in the ground state (C_{3v}) of ammonia to the vibrational levels of the nsa'_1 (D_{3h}) Rydberg orbitals, $n = 3, 4, 5, 6$, and 7 , respectively. All the final states have A''_2 symmetry (D_{3h}). The $\tilde{B} \leftarrow \tilde{X}$ and $\tilde{C} \leftarrow \tilde{X}$ bands involve excitation from the $3a_1$ orbital to the $3pe'$ and $3pa''_2$ orbitals (in D_{3h} symmetry) giving final states of E'' and A'_1 symmetry, respectively. Ammonia has four normal modes of vibration with ground-state frequencies of 3336.2, 932.5, 3443.6, and 1626.1 cm^{-1} [285]. However, in all the observed excited states the spacing between the vibronic peaks is ~ 0.11 eV (880 cm^{-1}) and this corresponds well with the v''_2 out-of-plane bending vibration (“umbrella mode”) frequency of 932.5 cm^{-1} in the ground state. Excitation of the out-of-plane bending mode is consistent with the large change in the geometry of the ammonia molecule in going from the ground electronic state of C_{3v} symmetry to the planar excited states of D_{3h} symmetry. The $\tilde{A} \leftarrow \tilde{X}$ band has the transition to $v''_2=0$ from the ground vibronic state at 5.73 eV and progresses through at least 14 further vibronic peaks with the transition of maximum intensity being at $v''_2=6$. Two additional very weak peaks observed in the present spectrum at 5.50 and 5.62 eV have been assigned previously as “hot-bands” [259]. While the lowest triplet state of ammonia has been found to lie at about 0.4 eV below the $\tilde{A} \leftarrow \tilde{X}$ onset [297–300] triplet state excitation is not expected under the dipole dominated conditions of high impact energy

(3000 eV) and zero degree mean scattering angle (i.e., negligible momentum transfer) used in the present work. Thus the weak peaks at 5.50 and 5.62 eV are not considered to result from transitions to triplet states. It has been suggested that there is a broad continuum underlying the $\tilde{A} \leftarrow \tilde{X}$ band [254], however this has not been validated experimentally. Studies using jet-cooled NH_3 [256, 258] show very well resolved peaks in this energy region and the apparent continuum decreases in intensity. Furthermore, calculations [301] have shown that the apparent continuum arises from the overlapping tails of the vibronic line shapes, and the goodness of the fit of the Gaussian peak shapes to the individual peaks in the $\tilde{A} \leftarrow \tilde{X}$ band in the present work supports this conclusion (see below). From higher resolution measurements [251] the $\tilde{B} \leftarrow \tilde{X}$ band has been observed to begin at 7.34 eV. However, in the present work the transition to $v'_2=0$ of the $\tilde{B} \leftarrow \tilde{X}$ band is not resolved from the transition to $v'_2=14$ of the $\tilde{A} \leftarrow \tilde{X}$ band although there is a clear asymmetry in this peak and also the next one. A third very weak progression ($\tilde{C} \leftarrow \tilde{X}$) has been reported to start at about 7.9 eV in earlier, much higher resolution, photoabsorption studies [16, 254], but this progression is largely obscured in the present work by the more intense neighboring $\tilde{B} \leftarrow \tilde{X}$ and $\tilde{D} \leftarrow \tilde{X}$ bands. Evidence for this third progression can nevertheless be seen in the slightly asymmetric peak shapes in the 8.0 to 8.5 eV region in figure 6.2a, as was also observed in earlier electron energy-loss spectra reported by Lassette *et al.* [16]. More recent spectroscopic work, using multiphoton ionization techniques, has shown evidence for a further progression ($\tilde{C}' \leftarrow \tilde{X}$), in this energy region [262–265]. The $\tilde{D} \leftarrow \tilde{X}$ band [248, 249, 252] begins at 8.66 eV. The transition to $v'_2=0$ of the $\tilde{E} \leftarrow \tilde{X}$ band has been previously reported at 9.33 eV [252]. However, in the present work both the transitions to $v'_2=0$ and $v'_2=1$ of the $\tilde{E} \leftarrow \tilde{X}$ band are obscured by higher transitions in the $\tilde{D} \leftarrow \tilde{X}$ band and the subsequent members of

the $\tilde{E} \leftarrow \tilde{X}$ band result in the asymmetric peak shapes in the 9.5 to 10.3 eV region of figure 6.2a. The origin of the $\tilde{F} \leftarrow \tilde{X}$ band has been found to be at 9.64 eV [252] and this band extends through 9 more transitions [273]. The origin of the $\tilde{G} \leftarrow \tilde{X}$ band is at 9.79 eV [273] and extends through at least 7 more transitions. Above ~ 10.5 eV the bands observed in the present work become broad because of an overlapping of the many vibronic transitions in the $\tilde{E} \leftarrow \tilde{X}$, $\tilde{F} \leftarrow \tilde{X}$ and $\tilde{G} \leftarrow \tilde{X}$ bands.

In the presently obtained high-resolution spectrum (figure 6.2a) the spectral lines of the lowest vibrational progression, corresponding to the $\tilde{A} \leftarrow \tilde{X}$ transition, have been fitted with Gaussian line shapes (see figure 6.3) and the area of each peak yields the oscillator strength for each individual vibronic transition. These values are shown in table 6.2. It is found that the widths of the fitted peaks increase monotonically with an increase in ν'_2 . The remainder of the peaks in the discrete excitation region of the spectrum are composed of one or more overlapping vibronic transitions. The integrated oscillator strengths obtained by integrating the present high-resolution differential oscillator strength spectrum over the observed peaks are given numerically in tables 6.3–6.6. Also included for comparison in tables 6.2–6.6 are integrated oscillator strength values determined by first digitizing then numerically integrating previously reported absolute photoabsorption spectra of ammonia [267, 268, 272, 273, 278, 280]. The errors in each of the curve-fitting and numerical integration procedures are estimated to be $\pm 5\%$.

Table 6.2 gives the integrated oscillator strengths for transitions in the $\tilde{A} \leftarrow \tilde{X}$ band. The present value of 0.07449 agrees within 5% with the results of Watanabe [268] and is $\sim 25\%$ lower than the result obtained from the data of Syage *et al.* [281]. In the energy ranges above 6.12 eV there is also good agreement with results for ($\nu'_2=4-14$) reported

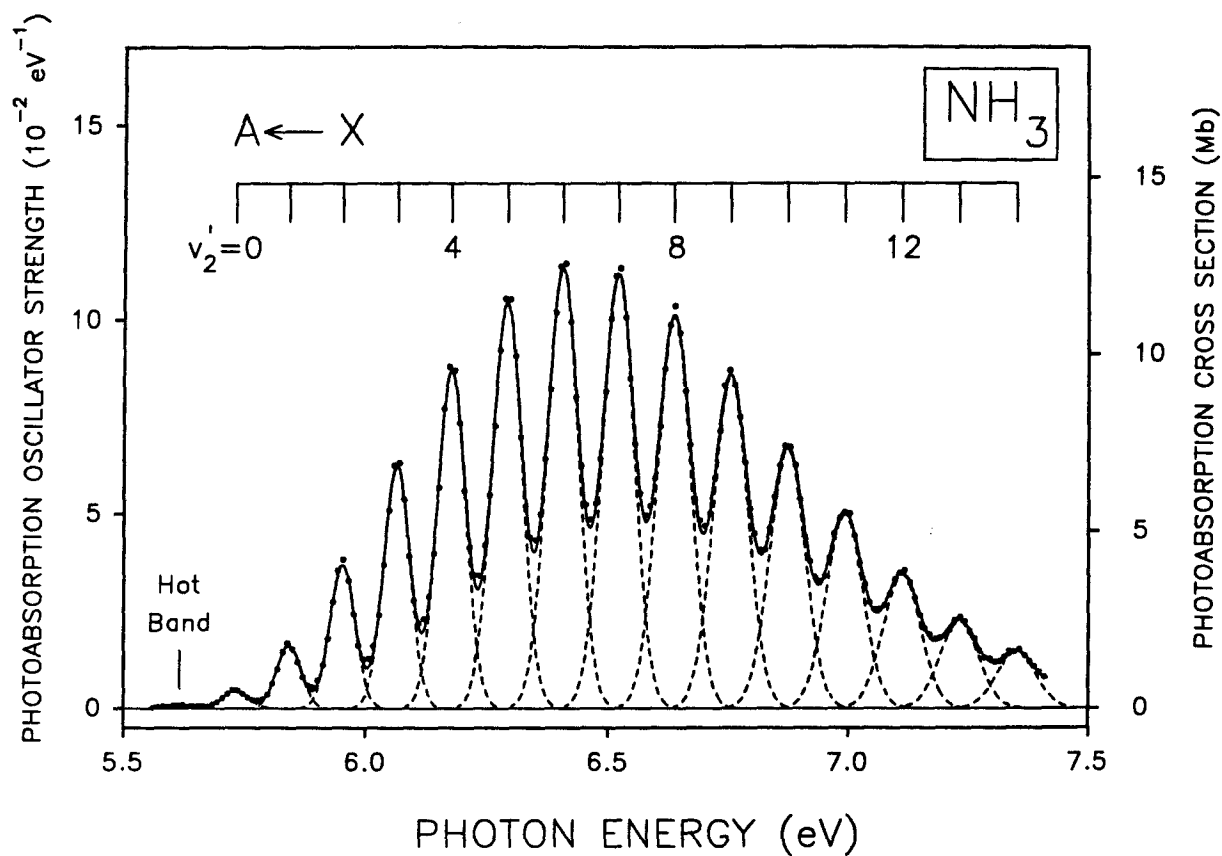


Figure 6.3: Absolute dipole oscillator strengths for the photoabsorption of NH_3 in the region of the $\tilde{A} \leftarrow \tilde{X}$ transition obtained at high resolution (0.048 eV fwhm). The dotted lines represent the Gaussian peak shapes that have been fitted to the high-resolution data. The solid line represents the sum of the fitted Gaussian peaks. The low-intensity transition at 5.62 eV has been assigned previously as a “hot band” [259].

by Suto and Lee [278]. Tannenbaum *et al.* [267] and Thompson *et al.* [272] have reported absolute cross sections below 7.2 eV and below 6.6 eV, respectively, and these results are $\sim 11\%$ higher and $\sim 33\%$ lower than the sum of the corresponding vibronic transitions in the present work. In other work [261] using electron energy loss spectroscopy the integrated oscillator strength for the $\tilde{A} \leftarrow \tilde{X}$ band has been determined by extrapolation of generalized oscillator strength measurements to zero momentum transfer and was reported to be 0.0696. Other values for this integral are 0.13, determined by photoabsorption [266], 0.072 determined by dispersion [288] and a calculated value of 0.0134 [266].

Table 6.3 gives the integrated oscillator strengths over the 7.42 to 8.62 eV energy region which encompasses the $\tilde{B} \leftarrow \tilde{X}$ ($v'_2=1-10$) and the $\tilde{C} \leftarrow \tilde{X}$ bands, but excludes the $\tilde{D} \leftarrow \tilde{X}$ band which begins at 8.66 eV. From table 6.3 it can be seen that the very-high resolution optical measurements [268, 273] agree well with each other, but are not consistent with either the somewhat lower resolution optical measurements [278] or the present work. The oscillator strengths in the lower resolution optical spectrum [278] are higher than those in the present work and the other optical measurements [268, 273] from ~ 8.2 to 8.6 eV, thus the integrated oscillator strength [278] over this region is almost certainly too high. The spectrum reported by Syage *et al.* [281] is consistently higher than the other spectra (the present work and [268, 273, 278]) over the entire 7.42–8.62 energy range. The results of the very-high resolution optical measurements [268, 273] may be too low in this energy region because of “line-saturation” (bandwidth) effects [25, 26]. It has been noted [263] that all of the excited states of ammonia show signs of predissociation, which tends to broaden the spectral lines. Since higher resolution studies of the \tilde{B} , and \tilde{C} (and \tilde{C}') bands show resolvable rotational structure [250, 251, 254, 262–265],

this indicates that predissociation has little effect on the linewidth of these bands. In this situation the two very-high resolution optical measurements [268, 273] could well suffer from the “line-saturation” effects, and result in too low a value for the integrated oscillator strength over the band.

Tables 6.4, 6.5 and 6.6 show the remainder of the discrete excitation region from 8.62 to 11.53 eV. The data of Watanabe [268] agree very well, within 5%, with the present data over the entire energy region. The data reported by Syage *et al.* [281] are as much as 33% higher than the present work. The fact that the data of Watanabe and Sood [268] agree so well with the present work over the whole discrete energy region, except from 7.42–8.62 eV as discussed above, further suggests that the differences between the present dipole (e,e) results and the optical absorption measurements in this particular energy region for ammonia, may be due to “line-saturation” errors in the optical work. The data of Watanabe and Sood [273] agree well, within 10%, with the present data over the energy region below 11.5 eV but show unexpected and unusual features in the 11.5–12.5 eV region. The data of Suto and Lee [278] agree well with the present data from 8.62 to 9.32 eV (table 6.4) but are much lower from 9.32 to 11.5 eV. The results (10.21–11.53 eV) of Xia *et al.* [280] are ~9% higher than the present measurements—see table 6.6.

6.3 Constrained Dipole Oscillator Strength Distributions and Related Properties

It should be noted that the DOSD and dipole properties reported in this section were calculated by Kumar and Meath [72] using the presently measured high- and low-resolution oscillator strength data normalized to 8.13. The choice of 8.13 as the normalization factor

was based on the work of Wight *et al.* [284], but the optimum normalization factor is 8.34, as has been discussed with respect to the reported low-resolution oscillator strength data in section 6.2.2. The slightly lower normalization factor used in this section is expected to have an almost negligible effect on the derived dipole properties for ammonia [302].

6.3.1 Dipole Oscillator Strength Distribution for Ammonia

A DOSD for NH_3 was constructed some time ago (1977) by Zeiss *et al.* [29] who employed methods that are the precursor to those used in this section. Such photoabsorption, or equivalent data, as was available at the time was considered. However, because of substantial disagreements amongst the available experimental data sets, and because of the lack of NH_3 data for higher photon energies, the DOSD was based on the (H_2 , N_2) mixture rule (equation 6.1) above 33 eV. It was noted [29] that the dipole oscillator strength (DOS) data (4–100 eV) of Van der Wiel and Brion [282] generally agreed with the mixture rule values to within 10%. New DOSDs for NH_3 were constructed based on new NH_3 oscillator strength data (see references [279, 303] and the present new experimental data reported in sections 6.2.2 and 6.2.3) which have become available since the original DOSD work on ammonia [29] was carried out. The dipole properties obtained from the resulting constrained DOSDs are then compared with those [29] evaluated from the DOSD of Zeiss *et al.* [29]. The sources of DOS data discussed and analyzed in reference [29] are not considered explicitly in the construction of the DOSD for NH_3 reported below. The data subsequently reported by Wight *et al.* [284] over the range 10–60 eV are also not considered explicitly in what follows since it is now apparent that adequate background subtraction procedures were not employed. This was confirmed by preliminary work [286] which indicated that the data of Wight *et al.* [284] are too high relative to the new

(background-subtracted) measurements reported in section 6.2.2.

The following experimental dipole oscillator strength data are considered for the construction of the DOSDs for NH_3 : 5.685–30.88 eV (high-resolution data of section 6.2.3, normalized to 8.13); 5.685–200 eV (low-resolution data of section 6.2.2, normalized to 8.13); 11.07–150.0 eV (Samson *et al.* [279]); 400–425 eV (Akimov *et al.* [303]). This experimental molecular NH_3 data is augmented by employing the following mixture rule, particularly for photon energies $E \geq 150$ eV,

$$(df/dE)(\text{NH}_3) = \frac{1}{2}(df/dE)(\text{N}_2) + \frac{3}{2}(df/dE)(\text{H}_2). \quad (6.1)$$

The input for this mixture rule uses the recommended N_2 and H_2 DOSDs of Zeiss *et al.* [29].

To construct the DOSD, the photoabsorption spectrum is divided into 26 energy intervals as suggested by the structure of the spectrum and by the photon energy regions corresponding to the various sources of DOS input data. The integrated DOSs for each individual source, and for each relevant energy interval, are given in table 6.7 which also contains the analogous results calculated from the adopted DOSD of Zeiss *et al.* [29]. The constraints used for constructing the DOSDs for NH_3 from the initial DOS input data, are provided by $S_0 = 10$ and by the experimental molar refractivity data of Frivold *et al.* [287] and Friberg [288] at $\lambda = 2753 \text{ \AA}$ and $\lambda = 5462 \text{ \AA}$, respectively. These are the same constraints as employed by Zeiss *et al.* [29].

Three new DOSDs were constructed by taking the following combinations of the initial dipole oscillator strength data:

DOSDA : 5.685–30.88 eV (present high-resolution data, normalized to 8.13); 30.88–200 eV (present low-resolution data, normalized to 8.13); 400–425 eV (Akimov

et al. [303]); all other energy regions (mixture rule equation 6.1).

DOSDB : 5.685–200 eV (present low-resolution data, normalized to 8.13); then as in DOSDA.

DOSDC: 11.07–150 eV (Samson *et al.* [279]); then as in DOSDA.

Each of these initial DOSDs was modified, through requiring the constraints to be satisfied, by using the constrained least squares procedure discussed earlier. The values of the standard deviation (STD), see equation 2.52, for the resulting distributions are 2.68, 0.90 and 2.19, respectively. The STDs for all three DOSDs compare favorably with those for many other DOSDs constructed using the methods employed here.

The constraints used to construct the DOSDs involve integrals over the DOSDs, weighted by simple functions of E , and therefore are effective in a “global” sense over a range of photon energies [66]. The constraints used are sensitive to different ranges of photon energies [54, 73–75]. For example the energy region 5.685–50.0 eV yields ~98% of the molar refractivity constraints while ~100% of S_0 arises from the energy region 5.685– 10^4 eV with ~92% arising from the 11.07– 10^3 eV region. Therefore the constrained DOSDs are generally reliable in the sense of yielding accurate results for various related dipole properties, but not in the sense of providing accurate DOS values at specific local energies or over narrow energy regions [66]. In the present context, while the smaller values of STD imply that less modification of the initial DOS data is required to satisfy the constraints, this cannot be used to discriminate between the input data since the STDs are all small. The difference between the STDs for DOSDA and DOSDB is essentially due to the energy region 5.685–7.563 eV, which contributes only ~1% of S_0 and ~10% of the molar refractivity constraints. The integrated oscillator strengths corresponding to all the input data, and to the constrained DOSDs A, B, and C,

are compared in table 6.7 which also contains the corresponding previously unpublished results obtained from the recommended DOSD (STD = 2.64) of Zeiss *et al.* [29].

For common energy regions above 11.07 eV, the integrated DOSs obtained directly from the presently reported high- and low-resolution data (estimated error $\pm 5\%$) agree with each other, and are in essential agreement with those obtained from the data of Samson *et al.* [279] (estimated error $\pm 3\%$), to within their combined experimental errors. Exceptions are the results obtained from the data of Samson *et al.* [279] for 11.07–12.40 eV and 124.4–150 eV which are $\sim 12\%$ and $\sim 15\%$ higher and lower, respectively, than the present experimental work over the same energy ranges. For photon energies below 11.07 eV the present high- and low-resolution integrated oscillator strengths also agree well with each other except apparently in the 7.563–8.590 eV region where the low-resolution data are larger by a factor of two. Of course in this narrow energy range the low-resolution data are not realistic, since the fine structure in the discrete excitation region cannot be resolved. Thus local oscillator strength values in the discrete region of the low-resolution spectrum where sharp structures exist are likely to be severely modified by the “filling in of valleys” and “clipping of peaks” that occurs at low resolution. However, the *integrated* oscillator strengths over the entire discrete region, obtained from the two sets of measurements at high and low resolution, may be compared with each other. For example, over the energy range 5.685–13.08 eV the high- and low-resolution integrated oscillator strengths are 0.7125 and 0.7580 respectively; the corresponding results from 5.685–30.88 eV are 4.649 and 4.728.

The integrated oscillator strengths obtained from the constrained DOSDs generally agree to within the estimated experimental error with the corresponding integrated DOSs obtained from the experimental NH_3 data. The largest difference ($\sim 11\%$) occurs in the

5.685–7.563 eV region for DOSDs A and C. Also the raw mixture rule data, used to construct the constrained DOSDs for most energies greater than 200 eV, is only modified by a few percent by the constraint procedures. Furthermore, the raw mixture rule data predicts results for the integrated oscillator strengths between 150–200 eV that differ by only $\sim 6\%$ with the values obtained from the constrained DOSDs. The integrated oscillator strengths for the constrained DOSDs A, B, and C agree very well over the whole energy domain with the largest disagreements being $\sim 12\%$ between DOSDs A and C and DOSDB for 5.685–7.563 eV and $\sim 11\%$ and 15% between DOSDs A and B and DOSDC for 11.07–12.40 eV and 124.4–150 eV respectively. The oscillator strength input used to construct the adopted DOSD of Zeiss *et al.* [29] differs significantly from that used to obtain the constrained DOSDs A, B, and C for the energy regions 5.685–150 eV and 400–425 eV and this results in the differences that occur between the relevant integrated oscillator strengths in table 6.7.

The photoabsorption cross sections reported by Akimov *et al.* [303] in the K-edge region exhibit structure with four peaks occurring at photon energies of 400.9, 402.4, 403.6 and 404.5 eV and the cross sections at these energies are 1.398, 4.025, 1.525 and 1.751 Mb (10^{-18} cm²), respectively. The use of the mixture rule, which was based on atomic nitrogen data at high energies, in this energy region yields a single absorption edge at $E = 401.5$ eV (i.e., the K-edge of N) with a cross section of 0.7670 Mb; the K-edge of N is very close to the average (401.6 eV) of the energies associated with the two most significant absorption peaks in the molecular K-edge measurements. The mixture rule absorption maximum is about five times smaller than the highest molecular K-edge maximum [303]. For the energy region 400–425 eV, around the K-edge, the integrated DOSs for the mixture rule data, and the data reported by Akimov *et al.* [303]

are 1.543(-1) and 2.610(-1), respectively. However at 400 eV, and for $E \geq 420$ eV, the mixture rule and molecular DOSs agree to within 10 and 20% respectively; the estimated experimental error in the molecular cross section data reported by Akimov *et al.* [303] is about 15%.

The disagreement between the mixture rule and the ammonia experimental data at, and close to, the K-edge reflects the very different photoabsorption effects occurring in atomic nitrogen and NH_3 at these photon energies. An analogous effect has also been discussed by Kumar and Meath [74, 75] for the L_1 absorption of HCl (see also Eberhardt *et al.* [304] and Yates *et al.* [246]). In general, mixture rules, which are based on additivity principles [54, 55, 244, 245], work reasonably well for photon energies greater than about 60 eV and become more reliable for high photon energies, except near photoabsorption edges where significant deviations from additivity can occur because of specific molecular effects; examples can be taken from table 6.7 and references [48, 66, 73–75, 120, 305, 306].

The averaged oscillator strength results obtained from constrained DOSDA, calculated for each energy block in table 6.7, are compared with the initial high- and low-resolution valence-shell oscillator strengths in a global perspective over the entire spectral range in figure 6.4. Figure 6.5 provides an alternative representation of the integrated DOSDA (table 6.7) on a linear scale in the region below 200 eV. These figures show that the *averaged* constrained DOSD data provide an effective representation of the experimental data from 5.685 to 200 eV.

6.3.2 Dipole Properties for Ammonia

The results for the S_k , $-12 \leq k \leq 2$, and the L_k and I_k , for $-2 \leq k \leq 2$, evaluated by using the constrained DOSDs A and B, and the initial DOSDA are compared in table 6.8

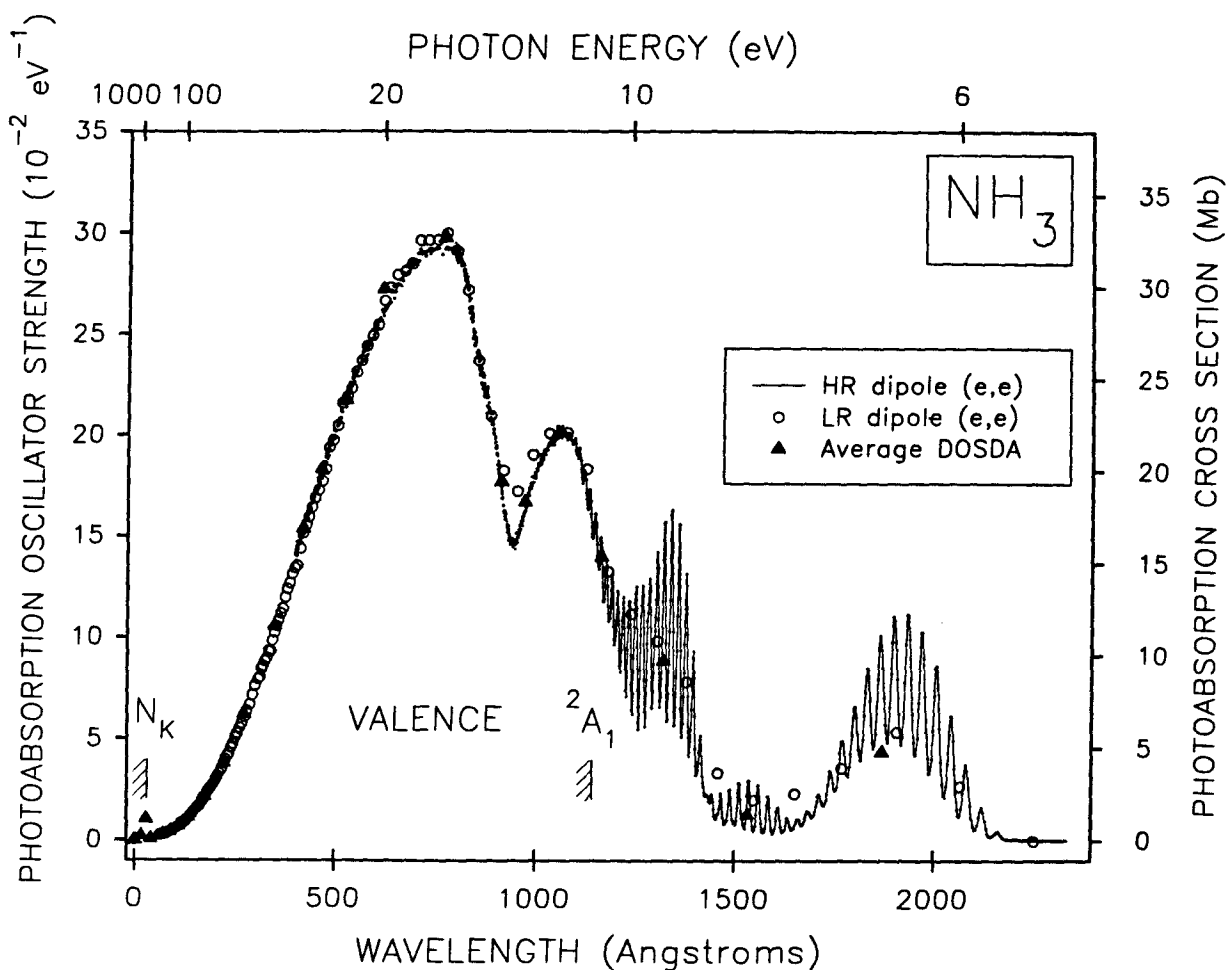


Figure 6.4: Absolute experimental low-resolution (~ 1 eV fwhm) and high-resolution (0.048 eV fwhm) photoabsorption data for NH_3 as a function of wavelength. The hatched lines indicate the positions of the lowest energy valence-shell vertical ionization potential (VIP) and the nitrogen K-shell VIP. The average constrained DOSD data points, calculated for each energy block in the valence- and nitrogen K-shell regions, are taken from DOSD A (table 6.7). The energy position of each of these data points is the midpoint of the energy region over which the particular integrated oscillator strength value was determined and the associated differential oscillator strength value for these data points is the integrated oscillator strength value divided by the width of the energy region.

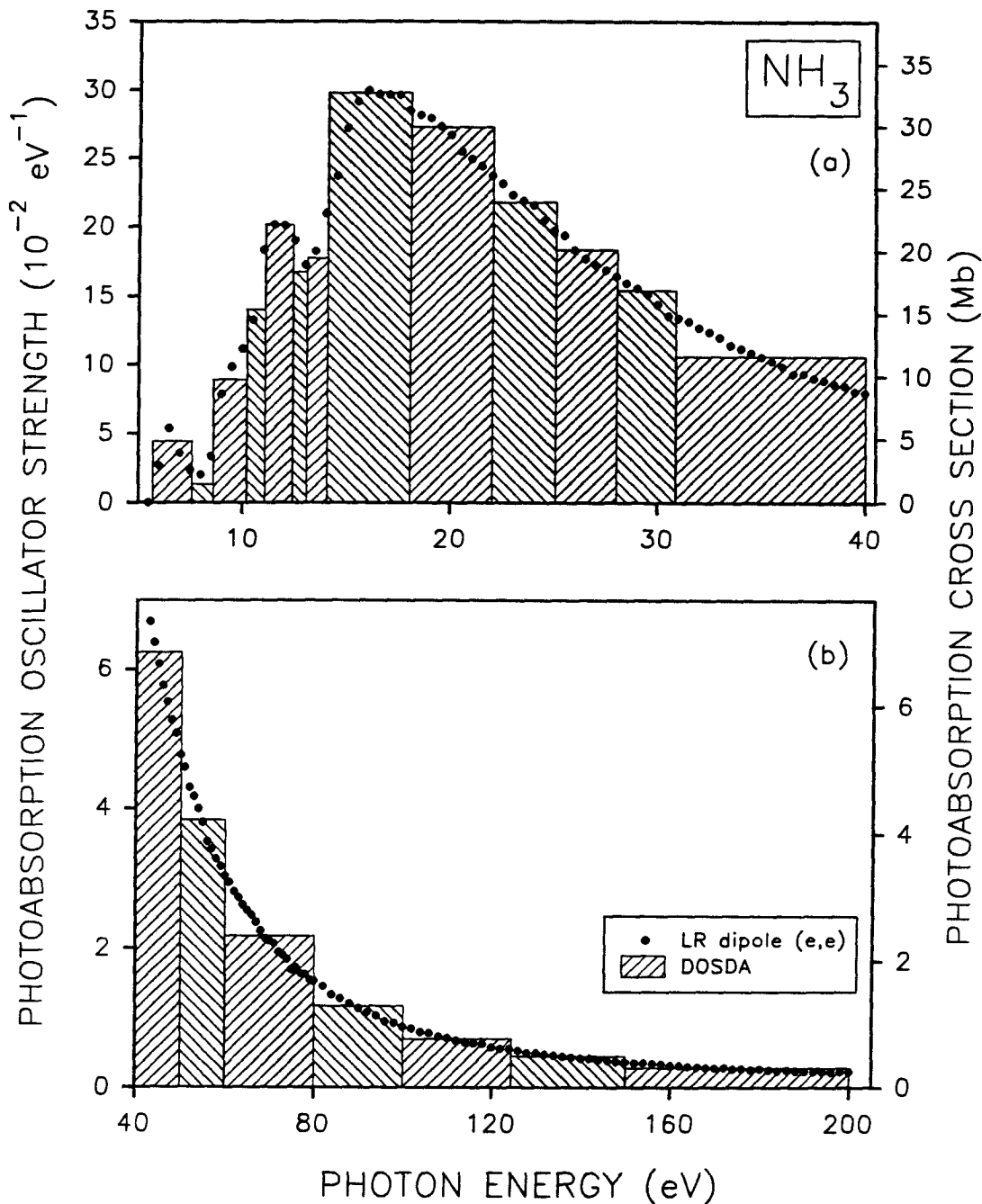


Figure 6.5: Absolute experimental low-resolution (~ 1 eV fwhm) oscillator strengths (filled circles) and constrained DOSD A results (hatched blocks): (a) 5.5–40 eV; (b) 40–200 eV. Each integrated oscillator strength value (table 6.7) is represented by a hatched block with a base which spans the energy range over which the value was determined and with an area equal to the integrated oscillator strength value.

with the results reported by Zeiss *et al.* [29]. The results for the constrained DOSDC are not included in the table since they differ insignificantly from those of constrained DOSDA and DOSDB. The dipole properties obtained from the constrained DOSDs agree very well with each other and certainly to well within the estimated errors in the present results for the dipole properties (these are discussed later in this section). Nominally we choose the results for the dipole properties obtained from constrained DOSDA as recommended values since they are derived using spectroscopically more reliable oscillator strength input data than DOSDB, especially in the low photon energy region of the NH_3 photoabsorption spectrum. The results for the molar refractivity of NH_3 evaluated using constrained DOSDA are compared with experiment [287–289] in table 6.9 as a function of wavelength; analogous results were not obtained in [29]. It is clear that the calculated results for R_λ are in excellent agreement with experiment with the maximum discrepancy being only $\sim 0.07\%$. The dipole property S_{-2} is related to the static dipole polarizability which in turn is proportional to R_∞ . The recommended result of $S_{-2} = 14.56$ can be compared with values obtained from refractivity measurements [307], 14.57, and from dielectric constant measurements [308, 309], 14.71 and 14.2.

The results for the dipole properties (table 6.8) evaluated using the initial (unmodified) DOSDA, leading to the constrained DOSDA for NH_3 , agree reasonably well with the recommended properties which indicates the high quality of the input DOSs. The effect of applying the constraint procedure is only 0.3% for S_2 , $\sim 1\%$ for S_1 , $\sim 2\%$ for S_0 , and increases as k decreases, to $\sim 3.5\%$ for S_{-1} , $\sim 4.5\%$ for S_{-2} , and $\sim 9.5\%$ for S_{-12} . For the L_k the differences are $\leq 1\%$ for $k \geq 0$ and $\sim 7\%$ for $k = -1$ and -2 . Berkowitz [83] analyzed the absolute photoabsorption data available before 1979 for NH_3 and used atomic additivity (Henke *et al.* [310]) to extend the molecular data for photon energies greater than

62 eV. The dipole sums so obtained are $S_0 = 9.38$, $S_{-1} = 8.70$ and $S_{-2} = 14.04$ which are $\sim 6.2\%$, 6.6% and 3.6% lower than the recommended values. Samson *et al.* [279] obtained $S_0 = 9.78$ by combining their DOS data from 11–150 eV with that used by Berkowitz below 11 eV and above 150 eV.

The recommended results for the dipole properties of NH_3 (table 6.8) generally agree with the results of Zeiss *et al.* [29] to within their estimated errors; this is partly due to the use of the same constraints in the construction of the corresponding DOSDs. For the S_k the discrepancies are $\sim 2.3\%$ for $k = 1$, $\leq 0.5\%$ for $k = 2$ and $-12 \leq k \leq 0$; for I_k they are $\leq 2\%$ for all k . Error estimates were not given for the L_k in reference [29]; the differences in the two sets of values are $\leq 1\%$ for $k = 2, -1, -2$, and $\sim 2.5\%$ for $k = 1$ and 0 respectively.

There are a number of *ab initio* calculations available for the electronic static dipole polarizability, $\alpha(\lambda = \infty) = a_0^3 S_{-2}$, of NH_3 . A coupled Hartree Fock calculation [311], using an extended complete neglect of differential overlap (CNDO) basis set, yielded $S_{-2} = 15.39$ while a value of $S_{-2} = 13.43$ was obtained [312] using an CNDO/2-FPP (finite perturbation plus polarization) approach. There are also *ab initio* calculations at the SCF level and these correspond to Hartree Fock, $S_{-2} = 12.71$ [313], coupled Hartree Fock, $S_{-2} = 12.90$ [314] and 12.80 [315], time-dependent coupled Hartree Fock, $S_{-2} = 12.95$ [316] and derivative Hartree Fock, $S_{-2} = 12.83$ [317], treatments. These results do not include the small vibrational averaging effect and are much smaller than the present recommended result of $S_{-2} = 14.56$. Only the calculations of Werner and Meyer [318] include vibrational averaging effects. Their pseudo natural orbital configuration interaction and coupled electron pair approximation results are $S_{-2} = 14.55$ and 14.96 , respectively; the former is in excellent agreement with the present recommended

result, the latter is $\sim 2.5\%$ higher. Diercksen and Sadlej [319] have used fourth-order many-body perturbation theory to compute S_{-2} and their result, including the vibrational averaging correction (0.26) evaluated by Werner and Meyer [318], is 14.63. Correlation contributions to S_{-2} have also been considered by Maroulis [320] and by Wormer and Hettema [321] using many-body perturbation theory methods and these calculations yield values of 14.01 and 14.136, respectively.

Reinsch [322] has computed the dynamic polarizability $\alpha(\lambda)$, see equation 2.44, of NH_3 for $\lambda = \infty$ and $2278.2 \leq \lambda \leq 9112.7 \text{ \AA}$, using a time-dependent Hartree Fock approach and the basis set B of Werner and Meyer [318]. The values obtained by Reinsch [322] for $\lambda = \infty$ and $\lambda = 9112.7 \text{ \AA}$ are $\sim 5\%$ lower than the present results obtained using constrained DOSDA and the discrepancy increases to $\sim 20\%$ at $\lambda = 2278.2 \text{ \AA}$.

6.3.3 The Reliability of Calculated Dipole Properties

The uncertainties in the recommended values of the dipole properties of ammonia determined by Kumar and Meath [72] can be estimated by employing procedures discussed previously [29, 48, 74, 75]. The approach is to compare the adopted results with those derived from alternative DOSDs satisfying the same constraints. The uncertainty estimates thus obtained are less reliable for those properties that do not depend significantly on the spectral regions which dominate the constraints, namely the properties corresponding to $k = 2$, and to a lesser extent $k = 1$ and $k < -4$. A detailed discussion of the photon energy dependence of the dipole properties can be found in references [54, 73–75]. For $k \geq 1$, the uncertainties in the dipole properties are influenced by the uncertainties in the very high energy DOS data used in constructing the DOSD, which are generally a few percent.

Using the results for various alternate DOSDs constructed for NH_3 (this work, and references [29, 286]) we estimate the uncertainties in the recommended results for the dipole properties to be $\leq 3\%$ for S_2 , S_1 , L_2 , L_1 , and I_2 , $\leq 1\%$ for S_k , $0 \leq k \leq -5$, and for L_{-2} , I_{-1} , and I_{-2} , $\leq 1-2\%$ for S_k , $-6 \leq k \leq -10$, L_{-1} and I_1 , and $\sim 3-4\%$ for S_{-12} . The uncertainty of $\sim 3\%$ in L_0 , and hence in I_0 , is relatively high because of a partial cancellation [74, 75] between the positive and negative parts of L_0 ; for NH_3 , $L_0(E \leq E_H) \sim -1.9$ while $L_0(E \geq E_H) \sim 8.4$. The uncertainties in the recommended results for the dipole properties of NH_3 are also based on the assumption that the molar refractivities, used as constraints in the construction of the DOSDs, have experimental errors associated with accurate measurements, namely a few tenths of a percent.

The application of the constrained DOSD method to NH_3 results in relatively little modification of the high- and low-resolution oscillator strength data of this work, or of the data of Samson *et al.* [279]. These three measurements are in close agreement over most of their common energy regions. The high quality of the experimental DOSD data used to construct the ammonia DOSDs is further exemplified by the comparison, made earlier, of the dipole properties obtained from the initial DOSDA with those from the constrained DOSDA. Relative to many other applications of the constrained DOSD method, very little modification of the initial data is required to satisfy the constraints and the differences between the two sets of dipole properties, see table 6.8, are relatively small. The recommended dipole properties reported here, as obtained from the constrained DOSDA, show only small differences from the results of the original calculations of Zeiss *et al.* [29]. However, the values obtained here are to be (nominally) preferred since they are based on newer, more reliable DOS input data which span a much wider energy range than the data available to Zeiss *et al.* [29]. On the other hand, the integrated

oscillator strengths for DOSDA and constrained DOSDA are clearly preferred relative to those obtained from the recommended DOSD of reference [29]. The excellent agreement between the recommended dipole properties and those of reference [29] is a good example of the usefulness of the constrained DOSD approach for evaluating molecular *properties*. Very similar properties are obtained from different sets of DOS input data provided that they are in agreement by $\sim 10\text{--}20\%$. For example, the recommended DOSD of Zeiss *et al.* [29] was based on the mixture rule DOS data for photon energies above 33 eV which are significantly different from the other input DOS data considered here for 30.88–100 eV.

Table 6.1: Absolute oscillator strengths for the total photoabsorption of ammonia from 5.5 to 200 eV measured by low-resolution (1 eV fwhm) dipole (e,e) spectroscopy.

Energy eV	Oscillator strength (10^{-2} eV $^{-1}$) ^a	Energy eV	Oscillator strength (10^{-2} eV $^{-1}$) ^a	Energy eV	Oscillator strength (10^{-2} eV $^{-1}$) ^a
5.5	0.00	14.0	21.51	22.5	23.72
6.0	2.74	14.5	24.29	23.0	22.90
6.5	5.50	15.0	27.87	23.5	22.44
7.0	3.66	15.5	29.86	24.0	22.15
7.5	2.38	16.0	30.73	24.5	21.00
8.0	2.07	16.5	30.40	25.0	20.25
8.5	3.42	17.0	30.39	25.5	19.90
9.0	8.02	17.5	30.39	26.0	18.78
9.5	10.09	18.0	29.20	26.5	18.19
10.0	11.47	18.5	28.84	27.0	17.71
10.5	13.61	19.0	28.64	27.5	17.34
11.0	18.80	19.5	28.00	28.0	16.86
11.5	20.64	20.0	27.36	28.5	16.36
12.0	20.60	20.5	26.12	29.0	15.97
12.5	19.53	21.0	25.56	29.5	15.56
13.0	17.70	21.5	25.04	30.0	14.76
13.5	18.72	22.0	24.31	30.5	13.91

Table 6.1: (continued) Absolute oscillator strengths for the total photoabsorption of ammonia.

Energy eV	Oscillator strength (10^{-2} eV $^{-1}$) ^a	Energy eV	Oscillator strength (10^{-2} eV $^{-1}$) ^a	Energy eV	Oscillator strength (10^{-2} eV $^{-1}$) ^a
31.0	13.77	39.5	8.26	56.0	3.62
31.5	13.49	40.0	8.15	57.0	3.51
32.0	13.03	41.0	7.84	58.0	3.37
32.5	12.74	42.0	7.36	59.0	3.26
33.0	12.30	43.0	6.87	60.0	3.12
33.5	11.74	44.0	6.56	61.0	3.03
34.0	11.48	45.0	6.25	62.0	2.89
34.5	11.15	46.0	5.92	63.0	2.81
35.0	10.84	47.0	5.68	64.0	2.70
35.5	10.51	48.0	5.40	65.0	2.63
36.0	10.12	49.0	5.20	66.0	2.55
36.5	9.57	50.0	4.89	67.0	2.45
37.0	9.57	51.0	4.70	68.0	2.32
37.5	9.24	52.0	4.41	69.0	2.21
38.0	9.08	53.0	4.28	70.0	2.18
38.5	8.82	54.0	4.11	71.0	2.13
39.0	8.70	55.0	3.90	72.0	2.01

Table 6.1: (continued) Absolute oscillator strengths for the total photoabsorption of ammonia.

Energy eV	Oscillator strength (10^{-2} eV^{-1}) ^a	Energy eV	Oscillator strength (10^{-2} eV^{-1}) ^a	Energy eV	Oscillator strength (10^{-2} eV^{-1}) ^a
73.0	1.96	100.0	0.90	134.0	0.48
74.0	1.90	102.0	0.87	136.0	0.46
75.0	1.74	104.0	0.82	138.0	0.45
76.0	1.77	106.0	0.81	140.0	0.44
77.0	1.69	108.0	0.75	142.0	0.43
78.0	1.68	110.0	0.74	144.0	0.41
79.0	1.60	112.0	0.69	146.0	0.41
80.0	1.57	114.0	0.67	148.0	0.40
82.0	1.49	116.0	0.66	150.0	0.38
84.0	1.38	118.0	0.64	152.0	0.37
86.0	1.31	120.0	0.60	154.0	0.37
88.0	1.24	122.0	0.58	156.0	0.35
90.0	1.17	124.0	0.57	158.0	0.35
92.0	1.11	126.0	0.55	160.0	0.34
94.0	1.06	128.0	0.52	162.0	0.33
96.0	0.98	130.0	0.51	164.0	0.32
98.0	0.96	132.0	0.49	166.0	0.31

Table 6.1: (continued) Absolute oscillator strengths for the total photoabsorption of ammonia.

Energy eV	Oscillator strength (10^{-2} eV^{-1}) ^a	Energy eV	Oscillator strength (10^{-2} eV^{-1}) ^a	Energy eV	Oscillator strength (10^{-2} eV^{-1}) ^a
168.0	0.30	180.0	0.28	192.0	0.24
170.0	0.30	182.0	0.27	194.0	0.24
172.0	0.30	184.0	0.26	196.0	0.23
174.0	0.28	186.0	0.26	198.0	0.24
176.0	0.28	188.0	0.25	200.0	0.24
178.0	0.27	190.0	0.25		

^a $\sigma(\text{Mb})=1.0975 \times 10^2 (df/dE)(\text{eV}^{-1})$.

Table 6.2: Absolute integrated oscillator strengths for the $\tilde{A} \leftarrow \tilde{X}$ band of the photoabsorption spectrum of NH_3 from 5.67 to 7.42 eV. The areas of the Gaussian peak shapes which have been fitted to the presently measured high-resolution photoabsorption oscillator strength data (see text for details) are given along with integrated oscillator strength data obtained from previously reported absolute photoabsorption data [267, 268, 272, 278, 281]. These differential oscillator strength spectra [267, 268, 272, 278, 281] have been digitized and have been numerically integrated over the listed energy ranges.

Vibrational Quantum Number v_2'	Photon Energy Range (eV)	Integrated Oscillator Strength (10^{-2})					
		HR data Present Work	[267]	[268]	[272]	[278]	[281]
0	5.67–5.78	0.0300	0.0294	0.0233	0.0233		0.0414
1	5.78–5.89	0.100	0.112	0.0877	0.0794		0.113
2	5.89–6.00	0.236	0.309	0.264	0.184		0.270
3	6.00–6.12	0.421	0.557	0.401	0.294		0.564
4	6.12–6.24	0.628	0.835	0.681	0.463	0.662	0.816
5	6.24–6.35	0.793	0.995	0.901	0.590	0.848	1.01
6	6.35–6.46	0.903	1.11	1.02	0.665	0.884	1.11
7	6.46–6.58	0.929	1.14	0.932	0.657	0.924	1.06
8	6.58–6.70	0.868	1.05	0.954	0.744	0.901	1.10
9	6.70–6.82	0.757	0.774	0.834		0.752	0.996
10	6.82–6.94	0.610	0.619	0.632		0.541	0.671
11	6.94–7.06	0.473	0.452	0.434		0.405	0.511
12	7.06–7.18	0.332	0.300	0.313		0.282	0.423
13	7.18–7.29	0.222		0.197		0.177	0.302
14	7.29–7.42 ^(a)	0.147		0.134		0.105	0.264
	Total	7.449	8.28	7.81	3.700	6.481	9.27

^aThe energy region from 7.29–7.42 eV includes contributions from the $\tilde{A}(v_2' = 14) \leftarrow \tilde{X}$ and $\tilde{B}(v_2' = 0) \leftarrow \tilde{X}$ vibronic transitions. The position of the origin of the $\tilde{B} \leftarrow \tilde{X}$ band was determined to overlap with the $\tilde{A}(v_2' = 14) \leftarrow \tilde{X}$ transition by Douglas and Hollas using high-resolution optical absorption spectroscopy [251].

Table 6.3: Absolute integrated oscillator strengths for the 7.42–8.62 eV energy region of the photoabsorption spectrum of NH_3 . The presently reported high-resolution differential oscillator strength data have been integrated over the listed energy regions. Previously reported photoabsorption spectra in the 7.42–8.62 eV energy range [268, 273, 278, 281] have been digitized and then integrated over the same energy regions for comparison.

Photon Energy Range (eV)	Integrated Oscillator Strength (10^{-2})				
	HR data				
	Present Work	[268]	[273]	[278]	[281]
7.42–7.52	0.0906	0.0784		0.0686	0.187
7.52–7.65	0.0930	0.0771	0.0624	0.0760	0.205
7.65–7.75	0.0994	0.0642	0.0660	0.0872	0.179
7.75–7.87	0.137	0.0911	0.0996	0.134	0.201
7.87–8.00	0.169	0.130	0.179	0.170	0.220
8.00–8.11	0.182	0.164	0.164	0.238	0.243
8.11–8.25	0.200	0.138	0.183	0.231	0.305
8.25–8.36	0.176	0.110	0.104	0.260	0.215
8.36–8.49	0.176	0.122	0.143	0.252	0.244
8.49–8.62	0.218	0.203	0.192	0.291	0.285
Total	1.541	1.178	1.193	1.808	2.284

Table 6.4: Absolute integrated oscillator strengths for the 8.62–9.32 eV energy region of the photoabsorption spectrum of NH_3 . The presently reported high-resolution differential oscillator strength data have been integrated over the listed energy regions. Previously reported photoabsorption spectra in the 8.62–9.32 eV energy range [268, 273, 278, 281] have been digitized and then integrated over the same energy regions for comparison.

Photon Energy Range (eV)	Integrated Oscillator Strength (10^{-2})				
	HR data Present Work	[268]	[273]	[278]	[281]
8.62–8.68	0.137	0.134	0.133	0.171	0.160
8.68–8.83	0.527	0.666	0.543	0.577	0.966
8.83–8.95	0.778	0.709	0.886	0.732	1.04
8.95–9.07	1.04	1.01	1.17	1.31	1.45
9.07–9.20	1.27	1.18	1.38	1.15	1.57
9.20–9.32	1.37	1.52	1.58	1.31	1.68
Total	5.12	5.22	5.69	5.25	6.85

Table 6.5: Absolute integrated oscillator strengths for the 9.32–10.21 eV energy region of the photoabsorption spectrum of NH_3 . The presently reported high-resolution differential oscillator strength data have been integrated over the listed energy regions. Previously reported photoabsorption spectra in the 9.32–10.21 eV energy range [268, 273, 278, 281] have been digitized and then integrated over the same energy regions for comparison.

Photon Energy Range (eV)	Integrated Oscillator Strength (10^{-2})				
	HR data				
	Present Work	[268]	[273]	[278]	[281]
9.32–9.45	1.38	1.50	1.41	1.24	1.55
9.45–9.59	1.45	1.57	1.47	1.25	1.47
9.59–9.72	1.31	1.25	1.52	0.968	1.37
9.72–9.84	1.21	1.25	1.42	0.978	1.26
9.84–9.97	1.22	1.19	1.28	0.979	1.29
9.97–10.09	1.21	1.08	1.20	0.968	
10.09–10.21	1.26	1.13	1.36	1.02	
Total	9.04	8.97	9.66	7.40	6.94

Table 6.6: Absolute integrated oscillator strengths for the 10.21–11.53 eV energy region of the photoabsorption spectrum of NH_3 . The presently reported high-resolution differential oscillator strength data have been integrated over the listed energy regions. Previously reported photoabsorption spectra in the 10.21–11.53 eV energy range [268, 273, 278, 280] have been digitized and then integrated over the same energy regions for comparison.

Photon Energy Range (eV)	Integrated Oscillator Strength (10^{-2})				
	HR data Present Work	[268]	[273]	[278]	[280]
10.21–10.34	1.35	1.27	1.48	1.07	1.26
10.34–10.47	1.45	1.37	1.62	1.20	1.53
10.47–10.60	1.69	1.68	2.19	1.44	1.79
10.60–10.72	1.64	1.62	1.69	1.41	1.83
10.72–10.84	1.95	1.84	1.97	1.66	2.18
10.84–10.97	2.15	2.09	2.24	1.80	2.36
10.97–11.11	2.54	2.44	2.65	2.16	2.77
11.11–11.23	2.37	2.26	2.61	1.92	2.70
11.23–11.38	2.92	2.71	3.02	2.38	3.21
11.38–11.53	2.97	3.17	2.98	2.37	3.26
Total	21.03	20.45	22.45	17.41	22.89

Table 6.7: Integrated dipole oscillator strengths in selected photon energy ranges for NH₃. This table contains the constrained integrated oscillator strengths and also the integrated oscillator strengths obtained from unmodified experimental or mixture rule data. The integrated DOSs obtained from the recommended DOSD of Zeiss *et al.* [29] are shown for comparison.

Energy Region (eV)	Integrated Oscillator Strength ^a							
	Constrained Values DOSDA ^b	Constrained Values DOSDB ^{b,c}	Constrained Values DOSDC ^b	High-Resolution Data ^d	Low-Resolution Data ^{c,d}	Samson <i>et al.</i> [279] PhAbs.	Mixture Rule Eq 6.1	Zeiss <i>et al.</i> [29] DOSD
5.685–7.563	8.278(-2)	7.349(-2) ^c	8.197(-2)	7.384(-2)	7.122(-2) ^c			8.023(-2)
7.563–8.590	1.334(-2)	2.622(-2) ^c	1.333(-2)	1.324(-2)	2.613(-2) ^c			1.141(-2)
8.590–10.19	1.418(-1)	1.445(-1) ^c	1.408(-1)	1.359(-1)	1.429(-1) ^c			1.460(-1)
10.19–11.07	1.231(-1)	1.322(-1) ^c	1.225(-1)	1.201(-1)	1.314(-1) ^c			1.267(-1)
11.07–12.40	2.677(-1)	2.645(-1)	2.936(-1)	2.574(-1)	2.618(-1)	2.873(-1)		2.769(-1)
12.40–13.08	1.136(-1)	1.251(-1)	1.152(-1)	1.121(-1)	1.246(-1)	1.145(-1)		1.161(-1)
13.08–14.06	1.736(-1)	1.855(-1)	1.709(-1)	1.707(-1)	1.845(-1)	1.695(-1)		1.765(-1)
14.06–18.05	1.187(0)	1.146(0)	1.166(0)	1.105(0)	1.119(0)	1.124(0)		1.170(0)
18.05–22.03	1.084(0)	1.069(0)	1.063(0)	1.040(0)	1.050(0)	1.040(0)		1.077(0)
22.03–25.09	6.657(-1)	6.729(-1)	6.663(-1)	6.532(-1)	6.657(-1)	6.592(-1)		6.731(-1)
25.09–28.02	5.371(-1)	5.275(-1)	5.235(-1)	5.304(-1)	5.232(-1)	5.197(-1)		5.353(-1)
28.02–30.88	4.403(-1)	4.311(-1)	4.347(-1)	4.365(-1)	4.283(-1)	4.323(-1)		4.167(-1)
30.88–40.0	9.647(-1)	9.639(-1)	9.644(-1)		9.504(-1)	9.541(-1)	8.820(-1)	9.096(-1)

Table 6.7: Integrated dipole oscillator strengths for NH₃ (continued).

Energy Region (eV)	Integrated Oscillator Strength ^a							
	Constrained Values DOSDA ^b	Constrained Values DOSDB ^{b,c}	Constrained Values DOSDC ^b	High-Resolution Data ^d	Low-Resolution Data ^{c,d}	Samson <i>et al.</i> [279] PhAbs.	Mixture Rule Eq 6.1	Zeiss <i>et al.</i> [29] DOSD
40.0-50.0	6.245(-1)	6.255(-1)	6.236(-1)		6.199(-1)	6.198(-1)	5.967(-1)	6.011(-1)
50.0-60.0	3.835(-1)	3.841(-1)	3.912(-1)		3.820(-1)	3.898(-1)	4.414(-1)	4.339(-1)
60.0-80.0	4.363(-1)	4.373(-1)	4.474(-1)		4.346(-1)	4.457(-1)	5.554(-1)	5.414(-1)
80.0-100.0	2.328(-1)	2.332(-1)	2.417(-1)		2.324(-1)	2.412(-1)	2.991(-1)	2.955(-1)
100.0-124.4	1.691(-1)	1.693(-1)	1.738(-1)		1.689(-1)	1.735(-1)	1.913(-1)	1.907(-1)
124.4-150.0	1.152(-1)	1.153(-1)	9.772(-2)		1.151(-1)	9.764(-2)	1.199(-1)	1.196(-1)
150.0-200.0	1.421(-1)	1.423(-1)	1.422(-1)		1.420(-1)		1.341(-1)	1.335(-1)
200.0-400.0	1.672(-1)	1.679(-1)	1.678(-1)				1.667(-1)	1.663(-1)
400.0-425.0	2.623(-1)	2.639(-1)	2.637(-1)			2.610(-1) ^e	1.543(-1)	1.543(-1)
425-1000.0	1.289(0)	1.314(0)	1.311(0)				1.268(0)	1.268(0)
1000.0-10 ⁴	3.802(-1)	3.814(-1)	3.812(-1)				3.793(-1)	3.795(-1)
10 ⁴ -10 ⁶	3.301(-3)	3.301(-3)	3.301(-3)				3.301(-3)	3.300(-3)
10 ⁶ -∞	5.832(-8)	5.832(-8)	5.832(-8)				5.832(-8)	5.830(-8)

^aPower of ten is in parentheses e.g. 8.278(-2)=8.278×10⁻².

^bDetermined by Kumar and Meath [72].

^cInvolves low-resolution data. As discussed in the text, the integrated oscillator strengths in the discrete excitation region (below 11.07 eV) may not be reliable due to resolution effects, whereas the *total* integrated oscillator strength from 5.685-11.07 eV is reliable.

^dExperiment, present work, see also reference [323] for further details.

^eAkimov *et al.* [303] nitrogen K-shell photoabsorption data.

Table 6.8: The dipole sums S_k , logarithmic dipole sums L_k , and mean excitation energies I_k for NH_3 calculated from various DOSDs. The previously reported results of Zeiss *et al.* [29] are shown for comparison. The values obtained from the constrained DOSDA are recommended.

Property	Initial DOSDA ^a	Constrained DOSDA	Constrained DOSDB	Zeiss <i>et al.</i> DOSDA [29]	Property	Initial DOSDA	Constrained DOSDA	Constrained DOSDB	Zeiss <i>et al.</i> DOSD [29]
S_2	6.175(3)	6.193(3)	6.214(3)	6.156(3)	S_{-12}	2.457(6)	2.746(6)	2.898(6)	2.758(6)
S_1	7.257(1)	7.329(1)	7.393(1)	7.162(1)					
S_0	9.772(0)	1.000(1)	1.000(1)	1.000(1)					
$S_{-1/2}$	8.341(0)	8.602(0)	8.581(0)	8.625(0)	L_2	3.846(4)	3.853(4)	3.861(4)	3.842(4)
S_{-1}	8.975(0)	9.310(0)	9.290(0)	9.319(0)	L_1	2.377(2)	2.395(2)	2.417(2)	2.340(2)
$S_{-3/2}$	1.077(1)	1.123(1)	1.122(1)	1.123(1)	L_0	6.970(0)	6.962(0)	7.049(0)	6.796(0)
S_{-2}	1.391(1)	1.456(1)	1.456(1)	1.456(1)	L_{-1}	-2.480(0)	-2.671(0)	-2.681(0)	-2.641(0)
$S_{-5/2}$	1.906(1)	2.004(1)	2.006(1)	2.005(1)	L_{-2}	-7.962(0)	-8.466(0)	-8.496(0)	-8.479(0)
S_{-3}	2.757(1)	2.913(1)	2.915(1)	2.916(1)					
S_{-4}	6.687(1)	7.140(1)	7.120(1)	7.144(1)	$I_2(\text{eV})$	1.380(4)	1.370(4)	1.359(4)	1.397(4)
S_{-5}	1.921(2)	2.073(2)	2.056(2)	2.071(2)	$I_1(\text{eV})$	7.195(2)	7.143(2)	7.151(2)	7.134(2)
S_{-6}	6.287(2)	6.855(2)	6.768(2)	6.840(2)	$I_0(\text{eV})$	5.553(1)	5.459(1)	5.507(1)	5.369(1)
S_{-8}	8.633(3)	9.547(3)	9.468(3)	9.527(3)	$I_{-1}(\text{eV})$	2.064(1)	2.043(1)	2.039(1)	2.050(1)
S_{-10}	1.404(5)	1.564(5)	1.588(5)	1.565(5)	$I_{-2}(\text{eV})$	1.535(1)	1.521(1)	1.518(1)	1.520(1)

^aPower of ten in parentheses e.g. 6.175(3)=6.175 × 10³.

Table 6.9: Values of the molar refractivity of NH₃ (ideal gas at STP, 0°C and 1 atm.) evaluated using the constrained DOSD A, and a comparison with previously reported experimental data [287–289].

λ (Å)	Molar Refractivity		λ (Å)	Molar Refractivity	
	Constrained DOSD A	Experiment		Constrained DOSD A	Experiment
6709.0	5.571	5.570 ^d	3861.0	5.876	5.878 ^c
6564.0	5.577	5.581 ^b	3544.0	5.976	5.978 ^c
6440.0	5.583	5.582 ^d	3342.0	6.060	6.062 ^c
5895.0	5.612	5.615 ^b	2968.0	6.292	6.290 ^c
5792.0	5.618	5.618 ^d	2926.0	6.327	6.326 ^c
5771.0	5.620	5.619 ^d	2894.0	6.356	6.356 ^c
5462.0	5.642 ^a	5.642 ^{bcd}	2857.0	6.391	6.391 ^c
5210.0	5.663	5.663 ^d	2760.0	6.496	6.495 ^c
5087.0	5.675	5.675 ^d	2753.0	6.504 ^a	6.504 ^c
4917.0	5.693	5.697 ^b , 5.694 ^c	2675.0	6.607	6.606 ^c
4801.0	5.707	5.708 ^d	2577.0	6.765	6.766 ^c
4359.0	5.770	5.773 ^b	2464.0	7.010	7.006 ^c
4109.0	5.818	5.820 ^c	2447.0	7.055	7.052 ^c
3985.0	5.845	5.848 ^c	2346.0	7.393	7.392 ^c

^aUsed as constraints in constructing the DOSD.

^bFrivold *et al.* [287].

^cFriberg [288], normalized to Frivold *et al.* [287] at $\lambda = 5462.0$ Å.

^dCuthbertson and Cuthbertson [289], normalized to Frivold *et al.* [287] at $\lambda = 5462.0$ Å.

Chapter 7

Photoabsorption and DOSD Studies of the Methylamines

7.1 Introduction

The absolute photoabsorption spectra of the methylamines are of interest and importance in many areas of science and technology. For example, monomethylamine has been observed in the interstellar medium [103], in the atmosphere of Halley's comet [324, 325], has been included in models of the atmospheres of Uranus and Saturn [326, 327], and is known from photochemistry to be a low-energy source of NH_2 and NH radicals [243]. The use of trimethylamine as an additive ("seed" compound) to improve the performance of UV pre-ionized lasers has been explored [328]. Therefore, absolute photoabsorption oscillator strength (cross-section) data for the methylamines, and the associated dipole properties, are of importance in astrophysics, laser physics, photochemistry, or in any other application where the interaction of high-energy radiation or particles with these molecules is to be understood. Such measurements and properties should also provide a test-bed for *ab initio* calculations of absolute oscillator strengths and dipole properties. However, few such calculations have been reported for the methylamines. The study of photoabsorption oscillator strength data and dipole properties for series of related molecules also yields useful information about functional group additivity trends and their effects on the absorption of highly energetic electromagnetic radiation. A systematic study of such trends can be used to predict the oscillator strength distributions and dipole

properties of larger, more complex molecules for which no data exist, or for which direct measurement may be difficult [54–56, 244].

There is very little absolute photoabsorption oscillator strength data available in the literature for the methylamines which is in striking contrast to the wealth of quantitative information available for the parent member of this series, NH_3 (see section 6.1). Absolute photoabsorption spectra for the methylamines and ammonia have been reported by Tannenbaum *et al.* [267] in the limited energy region 4.8–7.8 eV. In other work, Bertrand *et al.* [277] have measured differential photoabsorption oscillator strengths for CH_3NH_2 and $(\text{CH}_3)_2\text{NH}$ at 10.03 eV, and Grosjean and Bletzinger [328] have measured the absolute photoabsorption spectrum of $(\text{CH}_3)_3\text{N}$ from 8.0–10.8 eV.

In the experimental study of the methylamines CH_3NH_2 (monomethylamine, methanamine), $(\text{CH}_3)_2\text{NH}$ (dimethylamine, N-methylmethanamine), and $(\text{CH}_3)_3\text{N}$ (trimethylamine, N,N-dimethylmethanamine), detailed and wide-ranging absolute oscillator strength data are obtained for these molecules in the energy region from the first excitation threshold to 250 eV. In the associated theoretical work by Kumar and Meath these measured oscillator strengths are used along with mixture rule data, and molar refractivity and Thomas-Reiche-Kuhn (TRK) sum rule constraints, to determine constrained dipole oscillator strength distributions (DOSDs) for these molecules. The DOSDs are, in turn, used to determine reliable values for many of the important dipole properties for the methylamines. These absolute high- and low-resolution oscillator strength data for the methylamines are presented in section 7.2 along with a detailed discussion of the measured spectra and the spectral assignments. The general method used for the construction of the DOSDs and for the evaluation of the dipole properties of the methylamines is outlined in section 2.8, and the results are given in section 7.3 along with an

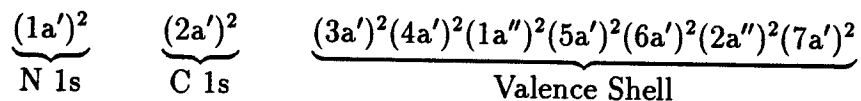
analysis of the uncertainty limits placed on the results for the dipole properties.

7.2 Results and Discussion

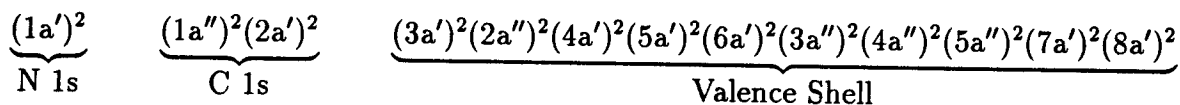
7.2.1 Electronic Structure of the Methylamines

The symmetry groups of highest symmetry that CH_3NH_2 , $(\text{CH}_3)_2\text{NH}$, $(\text{CH}_3)_3\text{N}$, belong to are C_s , C_s , and C_{3v} , respectively. The molecular orbital configurations of the ground states of these molecules in the independent particle model are:

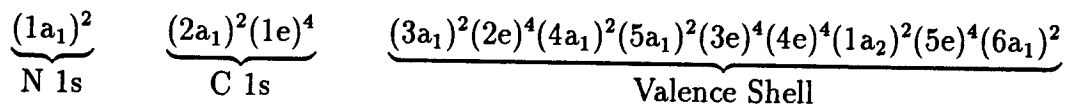
CH_3NH_2 :



$(\text{CH}_3)_2\text{NH}$:



$(\text{CH}_3)_3\text{N}$:



The vertical ionization potentials (VIPs) of the valence-shell states of the methylamines have been determined using high-resolution He(I) and He(II) photoelectron spectroscopy [134, 139, 329], while the inner shell states have been measured using X-ray photoelectron spectroscopy [291, 330–332]. The electronic configurations and vertical ionization potentials for the methylamines are summarized in table 7.1.

7.2.2 Absolute Photoabsorption Measurements for the Methylamines Obtained at Low Resolution

The absolute low-resolution photoabsorption oscillator strengths were determined by Bethe-Born conversion and partial TRK sum-rule normalization of the measured background-subtracted electron energy-loss spectrum as follows. The relative oscillator strength spectra were measured for each of the methylamines from the electronic excitation threshold to an equivalent photon energy of 250 eV. These data were placed on an absolute scale by first fitting a curve of the form

$$\frac{df}{dE} = AE^{-1.5} + BE^{-2.5} + CE^{-3.5} \quad (7.1)$$

to the high-energy portion of the valence-shell relative oscillator strength tail from 90 to 250 eV. In equation 7.1, df/dE is the differential oscillator strength, E is the energy loss (or equivalent photon energy) and A , B , and C are best-fit parameters to the data. The values of the parameters were found to be $7.326 \text{ eV}^{0.5}$, $108.3 \text{ eV}^{1.5}$, and $4.980 \times 10^4 \text{ eV}^{2.5}$, respectively, for monomethylamine, $9.932 \text{ eV}^{0.5}$, $151.6 \text{ eV}^{1.5}$, and $6.071 \times 10^4 \text{ eV}^{2.5}$, for dimethylamine, and $14.53 \text{ eV}^{0.5}$, $-200.6 \text{ eV}^{1.5}$, and $1.008 \times 10^5 \text{ eV}^{2.5}$, for trimethylamine. This curve was then integrated from 250 eV to infinite energy for each spectrum in order to estimate the valence-shell oscillator strength contribution above the last measured differential oscillator strength data point at 250 eV. Using these procedures it was found that $\sim 7\%$ of the total valence-shell oscillator strength distribution is located above 250 eV for each of the three methylamines. The total area under the valence-shell spectrum (i.e., the contribution from the measured oscillator strengths plus that under the extrapolated curve) was normalized to 14.54 for monomethylamine, 20.75 for dimethylamine, and 26.96 for trimethylamine. These integrated values correspond to the total number of

valence-shell electrons in these molecules plus a small contribution ($\sim 5\%$) to account for the Pauli-excluded transitions from the inner-shells (the nitrogen and carbon K shells) to the already-occupied valence-shell orbitals. The Pauli-excluded transition contribution was estimated for each molecule from sums of atomic corrections based on Hartree-Slater calculations (see section 3.1.1). The absolute oscillator strength data thus obtained are estimated to be accurate to $\pm 5\%$.

The low-resolution (~ 1 eV fwhm) valence-shell absolute photoabsorption oscillator strengths for monomethylamine, dimethylamine, and trimethylamine measured in the present work from the first excitation threshold to 250 eV using dipole (e,e) spectroscopy are shown in figures 7.1, 7.2, and 7.3, and are given numerically in tables 7.2, 7.3 and 7.4, respectively. Panel (a) of figures 7.1–7.3 shows the full measured spectra from the photoabsorption threshold to 250 eV, panel (b) shows the spectra from 30–100 eV, and panel (c) shows the 86–250 eV energy region. The absolute photoabsorption data below 30 eV are shown, and described, in greater detail in conjunction with the high-resolution results (see section 7.2.3 below). It is interesting to note from figures 7.1–7.3 that our measured low-resolution oscillator strength spectra each exhibit essentially the same trend with the sums of experimental [161] and calculated [162] atomic oscillator strengths for the constituent atoms. In particular, the summed atomic oscillator strength data agree quite well with the measured molecular photoabsorption oscillator strength data for the methylamines from 70 eV to the limit of the measured data at 250 eV. However, below 70 eV the summed atomic oscillator strength data [161, 162] are increasingly lower than the present data for all three molecules. Above 170 eV the atomic sums are slightly lower than the measured results.

It has often been assumed (see for example reference [333]) that the sums of atomic

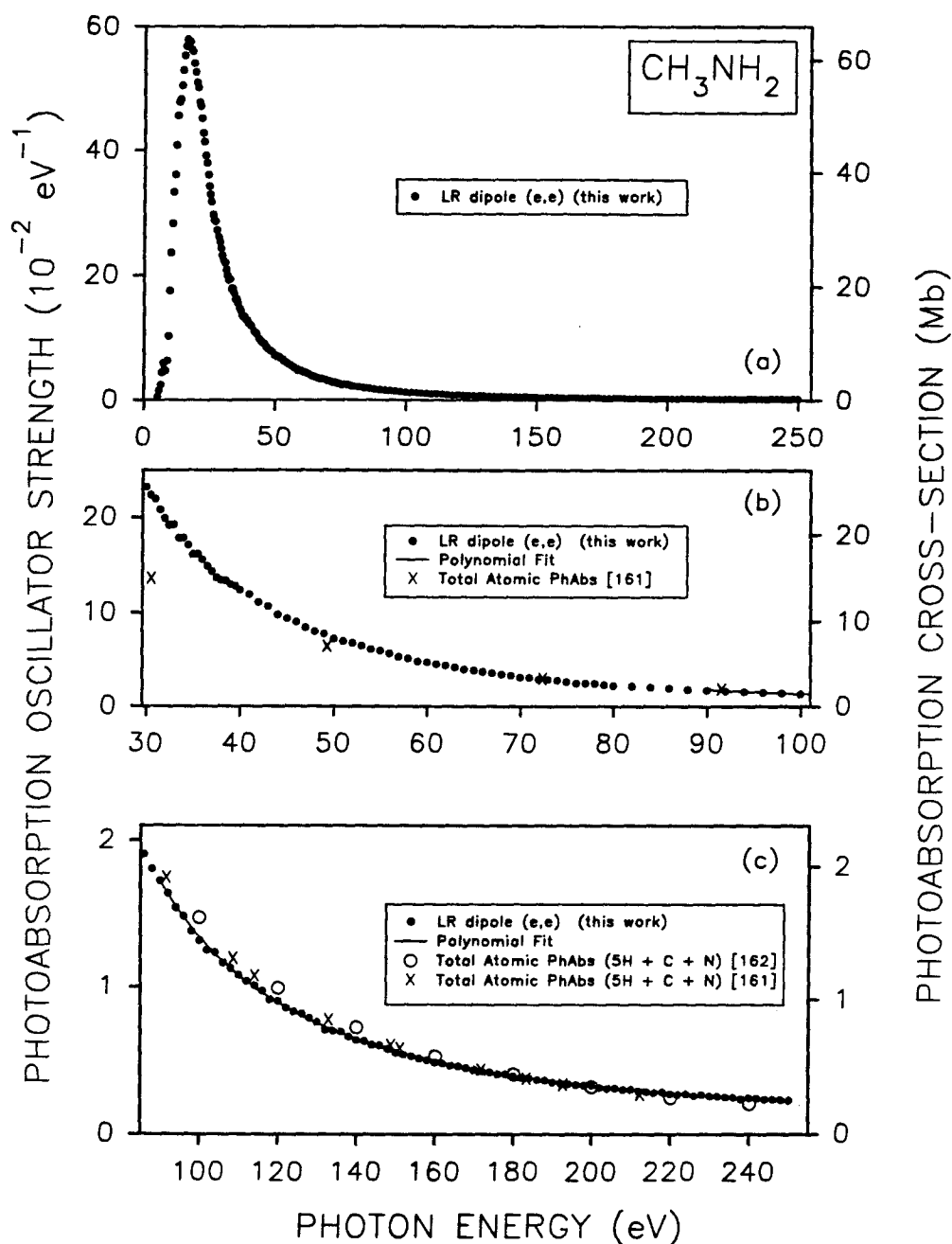


Figure 7.1: Absolute oscillator strengths for the photoabsorption of CH_3NH_2 obtained at a resolution of ~ 1 eV fwhm: (a) The entire measured spectrum from 5.5–250 eV. (b) 30–100 eV. (c) The high-energy valence-shell tail from 86–250 eV. Also shown on (b) and (c) are the valence-shell polynomial fit (solid line), and the experimental [161] and theoretical [162] summed atomic oscillator strengths for the constituent atoms of CH_3NH_2 (open circles and crosses, respectively).

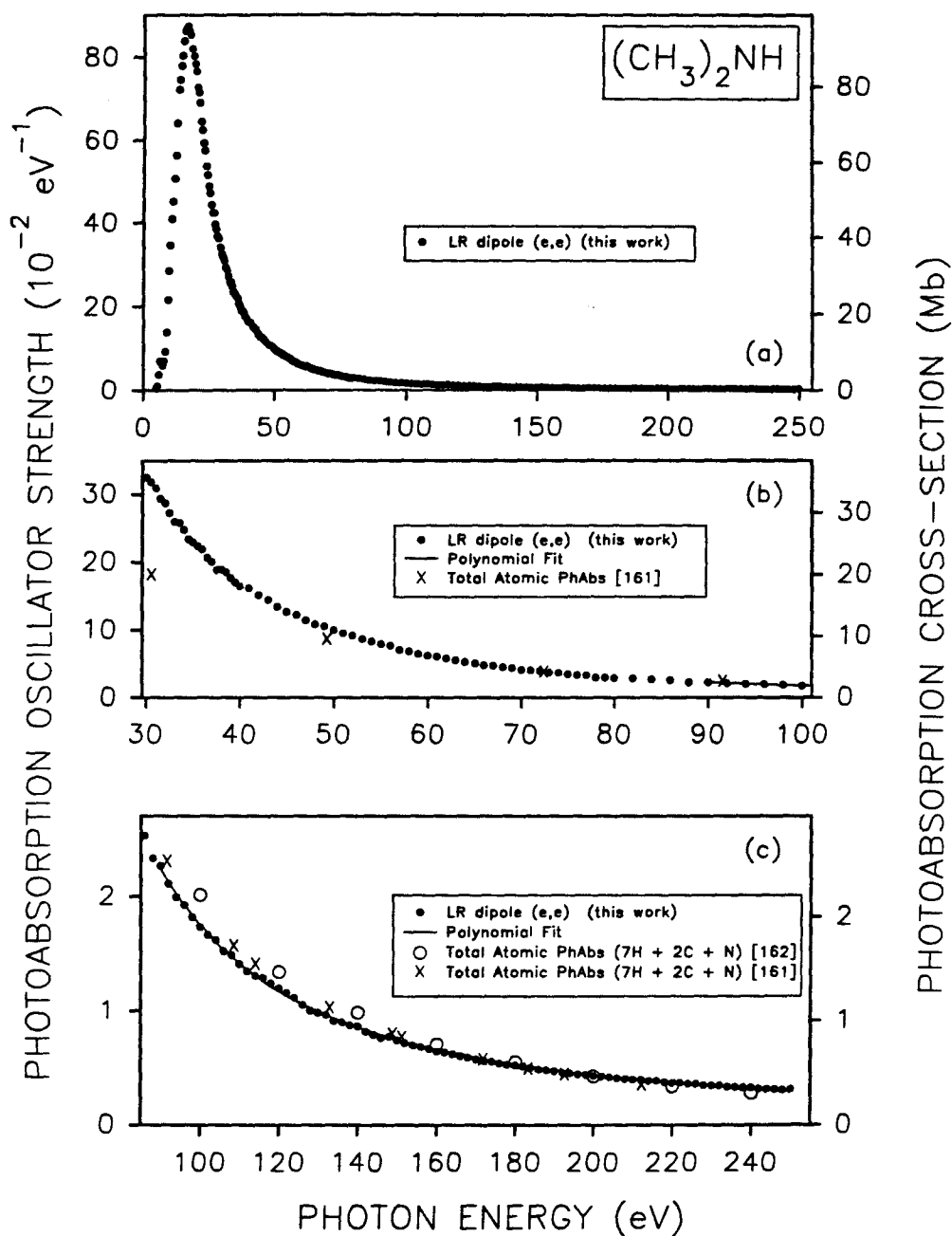


Figure 7.2: Absolute oscillator strengths for the photoabsorption of $(\text{CH}_3)_2\text{NH}$ obtained at a resolution of ~ 1 eV fwhm: (a) The entire measured spectrum from 5.0–250 eV. (b) 30–100 eV. (c) The high-energy valence-shell tail from 86–250 eV. Also shown on (b) and (c) are the valence-shell polynomial fit (solid line), and the experimental [161] and theoretical [162] summed atomic oscillator strengths for the constituent atoms of $(\text{CH}_3)_2\text{NH}$ (open circles and crosses, respectively).

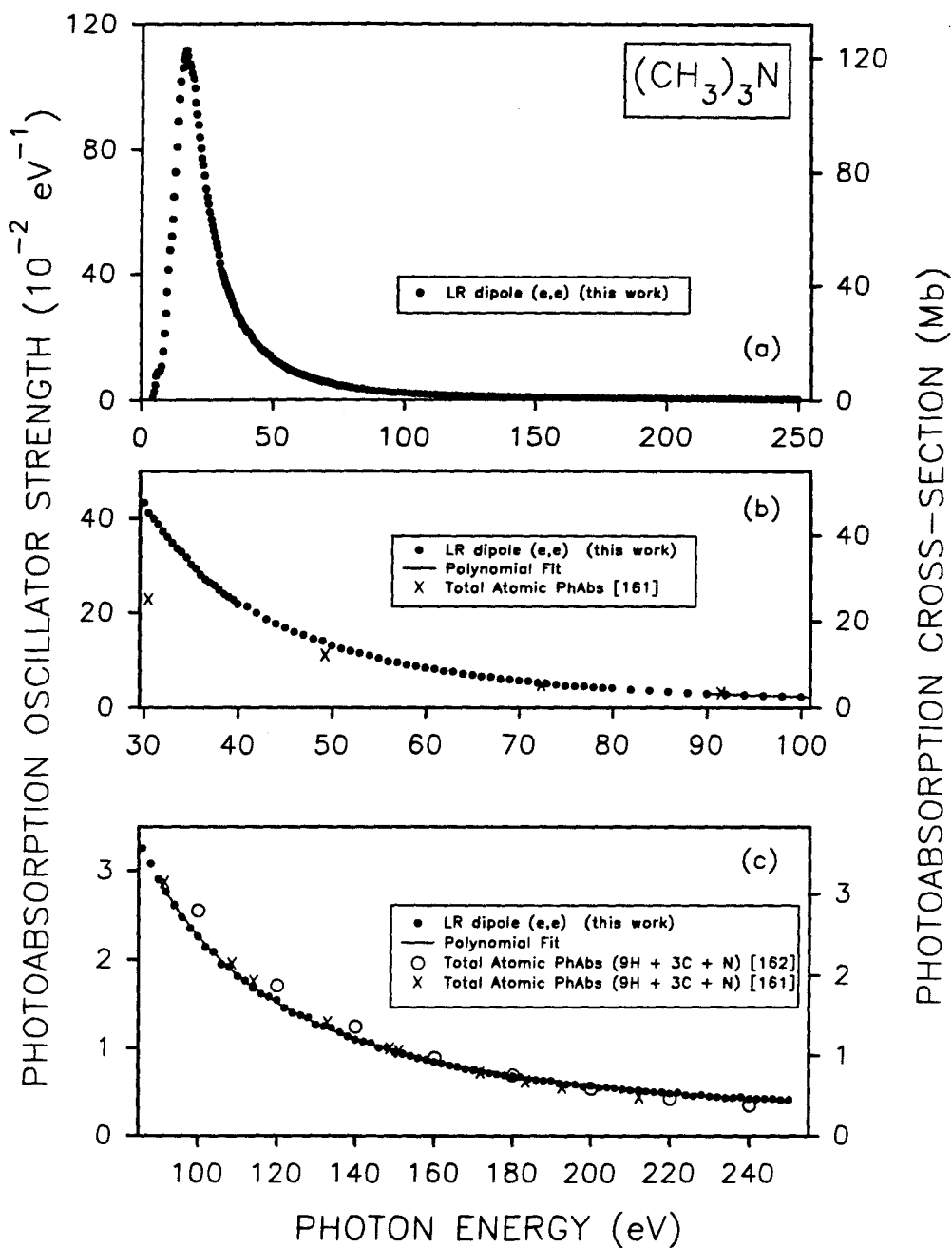


Figure 7.3: Absolute oscillator strengths for the photoabsorption of $(\text{CH}_3)_3\text{N}$ obtained at a resolution of ~ 1 eV fwhm: (a) The entire measured spectrum from 4.5–250 eV. (b) 30–100 eV. (c) The high-energy valence-shell tail from 86–250 eV. Also shown on (b) and (c) are the valence-shell polynomial fit (solid line), and the experimental [161] and theoretical [162] summed atomic oscillator strengths for the constituent atoms of $(\text{CH}_3)_3\text{N}$ (open circles and crosses, respectively).

oscillator strengths are equal to molecular oscillator strengths sufficiently far (≥ 30 eV) above an atomic *inner-shell* ionization edge. At such photoelectron energies it is assumed that molecular effects, such as shape resonances, have died out and that the ejected electron “sees” mainly an atomic core as it is ionized. However, in the 70–250 eV energy region of the valence-shell photoabsorption spectra of the methylamines the electron is not ejected from an atomic-like (core) orbital, so it is interesting to note that there is generally quite good agreement between the sums of atomic data, and our reported molecular oscillator strengths in this energy region. The fact that the curves cross at ~ 170 eV, that is, that the atomic oscillator strength sums for each methylamine are higher than the corresponding measured oscillator strengths from 90 to 170 eV, but are slightly lower from 170 to 250 eV, is not surprising since both sets of data should be subject to the same *total* integrated oscillator strength over the entire energy range (from zero to infinity) according to the TRK sum rule. The small differences between the experimental [161] and theoretical [162] summed atomic oscillator strength data from 100 to 240 eV, as seen in panel c of figures 7.1–7.3, are due, at least in part, to errors involved in the digitization of the logarithmic plots reported for the theoretical data [162]. The digitization error will compound as the number of carbon atoms increases.

7.2.3 Absolute Photoabsorption Measurements for the Methylamines Obtained at High Resolution

The high-resolution relative oscillator strength spectrum for each of the methylamines was placed on an absolute scale by single point normalization in the smooth continuum region to the corresponding low-resolution photoabsorption oscillator strength data

obtained in the present work. The high-resolution (0.048 eV fwhm) absolute photoabsorption spectra of monomethylamine, dimethylamine, and trimethylamine from 4–31 eV are shown on figures 7.4, 7.5, and 7.6, respectively. Also shown on the figures are the low-resolution oscillator strength data obtained in the present work (see section 7.2.2 above). It can be seen that the present high- and low-resolution oscillator strength data are in good agreement with each other over the entire range of measurement (4–31 eV). This is an important consistency check on our measurements since the high- and low-resolution dipole (e,e) spectrometers have different Bethe-Born factors owing to their different scattering kinematics and geometries.

Since no *ab initio* calculations of transition energies and oscillator strengths have been reported for the methylamines, definite assignments of the spectra cannot be made. Therefore, in the present work the transferability of Rydberg term values [334–336] has been used to make tentative assignments for the more prominent features observed in figures 7.4–7.6. It might be expected that the electronic spectra of the methylamines will be dominated by transitions to Rydberg orbitals from the occupied valence orbitals since this behaviour appears to be the situation for the related molecules CH₄ [87, 124] and NH₃ [124, 337]. The assignment of transitions to Rydberg upper states has been described earlier in section 2.6. Electron momentum spectroscopy has demonstrated that the highest occupied molecular orbitals (HOMOs) of the methylamines have a mixed s and p character with the s content increasing with successive methylation [338, 339]. Therefore transitions are expected from the HOMO to s, p and d Rydberg manifolds since atomic selection rule arguments have been found [334–336] to be a helpful guide for interpretation of molecular spectra. On this basis, we have assigned the lowest energy peaks in the spectra as transitions from the respective HOMO orbitals to the 3s and

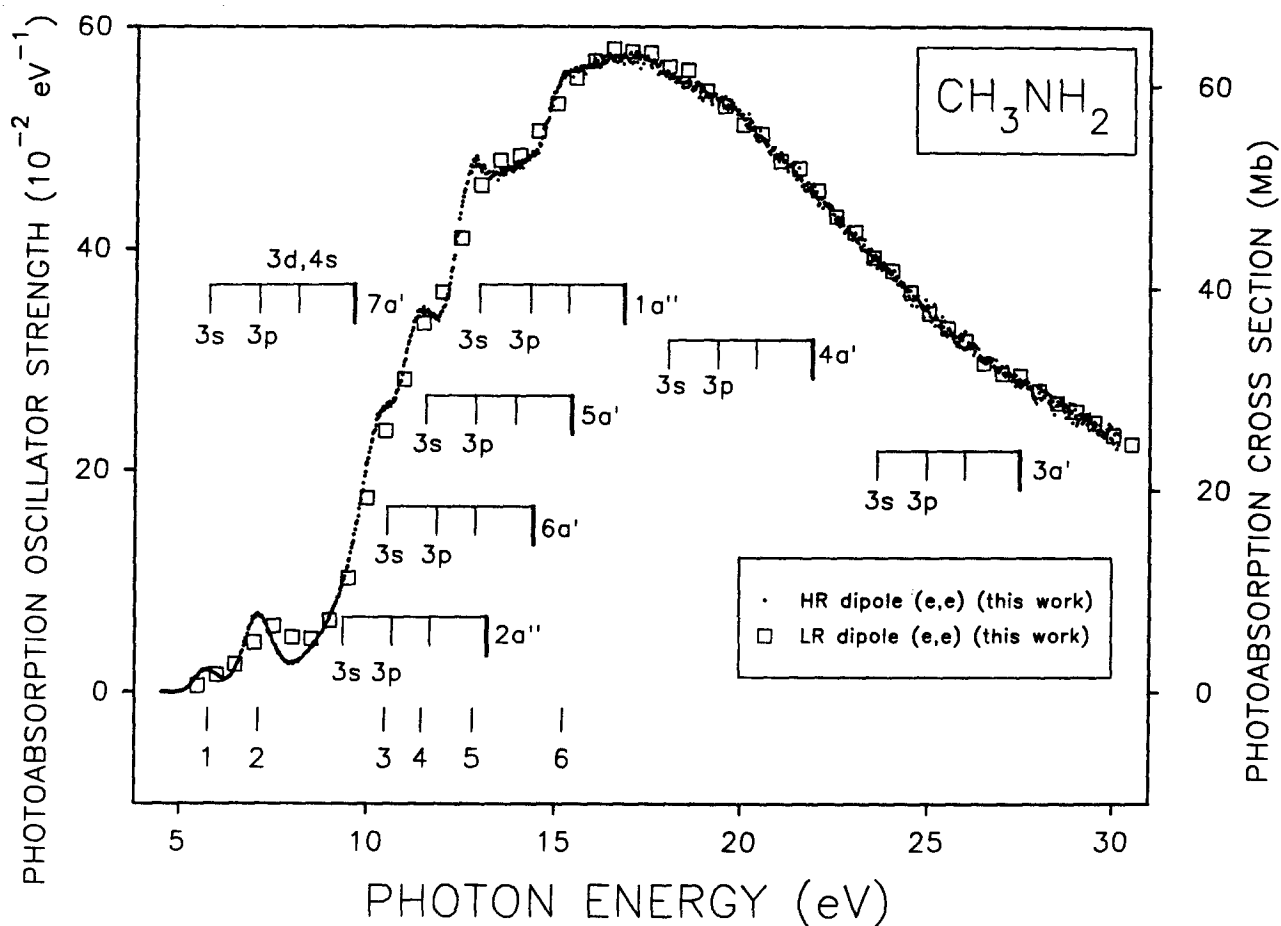


Figure 7.4: Comparison of the experimental high- and low-resolution (0.048 eV fwhm and ~ 1 eV fwhm, respectively) absolute oscillator strength spectra for the photoabsorption of CH_3NH_2 . The numbered vertical lines indicate the positions of the observed spectral features—see table 7.5. For each ion state the vertical ionization potential (heavy solid vertical line) is shown along with the positions (vertical lines) of the 3s and 3p Rydberg transitions as predicted using the same term values as for the lowest energy transitions (labelled 1 and 2) in the spectrum. The positions of the 3d,4s Rydberg transitions have been predicted using equation 2.33. The manifolds assume transferability of Rydberg term values (see text for details).

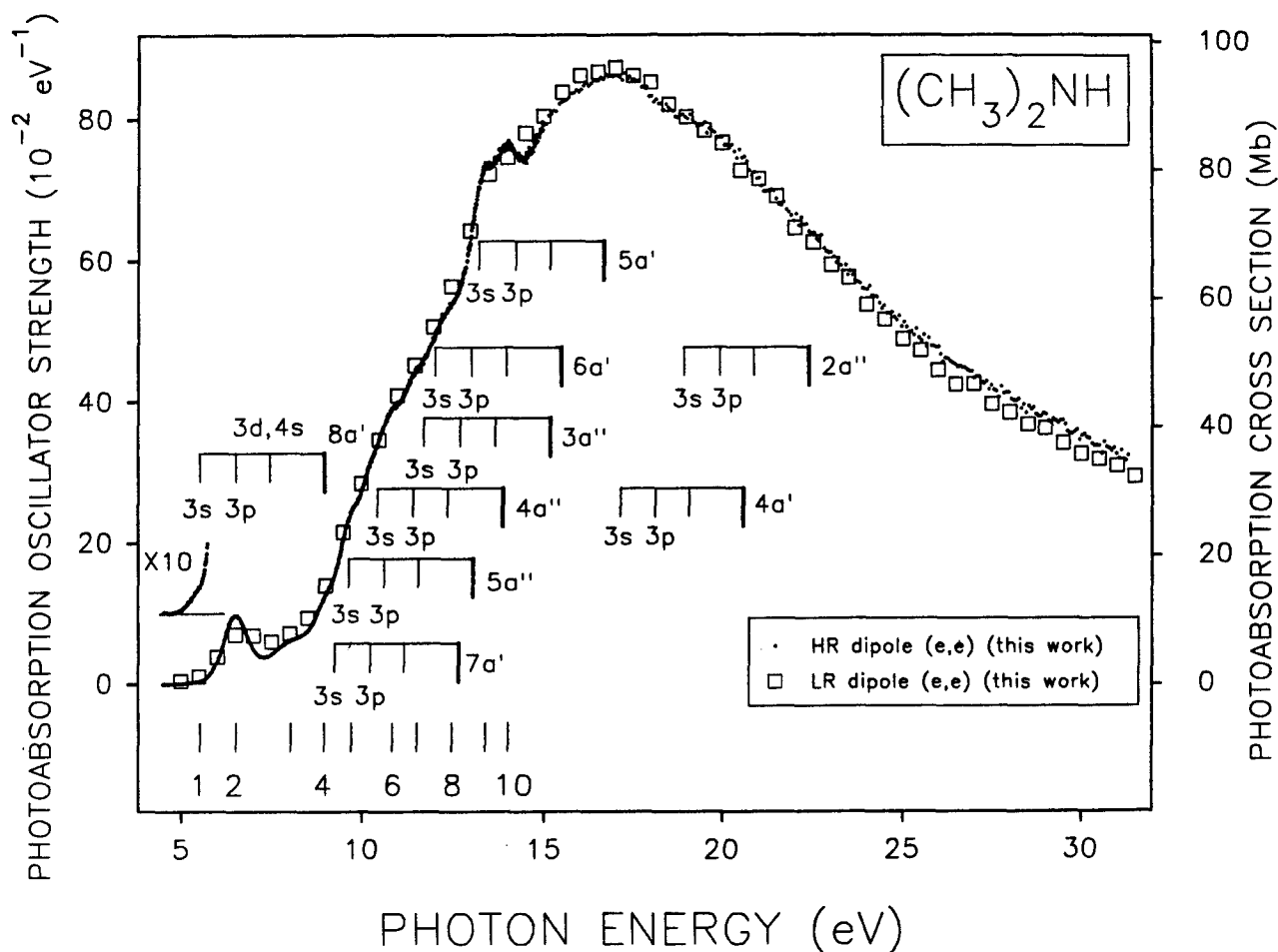


Figure 7.5: Comparison of the experimental high- and low-resolution (0.048 eV fwhm and ~ 1 eV fwhm, respectively) absolute oscillator strength spectra for the photoabsorption of $(\text{CH}_3)_2\text{NH}$. The numbered vertical lines indicate the positions of the observed spectral features—see table 7.6. For each ion state the vertical ionization potential (heavy solid vertical line) is shown along with the positions (vertical lines) of the 3s and 3p Rydberg transitions as predicted using the same term values as for the lowest energy transitions (labelled 1 and 2) in the spectrum. The positions of the 3d,4s Rydberg transitions have been predicted using equation 2.33. The manifolds assume transferability of Rydberg term values (see text for details).

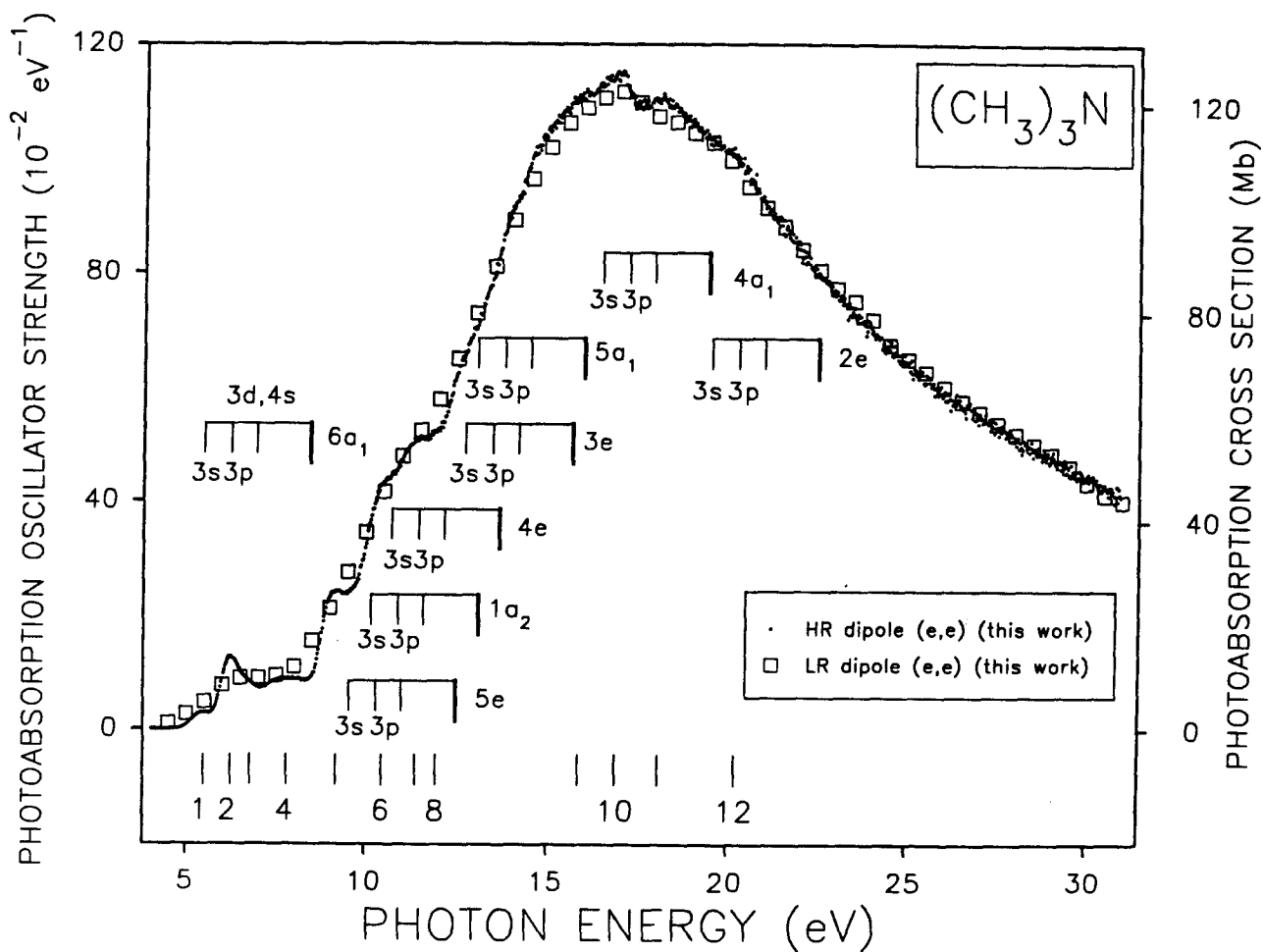


Figure 7.6: Comparison of the experimental high- and low-resolution (0.048 eV fwhm and ~ 1 eV fwhm, respectively) absolute oscillator strength spectra for the photoabsorption of $(\text{CH}_3)_3\text{N}$. The numbered vertical lines indicate the positions of the observed spectral features—see table 7.7. For each ion state the vertical ionization potential (heavy solid vertical line) is shown along with the positions (vertical lines) of the 3s and 3p Rydberg transitions as predicted using the same term values as for the lowest energy transitions (labelled 1 and 2) in the spectrum. The positions of the 3d,4s Rydberg transitions have been predicted using equation 2.33. The manifolds assume transferability of Rydberg term values (see text for details).

3p Rydberg orbitals for each of the methylamines. From these HOMO assignments the energies of the corresponding 3s and 3p transitions from the other occupied molecular orbitals have been calculated assuming transferrability of term values, and the resulting manifolds are shown on figures 7.4–7.6. The VIPs on the manifolds are from photoelectron spectroscopic measurements [134, 139, 329]. The positions of the 3d and 4s Rydberg orbitals are degenerate and are each predicted from equation 2.33 to have a term value of 1.51 eV, which assumes quantum defects of 1 and 0 for the s and d Rydberg orbitals, respectively [167]. It can be seen from figures 7.4–7.6 that the excitation spectra of the methylamines correspond quite closely to a superposition of peaks due to the predicted transitions to Rydberg orbitals. The assignments suggested by the transferrability of Rydberg term values, as shown on figures 7.4–7.6, are summarized in tables 7.5, 7.6, and 7.7, for monomethylamine, dimethylamine, and trimethylamine, respectively. For each observed transition the term value (tables 7.5–7.7) was calculated from the measured peak energy and the ionization potential of the initial state. Then, as a consistency check on each assignment, the denominator of the right-hand side of equation 2.33 was evaluated for each term value and the predicted principle quantum number, and the predicted character of the final Rydberg state were considered to be confirmed if the quantum defect was in the range $0.8 \leq \delta_l \leq 1.3$ for s Rydberg orbitals, $0.4 \leq \delta_l \leq 0.8$ for p Rydberg orbitals, and $0.0 \leq \delta_l \leq 0.2$ for d Rydberg orbitals [167]. As a result of this analysis and with the above assumptions, it is found that all of the major observed spectral features in the valence-shell photoabsorption spectra of the methylamines can be assigned using this Rydberg orbital scheme. The resulting Rydberg term values show good agreement with those for the corresponding transitions in the carbon and nitrogen K-shell inner-shell electron energy-loss (ISEELS) spectra of the methylamines reported

earlier from this laboratory by Wight and Brion [124], and by Sodhi and Brion [337]. Such transferrability between inner shell and valence shell spectra is to be expected for Rydberg transitions [334–336].

The low energy portions of the valence-shell spectra of the methylamines from 4–10 eV are shown in figure 7.7. In addition to the 3s, 3p, and the degenerate 3d,4s assignments discussed above, the predicted positions of the 4p and 5p Rydberg orbitals are also shown. It can be seen that there is good correspondence between all the predicted Rydberg transition energies and the various structures in the oscillator strength data. Also shown are the previously reported and limited range photoabsorption data of Grosjean and Bletzinger [328], Tannenbaum *et al.* [267], and Bertrand *et al.* [277]. It can be seen from the figure that the data reported by Tannenbaum *et al.* [267] are marginally higher, and have a slightly different shape than the present work for all three of the methylamines. The photoabsorption oscillator strength values reported by Bertrand *et al.* [277] at 123.6 nm (10.03 eV) are ~10% and ~20% higher than the present work for monomethylamine and dimethylamine, respectively. The data reported by Grosjean and Bletzinger [328] for trimethylamine agree well with the present results from 8.1–9.0 eV, but are lower above 9.0 eV to the limit of their data at 10.4 eV. In higher resolution optical work Tannenbaum *et al.* [267] observed vibrational progressions in the 3s \leftarrow 7a' and 3p \leftarrow 7a' transitions in monomethylamine, and in the 3p \leftarrow 8a' transition in dimethylamine. Evidence for these vibrational progressions in the 3p \leftarrow 7a' transition of monomethylamine and in the 3p \leftarrow 8a' transition of dimethylamine can be seen in the presently reported, somewhat lower resolution, spectra.

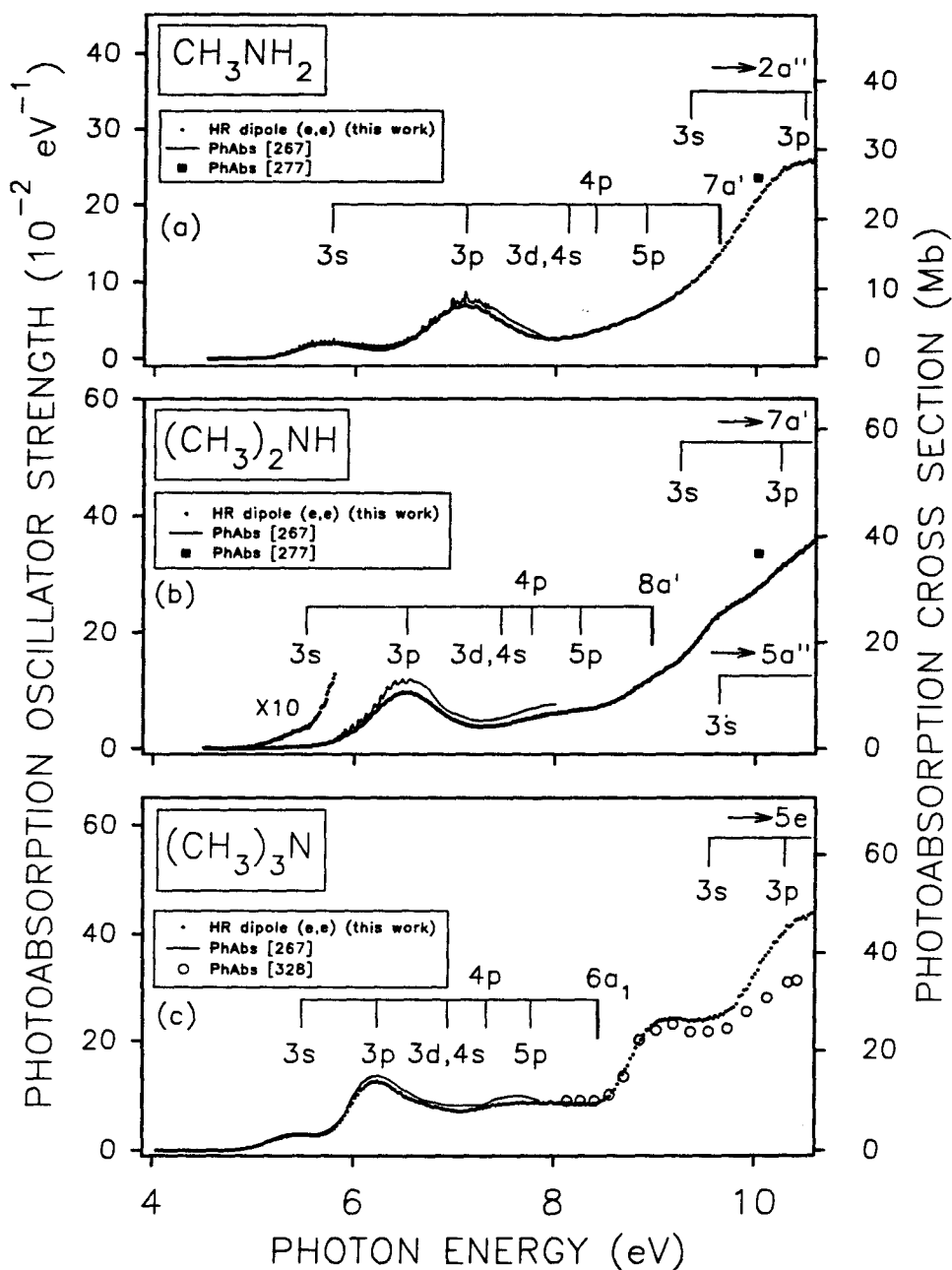


Figure 7.7: High-resolution (0.048 eV fwhm) absolute oscillator strengths for photoabsorption of the methylamines in the low-energy valence-shell region from 4–10 eV: (a) Monomethylamine. (b) Dimethylamine. (c) Trimethylamine. Also shown on the figures are previously reported absolute photoabsorption oscillator strength measurements [267, 277, 328]. The Rydberg manifolds are as on figures 7.4–7.6 and tables 7.5–7.7 with the addition of the predicted positions of the 4p and 5p Rydberg transitions (see text for details).

7.3 Dipole Oscillator Strength Distributions and Properties for the Methylamines

7.3.1 General Considerations

The experimental dipole oscillator strengths used by Kumar and Meath [340] to construct the DOSDs for the methylamines are the low- and high-resolution data reported in sections 7.2.2 and 7.2.3, respectively. Previous DOS data (see section 7.1), which are sparse as a function of photon energy and limited to the energy region below 10.8 eV, are not considered in the constrained DOSD analysis that follows. The input data are augmented, particularly for photon energies greater than 250 eV, by the mixture rules

$$\frac{df}{dE}((\text{CH}_3)_n\text{NH}_{3-n}) = \frac{df}{dE}(\text{NH}_3) + \frac{df}{dE}(\text{C}_{n+1}\text{H}_{2n+4}) - \frac{df}{dE}(\text{CH}_4), n = 1, 2, 3 \quad (7.2)$$

$$\begin{aligned} \frac{df}{dE}((\text{CH}_3)_n\text{NH}_{3-n}) &= \frac{df}{dE}(\text{NH}_3) + \frac{df}{dE}(\text{CH}_4) - \frac{df}{dE}(\text{H}_2), & n = 1 \\ &= \frac{df}{dE}(\text{CH}_3\text{NH}_2) & \\ &+ (n-1) \left[\frac{df}{dE}(\text{CH}_4) - \frac{df}{dE}(\text{H}_2) \right], & n = 2, 3 \end{aligned} \quad (7.3)$$

The input for these mixture rules are the recommended DOSD for NH_3 reported in chapter 6, and the recommended DOSDs for $\text{C}_{n+1}\text{H}_{2n+4}$, $n=1,2,3$, CH_4 , and H_2 developed by Jhanwar *et al.* [73], Thomas and Meath [305], and Zeiss *et al.* [29], respectively.

DOSDs for each methylamine have been constructed by considering the following combinations of DOS data:

DOSD1: E_0 - E_f^{HR} (high-resolution data); E_f^{HR} -250.0 eV (low-resolution data); > 250 eV (mixture rule 7.2). The electronic absorption thresholds (E_0) and the upper energy limit of the high-resolution measurements (E_f^{HR}) are: $E_0 = 5.083, 4.962,$

and 4.711 eV and $E_f^{\text{HR}} = 30.15, 31.26, \text{ and } 30.96$ eV for CH_3NH_2 , $(\text{CH}_3)_2\text{NH}$, and $(\text{CH}_3)_3\text{N}$, respectively.

DOSD2: As in DOSD1 except the high-resolution data is replaced by the low-resolution data from $E_0 - E_f^{\text{HR}}$.

DOSD3: As in DOSD1 except mixture rule 7.2 is replaced by mixture rule 7.3.

DOSD4: As in DOSD2 except mixture rule 7.2 is replaced by mixture rule 7.3.

The photon energies in each case were divided into $N_0 = 24$ energy intervals as suggested by the structure in the input DOS data. The four initial DOSDs were each modified, for each molecule, using the constrained least squares approach outlined in section 2.8, to satisfy $S_0 = N$ and molar refractivity constraints which depend on the particular molecule considered (see what follows).

7.3.2 Monomethylamine

The molar refractivity constraints used are the values of R_λ for $\lambda = 6440.24 \text{ \AA}$ and 4359.56 \AA , obtained from the refractive index measurements of Ramaswamy [341]. The STDs for the four resulting DOSDs are 2.17, 2.59, 2.18, and 2.57 for $i=1, 2, 3, \text{ and } 4$, respectively. These results indicate that there is little to choose between the two mixture rules and that the high-resolution DOS data is more reliable for low photon energies than the low-resolution data, as expected.

The integrated oscillator strengths for the constrained DOSD1, together with those corresponding to the initial DOS data for DOSD1, are given in table 7.8. Generally the integrated oscillator strengths obtained from the initial high- and low-resolution measurements agree with each other, and with the constrained results, to within the

estimated experimental errors of about $\pm 5\%$. All exceptions are marginal except in the case of the low-resolution result for 10–11.8 eV which disagrees with the constrained integrated oscillator strength by $\sim 12\%$. It should be pointed out that the integrated oscillator strengths obtained from the initial high- and low-resolution DOS data may be expected to differ in the discrete excitation energy region since the fine structure in the DOSs is not as well resolved in the low-resolution measurements [72].

The dipole properties evaluated using constrained DOSD i , $i=1-4$, differ little from each other, particularly for DOSD1 and DOSD3. Nominally the results obtained from constrained DOSD1 are chosen as recommended values since they are derived using spectroscopically more reliable input data (DOSD1 also has, marginally with respect to DOSD3, the smallest STD of the four constrained DOSDs for monomethylamine). The recommended dipole properties S_k , L_k , and I_k for CH_3NH_2 are given in table 7.9. Results for the molar refractivities of CH_3NH_2 , evaluated using the constrained DOSD1, are listed in table 7.10 which also contains the available experimental data for R_λ . The agreement with experiment is precise for the three values of R_λ not used as constraints; for most values of λ the results of table 7.10 augment the (sparse) experimental data for R_λ as a function of λ .

It is interesting to note that the recommended value of $S_{-2} = 26.50$ (table 7.9) is about 0.15% higher than the value obtained by Ramaswamy [341] by fitting the relation $(n(\lambda) - 1) = A/(B - \lambda^{-2})$ to his refractive index data. The value of $(n(\lambda) - 1)$ at $\lambda = 6440.24 \text{ \AA}$ generated by this relation is $\sim 0.1\%$ lower than the measured value and therefore the extrapolated value for $\lambda = \infty$ (which yields S_{-2}) is also expected to be low in support of the recommended result for S_{-2} . The value of $S_{-2} = 26.75$ reported by Wolf [308], obtained from dielectric constant measurements, is $\sim 0.9\%$ higher than the

recommended value.

Table 7.9 also contains the values of the dipole properties S_k , L_k and I_k obtained from the initial DOSD1 that lead to our constrained DOSD1 for methylamine. The results for the dipole and logarithmic dipole sums obtained from the initial DOSD are smaller in magnitude than the recommended values for all k (for example S_0 and S_{-2} are $\sim 3\%$ and $\sim 4.5\%$ lower). This is in agreement with the generally low, relative to the constrained integrated DOSs, initial DOS values used to construct the constrained DOSD.

There are apparently no *ab initio* calculations for the properties of CH_3NH_2 . Metzger and Rhee [312], using a complete neglect of differential overlap/finite perturbation plus polarization approach, obtained $S_{-2} = 26.93$ which is $\sim 1.6\%$ higher than the recommended result. A value of $S_{-2} = 25.10$, about 5.6% lower than the recommended value, has been calculated by Kaur *et al.* [342] using a double perturbation theory approach, developed by Amos and Yoffe [343], and a non-local pseudo-potential floating spherical gaussian model.

7.3.3 Dimethylamine and Trimethylamine

There are no refractive index measurements for these two molecules. Wolf [308] obtained a value of $S_{-2} = 39.06$ for $(\text{CH}_3)_2\text{NH}$ from dielectric constant measurements. For NH_3 and CH_3NH_2 his results for S_{-2} are $\sim 1\%$ higher than the recommended values evaluated from the constrained DOSDs for these molecules (see section 6.3.2 and section 7.3.2). Therefore Wolf's S_{-2} value is not used as a constraint for constructing the DOSD for $(\text{CH}_3)_2\text{NH}$; there is no analogous result for $(\text{CH}_3)_3\text{N}$. For dimethylamine and trimethylamine the refractivity constraints are developed as outlined below.

The unmodified DOSD1 for CH_3NH_2 yields $R_{\lambda_1} = 9.6713$ and $R_{\lambda_2} = 9.9389 \text{ cm}^3\text{mol}^{-1}$

for the values of λ , $\lambda_1 = 6440.24$ and $\lambda_2 = 4359.56$ Å, associated with the accurate values of R_λ , 10.1216 and 10.4032 cm³mol⁻¹, used as constraints in the construction of constrained DOSD1 for monomethylamine. These results yield ratios

$$\left. \begin{aligned} r_{\lambda_1} &= R_{\lambda_1}(\text{accurate})/R_{\lambda_1}(\text{unmodified DOSD1}) = 1.0466 \\ r_{\lambda_2} &= R_{\lambda_2}(\text{accurate})/R_{\lambda_2}(\text{unmodified DOSD1}) = 1.0467 \end{aligned} \right\} \quad (7.4)$$

The experimental oscillator strengths for all three amines are measured using the same techniques and the refractivity constraints are completely dominated by the DOS data for photon energies below 150 eV. Assuming that the experimental errors in the three sets of input data used to construct the DOSDs for the three molecules are essentially the same as a function of photon energy, we assume that the ratios given by equation 7.4 apply to (CH₃)₂NH and (CH₃)₃N as well as CH₃NH₂. The molar refractivity constraints for dimethylamine and trimethylamine are therefore chosen to be the values evaluated using unmodified DOSD1 and λ_1 and λ_2 scaled by the ratios given by equation 7.4, namely $R_{\lambda_1} = 14.7845$ and $R_{\lambda_2} = 15.1965$ cm³mol⁻¹ for (CH₃)₂NH and $R_{\lambda_1} = 19.0998$ and $R_{\lambda_2} = 19.6938$ cm³mol⁻¹ for (CH₃)₃N. The value of $S_{-2} = 38.70$ obtained by using the refractivity constraints for (CH₃)₂NH is ~0.9% lower than the result of Wolf [308] referred to earlier which is consistent with the analogous results for NH₃ and (CH₃)₂NH also discussed previously (section 6.3.2 and section 7.3.2).

For dimethylamine and trimethylamine the STDs for the four constrained DOSDs, DOSD_{*i*} with *i*=1-4, are STD = 2.19, 3.96, 2.20, and 3.93, and STD = 2.42, 6.43, 2.39, and 6.42, respectively. The dipole properties for each molecule evaluated using constrained DOSD_{*i*}, *i*=1-4, are very similar, especially for DOSD1 and DOSD3 which are based on the most spectroscopically reliable DOS data. The results obtained from DOSD1 and

DOSD3 are, nominally, recommended for $(\text{CH}_3)_2\text{NH}$ and $(\text{CH}_3)_3\text{N}$, respectively (they correspond, marginally, to the lowest STDs for the constrained DOSDs of the respective molecules).

The integrated oscillator strengths and the dipole properties S_k , L_k , and I_k corresponding to both the initial and constrained DOSD1 and DOSD3 for $(\text{CH}_3)_2\text{NH}$ and $(\text{CH}_3)_3\text{N}$, respectively, are given in tables 7.11–7.14; the molar refractivities evaluated from the constrained DOSDs are contained in table 7.15 for $6709 \text{ \AA} \geq \lambda \geq 2346 \text{ \AA}$. For both molecules the integrated oscillator strengths obtained from the initial high- and low-resolution measurements, and from the constrained DOSDs, generally agree with each other to within the estimated experimental errors of about $\pm 5\%$. All the exceptions are marginal except for the low-resolution data for both molecules below 9 eV; as pointed out in section 7.3.1, see also chapter 6, the integrated oscillator strengths, in the discrete energy region, evaluated with low-resolution data need not be realistic.

A comparison of the dipole properties evaluated using the initial versus the constrained DOSD1 and DOSD3 for $(\text{CH}_3)_2\text{NH}$ and $(\text{CH}_3)_3\text{N}$, respectively, can be used to discuss the effects of the constrained DOSD method for these molecules. Analogous to monomethylamine, the values for the dipole and logarithmic dipole sums evaluated using the initial DOSDs for dimethylamine and trimethylamine are smaller in magnitude than the recommended values for all k . The effects are similar for all three molecules, particularly for the properties dominated by the photoabsorption spectra for photon energies below 250 eV. For these properties, e.g., the S_k , $k \leq -1.5$, the effects of the constraint procedure are $\sim 4\text{--}5\%$ and are within the errors ($\pm 5\%$) associated with the high- and low-resolution experimental data used to construct the constrained DOSD for each molecule for photon energies below 250 eV. A detailed discussion of the photon energy dependence

of the dipole properties can be found in the literature [73–75, 244, 245].

The recommended dipole properties for $(\text{CH}_3)_2\text{NH}$ and $(\text{CH}_3)_3\text{N}$, evaluated using the constrained DOSD1 and DOSD3, respectively, given in tables 7.13 and 7.14 are apparently the only (reliable) values for these properties available in the literature to date.

7.3.4 The Reliability of the Calculated Dipole Properties

The uncertainties in the recommended values of the dipole properties of the methylamines determined by Kumar and Meath [340] can be estimated by comparing the recommended results with those derived from alternative constrained DOSDs satisfying the same constraints [29, 48]. The uncertainty estimates obtained in this way are less reliable for those properties that do not depend significantly on portions of the DOSD which dominate the constraints, for example properties corresponding to $k = 2$, to a lesser extent to $k = 1$, and for $k < -4$.

Using the results for the properties evaluated using various alternate constrained DOSDs for the methylamines, we estimate the uncertainties in the recommended results for the dipole properties of these molecules to be $\leq 2\text{--}3\%$ for $S_2, L_2, I_2, S_1, L_1, \leq 1\%$ for $S_k, -5 \leq k \leq 0, R_\lambda$ for all λ , and for $L_{-1}, L_{-2}, I_1, I_{-1}, I_{-2}, \leq 2\text{--}3\%$ for L_0 and I_0 . For $k \leq -6$ the errors in the S_k are estimated to be $\leq 1\text{--}2\%$ for S_{-6} , increasing to $\leq 8\%$ for S_{-12} . The estimation of the uncertainties in the recommended results for the dipole properties for the methylamines is based on the assumption that the molar refractivities used as constraints in the construction of the DOSDs have errors of the magnitude associated with accurate experimental measurements (a few tenths of a percent). While this is a valid assumption for monomethylamine, it becomes less probable for dimethylamine and

trimethylamine because of the method, outlined in section 7.3.3, used to obtain the R_λ constraints for the two larger methylamines. The effects on the calculated properties S_k , L_k , and I_k of varying the R_λ constraints have been discussed previously and, as expected from the structure of integrals 2.41 and 2.42, it is largest for $k \leq -2$ and increases as k decreases from $k = -2$ [74, 120].

Table 7.1: Vertical ionization potentials for the electronic states of the methylamines obtained from photoelectron spectroscopic measurements [134, 139, 291, 329–332].

Monomethylamine		Dimethylamine		Trimethylamine	
Electronic State	VIP eV	Electronic State	VIP eV	Electronic State	VIP eV
7a'	9.64 ^a	8a'	8.97 ^c	6a ₁	8.44 ^c
2a''	13.22 ^a	7a'	12.70 ^c	5e	(12.3, 12.74) ^c
6a'	14.42 ^a	5a''	13.09 ^e	1a ₂	13.1 ^e
5a'	15.45 ^a	4a''	13.9 ^e	4e	13.67 ^e
1a''	16.85 ^a	3a''	15.19 ^e	3e	15.68 ^e
4a'	21.9 ^b	6a'	15.5 ^e	5a ₁	16.0 ^e
3a'	27.5 ^b	5a'	16.69 ^e	4a ₁	19.46 ^e
		4a'	20.6 ^b	2e	22.5 ^b
		2a''	22.4 ^b	3a ₁	28.3 ^b
		3a'	28.0 ^b		
2a'	291.60 ^c	2a'	291.43 ^f	1e	291.26 ^g
		1a''		2a ₁	
1a'	405.17 ^d	1a'	404.93 ^d	1a ₁	404.82 ^d

^aReference [134].^bReference [139].^cReference [331].^dReference [291, 330].^eReference [329].^fQuoted by Sodhi and Brion [337] as the average of the carbon K-shell VIPs for monomethylamine and trimethylamine.^gReference [332] as corrected in reference [344].

Table 7.2: Oscillator strengths for the total photoabsorption of monomethylamine from 5.5 to 250.0 eV.

Energy eV	Oscillator strength ^a 10 ⁻² eV ⁻¹						
5.5	0.57	14.0	48.33	22.5	42.85	31.0	21.97
6.0	1.57	14.5	50.54	23.0	41.48	32.0	19.98
6.5	2.51	15.0	53.00	23.5	39.20	33.0	19.35
7.0	4.47	15.5	55.34	24.0	38.01	34.0	17.87
7.5	5.96	16.0	56.88	24.5	36.04	35.0	16.13
8.0	4.95	16.5	58.01	25.0	34.20	36.0	15.59
8.5	4.79	17.0	57.72	25.5	32.86	37.0	14.35
9.0	6.45	17.5	57.61	26.0	31.70	38.0	13.40
9.5	10.26	18.0	56.35	26.5	29.67	39.0	13.00
10.0	17.53	18.5	56.07	27.0	28.76	40.0	12.34
10.5	23.61	19.0	54.18	27.5	28.56	41.0	11.93
11.0	28.25	19.5	52.78	28.0	27.18	42.0	11.12
11.5	33.26	20.0	51.10	28.5	26.10	43.0	10.65
12.0	36.10	20.5	50.27	29.0	25.35	44.0	9.82
12.5	40.91	21.0	47.83	29.5	24.31	45.0	9.37
13.0	45.66	21.5	47.19	30.0	23.22	46.0	9.05
13.5	47.88	22.0	45.23	30.5	22.40	47.0	8.48

Table 7.2: (continued) Oscillator strengths for the total photoabsorption of monomethylamine.

Energy eV	Oscillator strength ^a 10 ⁻² eV ⁻¹						
48.0	8.04	63.0	4.18	78.0	2.47	145.0	0.60
49.0	7.81	64.0	3.98	79.0	2.31	150.0	0.55
50.0	7.28	65.0	3.85	80.0	2.22	160.0	0.48
51.0	6.99	66.0	3.73	85.0	1.97	170.0	0.43
52.0	6.85	67.0	3.54	90.0	1.72	180.0	0.39
53.0	6.49	68.0	3.45	95.0	1.51	190.0	0.35
54.0	6.17	69.0	3.33	100.0	1.32	200.0	0.32
55.0	5.95	70.0	3.09	105.0	1.20	210.0	0.30
56.0	5.67	71.0	3.08	110.0	1.08	220.0	0.27
57.0	5.36	72.0	2.89	115.0	0.99	230.0	0.25
58.0	5.15	73.0	2.87	120.0	0.90	240.0	0.24
59.0	4.85	74.0	2.76	125.0	0.82	250.0	0.22
60.0	4.73	75.0	2.64	130.0	0.76		
61.0	4.52	76.0	2.51	135.0	0.70		
62.0	4.37	77.0	2.47	140.0	0.64		

$${}^a\sigma(\text{Mb})=1.0975\times 10^2 df/dE(\text{eV}^{-1})$$

Table 7.3: Oscillator strengths for the total photoabsorption of dimethylamine from 5.0 to 250.0 eV.

Energy eV	Oscillator strength ^a 10 ⁻² eV ⁻¹						
5.0	0.45	13.5	72.26	22.0	64.55	31.0	30.92
5.5	1.10	14.0	74.58	22.5	62.58	32.0	28.72
6.0	3.82	14.5	77.99	23.0	59.42	33.0	25.93
6.5	7.02	15.0	80.45	23.5	57.60	34.0	24.79
7.0	6.90	15.5	83.82	24.0	53.73	35.0	23.02
7.5	6.00	16.0	86.18	24.5	51.70	36.0	22.02
8.0	7.18	16.5	86.71	25.0	48.89	37.0	20.08
8.5	9.41	17.0	87.31	25.5	47.30	38.0	18.89
9.0	13.99	17.5	86.15	26.0	44.41	39.0	17.73
9.5	21.53	18.0	85.24	26.5	42.44	40.0	16.49
10.0	28.47	18.5	82.01	27.0	42.47	41.0	16.17
10.5	34.64	19.0	80.30	27.5	39.62	42.0	15.16
11.0	40.92	19.5	78.40	28.0	38.42	43.0	14.50
11.5	45.21	20.0	76.60	28.5	36.75	44.0	13.44
12.0	50.68	20.5	72.71	29.0	36.23	45.0	12.76
12.5	56.39	21.0	71.54	29.5	34.09	46.0	12.26
13.0	64.23	21.5	69.09	30.0	32.52	47.0	11.45

Table 7.3: (continued) Oscillator strengths for the total photoabsorption of dimethylamine.

Energy eV	Oscillator strength ^a 10 ⁻² eV ⁻¹						
48.0	10.94	63.0	5.62	78.0	3.04	145.0	0.78
49.0	10.58	64.0	5.31	79.0	2.99	150.0	0.74
50.0	10.03	65.0	5.10	80.0	2.93	160.0	0.64
51.0	9.52	66.0	4.89	85.0	2.60	170.0	0.57
52.0	9.22	67.0	4.74	90.0	2.26	180.0	0.52
53.0	8.71	68.0	4.59	95.0	1.96	190.0	0.47
54.0	8.30	69.0	4.37	100.0	1.74	200.0	0.43
55.0	7.97	70.0	4.17	105.0	1.57	210.0	0.39
56.0	7.70	71.0	4.05	110.0	1.41	220.0	0.37
57.0	7.05	72.0	3.96	115.0	1.30	230.0	0.34
58.0	6.89	73.0	3.77	120.0	1.20	240.0	0.32
59.0	6.46	74.0	3.68	125.0	1.09	250.0	0.31
60.0	6.25	75.0	3.52	130.0	0.99		
61.0	6.05	76.0	3.34	135.0	0.91		
62.0	5.80	77.0	3.33	140.0	0.87		

$${}^a\sigma(\text{Mb})=1.0975\times 10^2 df/dE(\text{eV}^{-1})$$

Table 7.4: Oscillator strengths for the total photoabsorption of trimethylamine from 4.5 to 250.0 eV.

Energy eV	Oscillator strength ^a 10 ⁻² eV ⁻¹						
4.5	1.08	13.0	72.85	21.5	88.04	30.0	43.32
5.0	2.70	13.5	80.98	22.0	84.09	31.0	40.06
5.5	4.82	14.0	89.14	22.5	80.50	32.0	37.28
6.0	7.72	14.5	96.27	23.0	77.31	33.0	34.87
6.5	8.96	15.0	101.81	23.5	75.11	34.0	32.87
7.0	9.00	15.5	106.03	24.0	71.85	35.0	30.27
7.5	9.40	16.0	108.80	24.5	67.46	36.0	28.05
8.0	10.90	16.5	110.49	25.0	64.94	37.0	26.46
8.5	15.48	17.0	111.61	25.5	62.70	38.0	24.93
9.0	21.22	17.5	109.68	26.0	59.99	39.0	23.40
9.5	27.51	18.0	107.29	26.5	57.57	40.0	21.79
10.0	34.47	18.5	106.20	27.0	55.64	41.0	21.29
10.5	41.53	19.0	104.36	27.5	53.67	42.0	20.07
11.0	47.80	19.5	102.67	28.0	51.82	43.0	18.61
11.5	52.34	20.0	99.60	28.5	50.02	44.0	17.77
12.0	57.74	20.5	95.05	29.0	48.35	45.0	16.85
12.5	64.95	21.0	91.39	29.5	46.17	46.0	15.96

Table 7.4: (continued) Oscillator strengths for the total photoabsorption of trimethylamine.

Energy eV	Oscillator strength ^a 10 ⁻² eV ⁻¹						
47.0	15.30	62.0	7.75	77.0	4.45	140.0	1.10
48.0	14.55	63.0	7.51	78.0	4.35	145.0	1.03
49.0	14.05	64.0	7.10	79.0	4.11	150.0	0.95
50.0	13.10	65.0	6.85	80.0	4.04	160.0	0.84
51.0	12.42	66.0	6.61	85.0	3.39	170.0	0.75
52.0	11.95	67.0	6.48	90.0	2.90	180.0	0.68
53.0	11.46	68.0	6.10	95.0	2.54	190.0	0.62
54.0	11.03	69.0	5.91	100.0	2.26	200.0	0.57
55.0	10.35	70.0	5.78	105.0	2.02	210.0	0.52
56.0	9.79	71.0	5.62	110.0	1.82	220.0	0.48
57.0	9.49	72.0	5.34	115.0	1.65	230.0	0.45
58.0	9.10	73.0	5.17	120.0	1.54	240.0	0.42
59.0	8.70	74.0	4.94	125.0	1.39	250.0	0.41
60.0	8.36	75.0	4.60	130.0	1.26		
61.0	8.13	76.0	4.54	135.0	1.21		

$${}^a\sigma(\text{Mb})=1.0975\times 10^2 df/dE(\text{eV}^{-1})$$

Table 7.5: Energies, term values, and the proposed spectral assignments for the observed photoabsorption peaks in the high-resolution spectrum of monomethylamine.

Peak	Photon Energy eV	Term Value (eV)					Proposed Assignment Final Orbital				
		7a'	2a''	6a'	5a'	1a''	7a'	2a''	6a'	5a'	1a''
1	5.77	3.87	—	—	—	—	3s	—	—	—	—
2	7.10	2.54	—	—	—	—	3p	—	—	—	—
3	10.50	—	2.72	3.92	—	—	—	3p	3s	—	—
4	11.48	—	—	2.94	3.97	—	—	—	3p	3s	—
5	12.86	—	—	1.56	2.59	3.99	—	—	3d,4s	3p	3s
6	15.2	—	—	—	—	1.6	—	—	—	—	3d,4s
VIP (eV) ^a		9.64	13.22	14.42	15.45	16.85					

^aFrom the PES measurements of Potts *et al.* [139] and Katsumata *et al.* [134].

Table 7.6: Energies, term values, and the proposed spectral assignments for the observed photoabsorption peaks in the high-resolution spectrum of dimethylamine.

Peak	Photon Energy eV	Term Value (eV)							Proposed Assignment						
		8a'	7a'	5a''	4a''	3a''	6a'	5a'	Final Orbital						
		8a'	7a'	5a''	4a''	3a''	6a'	5a'	8a'	7a'	5a''	4a''	3a''	6a'	5a'
1	5.52	3.45	—	—	—	—	—	—	3s	—	—	—	—	—	—
2	6.52	2.45	—	—	—	—	—	—	3p	—	—	—	—	—	—
3	8.0	1.0	—	—	—	—	—	—	4p,5p	—	—	—	—	—	—
4	9.0	—	3.7	—	—	—	—	—	—	3s	—	—	—	—	—
5	9.7	—	3.0	3.4	—	—	—	—	—	3p	3s	—	—	—	—
6	10.9	—	—	2.2	3.0	—	—	—	—	—	3p	3s	—	—	—
7	11.5	—	—	1.6	2.4	3.7	—	—	—	—	3d,4s	3p	3s	—	—
8	12.5	—	—	—	—	2.7	3.0	—	—	—	—	—	3p	3s	—
9	13.41	—	—	—	—	—	2.1	3.28	—	—	—	—	—	3p	3s
10	14.02	—	—	—	—	—	1.5	2.67	—	—	—	—	—	3d,4s	3p
VIP (eV) ^a		8.97	12.70	13.09	13.9	15.19	15.5	16.69							

^aFrom the PES measurements of Potts *et al.* [139] and Kimura and Osafune [329].

Table 7.7: Energies, term values, and the proposed spectral assignments for the observed photoabsorption peaks in the high-resolution spectrum of trimethylamine.

Peak	Photon Energy eV	Term Value (eV)						Proposed Assignment Final Orbital					
		6a ₁	5e	1a ₂	4e	4a ₁	2e	6a ₁	5e	1a ₂	4e	4a ₁	2e
1	5.48	2.96	—	—	—	—	—	3s	—	—	—	—	—
2	6.23	2.21	—	—	—	—	—	3p	—	—	—	—	—
3	6.8	1.6	—	—	—	—	—	3d,4s	—	—	—	—	—
4	7.8	0.6	—	—	—	—	—	4p,5p	—	—	—	—	—
5	9.18	—	3.32	—	—	—	—	—	3s	—	—	—	—
6	10.46	—	2.00	2.6	3.21	—	—	—	3p	3p	3s	—	—
7	11.39	—	—	1.7	2.28	—	—	—	—	3d,4s	3p	—	—
8	12.0	—	—	1.1	1.7	—	—	—	—	4p	3d,4s	—	—
9	15.9	—	—	—	—	3.6	—	—	—	—	—	3s	—
10	16.90	—	—	—	—	2.56	—	—	—	—	—	3p	—
11	18.10	—	—	—	—	1.36	—	—	—	—	—	3d,4s	—
12	20.2	—	—	—	—	—	2.3	—	—	—	—	—	3p
VIP (eV) ^a		8.44	12.5 ^b	13.1	13.67	19.46	22.5						

^aFrom the PES measurements of Potts *et al.* [139] and Kimura and Osafune [329].

^bAverage of the energies of the two components of the 5e state [329].

Table 7.8: Integrated dipole oscillator strengths for CH_3NH_2 . This table contains the integrated oscillator strengths resulting from constrained DOSD1 and from the unmodified experimental or mixture rule data considered in this work.

Energy region (eV)	Constrained Values: DOSD1	High-resolution data	Low-resolution data	Mixture rule Equation 7.2	Mixture rule Equation 7.3
5.083-6.261	1.560(-2)	1.513(-2)	1.460(-2)		
6.261-8.059	7.829(-2)	7.406(-2)	7.918(-2)		
8.059-10.00	1.708(-1)	1.640(-1)	1.608(-1)		
10.00-11.80	5.563(-1)	5.204(-1)	4.887(-1)		
11.80-14.00	1.029(0)	9.617(-1)	9.544(-1)		
14.00-16.00	1.109(0)	1.059(0)	1.057(0)		
16.00-18.00	1.178(0)	1.136(0)	1.150(0)		
18.00-20.00	1.106(0)	1.077(0)	1.084(0)		
20.00-25.00	2.230(0)	2.143(0)	2.154(0)		
25.00-30.15	1.477(0)	1.445(0)	1.451(0)		
30.15-40.00	1.690(0)		1.654(0)	1.686(0)	1.909(0)
40.00-50.00	9.721(-1)		9.608(-1)	9.823(-1)	9.817(-1)
50.00-70.00	9.947(-1)		9.832(-1)	1.013(0)	1.011(0)
70.00-100.0	6.201(-1)		6.157(-1)	6.579(-1)	6.557(-1)
100.0-150.0	4.319(-1)		4.298(-1)	4.579(-1)	4.293(-1)
150.0-200.0	2.099(-1)		2.094(-1)	2.110(-1)	2.097(-1)
200.0-250.0	1.328(-1)		1.326(-1)	1.098(-1)	1.102(-1)
250.0-283.8	4.816(-2)			4.808(-2)	4.874(-2)
283.8-400.0	7.892(-1)			7.687(-1)	8.306(-1)
400.0-425.0	3.694(-1)			3.663(-1)	3.609(-1)
425.0-1000.0	2.191(0)			2.090(0)	2.007(0)
1000.0- 10^4	5.955(-1)			5.915(-1)	5.779(-1)
10^4 - 10^6	5.216(-3)			5.216(-3)	4.894(-3)
10^6 - ∞	8.555(-8)			8.555(-8)	8.556(-8)

Table 7.9: The dipole sums S_k , logarithmic dipole sums L_k , and mean excitation energies I_k , for various values of k , for CH_3NH_2 calculated using the initial and constrained DOSD1. The values obtained from the constrained DOSD are recommended.

Property	Initial DOSD1	Constrained DOSD1	Property	Initial DOSD1	Constrained DOSD1
S_2	9.583(3)	9.668(3)	S_{-12}	3.120(6)	3.243(6)
S_1	1.240(2)	1.272(2)			
S_0	1.745(1)	1.800(1)			
$S_{-1/2}$	1.508(1)	1.562(1)	L_2	5.864(4)	5.895(4)
S_{-1}	1.641(1)	1.706(1)	L_1	3.960(2)	4.052(2)
$S_{-3/2}$	1.977(1)	2.063(1)	L_0	1.208(1)	1.233(1)
S_{-2}	2.532(1)	2.650(1)	L_{-1}	-4.807(0)	-5.127(0)
$S_{-5/2}$	3.403(1)	3.569(1)	L_{-2}	-1.382(1)	-1.459(1)
S_{-3}	4.772(1)	5.014(1)			
S_{-4}	1.057(2)	1.113(2)	$I_2(\text{eV})$	1.236(4)	1.210(4)
S_{-5}	2.721(2)	2.865(2)	$I_1(\text{eV})$	6.628(2)	6.571(2)
S_{-6}	8.056(2)	8.468(2)	$I_0(\text{eV})$	5.437(1)	5.397(1)
S_{-8}	9.898(3)	1.036(4)	$I_{-1}(\text{eV})$	2.030(1)	2.015(1)
S_{-10}	1.628(5)	1.697(5)	$I_{-2}(\text{eV})$	1.577(1)	1.569(1)

Table 7.10: Values of the molar refractivity, in $\text{cm}^3\text{mol}^{-1}$, of CH_3NH_2 (ideal gas, STP) evaluated using the constrained DOSD1 and a comparison with the available experimental data [341].

λ (Å)	Molar Refractivity		λ (Å)	Molar Refractivity Constrained DOSD1
	Constrained DOSD1	Experiment [341]		
6709.0	10.10		4047.0	10.49
6440.24	10.12 ^a	10.12	3861.0	10.56
6328.0	10.13		3342.0	10.82
6104.0	10.15		2968.0	11.15
5893.0	10.17		2894.0	11.24
5462.25	10.21	10.21	2753.0	11.44
5087.23	10.26	10.26	2577.0	11.82
4801.25	10.31	10.31	2346.0	12.90
4359.56	10.40 ^a	10.40		

^aUsed as constraints in constructing the DOSD.

Table 7.11: Integrated dipole oscillator strengths for $(\text{CH}_3)_2\text{NH}$. This table contains the integrated oscillator strengths resulting from constrained DOSD1 and from the unmodified experimental or mixture rule data considered in this work.

Energy region (eV)	Constrained Values: DOSD1	High-resolution data	Low-resolution data	Mixture rule Equation 7.2	Mixture rule Equation 7.3
4.962-5.703	1.939(-3)	1.933(-3)	7.377(-3)		
5.703-7.256	9.370(-2)	8.806(-2)	8.795(-2)		
7.256-9.000	1.211(-1)	1.175(-1)	1.481(-1)		
9.000-11.00	5.753(-1)	5.424(-1)	5.605(-1)		
11.00-13.00	1.038(0)	9.819(-1)	1.024(0)		
13.00-15.00	1.558(0)	1.481(0)	1.486(0)		
15.00-18.00	2.671(0)	2.528(0)	2.565(0)		
18.00-20.00	1.644(0)	1.602(0)	1.608(0)		
20.00-25.00	3.312(0)	3.185(0)	3.128(0)		
25.00-31.26	2.610(0)	2.545(0)	2.410(0)		
31.26-40.00	1.997(0)		1.963(0)	2.355(0)	2.149(0)
40.00-50.00	1.320(0)		1.305(0)	1.358(0)	1.329(0)
50.00-70.00	1.331(0)		1.316(0)	1.400(0)	1.366(0)
70.00-100.0	8.140(-1)		8.086(-1)	9.021(-1)	8.634(-1)
100.0-150.0	5.696(-1)		5.669(-1)	6.166(-1)	5.769(-1)
150.0-200.0	2.794(-1)		2.787(-1)	2.796(-1)	2.780(-1)
200.0-250.0	1.794(-1)		1.791(-1)	1.467(-1)	1.694(-1)
250.0-283.8	6.439(-2)			6.429(-2)	6.478(-2)
283.8-400.0	1.560(0)			1.504(0)	1.557(0)
400.0-425.0	4.710(-1)			4.674(-1)	4.681(-1)
425.0-1000.0	2.981(0)			2.848(0)	2.908(0)
1000.0- 10^4	8.010(-1)			7.958(-1)	7.932(-1)
10^4 - 10^6	6.982(-3)			6.982(-3)	6.822(-3)
10^6 - ∞	1.128(-7)			1.127(-7)	1.128(-7)

Table 7.12: Integrated dipole oscillator strengths for $(\text{CH}_3)_3\text{N}$. This table contains the integrated oscillator strengths resulting from constrained DOSD3 and from the unmodified experimental or mixture rule data considered in this work.

Energy region (eV)	Constrained Values: DOSD3	High-resolution data	Low-resolution data	Mixture rule Equation 7.2	Mixture rule Equation 7.3
4.711-5.641	1.547(-2)	1.516(-2)	3.183(-2)		
5.641-7.005	1.260(-1)	1.179(-1)	1.128(-1)		
7.005-9.480	3.388(-1)	3.214(-1)	3.656(-1)		
9.480-11.35	7.668(-1)	7.295(-1)	7.502(-1)		
11.35-13.36	1.270(0)	1.213(0)	1.271(0)		
13.36-15.50	2.169(0)	2.062(0)	2.015(0)		
15.50-17.68	2.555(0)	2.444(0)	2.405(0)		
17.68-20.00	2.552(0)	2.462(0)	2.425(0)		
20.00-25.00	4.247(0)	4.042(0)	4.064(0)		
25.00-30.96	3.171(0)	3.067(0)	3.096(0)		
30.96-40.00	2.786(0)		2.709(0)	2.729(0)	2.994(0)
40.00-50.00	1.747(0)		1.717(0)	1.816(0)	1.687(0)
50.00-70.00	1.777(0)		1.746(0)	1.783(0)	1.737(0)
70.00-100.0	1.089(0)		1.078(0)	1.149(0)	1.107(0)
100.0-150.0	7.369(-1)		7.314(-1)	7.793(-1)	7.219(-1)
150.0-200.0	3.642(-1)		3.629(-1)	3.498(-1)	3.460(-1)
200.0-250.0	2.372(-1)		2.366(-1)	1.844(-1)	2.065(-1)
250.0-283.8	8.155(-2)			8.089(-2)	8.135(-2)
283.8-400.0	2.492(0)			2.277(0)	2.326(0)
400.0-425.0	5.733(-1)			5.739(-1)	5.667(-1)
425.0-1000.0	3.895(0)			3.634(0)	3.626(0)
1000.0- 10^4	1.001(0)			1.003(0)	9.909(-1)
10^4 - 10^6	8.428(-3)			8.748(-3)	8.427(-3)
10^6 - ∞	1.400(-7)			1.400(-7)	1.400(-7)

Table 7.13: The dipole sums S_k , logarithmic dipole sums L_k , and mean excitation energies I_k , for various values of k , for $(\text{CH}_3)_2\text{NH}$ calculated using the initial and constrained DOSD1. The values obtained from the constrained DOSD are recommended.

Property	Initial DOSD1	Constrained DOSD1	Property	Initial DOSD1	Constrained DOSD1
S_2	1.288(4)	1.299(4)	S_{-12}	3.713(6)	3.913(6)
S_1	1.737(2)	1.783(2)			
S_0	2.518(1)	2.600(1)			
$S_{-1/2}$	2.188(1)	2.269(1)	L_2	7.830(4)	7.871(4)
S_{-1}	2.390(1)	2.487(1)	L_1	5.474(2)	5.603(2)
$S_{-3/2}$	2.885(1)	3.011(1)	L_0	1.704(1)	1.741(1)
S_{-2}	3.699(1)	3.870(1)	L_{-1}	-7.131(0)	-7.590(0)
$S_{-5/2}$	4.973(1)	5.214(1)	L_{-2}	-2.023(1)	-2.134(1)
S_{-3}	6.977(1)	7.327(1)			
S_{-4}	1.548(2)	1.629(2)	$I_2(\text{eV})$	1.189(4)	1.163(4)
S_{-5}	3.989(2)	4.204(2)	$I_1(\text{eV})$	6.357(2)	6.297(2)
S_{-6}	1.177(3)	1.241(3)	$I_0(\text{eV})$	5.355(1)	5.316(1)
S_{-8}	1.395(4)	1.472(4)	$I_{-1}(\text{eV})$	2.019(1)	2.005(1)
S_{-10}	2.134(5)	2.251(5)	$I_{-2}(\text{eV})$	1.575(1)	1.568(1)

Table 7.14: The dipole sums S_k , logarithmic dipole sums L_k , and mean excitation energies I_k , for various values of k , for $(\text{CH}_3)_3\text{N}$ calculated using the initial and constrained DOSD3. The values obtained from the constrained DOSD are recommended.

Property	Initial DOSD3	Constrained DOSD3	Property	Initial DOSD3	Constrained DOSD3
S_2	1.606(4)	1.630(4)	S_{-12}	1.117(7)	1.168(7)
S_1	2.244(2)	2.341(2)			
S_0	3.265(1)	3.400(1)			
$S_{-1/2}$	2.813(1)	2.928(1)	L_2	9.726(4)	9.810(4)
S_{-1}	3.061(1)	3.192(1)	L_1	7.000(2)	7.247(2)
$S_{-3/2}$	3.699(1)	3.865(1)	L_0	2.274(1)	2.382(1)
S_{-2}	4.769(1)	4.990(1)	L_{-1}	-9.063(0)	-9.574(0)
$S_{-5/2}$	6.479(1)	6.790(1)	L_{-2}	-2.682(1)	-2.822(1)
S_{-3}	9.243(1)	9.698(1)			
S_{-4}	2.165(2)	2.277(2)	$I_2(\text{eV})$	1.161(4)	1.119(4)
S_{-5}	6.056(2)	6.377(2)	$I_1(\text{eV})$	6.156(2)	6.084(2)
S_{-6}	1.973(3)	2.080(3)	$I_0(\text{eV})$	5.461(1)	5.484(1)
S_{-8}	2.885(4)	3.038(4)	$I_{-1}(\text{eV})$	2.023(1)	2.016(1)
S_{-10}	5.353(5)	5.619(5)	$I_{-2}(\text{eV})$	1.550(1)	1.546(1)

Table 7.15: Values of the molar refractivity, in $\text{cm}^3\text{mol}^{-1}$, of $(\text{CH}_3)_2\text{NH}$ and $(\text{CH}_3)_3\text{N}$ (ideal gas, STP) evaluated using the constrained DOSD1, and DOSD3, respectively.

λ (Å)	Molar Refractivity		λ (Å)	Molar Refractivity	
	$(\text{CH}_3)_2\text{NH}$	$(\text{CH}_3)_3\text{N}$		$(\text{CH}_3)_2\text{NH}$	$(\text{CH}_3)_3\text{N}$
6709.0	14.76	19.06	4047.0	15.33	19.89
6440.24	14.78	19.10	3861.0	15.42	20.03
6328.0	14.80	19.12	3342.0	15.81	20.62
6104.0	14.82	19.15	2968.0	16.28	21.37
5893.0	14.85	19.19	2894.0	16.40	21.59
5462.25	14.92	19.29	2753.0	16.69	22.12
5087.23	14.99	19.39	2577.0	17.19	23.25
4801.25	15.06	19.49	2346.0	18.30	24.84
4359.56	15.20	19.69			

Chapter 8

Concluding Remarks

The amount of accurate absolute photoabsorption oscillator strength data available in the literature is limited. Yet such data are needed in many areas of science and technology. The present study has provided wide-ranging absolute oscillator strength data for the photoabsorption of CH_3OH , CCl_4 , NH_3 , CH_3NH_2 , $(\text{CH}_3)_2\text{NH}$, and $(\text{CH}_3)_3\text{N}$ at a resolution of 1 eV fwhm. The discrete excitation region below the first ionization potential of these molecules has also been studied at higher resolution (0.048 eV fwhm).

Atomic oscillator strength sums for the constituent atoms of a molecule have been used with some success previously to place relative inner-shell oscillator strength spectra on an absolute scale at 20–30 eV above the inner-shell ionization potential. In the presently reported photoabsorption studies of CH_3OH , and CCl_4 , a marked difference was observed in the inner-shell regions of these molecules between the measured molecular photoabsorption oscillator strength data and the summed oscillator strength data for the constituent atoms. This indicates that absolute oscillator strength data obtained using such normalization procedures, based on summed atomic data, should only be taken as approximate. These considerations are especially important in the case of CCl_4 where three inner-shell thresholds (Cl 2p,2s; C 1s) contribute in the 200–300 eV region.

Absolute partial photoionization oscillator strength data for the molecular and dissociative photoionization of CH_3OH and CCl_4 are also reported in this work. These results have led to a qualitative and quantitative understanding of the dipole-induced

breakdown pathways of these molecules. In other related work, a general procedure for determining the sensitivity of ion detectors to ions of different mass to charge ratio has been described, and has been used to characterize the two ion detectors used in this work. Such characterizations are important in applications where mass spectrometry is used for accurate quantitative analysis.

The absolute high- and low-resolution oscillator strength data for the photoabsorption of ammonia and the methylamines reported in this work have been used by Kumar and Meath at the University of Western Ontario to determine dipole oscillator strength distributions (DOSDs) and a wide range of related dipole properties for these molecules. The direct *ab initio* calculation of the oscillator strengths and dipole properties for molecules of the size studied here is not at present feasible, and therefore such data are limited. The present work represents the first determination of most of these dipole properties for these nitrogen-containing molecules. Future work should include a study of the higher n-alkylamines. From a comparison of the DOSDs and dipole properties of these molecules, and of ammonia and the methylamines, an indication of the effect on the oscillator strength distribution, and dipole properties, of adding a methyl or amino group to larger molecules can then be assessed.

Finally, details of the high-impact energy dipole (e,e) spectrometer designed and constructed during the course of this work have been presented. This new spectrometer will extend the energy loss range to 3 keV to permit the study of third row K-shells. It will also extend the range of possible targets to include free radicals, ions, and excited species. Absolute oscillator strength data for the photoabsorption of these types of molecules are, at present, extremely limited.

Bibliography

- [1] B. Baschek. *Physica Scripta*, **T8** (1984) 21.
- [2] N. Grevesse. *Physica Scripta*, **T8** (1984) 49.
- [3] M. Inokuti. *Photochem. Photobio.*, **44** (1986) 279.
- [4] J.W. Gallagher, C.E. Brion, J.A.R. Samson, and P.W. Langhoff. *J. Phys. Chem. Ref. Data*, **17** (1988) 9.
- [5] G. Margaritondo. *Introduction to Synchrotron Radiation* (Oxford University Press, Oxford, 1988).
- [6] G.N. Greaves and I.H. Munro. *Synchrotron Radiation Sources and Applications* (IOP, Bristol, 1989).
- [7] J.D. Jackson. *Classical Electrodynamics*, Second Edition (John Wiley & Sons, New York, 1975).
- [8] D. Roy and D. Tremblay. *Rept. Prog. Phys.*, **53** (1990) 621.
- [9] J. Franck and G. Hertz. *Verhandl. Deut. Phys. Ges.*, **16** (1914) 457.
- [10] R.M. Eisberg. *Fundamentals of Modern Physics* (John Wiley & Sons, New York, 1961).
- [11] H. Bethe. *Ann. Phys.*, **5** (1930) 325.
- [12] M. Inokuti. *Rev. Mod. Phys.*, **43** (1971) 297.
- [13] M. Inokuti, Y. Itikawa, and J.E. Turner. *Rev. Mod. Phys.*, **50** (1978) 23.
- [14] E.N. Lassettre, A.S. Berman, S.M. Silverman, and M.E. Krasnow. *J. Chem. Phys.*, **40** (1964) 1232.
- [15] E.N. Lassettre, M.E. Krasnow, and S. Silverman. *J. Chem. Phys.*, **40** (1964) 1242.
- [16] E.N. Lassettre, A. Skeberle, M.A. Dillon, and K.J. Ross. *J. Chem. Phys.*, **48** (1968) 5066.
- [17] M.J. Van der Wiel and G. Wiebes. *Physica*, **53** (1971) 225.

- [18] M.J. Van der Wiel and G. Wiebes. *Physica*, **54** (1971) 411.
- [19] C.E. Brion. In *Physics of Electronic and Atomic Collisions*, S. Datz ed. (North-Holland, Amsterdam, 1982).
- [20] C.E. Brion, S. Daviel, R. Sodhi, and A.P. Hitchcock. *AIP Conference Proceedings—X-ray and Atomic Inner-Shell Physics*, **94** (1982) 429.
- [21] C.E. Brion. *Comm. At. Mol. Phys.*, **16** (1985) 249.
- [22] W.F. Chan. *PhD Thesis*, University of British Columbia (1992).
- [23] L.G. Christophorou. *Atomic and Molecular Radiation Physics* (Wiley—Interscience, New York, 1971).
- [24] G.R. Wight. *PhD Thesis*, University of British Columbia (1974).
- [25] W.F. Chan, G. Cooper, R.N.S. Sodhi, and C.E. Brion. *Chem. Phys.*, **170** (1993) 81.
- [26] W.F. Chan, G. Cooper, and C.E. Brion. *Phys. Rev. A*, **44** (1991) 186.
- [27] W.F. Chan, G. Cooper, X. Guo, and C.E. Brion. *Phys. Rev. A*, **45** (1992) 1420.
- [28] R.D. Hudson. *Rev. Geophys. Space Phys.*, **9** (1971) 305.
- [29] G.D. Zeiss, W.J. Meath, J.C.F. MacDonald, and D.J. Dawson. *Can. J. Phys.*, **55** (1977) 2080.
- [30] U. Fano and J.W. Cooper. *Rev. Mod. Phys.*, **40** (1968) 441; and **41** (1969) 724.
- [31] A.P. Hitchcock. *PhD Thesis*, University of British Columbia (1978).
- [32] A.P. Hitchcock. *Ultramicroscopy*, **28** (1989) 165.
- [33] A. Hamnett, W. Stoll, G. Branton, C.E. Brion, and M.J. Van der Wiel. *J. Phys. B*, **9** (1976) 945.
- [34] J. Slater. *Quantum Theory of Matter*, Second Edition (Mc Graw-Hill, New York, 1968).
- [35] H.F. Wellenstein, R.A. Bonham, and R.C. Ulsh. *Phys. Rev. A*, **8** (1973) 304.
- [36] T.C. Wong, J.S. Lee, H.F. Wellenstein, and R.A. Bonham. *J. Chem. Phys.*, **63** (1975) 1538.
- [37] R.S. Barbieri and R.A. Bonham. *Phys. Rev. A*, **45** (1992) 7929.

- [38] H.A. Bethe and E.E. Salpeter. *Quantum Mechanics of One- and Two-Electron Atoms* (Springer-Verlag, Berlin, 1957).
- [39] K. Siegbahn, C. Nordling, C. Johansson, J. Hedman, P.F. Heden, K. Hamrin, U. Gelius, T. Bergmark, L.O. Werme, R. Manne, and Y. Baer. *ESCA Applied to Free Molecules* (North-Holland, Amsterdam, 1969).
- [40] R.S. Mulliken. *J. Am. Chem. Soc.*, **86** (1964) 3183; **88** (1966) 1849; **91** (1969) 4615.
- [41] A.B.F. Duncan. *Rydberg Series in Atoms and Molecules* (Academic Press, New York, 1971).
- [42] K.L. Bell and A.E. Kingston. *J. Phys. B*, **8** (1975) L265.
- [43] M. Ya Amusia, N.A. Cherepkov, V. Radojevic, and D. Zivanovic. *J. Phys. B*, **9** (1976) L469.
- [44] S.M. Silverman and E.N. Lassettre. *J. Chem. Phys.*, **40** (1964) 1265.
- [45] C. Backx, R.R. Tol, G.R. Wight, and M.J. Van der Wiel. *J. Phys. B*, **8** (1975) 2050.
- [46] R.A. Bonham. *Chem. Phys. Letters*, **31** (1975) 559.
- [47] E. Clementi. *J. Chem. Phys.*, **38** (1963) 996, 1001.
- [48] A. Kumar, G.R.G. Fairley, and W.J. Meath. *J. Chem. Phys.*, **83** (1985) 70, and some of the references therein. See also references [67, 68] and some of the references therein.
- [49] H. Margerau. *Phys. Rev.*, **37** (1931) 1425 and **56** (1939) 1000.
- [50] A. Dalgarno and N. Lynn. *Proc. Phys. Soc.*, **70** (1957) 802.
- [51] A. Dalgarno and A.E. Kingston. *Proc. Phys. Soc.*, **72** (1958) 1053, **73** (1959) 455; and **78** (1961) 607.
- [52] P.J. Leonard and J.A. Barker. In *Theoretical Chemistry, Advances and Perspectives*, **1** (1975) 117.
- [53] J.O. Hirschfelder, W. Byers Brown, and S.T. Epstein. *Adv. Quant. Chem.*, **1** (1964) 255.
- [54] G.D. Zeiss, W.J. Meath, J.C.F. MacDonald, and D.J. Dawson. *Radiat. Res.*, **70** (1977) 284.

- [55] B.L. Jhanwar, W.J. Meath, and J.C.F. MacDonald. *Radiat. Res.*, **96** (1983) 20.
- [56] B.L. Jhanwar, W.J. Meath, and J.C.F. MacDonald. *Radiat. Res.*, **106** (1986) 288.
- [57] G.D. Zeiss and W.J. Meath. *Mol. Phys.*, **33** (1977) 1155, and references therein.
- [58] D.J. Margoliash and W.J. Meath. *J. Chem. Phys.*, **68** (1978) 1426.
- [59] H.A. Bethe, L.M. Brown, and J.R. Stehn. *Phys. Rev.*, **77** (1949) 370.
- [60] J.M. Harriman. *Phys. Rev.*, **101** (1956) 594.
- [61] P.K. Kabir and E.E. Salpeter. *Phys. Rev.*, **108** (1957) 1256.
- [62] E.E. Salpeter and M.H. Zaidi. *Phys. Rev.*, **125** (1962) 248.
- [63] P. Jørgensen, J. Oddershede, and N.H.F. Beebe. *J. Chem. Phys.*, **68** (1978) 2527.
- [64] F. Mulder, G.F. Thomas, and W.J. Meath. *Mol. Phys.*, **41** (1980) 249.
- [65] F. Mulder and W.J. Meath. *Mol. Phys.*, **42** (1981) 629.
- [66] B.L. Jhanwar and W.J. Meath. *Chem. Phys.*, **67** (1982) 185.
- [67] W.J. Meath and A. Kumar. *Int. J. Quant. Chem.*, **24** (1990) 501.
- [68] A. Kumar and W.J. Meath. *Theor. Chim. Acta*, **82** (1992) 131.
- [69] G.H.F. Diercksen, J. Oddershede, I. Paidarova, and J. Sabin. *Int J. Quant. Chem.*, **39** (1991) 755.
- [70] A.J. Thakkar, H. Hettema, and P.E.S. Wormer. *J. Chem. Phys.*, **97** (1992) 3252, and also submitted for publication.
- [71] H.A. Kramers and W. Heisenberg. *Z. Phys.*, **31** (1925) 681.
- [72] G.R. Burton, W.F. Chan, G. Cooper, C.E. Brion, A. Kumar, and W.J. Meath. *Can. J. Chem.*, **71** (1993) 341.
- [73] B.L. Jhanwar, W.J. Meath, and J.C.F. MacDonald. *Can. J. Phys.*, **59** (1981) 185; and **61** (1983) 1027.
- [74] A. Kumar and W.J. Meath. *Can. J. Phys.*, **63** (1985) 417.
- [75] A. Kumar and W.J. Meath. *Can. J. Chem.*, **63** (1985) 1616.
- [76] C. Backx and M.J. Van der Wiel. *J. Phys. B*, **8** (1975) 3020.

- [77] Y. Iida, F. Carnovale, S. Daviel, and C.E. Brion. *Chem. Phys.*, **105** (1986) 211, and references therein.
- [78] X. Guo, G. Cooper, W.F. Chan, G.R. Burton, and C.E. Brion. *Chem. Phys.*, **161** (1992) 453.
- [79] X. Guo, G. Cooper, W.F. Chan, G.R. Burton, and C.E. Brion. *Chem. Phys.*, **161** (1992) 471.
- [80] C.E. Brion and A. Hamnett. *Adv. Chem. Phys.*, **45** (1981) 1.
- [81] R. Hoffmann, G. Gaukler, G. Nolte, H. Schmidt-Böcking, and R. Schuch. *Nucl. Instrum. Methods*, **197** (1982) 391.
- [82] G. Cooper, Y. Zheng, G.R. Burton, and C.E. Brion. *Rev. Sci. Instrum.*, **64** (1993) 1140.
- [83] J. Berkowitz. *Photoabsorption, Photoionization and Photoelectron Spectroscopy* (Academic Press, New York, 1979).
- [84] J.A. Wheeler and J.A. Bearden. *Phys. Rev.*, **46** (1934) 755.
- [85] M. Inokuti. Private communication.
- [86] G.R. Burton, W.F. Chan, G. Cooper, and C.E. Brion. *Chem. Phys.*, **167** (1992) 349.
- [87] J.W. Au, G. Cooper, G.R. Burton, T.N. Olney, and C.E. Brion. *Chem. Phys.*, **173** (1993) 209.
- [88] W.F. Chan, G. Cooper, X. Guo, G.R. Burton, and C.E. Brion. *Phys. Rev. A*, **46** (1992) 149.
- [89] J.A.R. Samson and L. Yin. *J. Opt. Soc. Am. B*, **6** (1989) 2326.
- [90] J.A.R. Samson. *J. Opt. Soc. Am.*, **54** (1964) 6.
- [91] B. Peart and M.F.A. Harrison. *J. Phys. E*, **14** (1974) 1374.
- [92] L.A. Dietz. *Rev. Sci. Instrum.*, **36** (1965) 1763.
- [93] S. Daviel, C.E. Brion, and A.P. Hitchcock. *Rev. Sci. Instrum.*, **55** (1984) 182.
- [94] C.E. Kuyatt and J.A. Simpson. *Rev. Sci. Instrum.*, **38** (1967) 103.
- [95] K. Jost. *J. Phys. E*, **12** (1979) 1006.

- [96] W.F. Chan, G. Cooper, K.H. Sze, and C.E. Brion. *J. Phys. B*, **23** (1990) L523.
- [97] R.F. Egerton. *Electron Energy Loss Spectroscopy in the Electron Microscope* (Plenum Press, New York, 1986).
- [98] E.E. Muschlitz, Jr. *Science*, **159** (1968) 599.
- [99] J. Berkowitz. *Radiat. Phys. Chem.*, **32** (1988) 23.
- [100] G.C. Angel and J.A.R. Samson. *Phys. Rev. A*, **38** (1988) 5578.
- [101] J.A.R. Samson and G.C. Angel. *Phys. Rev. A*, **42** (1990) 1307.
- [102] A.L. Gray. *Spectrochim. Acta*, **40B** (1985) 1525.
- [103] T.W. Harquist, ed. *Molecular Astrophysics - A Volume Honouring Alexander Dalgarno* (Cambridge Press, Cambridge, 1990).
- [104] T. Watanabe, I. Shimamura, M. Shimizu, and Y. Itikawa, eds. *Molecular Processes in Space* (Plenum Press, New York, 1990).
- [105] H.R. Dickinson and W.C. Johnson, Jr. *J. Am. Chem. Soc.*, **96** (1974) 5050.
- [106] M. Ogawa and G.R. Cook. *J. Chem. Phys.*, **28** (1958) 747.
- [107] M. Ogawa and G.R. Cook. *J. Chem. Phys.*, **28** (1958) 747, grazing incidence.
- [108] A.J. Harrison, B.J. Cederholm, and M.A. Terwilliger. *J. Chem. Phys.*, **30** (1959) 355.
- [109] R.H. Huebner and R.J. Celotta. *Argonne National Laboratory Report ANL-7960 Pt. 1*.
- [110] J.B. Nee, M. Suto, and L.C. Lee. *Chem. Phys.*, **98** (1985) 147.
- [111] J.C. Person and P.P. Nicole. *Argonne National Laboratory Report ANL-7760 Pt. 1*, p. 97.
- [112] J.C. Person and P.P. Nicole. *J. Chem. Phys.*, **55** (1971) 3390.
- [113] J.C. Person and P.P. Nicole. *Argonne Natl. Lab. Radiolog. Environ. Res. Div. Ann. Rep. ANL 75-3 (1973/74) Part 1*, p. 53.
- [114] D.R. Salahub and C. Sandorfy. *Chem. Phys. Lett.*, **8** (1971) 71.
- [115] L. Sanson and N. Damany-Astoin. *C. R. Acad. Sci. Paris*, **250** (1960) 4138.

- [116] H. Tsubomura, K. Kimura, K. Kaya, J. Tanaka, and S. Nagakura. *Bull. Chem. Soc. Japan*, **37** (1964) 417.
- [117] L. de Reilhac and N. Damany. *J. Phys. (Paris)*, **32** (1971) C4.
- [118] E.S. Gluskin, L.A. Rapatskii, A.M. Raitsmring, and Yu. D. Tsvetkov. *Khim. Vys. Energ.*, **15** (1981) 85.
- [119] I. Ishii and A.P. Hitchcock. *J. Electron Spectrosc. Relat. Phenom.*, **46** (1988) 55.
- [120] B.L. Jhanwar and W.J. Meath. *Can. J. Chem.*, **62** (1984) 373.
- [121] G. Herzberg and G. Scheibe. *Z. Physik Chem.*, **B7** (1930) 390.
- [122] W.C. Price. *J. Chem. Phys.*, **3** (1935) 256.
- [123] W.J.G. Beynon and E.J. Evans. *Phil. Mag.*, **25** (1938) 476.
- [124] G. Wight and C.E. Brion. *J. Electron Spectrosc. Relat. Phenom.*, **4** (1974) 25.
- [125] G. Doolan and D. Liberman. *Phys. Scr.*, **36** (1987) 77.
- [126] G. Cooper, T. Ibuki, and C.E. Brion. *Chem. Phys.*, **140** (1990) 133.
- [127] G. Cooper, T. Ibuki, and C.E. Brion. *Chem. Phys.*, **140** (1990) 147.
- [128] E.B. Zarate, G. Cooper, and C.E. Brion. *Chem. Phys.*, **148** (1990) 277.
- [129] E.B. Zarate, G. Cooper, and C.E. Brion. *Chem. Phys.*, **148** (1990) 289.
- [130] G. Cooper, E.B. Zarate, R.K. Jones, and C.E. Brion. *Chem. Phys.*, **150** (1991) 237.
- [131] G. Cooper, E.B. Zarate, R.K. Jones, and C.E. Brion. *Chem. Phys.*, **150** (1991) 251.
- [132] W. Zhang, G. Cooper, T. Ibuki, and C.E. Brion. *Chem. Phys.*, **137** (1989) 391.
- [133] H. Ogata, H. Onizuka, Y. Nihei, and H. Kamada. *Chem. Lett.*, (1972) 895.
- [134] S. Katsumata, T. Iwai, and K. Kimura. *Bull. Chem. Soc. Japan*, **46** (1973) 3391.
- [135] K. Kimura, Y. Achiba, M. Morishita, and T. Yamazaki. *J. Electron Spectrosc. Relat. Phenom.*, **15** (1979) 269.
- [136] K.A.G. MacNeil and R.N. Dixon. *J. Electron Spectrosc. Relat. Phenom.*, **11** (1977) 315.

- [137] H. Ogata, H. Onizuka, Y. Nihei, and H. Kamada. *Bull. Chem. Soc. Japan*, **46** (1973) 3036.
- [138] J.B. Peel and G.D. Willet. *Aust. J. Chem.*, **28** (1975) 2357.
- [139] A.W. Potts, T.A. Williams, and W.C. Price. *J. Chem. Soc. Farad. Trans.*, **54** (1972) 104.
- [140] M.B. Robin and N.A. Kuebler. *J. Electron Spectrosc. Relat. Phenom.*, **1** (1972/1973) 13.
- [141] C. Utsunomiya, T. Kobayashi, and S. Nagakura. *Bull. Chem. Soc. Japan*, **53** (1980) 1216.
- [142] W. Von Niessen, G. Bieri, and L. Asbrink. *J. Electron Spectrosc. Relat. Phenom.*, **21** (1980) 175.
- [143] P.H. Cannington and N.S. Ham. *J. Electron Spectrosc. Relat. Phenom.*, **31** (1983) 175.
- [144] D. Nordfors, A. Nilsson, N. Mårtensson, S. Svensson, U. Gelius, and H. Ågren. *J. Electron Spectrosc. Relat. Phenom.*, **56** (1991) 117.
- [145] A. Minchinton, C.E. Brion, and E. Weigold. *Chem. Phys.*, **62** (1981) 369.
- [146] J. Berkowitz. *J. Chem. Phys.*, **69** (1978) 3044.
- [147] S.W. Bennett, J.B. Tellinghuisen, and L.F. Phillips. *J. Phys. Chem.*, **75** (1971) 719.
- [148] B. Brehm, V. Fuchs, and P. Kebarle. *Int. J. Mass. Spectrom. Ion Phys.*, **6** (1971) 279.
- [149] I. Omura, T. Kaneko, Y. Yamada, and K. Tanaka. *J. Phys. Soc. Japan*, **27** (1969) 981.
- [150] K.M.A. Refaey and W.A. Chupka. *J. Chem. Phys.*, **48** (1968) 5205.
- [151] P. Warneck. *Z. Naturforsch. Teil A*, **26** (1971) 2047.
- [152] S.H. Allam, M.D. Migahed, and A. El-Khodary. *Egypt. J. Phys.*, **13** (1982) 167.
- [153] C.S. Cummings and W. Bleakney. *Phys. Rev.*, **58** (1940) 787.
- [154] L. Friedman, F.A. Long, and M. Wolfsberg. *J. Chem. Phys.*, **27** (1957) 613.
- [155] E. von Puttkamer. *Z. Naturforsch. Teil A*, **25** (1970) 1062.

- [156] P. Wilmenius and E. Lindholm. *Arkiv Fys.*, **21** (1962) 97.
- [157] W.F. Chan, G. Cooper, and C.E. Brion. *Chem. Phys.*, **170** (1993) 123.
- [158] W.F. Chan, G. Cooper, and C.E. Brion. *Chem. Phys.*, **168** (1992) 375.
- [159] W.F. Chan, G. Cooper, and C.E. Brion. *Chem. Phys.*, **170** (1993) 111.
- [160] W.F. Chan, G. Cooper, and C.E. Brion. *Chem. Phys.*, **170** (1993) 99.
- [161] B.L. Henke, P. Lee, J.J. Tanaka, R.L. Shimabukuro, and B.K. Fujikawa. *At. Data Nucl. Data Tables*, **27** (1982) 1.
- [162] J.J. Yeh and I. Lindau. *At. Data Nucl. Data Tables*, **32** (1985) 1.
- [163] M.A. Dillon and M. Inokuti. *J. Chem. Phys.*, **74** (1981) 6271.
- [164] M. Inokuti and M.A. Dillon. In lecture presented at *XIIIth Yugoslav Summer School and International Symposium on Physics of Ionized Gases (SPIG)*, Sibenik, Yugoslavia, September 1984.
- [165] M.A. Dillon and M. Inokuti. *J. Chem. Phys.*, **82** (1985) 4415.
- [166] M.A. Dillon, M. Inokuti, and Z.-W. Wang. *Radiat. Res.*, **102** (1985) 151.
- [167] M. Robin. *Higher Excited States of Polyatomic Molecules—Vol. 1* (Academic Press, New York, 1974).
- [168] G. Dujardin, S. Leach, O. Dutuit, P.M. Guyon, and M. Richard-Viard. *Chem. Phys.*, **88** (1984) 339.
- [169] S.G. Lias, J.E. Bartmess, J.F. Liebman, J.L. Holms, R.D. Levin, and W.G. Mallard. *J. Phys. Chem. Ref. Data Supp. 1*, **17** (1988) 1.
- [170] F. Carnovale and C.E. Brion. *Chem. Phys.*, **74** (1983) 253.
- [171] K.H. Tan, C.E. Brion, Ph.E. Van der Leeuw, and M.J. Van der Wiel. *Chem. Phys.*, **29** (1978) 299.
- [172] W. Zhang, G. Cooper, T. Ibuki, and C.E. Brion. *Chem. Phys.*, **151** (1991) 343.
- [173] W. Zhang, G. Cooper, T. Ibuki, and C.E. Brion. *Chem. Phys.*, **151** (1991) 357.
- [174] W. Zhang, G. Cooper, T. Ibuki, and C.E. Brion. *Chem. Phys.*, **153** (1991) 491.
- [175] Y. Niwa, T. Nishimura, H. Nozoye, and T. Tsuchiya. *Int. J. Mass. Spec. Ion Phys.*, **30** (1979) 63.

- [176] T. Nishimura, Y. Niwa, T. Tsuchiya, and H. Nozoye. *J. Chem. Phys.*, **72** (1980) 2222.
- [177] Y. Niwa and T. Tsuchiya. *Adv. Mass. Spectrom.*, **8A** (1980) 56.
- [178] M.J. Van der Wiel, W. Stoll, A. Hamnett, and C.E. Brion. *Chem. Phys. Lett.*, **37** (1976) 240.
- [179] B.C. Cox. Diss. Liverpool, 1953. as referenced by Wilmenius and Lindholm [156].
- [180] S.W. Leifson. *Astrophys. J.*, **63** (1926) 73.
- [181] C.R. Zobel and A.B.F. Duncan. *J. Am. Chem. Soc.*, **77** (1955) 2611.
- [182] R.E. Rebbert and P. Ausloos. *J. Res. Nat. Bur. Stand.*, **75A** (1971) 481.
- [183] B.L. Sowers, M.W. Williams, R.N. Hamm, and E.T. Arakawa. *J. Chem. Phys.*, **57** (1972) 167.
- [184] B.R. Russell, L.O. Edwards, and J.W. Raymond. *J. Am. Chem. Soc.*, **95** (1973) 2129.
- [185] D.E. Robbins. *Int. Conf. Probl. Relat. Stratos.*, NASA-CR-154106 (1976) 255.
- [186] G.C. Causley and B.R. Russell. *J. Electron Spectrosc. Relat. Phenom.*, **11** (1977) 383.
- [187] C. Hubrich and F. Stuhl. *J. Photochem.*, **12** (1980) 93.
- [188] C. Roxlo and A. Mandl. *J. Appl. Phys.*, **51** (1980) 2969.
- [189] T. Ibuki, N. Takahashi, A. Hiraya, and K. Shobatake. *J. Chem. Phys.*, **85** (1986) 5717.
- [190] L.C. Lee and M. Suto. *Chem. Phys.*, **114** (1987) 423.
- [191] B.E. Cole and R.N. Dexter. *J. Quant. Radiat. Transfer*, **19** (1978) 303.
- [192] G. O'Sullivan. *J. Phys. B*, **15** (1982) 2385.
- [193] A. Hitchcock and C.E. Brion. *J. Electron Spectrosc. Relat. Phenom.*, **14** (1978) 417.
- [194] W. Zhang, T. Ibuki, and C.E. Brion. *Chem. Phys.*, **160** (1992) 435.
- [195] M.J.S. Dewar and S.D. Worley. *J. Chem. Phys.*, **50** (1969) 654.

- [196] J.C. Green, M.L.H. Green, P.J. Joachim, A.F. Orchard, and D.W. Turner. *Phil. Trans. Roy. Soc. London A*, **268** (1970) 111.
- [197] A.W. Potts, H.J. Lempka, D.G. Streets, and W.C. Price. *Phil. Trans. Roy. Soc. London A*, **268** (1970) 59.
- [198] R.N. Dixon, J.N. Murrell, and B. Narayan. *Mol. Phys.*, **20** (1971) 611.
- [199] P.J. Bassett and D.R. Lloyd. *J. Chem. Soc. A*, **1971** 641.
- [200] R.G. Edgell, I.L. Fragala, and A.F. Orchard. *J. Electron Spectrosc. Relat. Phenom.*, **17** (1979) 267.
- [201] W. Von Niessen, L. Asbrink, and G. Bieri. *J. Electron Spectrosc. Relat. Phenom.*, **26** (1982) 173.
- [202] T.A. Carlson, M.O. Krause, F.A. Grimm, P. Keller, and J.W. Taylor. *J. Chem. Phys.*, **77** (1982) 5340.
- [203] P.R. Keller, J.W. Taylor, T.A. Carlson, and F.A. Grimm. *Chem. Phys.*, **79** (1983) 269.
- [204] M.N. Piancastelli, P.R. Keller, J.W. Taylor, F.A. Grimm, T.A. Carlson, M.O. Krause, and D. Lichtenberger. *J. Electron Spectrosc. Relat. Phenom.*, **34** (1984) 205.
- [205] H. Shiromaru and S. Katsumata. *Bull. Chem. Soc. Japan*, **57** (1984) 3543.
- [206] J.-H. Fock and E.E. Koch. *Chem. Phys.*, **96** (1985) 125.
- [207] R.E. LaVilla and R.D. Deslattes. *J. Chem. Phys.*, **45** (1966) 3446.
- [208] T.D. Thomas. *J. Am. Chem. Soc.*, **92** (1970) 4184.
- [209] V.I. Nefedov. *Zh. Struct. Khim.*, **12** (1971) 276.
- [210] W.B. Perry and W.L. Jolly. *Chem. Phys. Lett.*, **17** (1972) 611.
- [211] F. Hopfgarten and R. Manne. *J. Electron Spec. Relat. Phenom.*, **2** (1973) 13.
- [212] W.B. Perry and W.L. Jolly. *Inorg. Chem.*, **13** (1974) 1211.
- [213] T. Ohta and J. Kuroda. *Bull. Chem. Soc. Japan*, **49** (1976) 2939.
- [214] E.J. Aitken, M.K. Bahl, K.D. Bomben, J.K. Gimzewski, G.S. Nolan, and T.D. Thomas. *J. Am. Chem. Soc.*, **102** (1980) 4873.

- [215] R.F. Baker and J.T. Tate. *Phys. Rev.*, **53** (1938) 683.
- [216] J.W. Warren and J.D. Craggs. *Mass Spectrometry* (Institute of Petroleum, London, 1952), as referenced by Farmer *et al.* [218] and Reed and Snedden [219] .
- [217] R.B. Bernstein, G.P. Semeluk, and C.B. Arends. *Anal. Chem.*, **25** (1953) 139.
- [218] J.B. Farmer, I.H.S. Henderson, F.P. Lossing, and D.G.H. Marsden. *J. Chem. Phys.*, **24** (1956) 348.
- [219] R.I. Reed and W. Snedden. *J. Chem. Soc. Farad. Trans.*, **54** (1958) 301.
- [220] R.E. Fox and R.K. Curran. *J. Chem. Phys.*, **34** (1961) 1595.
- [221] K. Watanabe, T. Nakayama, and J. Mottl. *J. Quant. Spectrosc. Radiat. Transfer*, **2** (1962) 369.
- [222] A.S. Werner, B.P. Tsai, and T. Baer. *J. Chem. Phys.*, **60** (1974) 3650.
- [223] A.W. Hanner, L.E. Abbey, D.E. Bostwick, E.M. Burgess, and T.F. Moran. *Org. Mass. Spectrom.*, **17** (1982) 19.
- [224] F.C.-Y. Wang and G.E. Leroi. *Ann. Isr. Phys. Soc.*, **6** (1984) 210.
- [225] C. Guenat, F. Maquin, D. Stahl, W. Koch, and H. Schwartz. *Int. J. Mass Spectrom. Ion Proc.*, **63** (1985) 265.
- [226] W. Kischlat and H. Morgner. *J. Electron Spectrosc. Relat. Phenom.*, **35** (1985) 273.
- [227] Y.J. Kime, D.C. Driscoll, and P.A. Dowben. *J. Chem. Soc. Farad. Trans. 2*, **83** (1987) 403.
- [228] I.R. Lambert, S.M. Mason, R.P. Tuckett, and A. Hopkirk. *J. Chem. Phys.*, **89** (1988) 2675.
- [229] I.R. Lambert, S.M. Mason, R.P. Tuckett, and A. Hopkirk. *J. Chem. Phys.*, **89** (1988) 2683.
- [230] K.Y. Kondrat'ev. *Russ. Chem. Rev.*, **59** (1990) 920.
- [231] H. Muto and K. Nunome. *J. Chem. Phys.*, **94** (1991) 4741.
- [232] E.J. Hintsa, X. Zhao, W.M. Jackson, W.B. Miller, A.M. Wodtke, and Y.T. Lee. *J. Phys. Chem.*, **95** (1991) 2799.
- [233] L.E. Manzer. *Science*, **209** (1990) 31.

- [234] J.W. Au, G. Cooper, and G.R. Burton C.E. Brion. Manuscript in preparation.
- [235] S.T. Manson, A. Msezane, A.F. Starace, and S. Shahabi. *Phys. Rev. A*, **20** (1979) 1005.
- [236] J.M. Tedder and P.H. Vidaud. *J. Chem. Soc. Faraday Trans. 2*, **75** (1979) 1648.
- [237] C.E. Brion, Th.M. El-Sherbini, and M.J. Van der Wiel. *Chem. Phys. Lett.*, **7** (1970) 161.
- [238] A. Yagishita, S. Arai, C.E. Brion, T. Hayaishi, J. Murakami, Y. Sato, and M. Ukai. *Chem. Phys. Lett.*, **132** (1986) 437.
- [239] G.G.B. de Sousa, P. Morin, and I. Nenner. *Phys. Rev. A*, **34** (1986) 4770.
- [240] I. Nenner, P. Morin, M. Simon, N. Levasseur, and P. Millie. *J. Electron Spectrosc. Relat. Phenom.*, **52** (1990) 623.
- [241] K. Watanabe. *J. Chem. Phys.*, **26** (1957) 542.
- [242] E.I. Miner. *Phys. Today*, **43** July (1990) 40.
- [243] M.-J. Hubin-Franskin, J. Delwiche, F. Tollet, M. Furlan, and J.E. Collin. *J. Phys. B*, **21** (1988) 189.
- [244] G.D. Zeiss, W.J. Meath, J.C.F. MacDonald, and D.J. Dawson. *Mol. Phys.*, **39** (1980) 1055.
- [245] W.J. Meath, D.J. Margoliash, B.L. Jhanwar, A. Koide, and G.D. Zeiss. In *Intermolecular Forces*, B. Pullman ed., (Reidel, Dodrecht, 1981), pp 101.
- [246] B.W. Yates, D.M. Shinozaki, A. Kumar, and W.J. Meath. *J. Polymer Sci. (Physics)*, **30** (1992) 185.
- [247] J.K. Dixon. *Phys. Rev.*, **43** (1933) 711.
- [248] A.B.F. Duncan. *Phys. Rev.*, **47** (1935) 822.
- [249] A.B.F. Duncan. *Phys. Rev.*, **50** (1936) 700.
- [250] A.B.F. Duncan and G.R. Harrison. *Phys. Rev.*, **49** (1936) 211.
- [251] A.E. Douglas and J.M. Hollas. *Can. J. Phys.*, **39** (1961) 479.
- [252] A.D. Walsh and P.A. Warsop. *Trans. Faraday Soc.*, **57** (1961) 345.

- [253] C.M. Humphries, A.D. Walsh, and P.A. Warsop. *Discuss. Faraday Soc.*, **35** (1963) 148.
- [254] A.E. Douglas. *Discuss. Faraday Soc.*, **35** (1963) 158.
- [255] R.G. Schmitt and R.K. Brehm. *Appl. Opt.*, **5** (1966) 1111.
- [256] L.D. Ziegler. *J. Chem. Phys.*, **82** (1985) 664.
- [257] P. Rosmus, P. Botschwina, H.-J. Werner, V. Vaida, P.C. Engelking, and M.I. McCarthy. *J. Chem. Phys.*, **86** (1987) 6677.
- [258] V. Vaida, M.I. McCarthy, P.C. Engelking, P. Rosmos, H.J. Werner, and P. Botschwina. *J. Chem. Phys.*, **86** (1987) 6669.
- [259] W.R. Harshbarger. *J. Chem. Phys.*, **53** (1970) 903.
- [260] W.R. Harshbarger. *J. Chem. Phys.*, **54** (1970) 2504.
- [261] W.R. Harshbarger, A. Skeberle, and E.N. Lassettre. *J. Chem. Phys.*, **54** (1971) 3784.
- [262] G.C. Nieman and S.D. Colson. *J. Chem. Phys.*, **68** (1978) 5656.
- [263] G.C. Nieman and S.D. Colson. *J. Chem. Phys.*, **71** (1979) 571.
- [264] J.H. Glowonia, S.J. Riley, S.D. Colson, and G.C. Nieman. *J. Chem. Phys.*, **72** (1980) 5998.
- [265] J.H. Glowonia, S.J. Riley, S.D. Colson, and G.C. Nieman. *J. Chem. Phys.*, **73** (1980) 4296.
- [266] R.J. Thompson and A.B.F. Duncan. *J. Chem. Phys.*, **14** (1946) 573.
- [267] E. Tannenbaum, E.M. Coffin, and A.J. Harrison. *J. Chem. Phys.*, **21** (1953) 311.
- [268] K. Watanabe. *J. Chem. Phys.*, **22** (1954) 1564.
- [269] H. Sun and G.L. Weissler. *J. Chem. Phys.*, **23** (1955) 1160.
- [270] W.C. Walker and G.L. Weissler. *J. Chem. Phys.*, **23** (1955) 1540.
- [271] P.H. Metzger and G.R. Cook. *J. Chem. Phys.*, **41** (1964) 642.
- [272] B.A. Thompson, P. Harteck, and R.R. Reeves, Jr. *J. Geophys. Res.*, **68** (1963) 6431.

- [273] K. Watanabe and S.P. Sood. *Sci. Light*, **14** (1965) 36.
- [274] L. de Reilhac and N. Damany. *Spectrochim. Acta*, **26A** (1970) 801.
- [275] S. Durmaz, J.N. Murrell, J.M. Taylor, and R. Suffolk. *Mol. Phys.*, **19** (1970) 533.
- [276] K.A. Dick and A.O. Ziko. *Astrophys. J.*, **182** (1973) 609.
- [277] C. Bertrand, G. Collin, and H. Gagnon. *J. Chim. Phys.*, **72** (1975) 719.
- [278] M. Suto and L.C. Lee. *J. Chem. Phys.*, **78** (1983) 4515.
- [279] J.A.R. Samson, G.N. Haddad, and L.D. Kilcoyne. *J. Chem. Phys.*, **87** (1987) 6416.
- [280] T.J. Xia, T.S. Chien, C.Y.R. Wu, and D.L. Judge. *J. Quant. Spectrosc. Radiat. Transfer*, **45** (1991) 77.
- [281] J.A. Syage, R.B. Cohen, and J. Steadman. *J. Chem. Phys.*, **97** (1992) 6072.
- [282] M.J. Van der Wiel and C.E. Brion. *J. Electron Spectrosc. Relat. Phenom.*, **1** (1972/73) 443.
- [283] C.E. Brion, A. Hamnett, G.R. Wight, and M.J. Van der Wiel. *J. Electron Spectrosc. Relat. Phenom.*, **12** (1977) 323.
- [284] G.R. Wight, M.J. Van der Wiel, and C.E. Brion. *J. Phys. B*, **10** (1977) 1863.
- [285] G. Herzberg. *Molecular Spectra and Molecular Structure III. Electronic Spectra and Electronic Structure of Polyatomic Molecules* (Van Nostrand Reinhold Co., New York, 1966).
- [286] A. Kumar, W.J. Meath, G.R. Burton, G. Cooper, W.F. Chan, and C.E. Brion. Unpublished work.
- [287] O.E. Frivold, O. Hassel, and S. Rustad. *Phys. Z.*, **38** (1937) 191.
- [288] S. Friberg. *Z. Phys.*, **41** (1927) 378.
- [289] C. Cuthbertson and M. Cuthbertson. *Phil. Trans. R. Soc., London, Ser. A*, **213** (1913) 1.
- [290] K. Kimura, S. Katsumata, Y. Achiba, T. Yamazaki, and S. Iwata. *Handbook of HeI Photoelectron Spectra of Fundamental Organic Molecules* (Japan Scientific Press, Tokyo, 1981).
- [291] B.E. Mills, R.L. Martin, and D.A. Shirley. *J. Am. Chem. Soc.*, **98** (1976) 2380.

- [292] G.R. Wight, M.J. Van der Wiel, and C.E. Brion. *J. Phys. B*, **9** (1976) 675.
- [293] C. Backx, G.R. Wight, R.R. Tol, and M.J. Van der Wiel. *J. Phys. B*, **8** (1975) 3007.
- [294] B. Schiff and C.L. Peckeris. *Phys. Rev.*, **134** (1964) 638.
- [295] B. Schiff, C.L. Peckeris, and Y. Accad. *Phys. Rev. A*, **4** (1971) 885.
- [296] A.C. Allison and A. Dalgarno. *Mol. Phys.*, **19** (1970) 567.
- [297] R.N. Compton, J.A. Stockdale, and P.W. Reinhardt. *Phys. Rev.*, **180** (1969) 111.
- [298] K.E. Johnson and S. Lipsky. *J. Chem. Phys.*, **66** (1977) 4719.
- [299] T. Abuain, I.C. Walker, and D.F. Dance. *J. Chem. Soc. Faraday Trans. 2*, **80** (1984) 641.
- [300] M.B. Arfa and M. Tronc. *Chem. Phys.*, **155** (1991) 143.
- [301] P. Avouris, A.R. Rossi, and A.C. Albrecht. *J. Chem. Phys.*, **74** (1981) 5516.
- [302] W.J. Meath. Private communication.
- [303] V.N. Akimov, A.S. Vinogradov, and A.V. Zhadenov. *Opt. Spektrosk.*, **65** (1988) 349.
- [304] W. Eberhardt, T.K. Sham, R. Carr, S. Krummancer, M. Strogina, S.L. Weng, and D. Wesner. *Phys. Rev. Lett.*, **50** (1983) 1038.
- [305] G.F. Thomas and W.J. Meath. *Mol. Phys.*, **34** (1977) 113.
- [306] R.J. Pazur, A. Kumar, R.A. Thuraisingham, and W.J. Meath. *Can. J. Chem.*, **66** (1988) 615.
- [307] E.A. Moelwyn-Hughes. *Physical Chemistry*, 2 ed., (Pergamon Press, New York, 1964).
- [308] F.U. Wolf. *Hand-und-Jahrbuch der Chemischen Physik, Band. 6, Abschn. I, Leipzig, Germany*, (1935) s262.
- [309] J.M.A. De Bruyne and C.P. Smyth. *J. Am. Chem. Soc.*, **57** (1935) 1203.
- [310] B.L. Henke, R.L. Elgin, R.E. Lent, and R.B. Ledingham. *Norelco Rep.*, **14** (1967) 112.
- [311] M. Grupta and S. Bhattacharyya. *J. Chem. Soc. Faraday Trans. 2*, **80** (1984) 1405.

- [312] R.M. Metzger and C.H. Rhee. *Mol. Cryst. Liq. Cryst.*, **85** (1982) 81.
- [313] R.D. Amos, N.C. Handy, P.J. Knowles, J.E. Rice, and A.J. Stone. *J. Phys. Chem.*, **89** (1985) 2186.
- [314] P. Lazzeretti and R. Zanasi. *J. Chem. Phys.*, **74** (1981) 5216.
- [315] J.G.C.M. Van Duijneveldt-Van De Rijdt and F.B. Van Duijneveldt. *J. Mol. Struct.*, **89** (1982) 185.
- [316] M. Bulski, P.E.S. Wormer, and A. van der Avoird. *J. Chem. Phys.*, **94** (1991) 491.
- [317] S.Y. Liu, C.E. Dykstra, K. Kolenbrander, and J.M. Lisy. *J. Chem Phys.*, **85** (1986) 2077.
- [318] H.-J. Werner and W. Meyer. *Mol. Phys.*, **31** (1976) 855.
- [319] G.H.F. Diercksen and A.J. Sadlej. *Mol. Phys.*, **57** (1986) 509.
- [320] G. Maroulis. *Chem. Phys. Lett.*, **195** (1992) 85.
- [321] P.E.S. Wormer and H. Hettema. *J. Chem. Phys.*, **97** (1992) 5592.
- [322] E.-A. Reinsch. *J. Chem. Phys.*, **83** (1985) 5784.
- [323] G.R. Burton, W.F. Chan, G. Cooper, and C.E. Brion. *Chem. Phys.* Accepted for publication 1993.
- [324] S. Leach. 4th *Eur. Workshop on Molecular Spectroscopy and Photon Induced Dynamics* (Oxford) 1987.
- [325] M. Feston. 4th *Eur. Workshop on Molecular Spectroscopy and Photon Induced Dynamics* (Oxford) 1987.
- [326] B. Fegley, Jr. and R.G. Prinn. *Nature*, **318** (1985) 48; and *Astrophys. J.*, **299** (1985) 1067.
- [327] C.M. Leung, E. Herbst, and W.F. Huebner. *Astrophys. J.*, **56** (1984) 231.
- [328] D.F. Grosjean and P. Bletzinger. *IEEE J. Quant. Elec.*, **QE13** (1977) 898.
- [329] K. Kimura and K. Osafune. *Mol. Phys.*, **29** (1975) 1073.
- [330] P. Finn, R.K. Pearson, J.M. Hollander, and W.L. Jolly. *Inorg. Chem.*, **10** (1971) 378.
- [331] J.S. Jen and T.D. Thomas. *J. Electron Spectrosc. Relat. Phenom.*, **4** (1974) 43.

- [332] W.P. Perry, T.F. Schaar, and W.L. Jolly. *J. Am. Chem. Soc.*, **97** (1975) 4899.
- [333] R. McClaren, S.A.C. Clark, I. Ishii, and A.P. Hitchcock. *Phys. Rev. A*, **36** (1987) 1683.
- [334] R.N.S. Sodhi and C.E. Brion. *J. Electron Spectrosc. Relat. Phenom.*, **37** (1985) 97.
- [335] R.N.S. Sodhi and C.E. Brion. *J. Electron Spectrosc. Relat. Phenom.*, **37** (1985) 125.
- [336] R.N.S. Sodhi and C.E. Brion. *J. Electron Spectrosc. Relat. Phenom.*, **37** (1985) 145.
- [337] R.N.S. Sodhi and C.E. Brion. *J. Electron Spectrosc. Relat. Phenom.*, **36** (1985) 187.
- [338] A.O. Bawagan and C.E. Brion. *Chem. Phys. Letters*, **137** (1987) 573.
- [339] A.O. Bawagan and C.E. Brion. *Chem. Phys.*, **123** (1988) 51.
- [340] G.R. Burton, G. Cooper, W.F. Chan, C.E. Brion, A. Kumar, and W.J. Meath. *Can. J. Chem.* Accepted for publication 1993.
- [341] K.L. Ramaswamy. *Proc. Indian Acad. Sci.*, **A4** (1936) 675.
- [342] S. Kaur, V. Saxena, R.C. Rastogi, and N.K. Ray. *Indian J. Chem.*, **27A** (1988) 1013.
- [343] A.T. Amos and J.A. Yoffe. *J. Chem. Phys.*, **63** (1975) 4723.
- [344] A.A. Bakke, H.-W. Chen, and W.L. Jolly. *J. Electron Spectrosc. Relat. Phenom.*, **20** (1980) 333.